Systematic Design, Modeling and Simulation of a Biped Robot

Vom Promotionsausschuss der
Technischen Universität Hamburg

zur Erlangung des akademischen Grades

Doktor-Ingenieur (Dr.-Ing.)

genehmigte Dissertation (Monografie)

von
Shucen Du

aus
Shaanxi, China

2025

1. Gutachter: Prof. Dr.-Ing. habil. Prof. h. c. Dr. E. h. Josef Schlattmann

2. Gutachter: Prof. Dr. rer. nat. habil. Norbert P. Hoffmann

Tag der mündlichen Prüfung: 21.10.2024

Autor : https://orcid.org/0000-0002-2024-928X

DOI: https://doi.org/10.15480/882.13707

Handle: https://hdl.handle.net/11420/52056

Acknowledgement

This dissertation is part of the CENTAUROB research series conducted by the research group System Technologies and Engineering Design Methodology (AmP) at Hamburg University of Technology. My doctoral study here has been the most significant chapter of my life.

First and foremost, I would like to express my deepest gratitude to my supervisor, Professor Josef Schlattmann. His vast knowledge and insights have been a source of inspiration, his patience alleviated the anxieties of living abroad, and his unwavering support bolstered my determination to complete this study. It has been an honour to be his student.

I am equally grateful to Professor Norbert Hoffmann, my second supervisor, for his invaluable suggestions and for his thought-provoking questions that offered new perspectives on my research. My sincere thanks also go to the chair of the doctoral committee, Professor Hermann Lödding, for his meticulous organization of my oral defence and final examination.

I would like to extend my heartfelt thanks to my colleagues for their generous support throughout my studies. In particular, I wish to acknowledge Reinhold Grube, Mekonnen Tesfay Tesfu, Andreas Japing, Steffen Vagts, Viktor Krasmik, Alex Schimanowski, Oday Abdullah, Nicolaj Baramsky, and Ake Ewald. I am especially grateful to Arthur Seibel and Stefan Schulz, whose invaluable insights greatly contributed to my research.

A special note of appreciation is dedicated to Professor Mo, my former advisor during my master's studies, for his valuable advices at the early stages of my doctoral journey.

Finally, I am deeply indebted to my parents and my children for their unwavering support in all my decisions. Above all, I owe my profound gratitude to my beloved wife, Mrs. Yunhe Fan, for her boundless patience and encouragement. Without her steadfast support, this dissertation would not have been possible.

Shucen Du
Hamburg, October 2024

Abstract

This dissertation presents the design and development of CENTAUROB, a bipedal robot equipped with 6-DOF parallel kinematic mechanism (PKM) structured legs. Bipedal robots have significant potential across various fields, including industrial automation and healthcare. The research encompasses structure synthesis, kinematic and dynamic modelling, load prediction, and gait stability analysis.

After evaluating multiple PKM configurations, a PKM[6,3] structure with double Cardan joints was selected for its compactness and controllability. This configuration reduces computational demands for kinematics, which is essential for real-time control. Based on this configuration, a complete kinematic model was developed, considering the motion of every individual rigid body. The model facilitates the analysis of movement characteristics, focusing on optimizing workspace, dexterity, and avoiding singularities. Furthermore, this work addresses PKM-specific control challenges, such as forward kinematics and passive actuator rotations.

An inverse dynamic model (IDM), based on the virtual work principle, enables accurate predictions of dynamic loads, which are critical for optimizing actuator performance. The load-split algorithm ensures a balanced distribution of loads between the two legs, contributing to the stability of both feet.

Simulation-based analyses evaluate static and semi-dynamic stability using indicators such as the ground centre of mass (GCoM) and foot rotational indicator (FRI). The results demonstrate that CENTAUROB can achieve stable gait patterns with appropriate control strategies. Future work will focus on refining physical measurements, optimizing load distribution for energy efficiency, and developing advanced control algorithms, further enhancing CENTAUROB as a versatile and efficient platform for complex environments.

Keywords: biped robot, parallel kinematic mechanism, dynamics simulation, gait stability.

Zusammenfassung

Der zweibeinige Roboter CENTAUROB, entwickelt für das Gehen auf unebenem Terrain, besitzt zwei 6-DOF-Parallelschwenkmechanismen als Beine. Diese Arbeit umfasst die Entwicklungsphasen von Struktursynthese, kinematischer und dynamischer Modellierung bis zur Gangstabilität. Verschiedene Formationen von 6-DOF-Beinen wurden durch Analyse kinematischer Grundketten untersucht und das Design mit Doppel-Kardangelenken vorgestellt. Das Problem der Passivrotation wurde durch vollständige kinematische Modellierung gelöst. Das inverse Dynamikmodell wurde entwickelt und die halbdynamische Gangstabilität durch die Analyse des Fußrotationsindikators mittels Lastverteilungsalgorithmus sichergestellt.

Schlüsselwörter: Zweibeiniger Roboter, Parallelkinematikmechanismus, Dynamiksimulation, Gangstabilität.

Contents

Abbreviations and Symbols

Abbreviations

BKC	basic kinematic chains
C	Cardan joint
CoM	centre of mass
CoP	centre of pressure
CP	capture point
DOF	degree of freedom
eq.	equation
fig.	figure
FKP	forward kinematic problem
FRI	foot rotational indicator
FZMP	fictitious ZMP
GCI	global condition index
GCoM	ground centre of mass
H	helical kinematic pair
HSOC	hybrid SOC
IDM	inverse dynamic model
IKM	inverse kinematic model
L	linear actuators
l (subscript)	limbs, as SOC or HSOC
P	prismatic kinematic pair (underlined if actuated)

Pa (subscript)	PKM
PKM	parallel kinematic mechanism
R	rotational kinematic pair
S	spherical kinematic pair
S (subscript)	SOC
SLC	single looped kinematic chain
SOC	single open kinematic chain
U	universal joints
ZMP	zero moment point

Romanic Symbols

-A, -B, …, -F	index of linear actuators
$\boldsymbol{A_1}$	load split diagonal matrix between two feet
a_{f1x}, a_{f1y}, a_{m1z}	horizontal load split parameters
a_{f1z}, a_{m1x}, a_{m1y}	vertical load split parameters
$\boldsymbol{C}_{\mathrm{H}}$	Clifford operator
$\boldsymbol{d}$	3D translational displacement vector
e	unitary group member,
{E}	inertial coordinates system
$\boldsymbol{F}$	6-D force vector
F	mobility of a kinematic mechanism
f_i	DOF of the i-th kinematic pair
$(\boldsymbol{F}_{\Sigma}, \boldsymbol{M}_{\Sigma})$	dynamic load
{F$_i$}	coordinates system of foot platform i

$\boldsymbol{G}$	group
g	gravitational acceleration constant
$\boldsymbol{H}$	homogeneous *SE*(3) operator
{H}	coordinates system of hip platform
{H_i}	the local coordinates system of hip platform on leg-*i*
k	coupling degree, also the sequence index
$\boldsymbol{M}_{\mathrm{S}}$, $\boldsymbol{M}_{\mathrm{L}}$, $\boldsymbol{M}_{\mathrm{Pa}}$	output motion matrix of a SOC, a SLC and a PKM
$\dot{\boldsymbol{M}}_{\mathrm{S}}$, $\dot{\boldsymbol{M}}_{\mathrm{L}}$,$\dot{\boldsymbol{M}}_{\mathrm{Pa}}$	output velocity matrix of a SOC, a SLC and a PKM
P	pitch of a screw thread, also a point
$\boldsymbol{p}$	location vector of a point
$\boldsymbol{Q}$, $\boldsymbol{Q}^*$	quaternions and its conjugate
$\widehat{\boldsymbol{Q}}$	dual-quaternions
$\widehat{\boldsymbol{Q}}^*$ $\widehat{\boldsymbol{Q}}^\circ$ $\widehat{\boldsymbol{Q}}^\sim$	three forms of conjugates of a dual-quaternions
$\boldsymbol{q}$	generalized coordinates
$\boldsymbol{R}$	rotation matrix
$\Re$	real number field
Re	real part of a complex number
$\boldsymbol{I}$	unitary matrix, also moment of inertia
Im	imaginary part of a complex number
I_{s}	screw singular indicator
$\boldsymbol{J}$, $\boldsymbol{J}^{-1}$	Jacobian and inverse Jacobian matrix
j = A, B,…, F	index of linear actuators
$\boldsymbol{l}$, l	vector representing the linear actuator and its length
{$L_{ij\mathrm{N}}$}, {$L_{ij\mathrm{S}}$}	the screw nut and screw shaft of a linear actuator

$\boldsymbol{r}$	3D rotational displacement vector
$\mathcal{S}$	a screw
$\boldsymbol{s}$, $\boldsymbol{s}_0$	the primary part and auxiliary part of a screw
$\mathbb{S}$	a screw system
SE(3), *se*(3)	special Euclidean group and its *Lie* algebra
SO(3), *so*(3)	rotation group and its *Lie* algebra
$\boldsymbol{t}$	transformation displacement
t	time
$\boldsymbol{v}$	velocity vector
$\boldsymbol{X}$, $\dot{\boldsymbol{X}}$, $\ddot{\boldsymbol{X}}$	generalized coordinates and its 1st and 2nd order differentials
$\boldsymbol{x}$, $\boldsymbol{y}$, $\boldsymbol{z}$, x, y, z	axes of coordinates and vector components along them

Greek Symbols

α, β, γ	relative angular displacements
Δ_i	constraint degree of BKC-*i*
κ	condition number
λ	eigenvalue
ξ_{S}	rank of a output motion matrix, also the connectivity, of SOC
ξ_{SR}, ξ_{ST}	numbers of independent rotational and translational outputs
π	plane
$\boldsymbol{\tau}$, $\boldsymbol{\tau}_{ij}$	actuating force assemble vector and actuating force vectors
$\boldsymbol{\Omega}$	one element of *se*(3)
$\boldsymbol{\omega}$, $\tilde{\boldsymbol{\omega}}$	one element of *so*(3) and its skew-symmetric matrix
$\boldsymbol{\varpi}$	non-unitary $\boldsymbol{\omega}$

List of Figures

List of Tables

Chapter 1
Motivation and Introduction

Within the realm of robotics, there has been a noteworthy surge in advancements, especially in the exploration and development of bipedal robots. They are designed to emulate the human form with a pair of legs, carry profound significance across diverse domains, spanning from industrial applications to healthcare and disaster response.

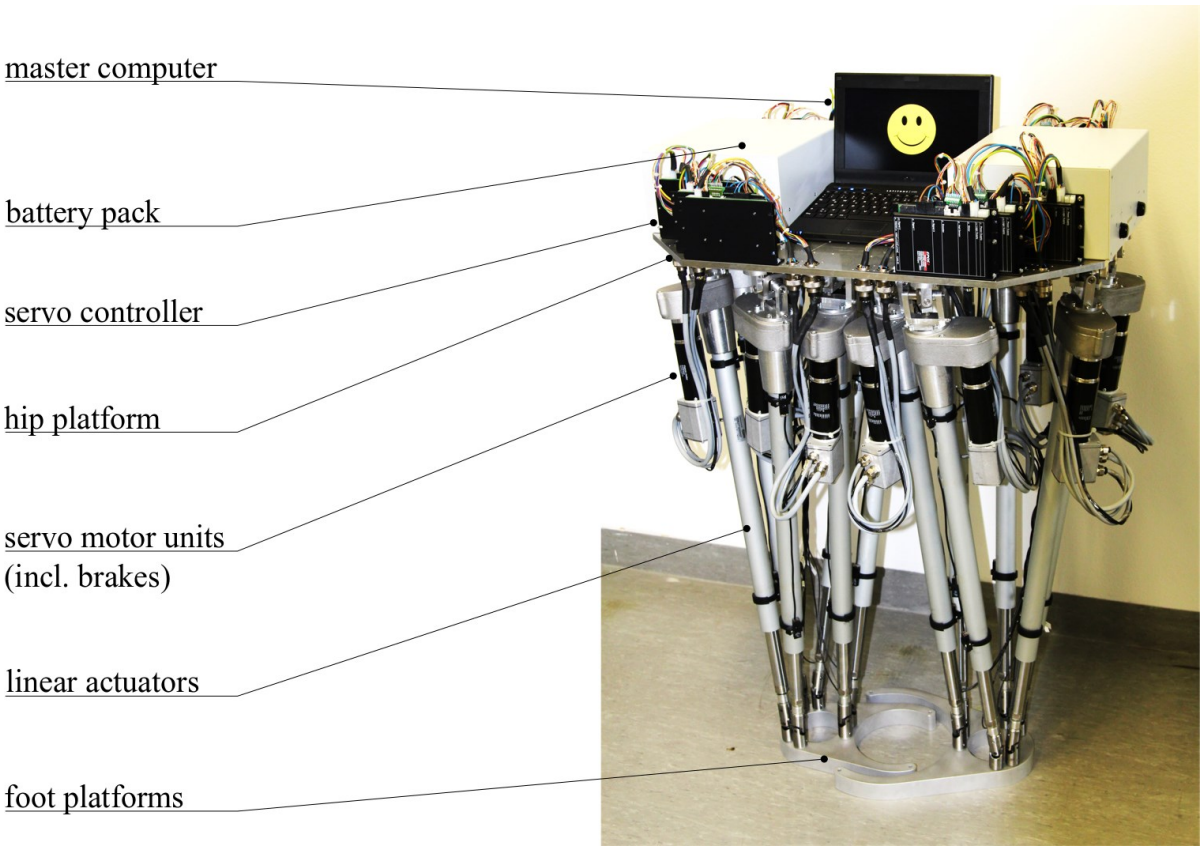

Figure 1.1. The composition of bipedal walking mechanism, CENTAUROB.

The design and development of a robot system are always systematic works. From the innovation of the working mechanism to the structure synthesis, parameter design, optimization, modelling and control, each phase refers to one or more subjects. The present researches focus mainly on one or more phases of the developments of a robot system, especially on the development of bipeds with serial kinematic mechanism (SKM) legs. Meanwhile, the biped robot with parallel kinematic mechanism (PKM) legs lacks studies and application practices. The aim of this work is to represent the systematic development process of a biped walking mechanism with parallel structured legs, CENTAUROB, as fig. 1.1.

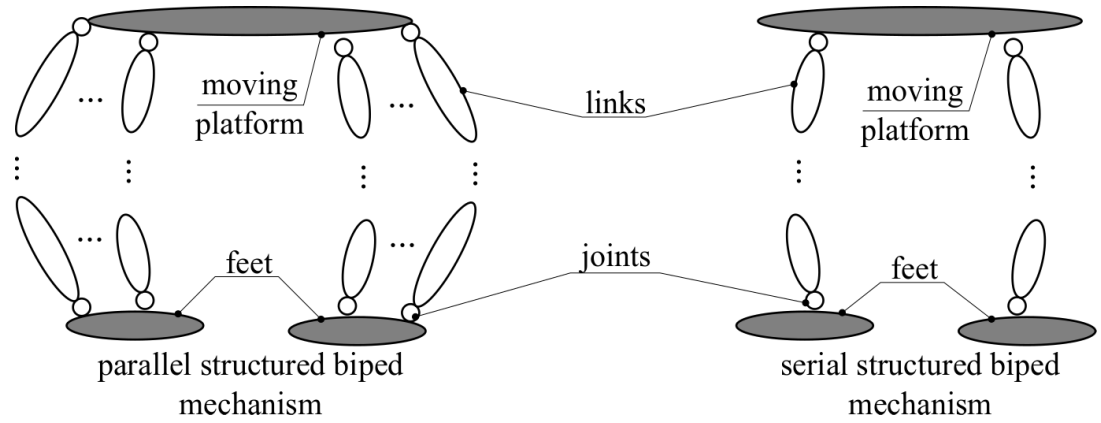

Figure 1.2. The topological formations of parallel and serial structured walking mechanisms.

The formation of a biped robot leg can be arranged in serially and parallel links. Their topological structure can be seen in fig. 1.2. Many comparisons between two ideas were made by researchers, such as Dukovski in [1.1], Patel and George in [1.2]. As the previous work compared in [1.3], the advantages of serial structure are widely thought as: larger workspaces, higher workspace/robot size ratios, easier dynamic solving, among the others. Contrarily, a parallel mechanism shows its advantages in: stiffness, payload/weight ratio, repeatability, small inertia, etc. For individual transportation, the demand for velocity and large step length is minor, but safety and quick response to force interference (e.g. movements of passenger) become more important. Also, along the development of digital processors and sensors, the difficulties of modelling and solving dynamics can be compensated in a rank. For personal transportation, a biped robot formed by parallel mechanisms could be a competitive alternative.

To confirm the structure and types of joints of a robot, a synthesis of a robot should be made. During this process, the objectives should be firstly defined, such as the desired degree of freedom (DOF), workspace, payloads, and tasks specification. Then, the kinematic structure should be determined considering the design objectives. Afterward, the types of joints should be confirmed. The widely used lower joints can be sorted as prismatic (linear), revolute (rotational), and spherical joints. Additionally, a lot of combinations of different joints derive different joints, such as helical pairs, universal joints, teeth pairs, and so on. The configuration should be then defined by considering the design objectives. Nevertheless, the structure synthesis is a process that should be continuously repeated during other development phases. If the conflict took place during the analysing, control designing, or even during utilization of a robot system, the synthesis should be repeated.

Once a composition method of a robot is confirmed, its kinematics model should be established. As the foundation of kinematic and dynamic analysis, the inverse Jacobians, or in other words, the velocity relation between all the rigid bodies and the moving platforms (feet and hip), should be derived. The inverse Jacobian of linear actuator lengths is the key parameter, since the lengths are the control variable and connect to many kinematic and dynamic properties. The kinematic properties should then be analysed to verify its feasibility in fulfilling the design objectives, such as the workspace, dexterity, and so on. This will provide the feedback for design optimization. At the same time, the risk of singularity in the workspace should be verified to prevent the control difficulties caused by unexpected additional DOF or loss of DOF.

There are two parasitic problems that must be solved due to the composition of CENTAUROB. The first problem is the passive rotation between the upper and lower part of the linear actuators. Due to the selection of lead screws, the relative rotation will change their length. This length deviation will cause a very rare kinetic burden during operation of the robot, but it will cause significant internal tension in the structure, whereas the PKM structure is adopted. This passive rotation was usually neglected by previous researches and can be predicted by fully solving the kinematics of individual rigid bodies.

The second problem is the forward kinematic problem (FKP) of PKMs. The importance of this problem is shown in the fields of position control, system calibration, real-time control, along with others. For a PKM, it is usually impossible to obtain a closed solution for FKP. The computation and solution numbers depend highly on the topological structure. In this work, a PKM-[6,3] structure (6 joint points on one platform and 3 on the other) will be used, and the FKP solution number is limited to four.

Due to the parallel structure, a real-time forward dynamic control is normally difficult. The reason is similar to that of the FKP of a PKM. To optimize the control of single actuators, predicting the dynamic load on each is necessary. The inverse dynamic model is the pre-condition. There are various methods of dynamic modelling. Here, the virtual work principle will be adopted. This method requires complete inverse Jacobians of rigid bodies in the system, if a more accurate prediction is needed. Thus, the 6-dimensional acceleration and velocity relations of each part with respect to feet and hip must be derived.

The aim of CENTAUROB is to realize bipedal walking. The stability is the most important consideration in this field. The choice of stability indicator depends on the type of walking. For static walking, the ground centre of mass (GCoM) should always fall inside the support polygon (SP). For a semi-dynamic walking, other indicators should be used, such as foot rotational indicator (FRI) and capture point (CP). For long term stability, the logic is different. The walking must not comprise of stable single steps, but rather of stable repeatability of one or several walking states. The walking stability analysis will provide the accordance of gait optimization.

In this work, the walking simulation will be based on semi-dynamic walking. Therefore, there will be a relatively long period of over-actuated state, namely, the hip will be driven by two 6-dimensional legs. The dynamic load must be split in this case to ensure the stability of both feet. This was also rarely considered in other bipedal robot research.

The thesis will be organized as follows. The structure synthesis will be performed first in Chapter 2. The different formations of 6-DOF PKMs will be analysed based on screw theory

and topological analysis. Before further analysis, some basic concepts of the group theory, its algebra and representation will be reviewed in Chapter 3. Then, the inverse kinematic model (IKM) will be founded in both matrix form and quaternions form in Chapter 4. Moreover, the FKP solution will be provided in this chapter. Based on the IKM, the kinematic performance will be evaluated with different criteria in Chapter 5. Chapter 6 will focus on building the inverse dynamic model (IDM) and the simulation of some example cases to predict the load of each actuator. Based on the IDM, the walking stability will be analysed in Chapter 7 and several typical walking scenarios will be simulated. At the end of this dissertation, a summary and suggestions for future works will be given.

Reference

[1.1] Pandilov, Zoran, and Vladimir Dukovski. "COMPARISON OF THE CHARACTERISTICS BETWEEN SERIAL AND PARALLEL ROBOTS." *Acta Technica Corviniensis-Bulletin of Engineering* 7.1 (2014).

[1.2] Patel, Y. D., and P. M. George. "Parallel manipulators applications—a survey." *Modern Mechanical Engineering* 2.03 (2012): 57.

[1.3] Du, Shucen, and Josef Schlattmann. "A new proceeding of control strategy for a parallel structural biped robot." *ASSISTIVE ROBOTICS: Proceedings of the 18th International Conference on CLAWAR 2015*. Published in 2016.

Chapter 2
Structure Synthesis of 6 DOF Parallel Kinematic Mechanisms

This chapter will introduce the structure synthesis problem of parallel kinematic mechanisms (PKM). The method based on screw algebra and the output motion matrix will be used. The difference between screw linear dependency and motion dependency will be explained. The formation of a PKM will be discussed and various limbs for 6 DOF PKM will be listed. The coupling degree will be introduced to determine the complexity of PKMs and different designs will be dissected into basic kinematic chains (BKC) for a better understanding of its topological properties. At the end of this chapter, the equality of designs with double spherical joint and with double universal joints will be proven.

2.1 Output Motion Matrix of Serial and Parallel Mechanisms

The mobility, as defined in [2.1], of a single-opened-chain (SOC) structure is

$$F = \sum_{i=1}^{m} f_i \,. \tag{2.1}$$

Where, m is the number of kinematic pairs (joints), f_i indicates the degree of freedom (DOF) of the i-th kinematic pair. The output motion for the end-effector of an SOC can be described as an output motion matrix [2.2],

$$\boldsymbol{M}_{\mathrm{S}}(\theta_1,\dots,\theta_F)=\begin{bmatrix} x(\theta_1,\dots,\theta_F) & y(\theta_1,\dots,\theta_F) & z(\theta_1,\dots,\theta_F) \\ \alpha(\theta_1,\dots,\theta_F) & \beta(\theta_1,\dots,\theta_F) & \gamma(\theta_1,\dots,\theta_F) \end{bmatrix}. \tag{2.2}$$

In which, x, y and z are the coordinates of the origin of a moving rigid body with respect to the fixed coordinates frame. At the same time, α, β and γ indicate the orientation of an object. The expression of posture here is arbitrary, which can be various proper Euler angles, Tait-Bryan angles or any expressions of Lie triple sub-groups. θ_i is the generalized variable for the i-th input. Correspondingly, the velocity of the end-effector of an SOC is defined as

$$\dot{\boldsymbol{M}}_{\mathrm{S}}(\dot{\theta}_1,\dots,\dot{\theta}_F)=\begin{bmatrix} \dot{x}(\dot{\theta}_1,\dots,\dot{\theta}_F) & \dot{y}(\dot{\theta}_1,\dots,\dot{\theta}_F) & \dot{z}(\dot{\theta}_1,\dots,\dot{\theta}_F) \\ \dot{\alpha}(\dot{\theta}_1,\dots,\dot{\theta}_F) & \dot{\beta}(\dot{\theta}_1,\dots,\dot{\theta}_F) & \dot{\gamma}(\dot{\theta}_1,\dots,\dot{\theta}_F) \end{bmatrix}. \tag{2.3}$$

Note that, in these two matrices, each element stands for a function of all (or part of) the input variables. Each matrix stands for six scalar equations. The rank ξ_{S} of the matrix represents the independency of the motion in different directions. The rank can further be divided as

$$\xi_{\mathrm{S}}=\xi_{\mathrm{SR}}+\xi_{\mathrm{ST}} \quad (\xi_{\mathrm{S}}\in[1,6] \quad \xi_{\mathrm{R}},\xi_{\mathrm{T}}\in[1,3]). \tag{2.4}$$

ξ_{SR} and ξ_{ST} are the number of independent rotational and translational outputs, respectively. The motion and velocity matrices can also be written in vector forms.

$$\boldsymbol{M}_{\mathrm{S}}=\begin{bmatrix}\boldsymbol{t}^{\xi_{\mathrm{ST}}}\\ \boldsymbol{r}^{\xi_{\mathrm{SR}}}\end{bmatrix} \quad \dot{\boldsymbol{M}}_{\mathrm{S}}=\begin{bmatrix}\dot{\boldsymbol{t}}^{\xi_{\mathrm{ST}}}\\ \dot{\boldsymbol{r}}^{\xi_{\mathrm{SR}}}\end{bmatrix} \tag{2.5}$$

To describe the motion of the end effector (moving platform) of a PKM, the output motion matrix and velocity matrix were defined as

$$\begin{aligned}\boldsymbol{M}_{\mathrm{Pa}}(\theta_1,\dots,\theta_F)&=\begin{bmatrix} x(\theta_1,\dots,\theta_F) & y(\theta_1,\dots,\theta_F) & z(\theta_1,\dots,\theta_F) \\ \alpha(\theta_1,\dots,\theta_F) & \beta(\theta_1,\dots,\theta_F) & \gamma(\theta_1,\dots,\theta_F) \end{bmatrix},\\ \dot{\boldsymbol{M}}_{\mathrm{Pa}}(\dot{\theta}_1,\dots,\dot{\theta}_F)&=\begin{bmatrix} \dot{x}(\dot{\theta}_1,\dots,\dot{\theta}_F) & \dot{y}(\dot{\theta}_1,\dots,\dot{\theta}_F) & \dot{z}(\dot{\theta}_1,\dots,\dot{\theta}_F) \\ \dot{\alpha}(\dot{\theta}_1,\dots,\dot{\theta}_F) & \dot{\beta}(\dot{\theta}_1,\dots,\dot{\theta}_F) & \dot{\gamma}(\dot{\theta}_1,\dots,\dot{\theta}_F) \end{bmatrix}\end{aligned} \tag{2.6}$$

Or in vector form,

$$\boldsymbol{M}_{\mathrm{Pa}}=\begin{bmatrix}\boldsymbol{t}^{\xi_{\mathrm{PaT}}}\\ \boldsymbol{r}^{\xi_{\mathrm{PaR}}}\end{bmatrix} \quad \dot{\boldsymbol{M}}_{\mathrm{Pa}}=\begin{bmatrix}\dot{\boldsymbol{t}}^{\xi_{\mathrm{PaT}}}\\ \dot{\boldsymbol{r}}^{\xi_{\mathrm{PaR}}}\end{bmatrix} \tag{2.7}$$

2.2 Screw Algebra and Its Practice in Structure Synthesis

2.2.1 Screw Algebra

The operation and computation of the output matrix are sophisticated. Usually, the derivation process will also involve complicated coordinates transformations and nonlinear algebraic equations. To avoid confusions and focus on the essence of mechanism design, the independency of a mechanism, screw algebra was introduced.

Definition 2.1 Screw [2.3]. In three dimensional space, a 6 dimensional geometric body was defined as a screw. A screw comprises of two 3 dimensional vectors, as

$$\mathcal{S} = \begin{bmatrix} \boldsymbol{s} \\ \boldsymbol{s}_0 \end{bmatrix} = \begin{bmatrix} \boldsymbol{s} \\ h\boldsymbol{s} + \boldsymbol{\rho} \times \boldsymbol{s} \end{bmatrix}. \tag{2.8}$$

In eq. (2.8), $\boldsymbol{s}$ is a 3 dimensional vector, used to describe the orientation and length of a screw axis. h is the pitch of a screw. $\boldsymbol{\rho}$ is the vector start from origin to any point of the screw axis.

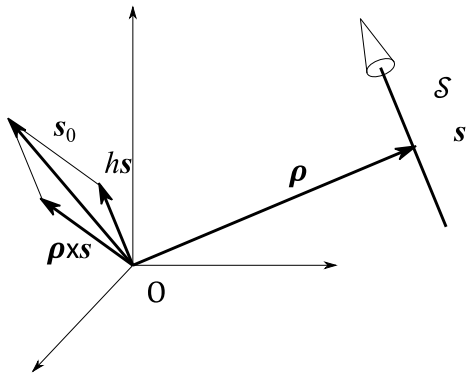

Figure 2.1. The definition of a screw.

Any inertial motion of rigid bodies in 3 dimensional space can be seen as a combination of a rotation and a translation along an axis. If the rotation axis is defined as $\boldsymbol{s} = \omega\boldsymbol{l}$ in definition 2.1, $\boldsymbol{s}_0$ will be the instantaneous motion of the point fixed to the moving body which coincides with the origin of the fixed coordinates. Where, $h\boldsymbol{s}$ was caused by the pitch and $\boldsymbol{\rho} \times \boldsymbol{s}$ was caused by the rotation. Normally, the $h\boldsymbol{s}$ was handled as any translational along the rotation axis.

According to the reference coordinates, a screw can be written as

$$\mathcal{S} = \begin{bmatrix} \boldsymbol{s}_0 \\ \boldsymbol{s} \end{bmatrix} = \begin{bmatrix} t_x & t_y & t_z \\ r_x & r_y & r_z \end{bmatrix}. \tag{2.9}$$

Note that, to conform to the form of output motion matrix, the two vectors of a screw were replaced by each other. As earlier discussed, the screw can describe the instantaneous motion of a rigid body, thus, the screw can describe the velocity characteristic of a rigid body,

$$\mathcal{S} = \begin{bmatrix} \boldsymbol{s}_0 \\ \boldsymbol{s} \end{bmatrix} = \begin{bmatrix} t_x & t_y & t_z \\ r_x & r_y & r_z \end{bmatrix} = \dot{\boldsymbol{M}}_{\mathrm{S}} = \begin{bmatrix} \dot{x} & \dot{y} & \dot{z} \\ \dot{\alpha} & \dot{\beta} & \dot{\gamma} \end{bmatrix}. \tag{2.10}$$

Similarly, $\boldsymbol{s}_0$ indicates the translational velocity of the point fixed to the moving body and coincides with the origin of the fixed frame, $\boldsymbol{s}$ indicates the rotational velocity. The screw was called *twist* in this case. The screws are used to express pure translational motions with an infinite $\boldsymbol{s}_0$ or zero $\boldsymbol{s}$, to express pure rotations with a zero h.

For a motion with different output DOFs, the output motion matrix can be written in dual vector form of a screw, as eq. (2.7). In this case, $\boldsymbol{M}_{\mathrm{Pa}}$ and $\dot{\boldsymbol{M}}_{\mathrm{Pa}}$ are no longer coordinate related. Geometrical relation between screws is the main factor to determine the output DOFs.

1) Related Definitions

Definition 2.2 Screw System.

A s*crew system* $\mathbb{S}$ is an assembly, that comprises of all the linear combinations of a set of linearly independent screws $\{\mathcal{S}_1, \dots, \mathcal{S}_n\}$. This set of linearly independent screws is a *basis* of the screw system. The number of screws in a basis is the *rank* of this screw system.

Definition 2.3 Union and ***Intersection*** of Screw Systems.

Given two screw systems $\mathbb{S}_1$ and $\mathbb{S}_2$, the *union* of them is defined as an assemble fulfils

$$\mathbb{S}_1 \cup \mathbb{S}_2 = \{\mathcal{S} | \mathcal{S} \in \mathrm{span}(\{\mathcal{S}_1, \dots, \mathcal{S}_n, \mathcal{S}_{n+1}, \dots, \mathcal{S}_{n+m}\})\}. \tag{2.11}$$

Where, $\{\mathcal{S}_1, \dots, \mathcal{S}_n\}$ is the basis of $\mathbb{S}_1$, $\{\mathcal{S}_{n+1}, \dots, \mathcal{S}_{n+m}\}$ is the basis of $\mathbb{S}_2$. The union is the span of the union of two bases, but includes not only the members in two screw systems.

The *intersection* of two screw systems includes all the members belong to both systems,

simultaneously,

$$\mathbb{S}_1 \cap \mathbb{S}_2 = \{\mathcal{S} | \mathcal{S} \in \mathbb{S}_1, \mathcal{S} \in \mathbb{S}_2\}. \tag{2.12}$$

Definition 2.4 Linear Dependency of Screws.

If there exists a set of real scalars, not all zero, such that

$$\lambda_1 \mathcal{S}_1 + \lambda_2 \mathcal{S}_2 + \cdots + \lambda_{n-1} \mathcal{S}_{n-1} = 0, \tag{2.13}$$

the screws $\{\mathcal{S}_1, \dots, \mathcal{S}_n\}$ are linear depent.

2) Screw Algebra in Robotic Topology

Serial connected screws

If *n* rigid bodies were connected in series to a base using a series of screws, the velocity of the last rigid body at this configuration can be expressed in screw form, as

$$\mathcal{S} = \lambda_1 \mathcal{S}_1 + \lambda_2 \mathcal{S}_2 + \cdots + \lambda_{n-1} \mathcal{S}_{n-1}. \tag{2.14}$$

λ_i is the velocity magnitude of the *i*-th twist. This equation conforms to the definition of the union of screw systems. Thus, the possible velocity of the end link, $\mathbb{S}_{\text{end}}$, is the union of all the screws systems.

$$\mathbb{S}_{\text{end}} = \cup_{i=1}^{n} \mathbb{S}_i \tag{2.15}$$

Parallel connected screws

If one rigid body is connected by multiple screws, the velocity of it should obey all the screw systems, simultaneously. The screw of the moving body should be the intersection of all the screws connected to its motion.

$$\mathbb{S}_{\text{end}} = \cap_{i=1}^{n} \mathbb{S}_i \tag{2.16}$$

That means, the velocity of end effector should belong to all the velocity spaces of all the limbs. The twist of it is

$$\mathcal{S} \in \mathbb{S}_i, \quad i = 1, \dots, n. \tag{2.17}$$

2.2.2 Linear Dependency of Motion Screws

The linear dependency of screws decides if a screw can be expressed by other screws. Correspondingly, the motion screws' dependency decides that if a motion can be formed by the combination of other motions. Dai's work [2.3] has given the approaches of judging the dependency of screws. The principle of them is to judge if the determinant of reciprocal products matrix is zero. The essence of this approach is to judge if the screws form a basis, or if the matrix they form is full rank.

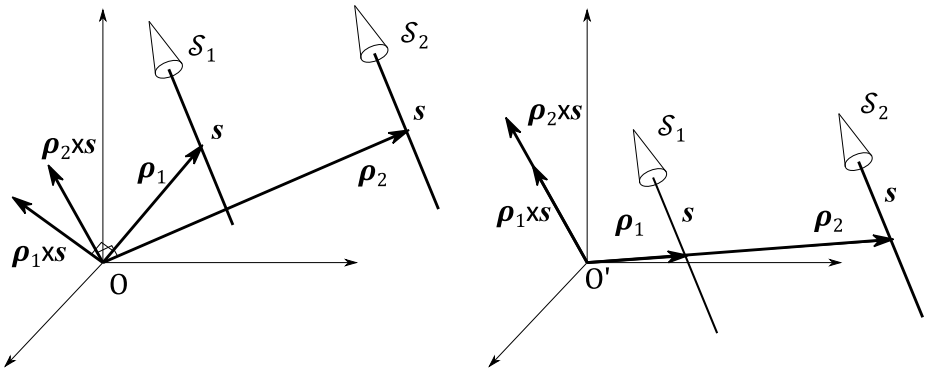

(a) (b)

Figure 2.2 The dependency of two screws. (a) Two parallel screws are not dependent, however, (b) the motions they represented can be dependent.

Table 2.1 Dependent motion screws. (: rotations, : translations)

Parallel translational motions	Three or more translations parallel to one plane	Four or more translations not parallel to one plane	Parallel rotations	Four or more rotations in different directions
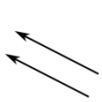	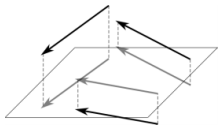	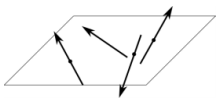	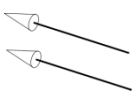	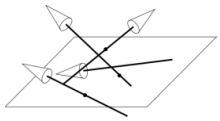
1 output	2 outputs	Maximum 3 outputs	1 output	Maximum 3 outputs

However, in the process of topological designing, the rank (or DOF) of output motion is the primary task. The dependency between motion screws is not depending on the coordinates, some dependency will change under different frames. For the sake of enduing some specific DOFs for the output link, the location of links can be swiftly adjusted. For example, two rotations are linear dependent only if they are coaxial. Under some specific coordinates frame, they are still linear dependent, if they are only parallel to each other. As shown in fig. 2.2 (b), the two screws will generate equal rotation and parasitic translational at a moved origin O'. In this case, the two screws are dependent. Hereby, a list of five sets typical dependent motions and their output independent DOFs are listed in table 2.1.

2.2.3 Screws of Various Joints

Kinematic pairs (joints) are the movable connections between links. Meanwhile, they are the kinematic description between links. Different types of joints limit the relation of two or more links to a specific DOF. Based on installation or motion process, joints endue different outputs, but the DOF they endued is constant.

Among the motions a joint provides, there are dependent DOFs and independent DOFs. A rotation joint, e. g., provides an independent rotational DOF and a dependent parasitic translational DOF at the origin point, if the origin deviates from the axis of the joint.

A dependent DOF is not changing the dependency of following joints in a serial connected kinematic chain. Once the independent DOF of a joint was changed by joints in advance, the customary dependent DOF should be treated as a possible independent DOF. For instance, if the former serial connected joints provide three rotational DOFs, the rational joint will provide a independent translational motion and a dependent rotation. Dependency of some typical one DOF joints and their dependency priorities are listed in table 2.2. Besides the *parallel* (∥) and *orthogonal* (⊥), there more geometric relations between joints, such as *concentric* ($\widehat{\ }$), *coaxial* (/), *parallel to coplane* (∥ □), *indeterminate connection* (−), etc.. These realations are irrelevant to coordinates, but determinant to the rank of output motion matrix.

Table 2.2 Output motions of one dimensional joint and their priorities.

Joints' notation	Outputs and their dependency priority		Output motion matrix ({·}: dependent outputs)
P (prismatic joints)		1. translational	$\begin{bmatrix} \boldsymbol{t}^1(\parallel \mathrm{P}) \\ \boldsymbol{r}^0 \end{bmatrix}$
R (rotational joints)		1. axial rotation	$\begin{bmatrix} \{\boldsymbol{t}^1(\perp \mathrm{R}, \rho)\} \\ \boldsymbol{r}^1(\parallel \mathrm{R}) \end{bmatrix}$
		2. parasitic translational	$\begin{bmatrix} \boldsymbol{t}^1(\perp \mathrm{R}, \rho) \\ \{\boldsymbol{r}^1(\parallel \mathrm{R})\} \end{bmatrix}$
H (helical joints)		1. axial rotation	$\begin{bmatrix} \{\boldsymbol{t}^1(\parallel \mathrm{H})\} + \{\boldsymbol{t}^1(\perp \mathrm{H}, \rho)\} \\ \boldsymbol{r}^1(\parallel \mathrm{H}) \end{bmatrix}$
		2. axial translational (pitch)	$\begin{bmatrix} \boldsymbol{t}^1(\parallel \mathrm{H}) + \{\boldsymbol{t}^1(\perp \mathrm{H}, \rho)\} \\ \{\boldsymbol{r}^1(\parallel \mathrm{H})\} \end{bmatrix}$
		3. parasitic translational	$\begin{bmatrix} \{\boldsymbol{t}^1(\parallel \mathrm{H})\} + \boldsymbol{t}^1(\perp \mathrm{H}, \rho) \\ \{\boldsymbol{r}^1(\parallel \mathrm{H})\} \end{bmatrix}$

2.3 Structure Analysis of Parallel Kinematic Mechanisms

2.3.1 Single Open Kinematic Chain (SOC) and Single Looped Kinematic Chain (SLC)

An *SOC* comprises of serially connected joints and links, each joint or link has binary connections with other links or joints, expect the extreme ones (end effector and fixed base). The *mobility* of an SOC is the dimension number of its joint space, as [2.1] defined,

$$F_{\mathrm{S}} = \sum_{i=1}^{m} f_i \tag{2.18}$$

f_i is the DOF of the i-th joint, m is the number of joints. The *connectivity* of an SOC is the dimension number of the independent motion space, as

$$\xi_{\mathrm{S}} = \mathrm{rank}(\boldsymbol{M}_{\mathrm{S}}) \tag{2.19}$$

$\boldsymbol{M}_{\mathrm{S}}$ is the output motion matrix. This can be computed through analytical method in limited cases. More efficient method would be the geometrical dependency determination, as, e.g., listed in table 2.1 and table 2.2.

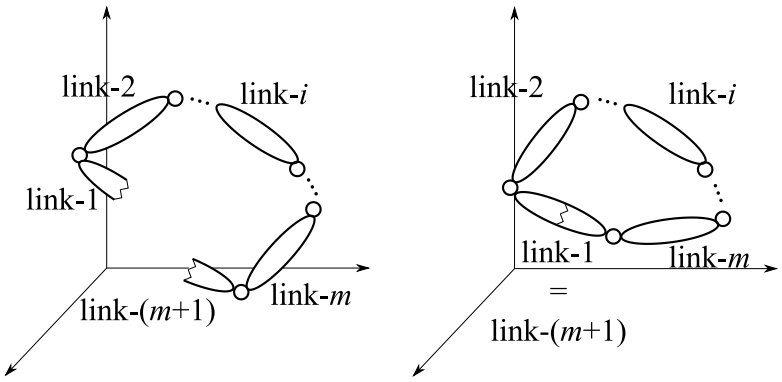

Figure 2.3 The formation of an SLC

All the parts in an *SLC* are binary connected, including the base and end effector. If an SLC was opened from any link, it forms an SOC. This is called the associated SOC of the SLC. The ranks of output motion matrices of SLC and of associated SOC are equal. The difference is that, the output motion matrix of SLC, $\boldsymbol{M}_{\mathrm{L}}$, is equal to a zero matrix.

$$\boldsymbol{M}_{\mathrm{S}} = \sum_{i=1}^{m} \begin{bmatrix} \boldsymbol{t}_i^{\xi_{\mathrm{T}}} \\ \boldsymbol{r}_i^{\xi_{\mathrm{R}}} \end{bmatrix}, \quad \boldsymbol{M}_{\mathrm{L}} = \sum_{i=1}^{m} \begin{bmatrix} \boldsymbol{t}_i^{\xi_{\mathrm{T}}} \\ \boldsymbol{r}_i^{\xi_{\mathrm{R}}} \end{bmatrix} = \boldsymbol{0} \tag{2.20}$$

$\boldsymbol{t}_i^{\xi_{\mathrm{T}}}$ and $\boldsymbol{t}_i^{\xi_{\mathrm{R}}}$ are the translational and rotational displacements of the i-th joint. Thus, the motion of the m-th link is limited to the kernel space of this associated SOC output motion matrix. The mobility of an SLC is defined to be equal with its associated SOC. The mobility of an SLC is inheriting defined as

$$F_{\mathrm{L}} = \sum_{i=1}^{m} f_i - \xi_{\mathrm{S}}. \tag{2.21}$$

It indicates the joint space dimension of an SLC.

2.3.2 Formation of Parallel Kinematic Mechanism

A *parallel kinematic mechanism* (PKM) contains more than one limbs, a moving platform ({MP}) and a fixed base ({FB}). The limbs can be SOCs or hybrid SOCs (HSOC). A PKM can be expressed as

$$\mathrm{PKM} = \{\mathrm{MP}\} + \{\mathrm{FB}\} + \sum_{j=1}^{v+1} \{\mathrm{HSOC}_j\}. \tag{2.22}$$

v is the number of loops that can be calculated as $v = m - n + 1$. Where, m is the number of joint, n is the number of links. The HSOC can be an SLC or a chain formed by multi-loops.

The output motion matrix of a PKM, $\boldsymbol{M}_{\mathrm{Pa}}$, is defined as the motion characteristic of the {MP}, which is a function of active inputs, seeing eq. (2.7). As described in eq. (2.16), $\boldsymbol{M}_{\mathrm{Pa}}$, as a screw system, should be the intersection of all the output matrices of all the limbs connecting {MP} and {FB}, i.e.

$$\boldsymbol{M}_{\mathrm{Pa}} = \bigcap_{j=1}^{n_{\mathrm{l}}} \boldsymbol{M}_{\mathrm{S}j}. \tag{2.23}$$

n_{l} is the number of limbs (SOCs and HSOCs).

2.3.3 PKM in a View of Basic Kinematic Chain

The synthesis of PKM includes the design of limbs, configuration of limbs' origins and their connections to moving platform. Different designs will fulfil the same kinematic requirement of the output part. However, different designs will lead to different complexity of the mechanism. For example, in fig. 2.4, both designs endue the end effector (shadowed) a 4 dimensional motion space. It is obvious that the design in fig. 2.4(b) is topologically simpler, since the position of one point of the end effector with respect to the line $\overline{\mathrm{S_{1A}S_{1B}}}$ is apparent. While, the

rotation and translational motion of the whole end effector in fig. 2.4(a) are coupled, i. e., any item in eq. (2.6) is the function of all the inputs. There is, therefore, a demand of describing the *complexity* degree of PKM.

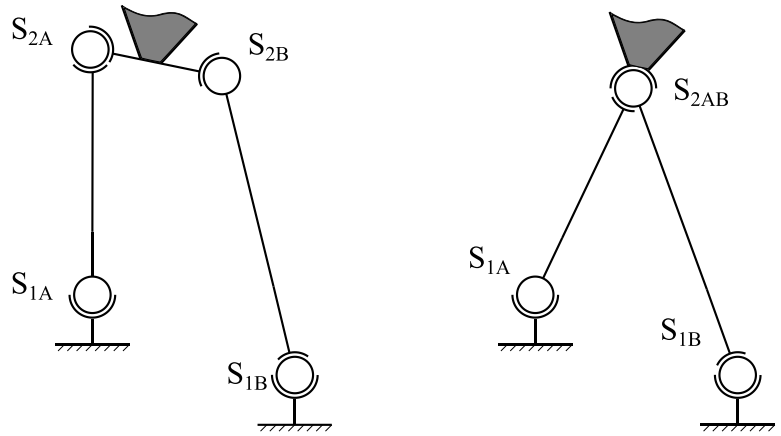

Figure 2.4 Two designs of 4 DOF SLC, while motion point S_{2AB} in (b) is one dimensional.

To express the complexity of a PKM in a proper manner, Yang and Yao have proposed another view of dissecting in their former work ([2.2]). Its basic idea is to view a PKM as a composition of SOCs. The 1st SOC closes its extreme links to form the 1st basic loop. The 2nd SOC will be connected to the 1st SOC with its extreme links, et cetera, until it forms v basic loops. The SOCs to form a basic loop should be selected from the ones which obtain the minimum absolute constraint degree, $|\Delta_i|$.

The loops can be distinguished as two types: dependent and independent. A dependent basic loop connects its extreme links, while, an independent loop connects its extreme links to other basic loops. As illustrated in fig. 2.5, the 2nd loop is independent and the v^{th} loop is dependent. For this reason, an independent loop is in general an HSOC. Considering the minimum $|\Delta_i|$ principle mentioned in advance, if an SOC forms an independent loop or a part of a dependent one, depends only on which leads to a smaller $|\Delta_i|$.

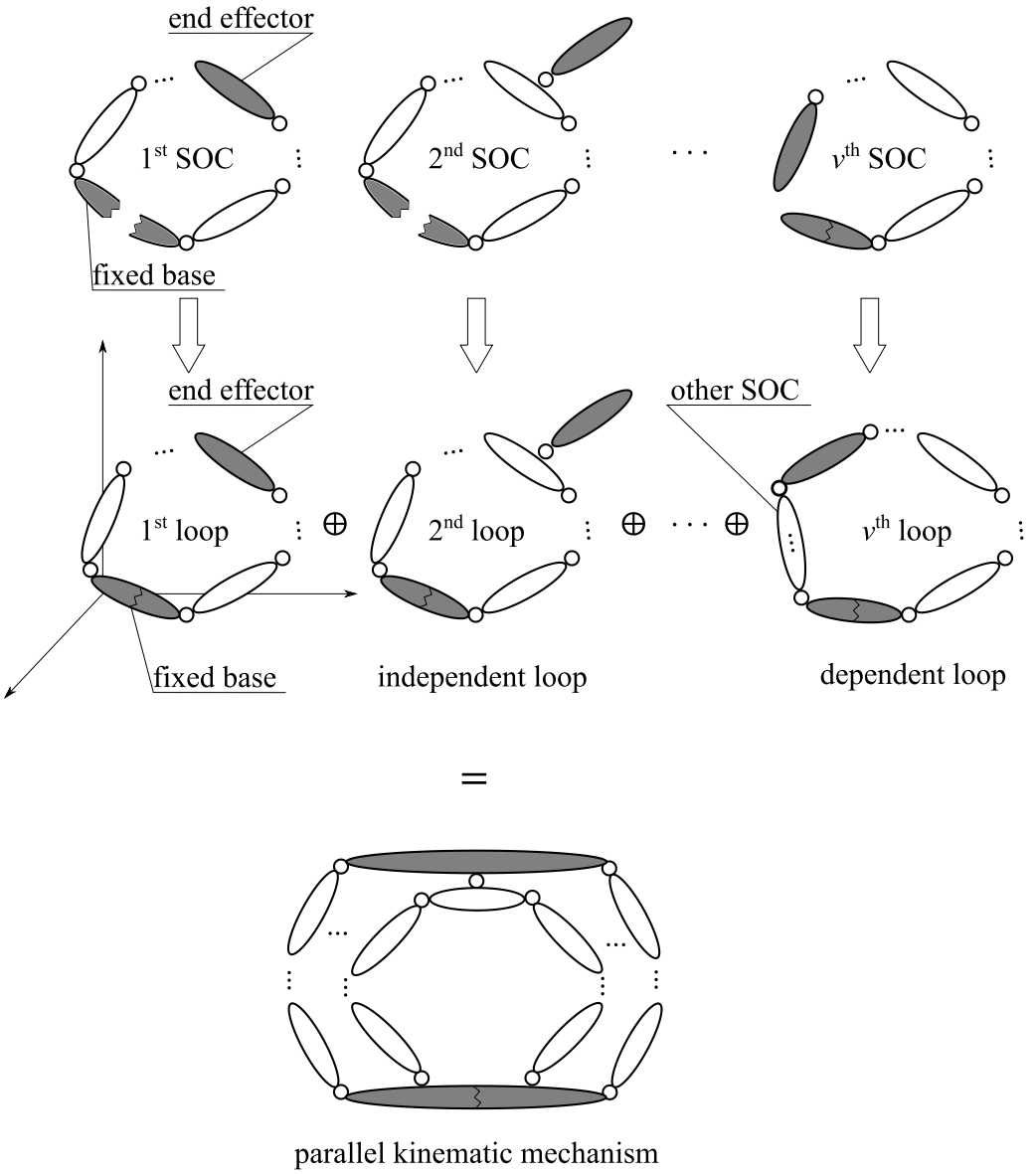

Figure 2.5 Formation of a PKM.

1) Constraint Degree Δ_i

Constraint degree, Δ_i, reveals how the present kinematic chain affects other chains or the whole mechanism. A negative Δ_i will constrain other chains and reduce the DOF of whole mechanism; a positive Δ_i will provide extra DOFs for the whole mechanism and be constrained by some negative Δ_i chains; a zero Δ_i is not affecting other chains. As mentioned in [2.2], for SOC_i

$$\Delta_i = \sum_{j=1}^{m_i} f_j - I_i - \xi_{1i}. \tag{2.24}$$

In which, m_i is the number of joints in SOC$_i$, f_j is the DOF of j-th joint, I_i is the number of driving joints in SOC$_i$ and ξ_{li} is the minimum rank among the ranks of all the loops including SOC$_i$. Note that, the f_i in eq. (2.24) does not include the local DOF between joints.

It is not hard to find the similarities between Δ_i and the mobility of SLC, m_{li}, in eq. (2.21). The difference is in eq. (2.24), only the DOF of present SOC was considered, but not of the whole loop as eq. (2.21). Δ_i, thus, indicates the DOF contribution of a part of a loop to the whole loop. As the m_i increasing, the kernel space of equation (2.20) expends. Thus, the DOF of the SLC formed by this loop increases. I_j driving joints are controlled by the user, which are not providing 'freedom degree'.

Since the computation of constraint degree bases on mobility, but not connectivity, the over-constrained mechanisms, such as a Sarrus linkage, are not considered. The over constrained degree should be calculated in advance through geometrical method and eq. (2.16), then the constraint degree and coupling degree can be obtained. This present work will ignore this problem and focus on 6 DOF PKM, by which over constrained problem occurred rarely.

2) Coupling Degree k

The *coupling degree*, *k*, is half the sum of absolute constraint degrees. It indicates how complex the mechanism is. Let *v* be the number of loops in this mechanism, *k* can be calculated as

$$k = \frac{1}{2}\sum_{i=1}^{v}|\Delta_i|. \tag{2.25}$$

The value of *k* is the least searching dimension of solving the FKP of a PKM, as mentioned in [2.5] [2.6]. For a PKM with *k*=0, all the joint parameters of loops can be directly computed. In the case *k*=1, all the joint parameters can be obtained through 1 dimensional searching.

3) Basic Kinematic Chains

A *basic kinematic chain* (as BKC in [10]) is a kinematic chain with 0 mobility. It is can be determined as

$$\mathrm{BKC} = \bigcup_{i=1}^{\nu_j} \mathrm{SOC}_i \quad \left\{ \mathrm{SOC}_i \left| \sum_{i=1}^{\nu_j} |\Delta_i| = 0, \sum_{i=1}^{\nu_k < \nu_j} |\Delta_i| \neq 0 \right. \right\} \quad \nu_j \leq \nu. \tag{2.26}$$

v_j is the number of loops in this BKC.

Through dividing a PKM into BKCs, the location of coupling degree will be confirmed. The solution of FKP of a coupled PKM will be transferred into the solution of different BKCs, each type of which obtain a fixed number of coupling degree and solution numbers.

4) Local DOF and Pseudo-Local DOF

If one DOF of a link in a kinematic chain will not affect the shape of the kinematic chain, it is defined as *local DOF* of this chain. If a link with local DOF connects and affects the kinematic of other chains, the local DOF is defined as *pseudo*. As mentioned in advance, constraint degree indicates the DOF relation of a chain with others.

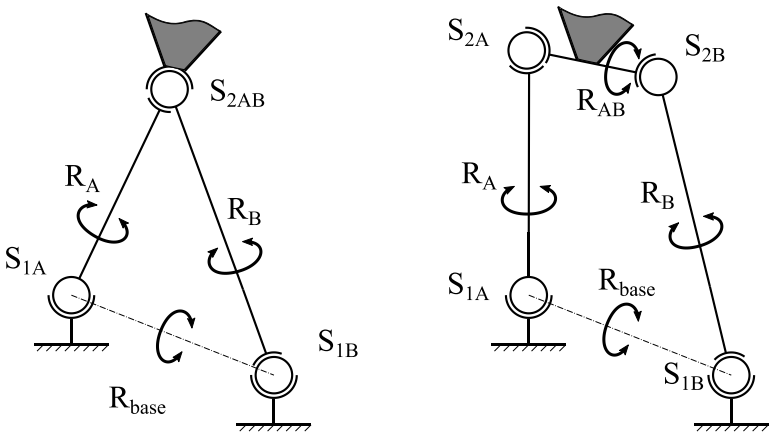

(a) (b)

Figure 2.6 Local DOFs in two SLCs. The S_{2AB} in (a) turns to a pseudo-local DOF, R_{AB}, in (b). R_{base} in both is always pseudo-local.

However, some chains with zero Δ_i apparently affect the DOF of other chains. This is due to that the pseudo-local DOF was eliminated in the present chain, but must be considered as a part of other chain. As illustrated in fig. 2.6, the local DOF R_A and R_B are isolated from other joints or chains, except the spherical joints on their both sides. The links with local DOF R_{AB} and R_{base} are connected to other links and must be considered in other chains.

2.4 Structural Synthesis and Analysis of 6 DOF PKM

Gogu ([2.1]) has given a lot of systematic definitions and methods of structure logical associated graph of a kinematic chain. His works base on linear transformation and evolutionary morphology.

Yang' s work([2.2],[2.4]) provided a generalized procedure of parallel mechanisms structure synthesis. The method is inclined to utilize the geometric relation between joints inside or between limbs with the sake of screw theory. The multifarious function relations and coordinates transformation was wittingly simplified. This reveals the essence of kinematic relations of a parallel mechanism, the dependency between limbs and basic kinematic chains.

2.4.1 Type Synthesis of Limbs for a 6 DOF PKM

A 6 DOF PKM should obtain an output as $\boldsymbol{M}_{\mathrm{Pa}} = [\boldsymbol{t}^3 \quad \boldsymbol{r}^3]^{\mathrm{T}}$. Based on eq. (2.15), eq. (2.16) and eq. (2.23), output matrix of every limb in a PKM with 6 DOF should be

$$\boldsymbol{M}_{\mathrm{l}j} = \boldsymbol{M}_{\mathrm{Pa}} = \begin{bmatrix} \boldsymbol{t}^3 \\ \boldsymbol{r}^3 \end{bmatrix}. \tag{2.27}$$

The SOC and HSOC limbs should thereout be structured.

1) SOCs with 6 DOF

Referred to table 2.2, various SOCs can be obtained, as 3P3R, 2P4R, 1P5R, 6R, where the sequence of joints can be varied and every joint can be replaced by a helical joint. Note that, due to the local DOF, output motion matrix rank of an $\mathrm{SOC}\{-\mathrm{S}-\mathrm{S}-\}$ is equal to a 5R: $\{-\widehat{\mathrm{RR}}-\widehat{\mathrm{RRR}}-\}$, which of a 6R $\mathrm{SOC}\{-\widehat{\mathrm{RRR}}-\widehat{\mathrm{RRR}}-\}$ is also equal to a 5R SOC.

2) HSOCs with 6 DOF

An HSOC can be a combination or a derivative of different SOCs. Some DOFs or sub-chains of an SOC can be replaced by some DOF-equivalent kinematic loops, even by more complicated PKMs. Through this, diverse kinematic limbs could be generated to fulfil diverse design aims.

As table 2.3 illustrated, the limbs with 6 DOF can be classified as SOCs and HSOCs. For SOCs, type I is a kinematic chain with all kinds of basic lower kinematic pairs, type II includes chains with part of basic lower kinematic pairs. HSOCs of type A use SLCs to replace part of their DOFs, while HSOCs of type B were generated by duplicating and combining their origin SOCs. Based on these design thoughts, there exists numerous forms of limbs with 6 DOF.

Table 2.3 Types of 6 DOF limbs.

Types	SOC		HSOC		
	I	II	I	II	III
A(1)			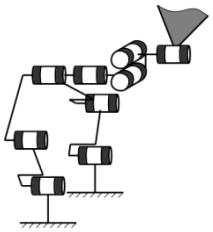	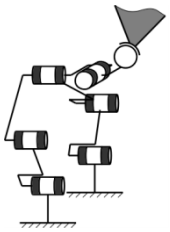	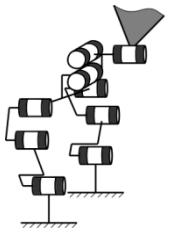
A(2)			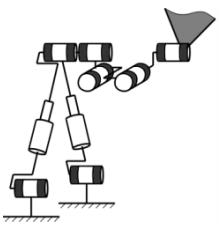	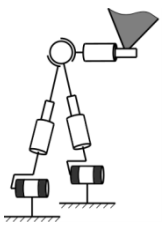	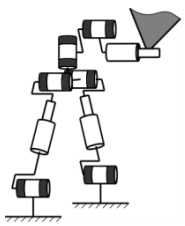
B(1)		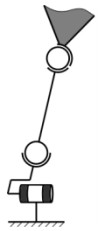	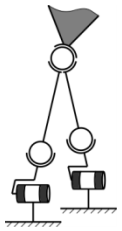	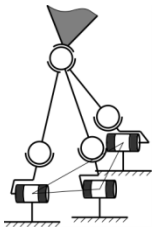	…
B(2)		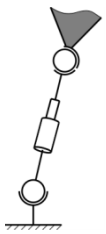	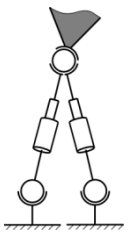	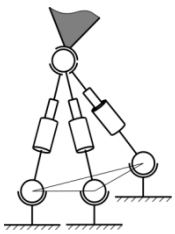	…

2.4.2 Topological Analysis of Various 6 DOF Parallel Kinematic Mechanisms

As discussed in last section, there are numerous designs of limbs with 6 DOF connectivity. During the designing of a PKM, these limbs should be selected considering some requirements, for example, space, load direction and range, coupling degree, manufacturing limitations, etc. For a narrow installation space, more multi-conjunction joints, such as double spherical joints, should be adapted. For high load scenarios, over-constraint structure should be arranged along the main load direction. For high-precision and real-time demanding cases, coupling degree should be considered reasonably. For an industrial mass production case or a cost-sensitive occasion, the designs with high machining requirements, such as triple spherical joints, should be avoided. But in the starting phase of designing, the emphasis should incline to the topological property of designs. Following, four designs of 6 DOF PKMs will be discussed.

1) Gough- Stewart 6 DOF PKM

A very typical design of this type mechanism is the well-known hexapod, Gough- Stewart platform, as shown in fig. 2.7(a). It was generated based on the SOC in group SOC B(2)-II of table 2.3. Since the uniformity of every limb, the first SOC can be chosen randomly. Its constraint degree, according to eq. (2.24)., is

$$\mathrm{SOC}_1\{-\mathrm{S}_{1\mathrm{A}} - \mathrm{P}_{2\mathrm{A}} - \mathrm{S}_{3\mathrm{A}} - \mathrm{S}_{3\mathrm{B}} - \mathrm{P}_{2\mathrm{B}} - \mathrm{S}_{1\mathrm{B}} -\},$$
$$\Delta_1 = (14-4) - 2 - 6 = +2.$$

The second SOC can be chosen and its constraint degree is

$$\mathrm{SOC}_2\{-\mathrm{R}_{(1\mathrm{A}-1\mathrm{B})} - \mathrm{R}_{(3\mathrm{A}-3\mathrm{B})} - \mathrm{S}_{3\mathrm{C}} - \mathrm{P}_{2\mathrm{C}} - \mathrm{S}_{1\mathrm{C}} -\},$$
$$\Delta_2 = (9-1) - 1 - 6 = +1.$$

Which excludes local rotation inside limb-C. The rotational joints $\mathrm{R}_{(1\mathrm{A}-1\mathrm{B})}$ and $\mathrm{R}_{(3\mathrm{A}-3\mathrm{B})}$ are derived by the pseudo-local DOFs between limb-A and limb-B, seeing fig. 2.7(b). Correspondingly, constraint degrees of the rest limbs are calculated as following.

$$\mathrm{SOC}_3\{-\mathrm{S}_{1\mathrm{D}} - \mathrm{P}_{2\mathrm{D}} - \mathrm{S}_{3\mathrm{D}} -\}, \Delta_3 = (7-1) - 1 - 6 = -1,$$
$$\mathrm{SOC}_4\{-\mathrm{S}_{1\mathrm{E}} - \mathrm{P}_{2\mathrm{E}} - \mathrm{S}_{3\mathrm{E}} -\}, \Delta_4 = (7-1) - 1 - 6 = -1,$$

$$\mathrm{SOC}_5\{-\mathrm{S}_{1\mathrm{F}} - \mathrm{P}_{2\mathrm{F}} - \mathrm{S}_{3\mathrm{F}} -\}, \Delta_5 = (7-1) - 1 - 6 = -1.$$

A BKC should be a structure with 0 DOF, while, it obtains positive DOF by removing any links. Therefrom, the mechanism contains only one BKC, its coupling degree, from eq. (2.25) is

$$k = \frac{1}{2}\sum_{j=1}^{5} |\Delta_j| = 3.$$

Therefore, solution of FKP will suffer a searching process in 3 dimensions. The mechanism can be expressed as

$$\mathrm{PKM}[6,6] = 6_{J_{in}} + \mathrm{BKC}_1[+2,-1,-1] + \mathrm{BKC}_2[+1,-1].$$

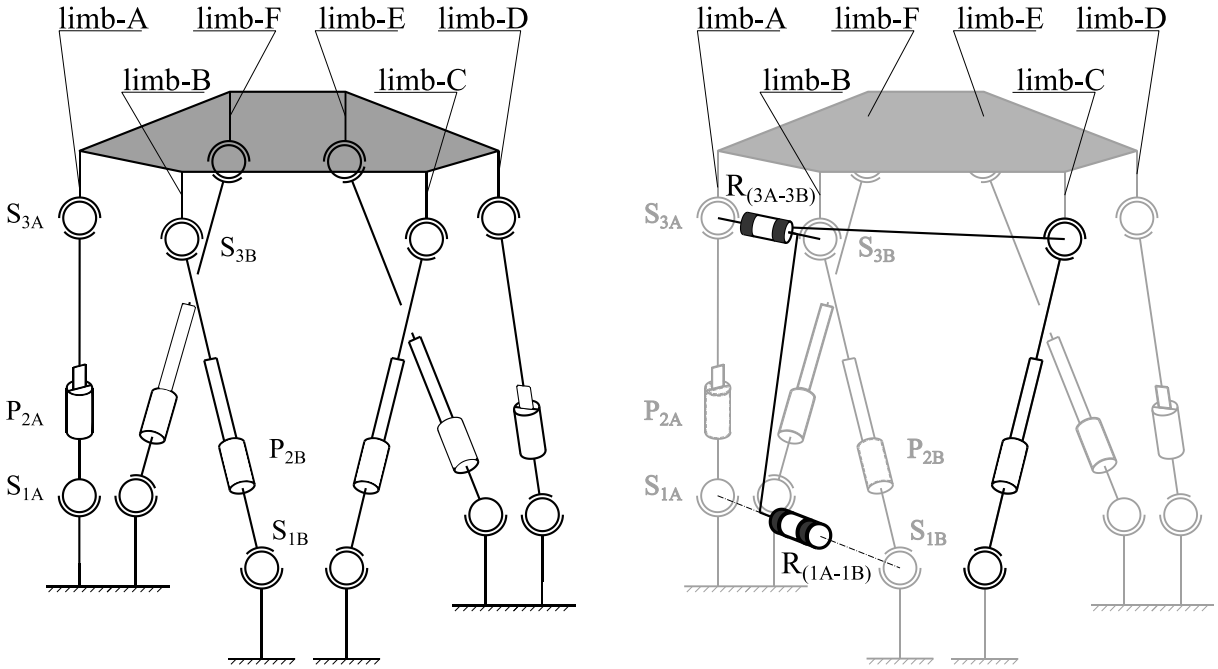

Figure 2.7 6 DOF Gough-Stewart platform and its topological dissect.

This PKM contains 6 base connections, 6 moving platform connections (as [6,6]) and two BKCs. The constraint degrees of all the SOCs are listed in the square brackets after BKCs.

2) First Derivative of Gough- Stewart 6 DOF PKM

A derivative of Gough-Stewart platform was illustrated in fig. 2.8(a). This design realises 3T-3R motion of the moving platform, while in this derivative, moving platform obtains only 3

connections with limbs. Each pair of limbs intersects through a “double sphere joint”. The intersections of limbs reduce the coupling degree of the whole mechanism.

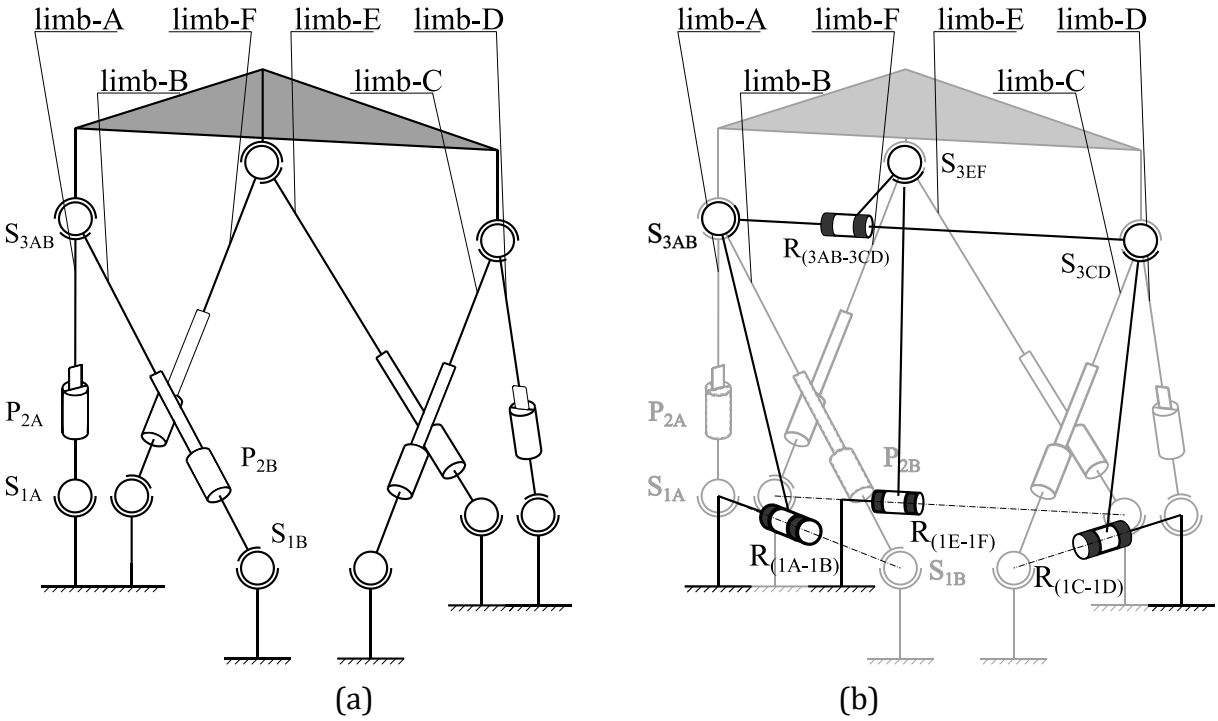

Figure 2.8 First derivative of Gough-Stewart platform and its topological dissect.

There are three identical basic closed loops. The basic closed loops are connected to the moving platform with sphere joints. Meanwhile, the limbs are connected to each other with sphere joints, too. We randomly chose one loop as the first single open chain, then the constraint degree can be calculated.

$$\mathrm{SOC}_1\{-\mathrm{S}_{1\mathrm{A}}-\mathrm{P}_{2\mathrm{A}}-\mathrm{S}_{3\mathrm{A}}(\mathrm{S}_{3\mathrm{B}})-\mathrm{P}_{2\mathrm{B}}-\mathrm{S}_{1\mathrm{B}}-\},$$
$$\Delta_1=(11-3)-2-6=0.$$

Comparing to the Gough-Stewart platform, there is no local DOF between $\mathrm{S}_{3\mathrm{A}}$ and $\mathrm{S}_{3\mathrm{B}}$. A zero constraint degree indicates the independence of this SOC. In other words, this SOC will not affect the DOF of the whole mechanism. Due to the zero constraint degree, SOC_1, excluding the driving prismatic joints, itself forms a BKC whose coupling degree is also zero. This indicates a certainty of its shape. Similarly, the other 2 identical closed loops can be taken as SOC_2 and SOC_3. Their constraint degrees are,

$$\mathrm{SOC}_2\{-\mathrm{S}_{1\mathrm{C}}-\mathrm{P}_{2\mathrm{C}}-\mathrm{S}_{3\mathrm{C}}(\mathrm{S}_{3\mathrm{D}})-\mathrm{P}_{2\mathrm{D}}-\mathrm{S}_{1\mathrm{D}}-\},\Delta_2=(11-3)-2-6=0.$$

$$SOC_3\{-S_{1E} - P_{2E} - S_{3E}(S_{3F}) - P_{2F} - S_{1F} -\}, \Delta_3 = (11-3) - 2 - 6 = 0.$$

As illustrated in fig. 2.8(b), SOC_4, and its constraint degree are

$$SOC_4\{-R_{(1A-1B)} - S_{3AB} - S_{3CD} - R_{(1C-1D)} -\}, \Delta_4 = (8-1) - 6 = +1.$$

In which, $R_{(1A-1B)}$ and $R_{(1C-1D)}$ are derivatives of pseudo-local DOFs between S_{1A} and S_{1B}, and between S_{1C} and S_{1D}. S_{3AB} and S_{3CD} are the pairs between SOC_1, SOC_2 and the moving platform. The local DOF between S_{3AB} and S_{3CD} was excluded from the constraint degree. The last SOC was defined as

$$SOC_5\{-R_{(1E-1F)} - S_{3EF} - R_{(3AB-3CD)} -\}, \Delta_5 = 5 - 6 = -1.$$

Where, $R_{(1E-1F)}$ is a derivative of pseudo-local DOF between S_{1E} and S_{1F}, $R_{(3AB-3CD)}$ is a derivative of local DOF between S_{3AB} and S_{3CD}. This mechanism comprises apparently 4 BKCs, they are $BKC_1[SOC_1]$, $BKC_2[SOC_2]$, $BKC_3[SOC_3]$ and $BKC_4[SOC_4 \oplus SOC_5]$. The coupling degrees of the former three BKCs are all zero. The coupling degree of the last BKC is 1. The mechanism can be thus expressed as

$$PKM[6,3] = 6_{J_{in}} + BKC_1[0] + BKC_2[0] + BKC_3[0] + BKC_4[+1,-1].$$

Thus, the shape of three visible loops can be analytically solved, while the numerical solution of the related pose among these three loops must be solved through 1 dimensional search.

3) Second Derivative of Gough- Stewart 6 DOF PKM

Another derivative of Gough-Stewart platform can be found in fig. 2.9(a). It contains 6 limbs which form two HSOCs and one SOC. Through a triple sphere joint, limbs-B, C and D are connected to one point on the moving platform, while, limbs-E and F are connected through a double sphere joint to the moving platform.

Similarly to last configuration, the closed loop formed by limbs-E and F was chosen as SOC_1, its constraint degree is

$$SOC_1\{-S_{1E} - P_{2E} - S_{3EF} - P_{2F} - S_{1F} -\}, \Delta_1 = (11-3) - 2 - 6 = 0.$$

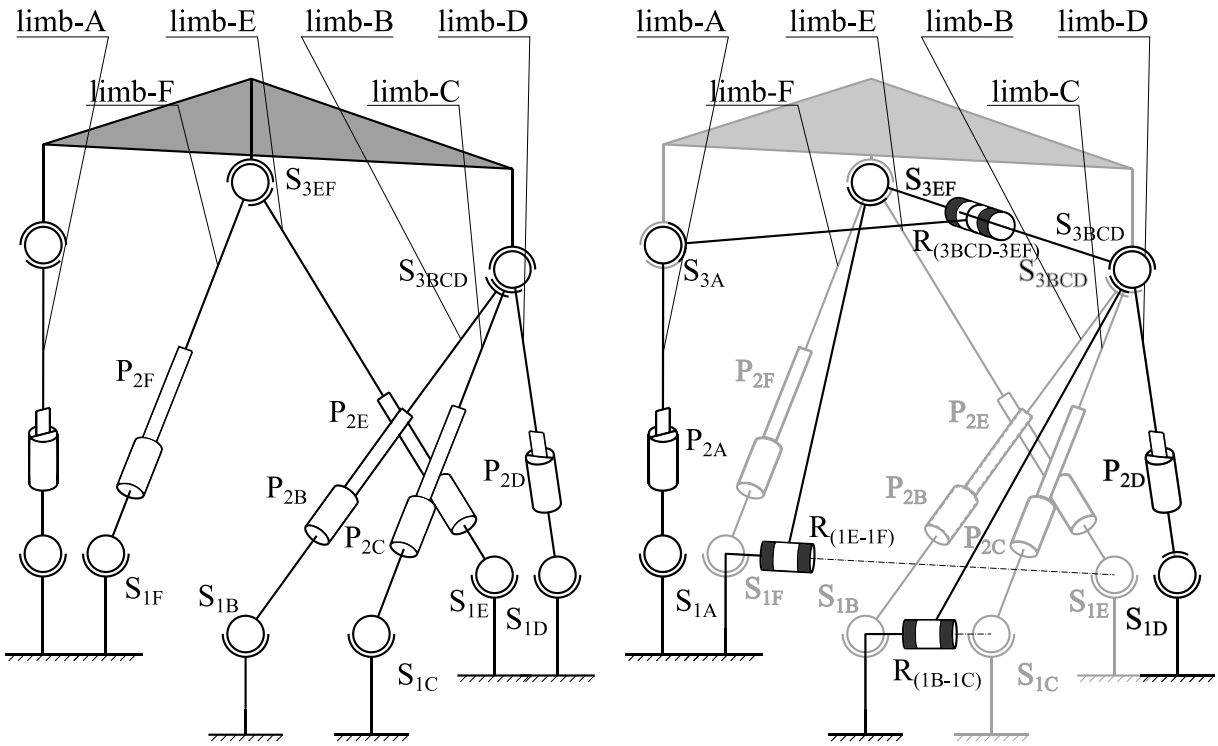

Figure 2.9 Second derivative of Gough-Stewart platform and its topological dissect.

SOC_2 is formed by limb-B and limb-C. Its constraint degree is

$$\mathrm{SOC}_2\{-\mathrm{S}_{1\mathrm{B}}-\mathrm{P}_{2\mathrm{B}}-\mathrm{S}_{3\mathrm{BCD}}-\mathrm{P}_{2\mathrm{D}}-\mathrm{S}_{1\mathrm{C}}-\},\Delta_2=(11-3)-2-6=0.$$

The local DOFs between $\mathrm{S}_{3\mathrm{B}}(\mathrm{S}_{3\mathrm{C}})$ and $\mathrm{S}_{1\mathrm{C}}$, between $\mathrm{S}_{1\mathrm{B}}$ and $\mathrm{S}_{3\mathrm{B}}(\mathrm{S}_{3\mathrm{C}})$, and between $\mathrm{S}_{1\mathrm{B}}$ and $\mathrm{S}_{1\mathrm{C}}$, were excluded. Adhering to the *minimal constraint principle*, the rest of SOCs are confirmed, their constraint degrees are calculated as following.

$$\mathrm{SOC}_3\{-\mathrm{R}_{(1\mathrm{B}-1\mathrm{C})}-\mathrm{S}_{3\mathrm{BCD}}-\mathrm{P}_{2\mathrm{D}}-\mathrm{S}_{1\mathrm{D}}-\},\Delta_3=(8-1)-1-6=0.$$

$$\mathrm{SOC}_4\{-\mathrm{R}_{(1\mathrm{E}-1\mathrm{F})}-\mathrm{S}_{3\mathrm{EF}}-\mathrm{S}_{3\mathrm{BCD}}-\},\Delta_4=(7-1)-6=0.$$

$$\mathrm{SOC}_5\{-\mathrm{S}_{1\mathrm{A}}-\mathrm{P}_{2\mathrm{A}}-\mathrm{S}_{3\mathrm{A}}-\mathrm{R}_{(3\mathrm{BCD}-3\mathrm{EF})}-\},\Delta_5=(8-1)-1-6=0.$$

Notice that, the $\mathrm{S}_{3\mathrm{EF}}$ and $\mathrm{S}_{3\mathrm{BCD}}$ represent different kinematic pairs in different SOCs. In SOC_1 and SOC_2, $\mathrm{S}_{3\mathrm{EF}}$ is the pair between limb-E and limb-F, $\mathrm{S}_{3\mathrm{BCD}}$ is the pair between limb-B and limb-C. In SOC_3, $\mathrm{S}_{3\mathrm{BCD}}$ is the pair between limb-D and the HSOC formed by limb-B and limb-C. In SOC_4 $\mathrm{S}_{3\mathrm{EF}}$ and $\mathrm{S}_{3\mathrm{BCD}}$ are the pairs between moving platform and limbs. The coupling degree for each SOC is zero. Consequently, the mechanism contains five BKCs and can be expressed as

$$\mathrm{PKM}[6,3] = 6_{J_{in}} + \mathrm{BKC}_1[0] + \mathrm{BKC}_2[0] + \mathrm{BKC}_3[0] + \mathrm{BKC}_4[0] + \mathrm{BKC}_5[0].$$

This PKM configuration can be thus analytically solved.

4) Third Derivative of Gough- Stewart 6 DOF PKM

Inspired by the first derivative of Gough-Stewart, a more compact mechanism was developed, as shown in fig. 2.10(a). Topologically speaking, the two mechanisms are identical. The intersections on the base are not changing the connection number between limbs and base, since all the limbs (or SOCs) grow from the base through various pairs.

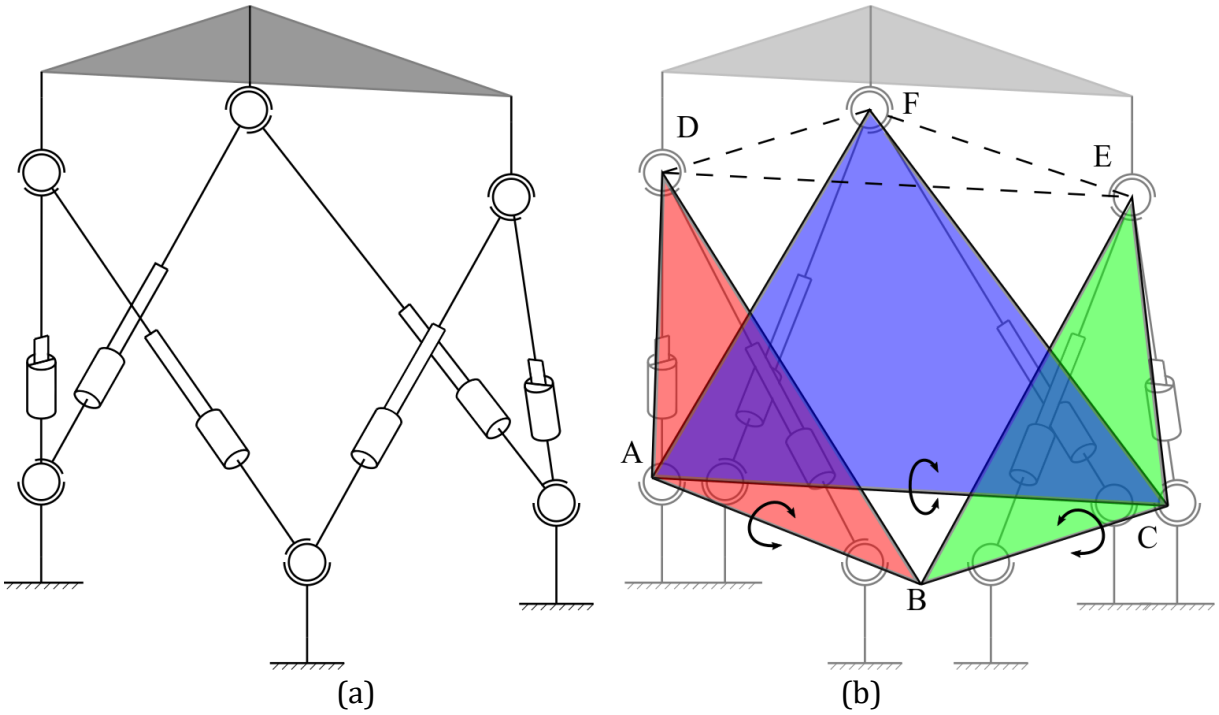

Figure 2.10 Third derivative of Gough-Stewart platform and its equality with the first derivative of Gough-Stewart platform.

Geometrically speaking, the dissections of both mechanisms are indeed to solve the following problem: *given shapes of three triangles and the location of one side of each triangle, to find a posture, where the vertexes form a specific triangle*. The equivalence of two mechanisms are illustrated as fig. 2.10(b). Once the lengths of driving linear actuators are determined, the BKCs are representing nothing but the location of point D, E and F. Hence, the coupling degree of both mechanisms are 1, indicates a one dimensional searching process in FKP solving. The solution will be discussed in Chapter 4.

5) Derivative of Gough- Stewart 6 DOF PKM with Cardan Joints

In order to realize a 6 DOF motion of the moving platform, the SOCs or HSOCs should obtain 6 DOF motion outputs. The sphere joints can also be replaced by various joints. As mentioned in former work [2.7] and [2.8], different joints obtain different input-output characteristics. However, the topology structure of the 6 DOF PKM is not changed, as seen in fig. 2.11(a). The only difference is that, the local DOF between two S joints of one limb was eliminated and replaced by the relative rotation between lower and upper part of one limb. Similar to mechanism in fig. 2.7, there are five BKMs in fig. 2.11(a) and the coupling degree is 3.

One of the most indisputable disadvantages of the mechanisms in fig. 2.9 (a) and fig. 2.10(a) is the limited working space of double or triple concentric sphere joints. At the same time, their load capacity and mechanical complexity are not competitive. Thus, the double Cardan joint was adopted and studied in this work, as shown in fig. 2.11(b).

Fig. 2.11(c,d) illustrate the mechanical drawing and topological diagram of this joint. From the base, the assemble connect two outputs through three axes. All axes intersect at one common point. The two outputs share one axis at the end of their own chain. There are three mechanical chains in this assemble: base- output$_A$, base- output$_B$ and output$_A$- output$_B$. As configured in fig. 2.11(b), the *double Cardan joint, with extra rotational DOFs* (outside the line box in fig. 2.11(d)) *on both outputs, effects equally as a concentric double sphere joint* in fig.2.11(e).

Proof.

Output motion characteristic equation of a sphere joint is

$$\boldsymbol{M}_{\mathrm{S}} = \begin{bmatrix} \mathbf{0} \\ \boldsymbol{r}^3 \end{bmatrix}. \tag{2.28}$$

That between both outputs of a double Cardan joint is

$$\boldsymbol{M}_{\mathrm{A'-B'}} = \begin{bmatrix} \mathbf{0} \\ \boldsymbol{r}^1 \end{bmatrix}_{4\mathrm{A}} + \begin{bmatrix} \mathbf{0} \\ \boldsymbol{r}^1(\perp \mathrm{R}_{4\mathrm{A}}) \end{bmatrix}_{3\mathrm{A}} + \begin{bmatrix} \mathbf{0} \\ \{\boldsymbol{r}^1(\equiv \mathrm{R}_{3\mathrm{A}})\} \end{bmatrix}_{3\mathrm{B}} + \begin{bmatrix} \mathbf{0} \\ \boldsymbol{r}^1(\perp \mathrm{R}_{3\mathrm{A}}) \end{bmatrix}_{4\mathrm{B}} = \begin{bmatrix} \mathbf{0} \\ \boldsymbol{r}^3 \end{bmatrix}. \tag{2.29}$$

That between the base and the two outputs

$$\boldsymbol{M}_{\text{base}-\text{A}'(\text{B}')} = \begin{bmatrix} \mathbf{0} \\ \boldsymbol{r}^1 \end{bmatrix}_1 + \begin{bmatrix} \mathbf{0} \\ \boldsymbol{r}^1(\perp \text{R}_1) \end{bmatrix}_2 + \begin{bmatrix} \mathbf{0} \\ \boldsymbol{r}^1(\perp \text{R}_2, \equiv \text{R}_{3\text{A}(3\text{B})}) \end{bmatrix}_{3\text{A}(3\text{B})}$$

$$+ \begin{bmatrix} \mathbf{0} \\ \{\boldsymbol{r}^1(\perp \text{R}_{3\text{A}(3\text{B})})\} \end{bmatrix}_{4\text{A}(4\text{B})} = \begin{bmatrix} \mathbf{0} \\ \boldsymbol{r}^3 \end{bmatrix}. \tag{2.30}$$

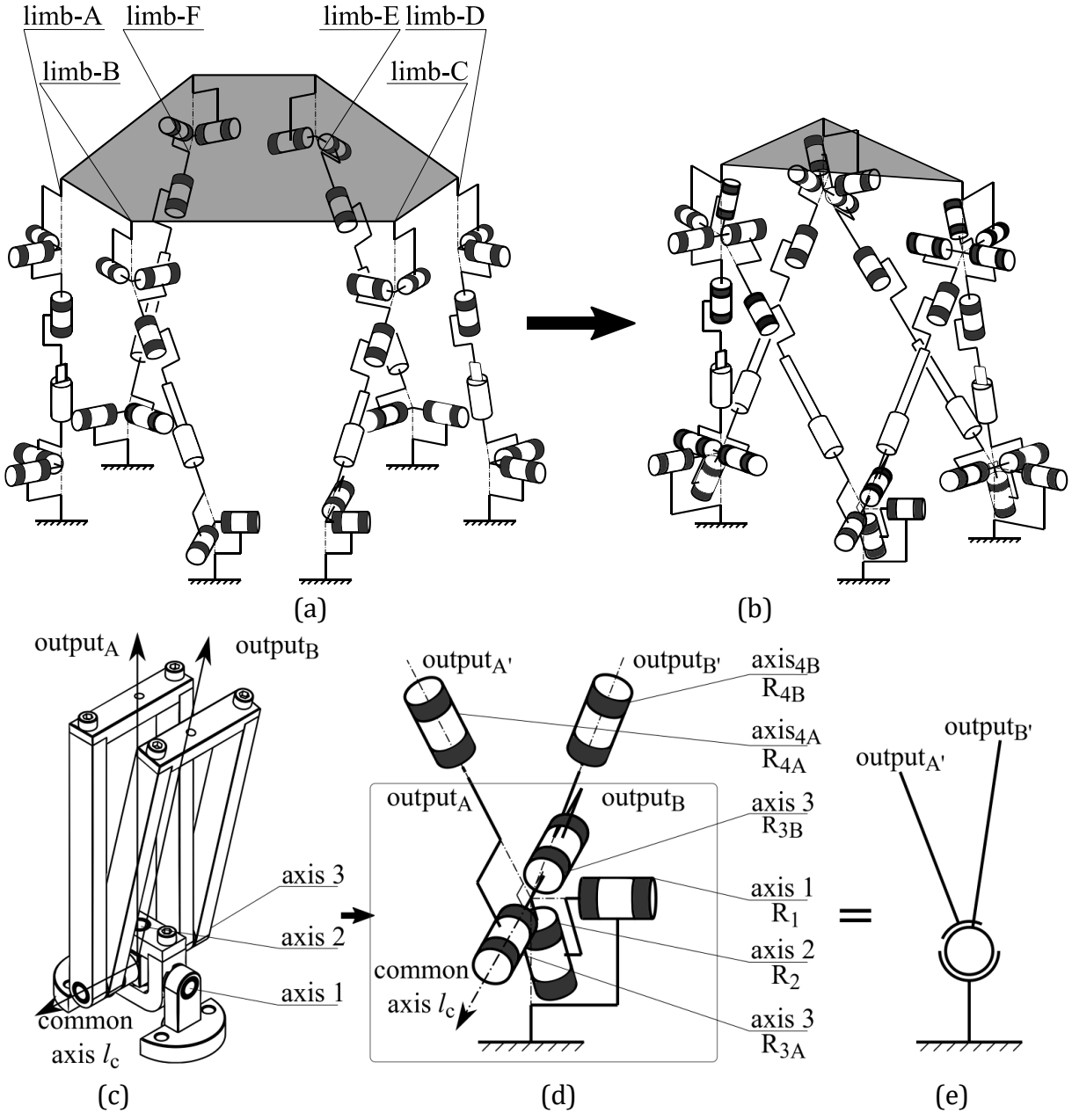

Figure 2.11 The consideration of a re-design from original Gough-Stewart platform to a double Cardan joint integrating design. (a) 6 DOF PKM with Cardan joints; (b) 6 DOF PKM with double Cardan joints; (c) double Cardan joint; (d) topological diagram of double Cardan joints (inside square frame); (e) equivalent double sphere joint.

Note that, the two redundant DOFs in $R_{4A(4B)}$ in eq. (2.30) are not local DOFs. They will not cause any extra local motion, but were constrained by the uniqueness of common axis l_C. Out of the same reason, the local DOF in R_{3B} of the former equation was constrained, too. The motion pattern among output$_{A'}$, output$_{B'}$ and base are the same with the three ends of a concentric double sphere joint. □

If the concentric double sphere joints in fig. 10(a) were replaced by the mechanism in fig. 2.11(d), one extra rotational joint in each limb can be eliminated. Further, the double-double mechanism in fig. 11(b) will be derived. This mechanism is topologically identical with fig. 2.10(a), despite the local DOFs in each limb. However, double Cardan joints obtain advantages, such as, simpler structure, lower manufacture requirement, higher mechanical strength, wider operational space. These properties will be further discussed in Chapter 5.

2.5 Chapter Summary and Discussions

In this chapter, the structural synthesis and topological design of 6 DOF PKM were discussed. Screw theory was used during the topological analysis. This chapter also adapted the output motion matrix and combined it with screw theory. This combination does not dwell on the analytical computation of the rank of Jacobian matrix, but focuses on the geometric relations between the joints represented by screws. The rank, or the motion dimension, of a series connected joints was obtained by the determination of their dependencies. The concepts, coupling degree and basic kinematic chain, were utilized design and analyse the topological structures of different types of 6 DOF PKMs. These concepts provided a range of judging between designs.

At the end of this chapter, various derivative of 6 DOF PKMs were analysed. Through finding BKCs of them, the coupling degree was clarified. In the last derivative, the equality of using spherical joints and double Cardan joints was discussed. The feasibility of the design was proven.

Reference

[2.1] Gogu, Grigore, ed. *Structural synthesis of parallel robots*. Dordrecht: Springer Netherlands, 2008.

[2.2] Yang, T, & Yao, F. "Topological Characteristics and Automatic Generation of Structural Synthesis of Spatial Mechanisms: Part I — Topological Characteristics of Mechanical Networks." *Proceedings of the ASME 1992 Design Technical Conferences*. *22nd Biennial Mechanisms Conference: Flexible Mechanisms, Dynamics, and Analysis*. Scottsdale, Arizona, USA. September 13–16, 1992. pp. 179-185. ASME.

[2.3] Dai, J. S (2019) *Screw Algebra and Kinematic Approaches for Mechanisms and Robotics*, Springer, London.

[2.4] Yang, Ting-Li, and Fang-Hua Yao. "Topological Characteristics and Automatic Generation of Structural Synthesis of Spatial Mechanisms: Part II—Automatic Generation of Structural Types of Kinematic Chains." *International Design Engineering Technical Conferences and Computers and Information in Engineering Conference*. Vol. 9419. American Society of Mechanical Engineers, 1992.

[2.5] Shen, Hui-Ping, and Ting-Li Yang. "A New Method and Automatic Generation for Kinematic Analysis of Complex Planar Mechanisms Based on the Ordered Single-Opened-Chains." *International Design Engineering Technical Conferences and Computers and Information in Engineering Conference*. Vol. 12846. American Society of Mechanical Engineers, 1994.

[2.6] Shen, Huiping, Kwun-Lon Ting, and Tingli Yang. "Configuration analysis of complex multiloop linkages and manipulators." *Mechanism and Machine Theory* 35.3 (2000): 353-362.

[7] Du, S., Schlattmann, J., Schulz, S., Seibel, A.: Comparison of three methods of length compensation in a parallel kinematic and their equivalence conditions. MEAE 2018, MATEC Web Conf. p. 198 02003 (2018)

[8] Du, S., Schlattmann, J., Schulz, S., Seibel, A. (2019). Passive Rotation of Rotational Joints and Its Computation Method. In: Uhl, T. (eds) Advances in Mechanism and Machine Science. IFToMM WC 2019. Mechanisms and Machine Science, vol 73. Springer, Cham. https://doi.org/10.1007/978-3-030-20131-9_36

[9] Shen, Hui-Ping, et al. "Topological structure coupling-reducing of parallel mechanisms." *Proceedings of the 14th IFToMM World Congress*. 2015.

[10] YANG, Ting-Li, et al. Composition principle based on SOC unit and coupling degree of BKC for general spatial mechanisms. In: *Proceedings of the 14th IFToMM World Congress*. 2015. S. 437-446.

Chapter 3
Basis of Lie Group, Algebra and Displacements Operators

The expression of the motion in the space is a classical topic in graphic theory, kinematics and mechanics. A better expression form of rigid body motion can increase the computation speed and accuracy. In this chapter, some basic ideas of group theory and its accompanied algebra will be introduced, which are highly connected to the displacement operators. The group actions on the algebra will be represented. Some classical displacement operators will be listed and discussed, as the foundation of kinematic and dynamic analysis in the following chapters.

3.1 A Brief Review and Introduction

A reliable study of classic displacement operator commenced with the Rodrigues parameters ([3.1]), which applies half of the rotation angles and the rotation axis to represent a rotation motion. Based on it, the Rodrigues formula was formed. The Euler-Rodrigues formula ([3.2]) was also derived from this point. Cayley formulated the skew-symmetric rotation matrix based on Rodrigues parameters ([3.3]). Rodrigues also suggested a tuple of four parameters in [3.1], and derived Rodrigues quaternions, which promoted the derivation of Euler-Rodrigues formula. Quaternions itself is also an ancient concept firstly invented by Hamilton ([3.4]) in the middle of 19^{th} century to express the rotations. It shows advantages in long term practical utilizations. Inspired by this concept, Clifford introduced dual-quaternions in [3.5]. As a representation of elements of $SE(3)$, the primary part of a dual-quaternions is the quaternions formed by

Rodrigues four-parameters, its secondary part is a quaternions product of the primary part and the translational pure quaternions.

This chapter will follow the layout below: First, a brief introduction of group theory will be presented, and some representations will also be introduced; then, the Lie Algebra and their representations will be discussed; third, the relation between displacements and velocity vector space, as exponential maps, will be derived in a compact form; some other displacement operators will be listed; lastly, the chapter will be summarized.

3.2 Lie Groups

In kinematics, Lie group theory is used to describe and analyse the symmetries, transformations, and configurations of mechanical systems, particularly those involving rotations and translations. It provides a powerful mathematical framework for studying and analysing the geometric aspects of motion and transformations in kinematics. It is widely applied in robotics, mechanical engineering, computer graphics, and related fields to model, simulate, and control the motion of objects and systems.

3.2.1 Groups and Lie Group

Definition 3.1 ([3.6]): A ***group*** is an ordered pair $(\boldsymbol{G},\circ)$ such that $\boldsymbol{G}$ is a set, $\circ$ is an associative binary operation on $\boldsymbol{G}$, and $\exists e \in \boldsymbol{G}$ such that

i. if $a \in \boldsymbol{G}$, then $a \circ e \in \boldsymbol{G}$,

ii. if $a \in \boldsymbol{G}$, then $\exists a^{-1} \in \boldsymbol{G}$ such that $a \circ a^{-1} = e$.

The first axiom ensures the closeness of a group, and the second ensures the identity of a group. Without misunderstanding, the group can be denoted as $\boldsymbol{G}$. From the definition axioms two theorems can be derived,

Theorem 3.1: if $a \in \boldsymbol{G}$, then $a \circ e = a$ and $e \circ \mathrm{a} = a$

Theorem 3.2: if $a \in \boldsymbol{G}$ and $b \in \boldsymbol{G}$, there must be $x \in \boldsymbol{G}$, so that, $a \circ x = b$.

Definition 3.2: A ***Lie group*** is a set $\boldsymbol{G}$ equipped with both a group structure and a smooth manifold structure such that the group multiplication and inversion operations are smooth.

In other words, the multiplication and inversion operations in the Lie group are continuous and differentiable, making $\boldsymbol{G}$ a smooth manifold with a well-behaved group structure. The smooth manifold structure allows Lie groups to be described locally by coordinates. Additionally, the smoothness of the group operations ensures the group elements to be smoothly transformed into one another. This property is of great importance in kinematic analysis among the other areas.

3.2.2 *SO*(3) and Rotation Matrix

The *rotation group*, *SO*(3), also known as the *Special Orthogonal Group* in three dimensions, is a specific type of Lie group. It consists of all the proper rotations in three-dimensional Euclidean space that preserve the orientation of objects. The *special* in the name refers to the determinant of the rotation matrices being equal to 1.

Definition 3.3: A ***rotation group***, ***SO*(3)**, is the set of all the 3-dimensional Euclidean proper rotations. In matrix form, it contains all the 3×3 orthogonal matrices whose determinant is 1.

In the kinematic analysis, the *SO*(3) is normally considered equivalent to a rotation matrix. It is not difficult to realize that the formation of a rotation matrix is not unique. It can be represented as various Euler angles, screws or unitary quaternions (both are representations of rotation axis and angle) and the exponential map of its Lie algebra, *so*(3). The pose variation caused by the motion of a mechanism is a curve in the vector space, as $\boldsymbol{R}(t) \subset SO(3)$, which defines the pose space of the mechanism. A rotation matrix can be written as

$$\boldsymbol{R} = \begin{bmatrix} r_{xx} & r_{yx} & r_{zx} \\ r_{xy} & r_{yy} & r_{zy} \\ r_{xz} & r_{yz} & r_{zz} \end{bmatrix} \tag{3.1}$$

There are some practical and important properties of a rotation matrix.

Property 1. $\boldsymbol{R}\boldsymbol{R}^{\mathrm{T}} = \boldsymbol{I}$, where, $\boldsymbol{I}$ is the identity matrix.

Property 2. $\det\boldsymbol{R} = 1$, follows the definition of *SO*(3).

Property 3. $\cos\theta = (\mathrm{tr}\boldsymbol{R} - 1)/2$, where θ is the rotation angle along the rotation axis, $\mathrm{tr}\boldsymbol{R}$ is the trace of rotation matrix.

Property 4. $\boldsymbol{\omega} = \boldsymbol{u}/\|\boldsymbol{u}\|$, where $\boldsymbol{\omega}$ is the unitary rotation axis and $\boldsymbol{u} = [r_{yz} - r_{zy} \quad r_{zx} - r_{xz} \quad r_{xy} - r_{yx}]^{\mathrm{T}}$.

Property 5. $\boldsymbol{R} = [\boldsymbol{x} \quad \boldsymbol{y} \quad \boldsymbol{z}]$, where, $\boldsymbol{x}$ $\boldsymbol{y}$ and $\boldsymbol{z}$ are the orthonormal basis of the rotated frame projected in the old coordinates frame.

3.2.3 *SE*(3) and Homogeneous Displacement Operator

Definition 3.4: The ***special Euclidean group*** in three dimensions, denoted as ***SE*(3)**, is a group that includes all rigid motions in an Euclidean space, including rotations and displacements but not reflections.

Although *SE*(3) is defined in the Euclidean space, it is not considered as an Euclidean space in the traditional sense, because it preserves not only the metric but also the angular displacements. A 3-dimensional Euclidean space is the geometric space where points and distances are defined, while the special Euclidean group, *SE*(3), is a group of transformations acting on this Euclidean space, preserving its geometric properties (distances and angles) under the transformations. An element of *SE*(3) can be represented as a dual-matrix

$$\boldsymbol{D} = \boldsymbol{R} + \epsilon\tilde{\boldsymbol{t}}\boldsymbol{R} \tag{3.2}$$

Where, $\boldsymbol{R}$ is an element of *SO*(3), as eq. (3.1), $\boldsymbol{t}$ is the translational displacement and ϵ is a dual-unit, $\epsilon^2 = 0$. In block matrix form, it can be represented as

$$\boldsymbol{N} = \begin{bmatrix} \boldsymbol{R} & \boldsymbol{0} \\ \tilde{\boldsymbol{t}}\boldsymbol{R} & \boldsymbol{R} \end{bmatrix} \tag{3.3}$$

Definition 3.5: $\mathrm{Ad}(g)$ is the ***adjoint operator of a Lie group***, it can apply adjoint action on Lie group elements or on Lie algebra.

$\mathrm{Ad}(g)$ itself is an element of Lie group, it can be represented as matrix. E.g. if $g \in SO(3)$, the adjoint operator of g can be written as rotation matrix $\boldsymbol{R}$, if $g \in SE(3)$, it can be written as 4×4 matrix $\boldsymbol{H}$, or 6×6 matrix $\boldsymbol{N}$. These two representations act on Lie algebra elements in different forms. For a Lie algebra element, $\boldsymbol{X}$, represented as matrix,

$$\mathrm{Ad}(g)\boldsymbol{X} = g\boldsymbol{X}g^{-1}. \tag{3.4}$$

While, for the same element represented as 6-dimensional vector, as $\mathcal{S}$ in eq. (2.8)

$$\mathrm{Ad}(g)\ \ \mathcal{S} = \boldsymbol{N}\mathcal{S}. \tag{3.5}$$

The *standard* 4×4 *representation* of $SE(3)$, also known as ***homogeneous displacement operator***, is derived from the exponential map of standard 4×4 representation of an element of $se(3)$, as eq. (3.12) in Section 3.3,

$$\boldsymbol{H} = e^{\boldsymbol{V}} = \begin{bmatrix} \boldsymbol{R} & \boldsymbol{t} \\ \boldsymbol{0} & 1 \end{bmatrix} \tag{3.6}$$

The *adjoint representation* of $SE(3)$ is given as eq. (3.3).

3.3 Lie Algebra

Lie algebra enables one to analyse the behaviour of motion in a mathematically elegant and insightful way, particularly when dealing with small changes and local characteristics. It is an essential tool in kinematics for modelling, understanding, and manipulating the geometric aspects of motion in mechanical systems. In kinematics, Lie brackets provide insight into the relationships between different types of motion, helping to derive velocity equations that relate linear and angular velocities.

3.3.1 Lie Bracket and Algebra

Lemma 3.1: The *Lie bracket* is binary operator of finite-dimensional vector space, as

$$[\quad,\quad]:\ \Re^n \times \Re^n \to \Re^n, \tag{3.7}$$

and for $\boldsymbol{X}, \boldsymbol{Y}, \boldsymbol{Z} \in \Re^n$ fulfils

i. Bilinearity: $[a\boldsymbol{X} + b\boldsymbol{Y}, \boldsymbol{Z}] = a[\boldsymbol{X}, \boldsymbol{Z}] + b[\boldsymbol{Y}, \boldsymbol{Z}], [\boldsymbol{X}, a\boldsymbol{Y} + b\boldsymbol{Z}] = a[\boldsymbol{X}, \boldsymbol{Y}] + b[\boldsymbol{X}, \boldsymbol{Z}]$, in which, *a* and *b* are scalars;

ii. Antisymmetry: $[\boldsymbol{X}, \boldsymbol{Y}] = -[\boldsymbol{Y}, \boldsymbol{X}]$, and therefore, . $[\boldsymbol{X}, \boldsymbol{X}] = \boldsymbol{0}$;

iii. Jacobi Identity: $\big[\boldsymbol{X}, [\boldsymbol{Y}, \boldsymbol{Z}]\big] + \big[\boldsymbol{Z}, [\boldsymbol{X}, \boldsymbol{Y}]\big] + \big[\boldsymbol{Y}, [\boldsymbol{Z}, \boldsymbol{X}]\big] = \boldsymbol{0}$.

Definition 3.6: ***Lie Algebra***, $\boldsymbol{g}$, is a finite-dimensional vector space equipped with Lie bracket.

There is a Lie algebra associated to every Lie group. The Lie bracket essentially measures the "commutator" of two elements in the Lie algebra, providing a notion of the algebra's infinitesimal structure. A Lie bracket is a computation of two vectors to derive a third vector. If a Lie group G has a smooth manifold structure, then its Lie algebra can be thought of as the tangent space at the identity element, which captures the local behaviour of group elements near the identity. Lie algebra is also a vector field, e.g. the Lie algebra *se*(3) of *SE*(3) and *so*(3) of *SO*(3) are 6- and 3- dimensional vector spaces, respectively.

3.3.2 Adjoint Representation

Definition 3.7: The ***adjoint representation*** of Lie algebra is the mapping from Lie algebra vector space to a general linear Lie algebra. For each element, $\boldsymbol{X} \in \boldsymbol{g}$, the adjoint representation $\mathrm{ad}(\boldsymbol{X})$ is a linear transformation on $\boldsymbol{g}$ that maps each element $\boldsymbol{Y} \in \boldsymbol{g}$ to the Lie bracket $[\boldsymbol{X}, \boldsymbol{Y}]$.

$$\varphi: \boldsymbol{X} \to \mathrm{ad}(\boldsymbol{X}) \tag{3.8}$$

$$\mathrm{ad}(\boldsymbol{X})\boldsymbol{Y} = [\boldsymbol{X}, \boldsymbol{Y}] \tag{3.9}$$

The adjoint representation of an element of $\boldsymbol{g}$ can also be in several forms, such as, screws, dual number, pure quaternions and matrix.

Theorem 3.3: *Ado's theorem* ([3.7]) states that every finite-dimensional Lie algebra over a field K near identity can be viewed as a Lie algebra of square matrices under the commutator

bracket.

There are three forms of Lie algebra: vectors, dual-vectors and quaternions. Hereby, only the vector form is given,

$$\boldsymbol{\omega} = \begin{bmatrix} \omega_x \\ \omega_y \\ \omega_z \end{bmatrix}, \boldsymbol{\Omega} = \begin{bmatrix} \boldsymbol{v} \\ \boldsymbol{\omega} \end{bmatrix}. \tag{3.10}$$

In which, $\boldsymbol{\omega} \in so(3)$, $\boldsymbol{v} \in \Re^3$ and $\boldsymbol{\Omega} \in se(3)$. Theorem 3.3 allows any finite-dimensional Lie algebra to be represented by an *n*×*n* matrix that fulfils Lie bracket. Thus, the adjoint representation of *so*(3) is a 3×3 skew-symmetric matrix, as

$$\mathrm{ad}(\boldsymbol{\omega}) = \tilde{\boldsymbol{\omega}} = \begin{bmatrix} 0 & -\omega_z & \omega_y \\ \omega_z & 0 & -\omega_x \\ -\omega_y & \omega_x & 0 \end{bmatrix}. \tag{3.11}$$

Hence it can be seen, the Lie bracket of *so*(3) is in fact the cross product between two elements of it. There are two representations of *se*(3). The *standard* 4×4 *representation* is

$$\boldsymbol{V} = \begin{bmatrix} \tilde{\boldsymbol{\omega}} & \boldsymbol{v} \\ \boldsymbol{0} & 0 \end{bmatrix} \tag{3.12}$$

In which, $\tilde{\boldsymbol{\omega}}$ is the *adjoint representation* in *so*(3) and $\boldsymbol{v} \in \Re^3$. Thus, the elements of *se*(3) constitute a sub-space of $\Re^{4\times4}$. Another representation of *se*(3) is the 6×6 adjoint representation, as

$$\boldsymbol{W} = \mathrm{ad}(\boldsymbol{\Omega}) = \begin{bmatrix} \tilde{\boldsymbol{\omega}} & \boldsymbol{0} \\ \tilde{\boldsymbol{v}} & \tilde{\boldsymbol{\omega}} \end{bmatrix}. \tag{3.13}$$

The two matrix representations are 6 dimensional and isomorphism (1-to-1 correspondence mapping, preserving group multiplication).

3.4 Exponential Mapping

The exponential map of a Lie algebra element is a powerful concept with wide-ranging importance in various areas of mathematics, physics, and engineering, especially, in trajectory planning and poses estimation. In this section, the derivation of an *SE*(3) element from an *se*(3)

element will be given. The derivation process is based on the motion of a rigid body.

Definition 3.8: A ***single parameter subgroup*** of a Lie group is a group fulfils the smooth map $\gamma: \Re \to G$, so that

$$\gamma(s+t) = \gamma(s)\gamma(t). \quad s,t \in \Re$$

Note that, the mapping γ also maps the addition in real number domain to group multiplication. A single parameter subgroup is in fact one integral curve on the manifold of a Lie group.

Definition 3.9: ***Exponential mapping*** is a smooth mapping from Lie algebra, $\boldsymbol{g}$, to Lie group, $\boldsymbol{G}$, as

$$\exp: \boldsymbol{g} \to G,$$

$$\exp(\boldsymbol{X}t) = e^{\boldsymbol{X}t} = \gamma(t). \quad t \in \Re, \boldsymbol{X} \in \boldsymbol{g}$$

The proof of this definition can be found from works of Murray ([3.8]). Note that, only if $[\boldsymbol{X}_1, \boldsymbol{X}_2] = \boldsymbol{0}$, $\exp(\boldsymbol{X}_1 + \boldsymbol{X}_2) = \exp(\boldsymbol{X}_1) + \exp(\boldsymbol{X}_2)$.

3.4.1 $\boldsymbol{so(3) \mapsto SO(3)}$: Exponential Mapping of a Rotation

Based on Taylor series and the fact that for a unitary $\widetilde{\boldsymbol{\omega}}$, $\widetilde{\boldsymbol{\omega}}^3 = -\widetilde{\boldsymbol{\omega}}$, we obtain the exponential coordinates of a rotation.

$$e^{\widetilde{\omega} t_n} = \boldsymbol{I} + \widetilde{\boldsymbol{\omega}} \sin t_n + \widetilde{\boldsymbol{\omega}}^2 (1 - \cos t_n) \tag{3.14}$$

This result coincides with Euler-Rodrigues formula ([3.9]).

3.4.2 $\boldsymbol{se(3) \mapsto SE(3)}$: Exponential Mapping of a Twist and Related Equations

Any alteration of a rigid body configuration can be concerned as a combination of a rotation about one axis $\boldsymbol{\omega}$ and a translation along one translational velocity $\boldsymbol{v}_\theta$. Consider a motion defined as fig. 3.1. In fig. 3.1, point $\boldsymbol{q}$ is a point on the line where vector $\boldsymbol{\omega}$ locates. The instantaneous velocity of point $\boldsymbol{p}$ is

$$\boldsymbol{v}_p = \boldsymbol{v}_\theta + \boldsymbol{v}_\omega. \tag{3.15}$$

In which, $\boldsymbol{v}_\omega = \tilde{\boldsymbol{\omega}}(\boldsymbol{p}-\boldsymbol{q})$ is the velocity of $\boldsymbol{p}$ caused by rotation. Moreover, this velocity relation can be expressed as a first-order linear differential equation,

$$\dot{\boldsymbol{p}} = \boldsymbol{v}_\theta(t) + \tilde{\boldsymbol{\omega}}\big(\boldsymbol{p}(t) - \boldsymbol{q}(t)\big). \tag{3.16}$$

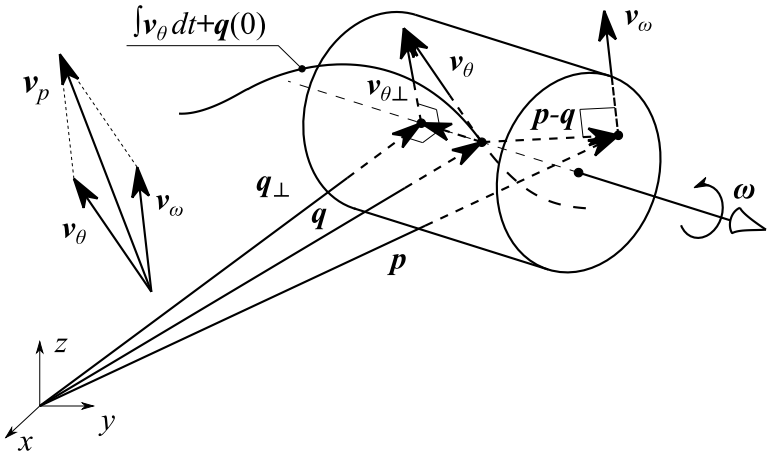

Figure 3.1. The motion analysis of one random rigid body and its vector definitions.

Considering that, $\boldsymbol{q}(t)$ is only driven by the tranlational velocity $\boldsymbol{v}_\theta$, there exists $\boldsymbol{q}(t) = \boldsymbol{q}(0) + \int_0^t \boldsymbol{v}_\theta(u)\,du$. Then, velcoity of point $\boldsymbol{p}$ can be written as

$$\dot{\boldsymbol{p}} = \boldsymbol{v}_\theta(t) + \tilde{\boldsymbol{\omega}}\boldsymbol{p}(t) - \tilde{\boldsymbol{\omega}}\left(\boldsymbol{q}(0) + \int_0^t \boldsymbol{v}_\theta(u)\,du\right) \tag{3.17}$$

and its homogeneous form, according to eq. (3.12), is

$$\dot{\bar{\boldsymbol{p}}}(t) := \begin{bmatrix}\dot{\boldsymbol{p}}\\ 0\end{bmatrix} = \begin{bmatrix}\tilde{\boldsymbol{\omega}} & \boldsymbol{v}_\theta(t) - \tilde{\boldsymbol{\omega}}\left(\boldsymbol{q}(0) + \int_0^t \boldsymbol{v}_\theta(u)\,du\right)\\ \boldsymbol{0} & 0\end{bmatrix}\begin{bmatrix}\boldsymbol{p}(t)\\ 1\end{bmatrix} := \begin{bmatrix}\tilde{\boldsymbol{\omega}} & \boldsymbol{v}\\ \boldsymbol{0} & 0\end{bmatrix}\begin{bmatrix}\boldsymbol{p}\\ 1\end{bmatrix} = \boldsymbol{V}\bar{\boldsymbol{p}}(t). \tag{3.18}$$

The 4×4 matrix $\boldsymbol{V}$ is a Lie algebra element, scilicet, an element of *se*(3). This $\boldsymbol{V}$ is also a time-varying twist since $\boldsymbol{q}$ is changing due to $\boldsymbol{v}_\theta$. Note that, in eq. (3.18), $\boldsymbol{\omega}$ is time-invariant, while $\boldsymbol{v}_\theta$ is not arbitrarily parallel to $\boldsymbol{\omega}$ and, thus, $\boldsymbol{q}$ is not constant during the motion. As well known, to approach a general closed-form solution, a necessary condition is a constant coefficient. This leads to no closed-form solution of $\bar{\boldsymbol{p}}$. To this end, we let

$$\boldsymbol{m}(t) = \boldsymbol{p}(t) - \int_0^t \boldsymbol{v}_\theta(u)\, du\,.$$

(3.19)

Rewrite equation (3.16) and bring equation (3.19) into it, we have

$$\dot{\boldsymbol{p}} - \boldsymbol{v}_\theta = \tilde{\boldsymbol{\omega}}\left(\boldsymbol{p}(t) - \int_0^t \boldsymbol{v}_\theta(u)\, du\right) - \tilde{\boldsymbol{\omega}}\boldsymbol{q}(0) \Longrightarrow \dot{\boldsymbol{m}}(t) = \tilde{\boldsymbol{\omega}}\boldsymbol{m}(t) - \tilde{\boldsymbol{\omega}}\boldsymbol{q}(0).$$

(3.20)

Or in homogeneous form,

$$\dot{\bar{\boldsymbol{m}}}(t) = \boldsymbol{V}_m\bar{\boldsymbol{m}}(t) \coloneqq \begin{bmatrix}\tilde{\boldsymbol{\omega}} & -\tilde{\boldsymbol{\omega}}\boldsymbol{q}(0)\\ \boldsymbol{0} & 0\end{bmatrix}\bar{\boldsymbol{m}}(t). \tag{3.21}$$

$\boldsymbol{V}_m$ is time-invariant and leads to a closed form solution, as

$$\bar{\boldsymbol{m}}(t) = e^{\hat{\xi}_m t}\bar{\boldsymbol{m}}(0) \tag{3.22}$$

Giving an arbitrary modification rigid motion

$$g_m =: \begin{bmatrix}\boldsymbol{I} & -\hat{\boldsymbol{\omega}}^2\|\boldsymbol{\omega}\|^{-2}\boldsymbol{q}(0)\\ 0 & 1\end{bmatrix} \epsilon SE(3), \tag{3.23}$$

and bring in equation (3.21), based on the inverse of eq. (3.4), the coordinates projection of $\boldsymbol{V}_m$ in coordinates g_m is

$$\boldsymbol{V}_m{}' =: g_m^{-1}\boldsymbol{V}_m g_m = \begin{bmatrix}\boldsymbol{I} & \dfrac{\tilde{\boldsymbol{\omega}}^2}{\|\boldsymbol{\omega}\|^2}\boldsymbol{q}(0)\\ 0 & 1\end{bmatrix}\begin{bmatrix}\tilde{\boldsymbol{\omega}} & -\tilde{\boldsymbol{\omega}}\boldsymbol{q}(0)\\ \boldsymbol{0} & 0\end{bmatrix}\begin{bmatrix}\boldsymbol{I} & -\dfrac{\tilde{\boldsymbol{\omega}}^2}{\|\boldsymbol{\omega}\|^2}\boldsymbol{q}(0)\\ 0 & 1\end{bmatrix} = \begin{bmatrix}\tilde{\boldsymbol{\omega}} & \boldsymbol{0}\\ \boldsymbol{0} & 0\end{bmatrix}. \tag{3.24}$$

Here, the facts that, for a skew symmetric matrix $\boldsymbol{\omega}$, $\boldsymbol{\omega}\boldsymbol{\omega}^{\mathrm{T}} = \boldsymbol{I}\|\boldsymbol{\omega}\|^2 + \hat{\boldsymbol{\omega}}^2$ and $\boldsymbol{\omega}^{\mathrm{T}}\hat{\boldsymbol{\omega}} = \boldsymbol{0}$, are used. Expand the exponantial form of equation (3.24) into a Taylor series form,

$$e^{\boldsymbol{V}_m{}' t} = \begin{bmatrix}\sum_{k=0}^{\infty}\dfrac{1}{k!}(\tilde{\boldsymbol{\omega}}t)^k & \boldsymbol{0}\\ \boldsymbol{0} & 1\end{bmatrix} = \begin{bmatrix}e^{\tilde{\boldsymbol{\omega}}t} & \boldsymbol{0}\\ \boldsymbol{0} & 1\end{bmatrix}. \tag{3.25}$$

Bring in equation (3.23), (3.24) and (3.28), the displacement matrix in equation (D) is

$$\boldsymbol{g}'(t) := e^{\boldsymbol{V}_m t} = e^{g_m \boldsymbol{V}_m' t g_m^{-1}} = g_m e^{\boldsymbol{V}_m' t} g_m^{-1} = \begin{bmatrix} e^{\tilde{\boldsymbol{\omega}} t} & \left(e^{\tilde{\boldsymbol{\omega}} t} - \boldsymbol{I}\right) \frac{\tilde{\boldsymbol{\omega}}^2}{\|\boldsymbol{\omega}\|^2} \boldsymbol{q}(0) \\ \mathbf{0} & 1 \end{bmatrix}$$
$$= \begin{bmatrix} e^{\tilde{\boldsymbol{\omega}} t} & \left(\boldsymbol{I} - e^{\tilde{\boldsymbol{\omega}} t}\right) \boldsymbol{q}(0) \\ \mathbf{0} & 1 \end{bmatrix}$$
$$= \begin{bmatrix} e^{\tilde{\boldsymbol{\omega}} t} & -\left[\frac{\tilde{\boldsymbol{\omega}}}{\|\boldsymbol{\omega}\|} \sin(\|\boldsymbol{\omega}\| t) + \frac{\tilde{\boldsymbol{\omega}}^2}{\|\boldsymbol{\omega}\|^2} (1 - \cos(\|\boldsymbol{\omega}\| t))\right] \boldsymbol{q}(0) \\ \mathbf{0} & 1 \end{bmatrix}. \tag{3.26}$$

Which leads to the motion of point $\boldsymbol{m}$

$$\overline{\boldsymbol{m}}(t) = e^{\boldsymbol{V}_m t} \overline{\boldsymbol{m}}(0).$$

Bring in equation (3.19), the displacement of point $\boldsymbol{p}$ is

$$\boldsymbol{p}(t) = e^{\tilde{\boldsymbol{\omega}} t} \boldsymbol{p}(0) + \left(\boldsymbol{I} - e^{\tilde{\boldsymbol{\omega}} t}\right) \boldsymbol{q}(0) + \int_0^t \boldsymbol{v}_\theta(u)\, du$$

In homogeneous form

$$\overline{\boldsymbol{p}}(t) = \boldsymbol{g}'(t) \overline{\boldsymbol{p}}(0) = \begin{bmatrix} e^{\tilde{\boldsymbol{\omega}} t} & \left(\boldsymbol{I} - e^{\tilde{\boldsymbol{\omega}} t}\right) \boldsymbol{q}(0) + \int_0^t \boldsymbol{v}_\theta(u)\, du \\ \mathbf{0} & 1 \end{bmatrix} \begin{bmatrix} \boldsymbol{p}(0) \\ 1 \end{bmatrix} \tag{3.27}$$

□

At this end, an expression of a combination of a rotation and a translation was given. This fact is also an expression of the quotient group property of *SE*(3) over *T*(3), which is SO(3). This is a semi-direct product of *T*(3), and SO(3), illustrated by a rotation effect over translation.

3.4.3 $SE(3) \mapsto se(3)$: Inverse Exponential Mapping of Rigigd Motion and Related Equations

Let a displacement of one rigid body be

$$\boldsymbol{g}(t) = \begin{bmatrix} \boldsymbol{R} & \boldsymbol{t} \\ \mathbf{0} & 1 \end{bmatrix}. \tag{3.28}$$

Here, $\boldsymbol{t}$ is the displacement of the coordinate centre of the moving rigid body. Considering eq.

(3.27), we have

$$\boldsymbol{t} = \left(\boldsymbol{I} - e^{\tilde{\boldsymbol{\omega}}t}\right)\boldsymbol{q}(0) + \int_0^t \boldsymbol{v}_\theta(u)\, du\,.$$

(3.29)

Thus, the displacement caused by translational velocity is

$$\int_0^t \boldsymbol{v}_\theta(u)\, du = \quad \boldsymbol{t} - \left(\boldsymbol{I} - e^{\tilde{\boldsymbol{\omega}}t}\right)\boldsymbol{q}(0).$$

(3.30)

The translational velocity is

$$\boldsymbol{v}_\theta(t) = \frac{d}{dt}\left[\boldsymbol{t} - \left(\boldsymbol{I} - e^{\tilde{\boldsymbol{\omega}}t}\right)\boldsymbol{q}(0)\right] = \frac{d}{dt}\boldsymbol{t} + e^{\tilde{\boldsymbol{\omega}}t}\tilde{\boldsymbol{\omega}}\boldsymbol{q}(0).$$

(3.31)

Bring equation (3.31) into equation (3.18) and considering that $\boldsymbol{q}(t) = \int_0^t \boldsymbol{v}_\theta(u)\, du + \boldsymbol{q}(0)$, the twist of this displacement in equation (3.28) is

$$\boldsymbol{V} = \begin{bmatrix} \tilde{\boldsymbol{\omega}} & \boldsymbol{v}_\theta(t) - \tilde{\boldsymbol{\omega}}\boldsymbol{q}(t) \\ \boldsymbol{0} & 0 \end{bmatrix} = \begin{bmatrix} \tilde{\boldsymbol{\omega}} & \frac{d}{dt}\boldsymbol{t} - \tilde{\boldsymbol{\omega}}\boldsymbol{t} \\ \boldsymbol{0} & 0 \end{bmatrix}.$$

(3.32)

□

3.5 Other Displacement Operators

Besides the 3×3 rotation matrix, 4×4 homogeneous representations and 6×6 adjoint representations, there are several familiar displacement operators.

3.5.1 Rodrigues Formula

Illustrated in fig. 3.2, the rotation of a rigid body with rotation angle θ and rotation axis $\boldsymbol{\omega} = [\omega_x \quad \omega_y \quad \omega_z]^{\mathrm{T}}$ can be expressed by *Rodrigues parameters*, as

$$r_x = \tan\frac{\theta}{2}\omega_x, \quad r_y = \tan\frac{\theta}{2}\omega_y, \quad r_z = \tan\frac{\theta}{2}\omega_z. \tag{3.33}$$

One vector, $\boldsymbol{v}_1$, on the rigid body passes $\boldsymbol{\omega}$, will be rotated to $\boldsymbol{v}_2$. Then the rotation can be expressed by the *Rodrigues formula*, as

$$\boldsymbol{v}_2 - \boldsymbol{v}_1 = \tilde{\boldsymbol{r}}(\boldsymbol{v}_2 + \boldsymbol{v}_1). \tag{3.34}$$

Where, $\boldsymbol{r} = [r_x \quad r_y \quad r_z]^{\mathrm{T}}$.

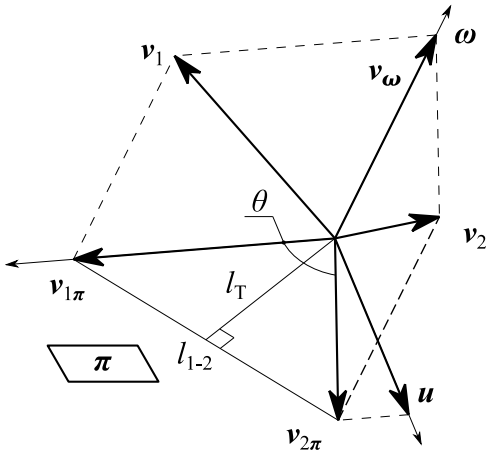

Figure 3.2. The rotation of one vector based on Rodrigues parameters.

3.5.2 Euler-Rodrigues Rotation Formula

Given a plane, $\boldsymbol{\pi}$, vertical to the rotation axis and pass through the origin of the vector $\boldsymbol{v}_1$, the projections of $\boldsymbol{v}_1$ and $\boldsymbol{v}_2$ on the plane will be $\boldsymbol{v}_{1\boldsymbol{\pi}}$ and $\boldsymbol{v}_{2\boldsymbol{\pi}}$. Projection of them on the rotation axis will be $\boldsymbol{v}_{\boldsymbol{\omega}}$. Then,

$$\boldsymbol{v}_2 = \boldsymbol{v}_{2\boldsymbol{\pi}} + \boldsymbol{v}_{\boldsymbol{\omega}}. \tag{3.35}$$

Also,

$$\boldsymbol{v}_2 = \boldsymbol{v}_{1\boldsymbol{\pi}}\cos\theta + \boldsymbol{u}\sin\theta + \boldsymbol{v}_{\boldsymbol{\omega}}. \tag{3.36}$$

Considering that $\boldsymbol{v}_{1\boldsymbol{\pi}} = \boldsymbol{v}_1 - \boldsymbol{v}_{\boldsymbol{\omega}}$, $\boldsymbol{v}_{\boldsymbol{\omega}} = (\boldsymbol{v}_1{}^{\mathrm{T}}\boldsymbol{\omega})\boldsymbol{\omega}$ and $\boldsymbol{u} = \tilde{\boldsymbol{\omega}}\boldsymbol{v}_1$, eq. (3.36) will transform to

$$\begin{aligned}\boldsymbol{v}_2 &= [\boldsymbol{v}_1 - (\boldsymbol{v}_1{}^{\mathrm{T}}\boldsymbol{\omega}) \quad \boldsymbol{\omega}]\cos\theta + \tilde{\boldsymbol{\omega}}\boldsymbol{v}_1\sin\theta + (\boldsymbol{v}_1{}^{\mathrm{T}}\boldsymbol{\omega})\boldsymbol{\omega} \\ &= \boldsymbol{v}_1\cos\theta + \tilde{\boldsymbol{\omega}}\boldsymbol{v}_1\sin\theta + (\boldsymbol{v}_1{}^{\mathrm{T}}\boldsymbol{\omega})\boldsymbol{\omega}(1-\cos\theta) \\ &= [\cos\theta\,\boldsymbol{I} + \sin\theta\,\tilde{\boldsymbol{\omega}} + (1-\cos\theta)\boldsymbol{\omega}\boldsymbol{\omega}^{\mathrm{T}}]\boldsymbol{v}_1 = \boldsymbol{R}\boldsymbol{v}_1.\end{aligned} \tag{3.37}$$

And the *Euler-Rodrigues rotation formula* is thus

$$\boldsymbol{R} = \cos\theta\, \boldsymbol{I} + \sin\theta\, \tilde{\boldsymbol{\omega}} + (1 - \cos\theta)\boldsymbol{\omega}\boldsymbol{\omega}^{\mathrm{T}} \tag{3.38}$$

In which $\boldsymbol{\omega}\boldsymbol{\omega}^{\mathrm{T}}$ is the tensor product of $\boldsymbol{\omega}$. It can be proven that eq. (3.38) is equivalent to eq. (3.14).

3.5.3 Cayley Rotation Formula

As shown in fig. 3.2, the two lines are vertical, $l_{\mathrm{T}} \perp l_{1-2}$, this brings up

$$(\boldsymbol{v}_{2\pi} + \boldsymbol{v}_{1\pi})(\boldsymbol{v}_{2\pi} - \boldsymbol{v}_{1\pi}) = 0. \tag{3.39}$$

Let the rotation operator being $\boldsymbol{R}$, then $\boldsymbol{v}_{2\pi} = \boldsymbol{R}\boldsymbol{v}_{1\pi}$, there will be

$$\boldsymbol{v}_{2\pi} - \boldsymbol{v}_{1\pi} = (\boldsymbol{R} - \boldsymbol{I})\boldsymbol{v}_{1\pi} = (\boldsymbol{R} - \boldsymbol{I})(\boldsymbol{R} + \boldsymbol{I})^{-1}(\boldsymbol{v}_{2\pi} + \boldsymbol{v}_{1\pi}) = \boldsymbol{C}(\boldsymbol{v}_{2\pi} + \boldsymbol{v}_{1\pi}). \tag{3.40}$$

It can be found, the form of eq. (3.40) is identical to eq. (3.34). The matrix $\boldsymbol{C}$ in fact equals to $\tilde{\boldsymbol{r}}$ ([3.10]). Then, the *Cayley formula* can be derived as

$$\boldsymbol{R} = (\boldsymbol{I} - \boldsymbol{C})^{-1}(\boldsymbol{I} + \boldsymbol{C}) = (\boldsymbol{I} - \tilde{\boldsymbol{r}})^{-1}(\boldsymbol{I} + \tilde{\boldsymbol{r}}). \tag{3.41}$$

3.5.4 Quaternions Rotation Operator

Quaternions is a combination of one scalar and one 3-dimensional vector; it is an extension of complex number. It can be written as

$$\boldsymbol{Q} = q_0 + \boldsymbol{q} = q_0 + q_1\boldsymbol{i} + q_2\boldsymbol{j} + q_3\boldsymbol{k}. \tag{3.42}$$

Its *conjugate* is

$$\boldsymbol{Q}^* = q_0 - \boldsymbol{q}. \tag{3.43}$$

The symbols $\boldsymbol{i}$, $\boldsymbol{j}$ and $\boldsymbol{k}$ should not be treated as imaginary number symbol, *i*, since they equip different multiplication rules, as

i. $\boldsymbol{ij} = \boldsymbol{k}, \quad \boldsymbol{jk} = \boldsymbol{i}, \quad \boldsymbol{ki} = \boldsymbol{j}; \quad \boldsymbol{ji} = -\boldsymbol{k}, \quad \boldsymbol{kj} = -\boldsymbol{i}, \quad \boldsymbol{ik} = -\boldsymbol{j};$

ii. $\boldsymbol{i}^2 = \boldsymbol{j}^2 = \boldsymbol{k}^2 = -1$

Hence, treating a quaternion as the combination of one scalar and one vector, the *production of two quaternions* in vector form can be calculated as

$$\boldsymbol{Q}_1\boldsymbol{Q}_2 = (q_{10} + \boldsymbol{q}_1)(q_{20} + \boldsymbol{q}_2) = q_{10}q_{20} - \boldsymbol{q}_1 \cdot \boldsymbol{q}_2 + q_{10}\boldsymbol{q}_2 + q_{20}\boldsymbol{q}_1 + \boldsymbol{q}_1 \times \boldsymbol{q}_2 \tag{3.44}$$

It can also be written in a matrix form, as

$$\boldsymbol{Q}_1\boldsymbol{Q}_2 = [1 \quad \boldsymbol{i} \quad \boldsymbol{j} \quad \boldsymbol{k}] \begin{bmatrix} q_{10} & -q_{11} & -q_{12} & -q_{13} \\ q_{11} & q_{10} & -q_{13} & q_{12} \\ q_{12} & q_{13} & q_{10} & -q_{11} \\ q_{13} & -q_{12} & q_{11} & q_{10} \end{bmatrix} \begin{bmatrix} q_{20} \\ q_{21} \\ q_{22} \\ q_{23} \end{bmatrix} = [1 \quad \boldsymbol{i} \quad \boldsymbol{j} \quad \boldsymbol{k}]\boldsymbol{H}_1\boldsymbol{v}_2. \tag{3.45}$$

Referring eq. (3.42) and eq. (3.33), letting $\boldsymbol{q} = [\boldsymbol{i} \quad \boldsymbol{j} \quad \boldsymbol{k}]\boldsymbol{\omega}$, the *Rodrigues quaternions* can be expressed as

$$\boldsymbol{Q} = \cos\frac{\theta}{2} + \sin\frac{\theta}{2}\boldsymbol{q}. \tag{3.46}$$

The four Rodrigues parameters are included in it; thus it belongs to a four dimensional Lie group. Introducing the constraint that

$$\|\boldsymbol{Q}\|^2 = {q_0}^2 + {q_1}^2 + {q_2}^2 + {q_3}^2 = 1, \tag{3.47}$$

The $\boldsymbol{Q}$ in eq. (3.46) will degenerate to unitary quaternions with 3 dimensions. The multiplication of unitary quaternions is smooth and follows Definition 3.1, so that the set of unitary quaternions forms a Lie homomorphism to *SU*(2) group (the complex 2 by 2 matrices with determinant equals positive 1), as well as, to *SO*(3). Thus, the unitary quaternions can be used as a *quaternions rotation operator*.

A *pure quaternions* (or *vector quaternions*) is one representation of *so*(3), as

$$\boldsymbol{Q}_V = [\boldsymbol{i} \quad \boldsymbol{j} \quad \boldsymbol{k}]\boldsymbol{v}. \tag{3.48}$$

A pure quaternions is a special case of $\boldsymbol{Q}$ in eq. (3.42). Its matrix form as $\boldsymbol{H}_1$ in eq. (3.45) is called the *Hamilton operator*, noted as $\boldsymbol{H}_V$. The adjoint action of unitary quaternions group on the vector quaternions is represented as the conjugate quaternions multiplication, as

$$\boldsymbol{Q}_{\boldsymbol{V}'} = \quad \boldsymbol{Q}\boldsymbol{Q}_{\boldsymbol{V}} \quad \boldsymbol{Q}^{*} \tag{3.49}$$

This gives the coordinates transformation of vector, $\boldsymbol{V}$, under the rotation , $\boldsymbol{Q}$.

3.5.5 Dual-Quaternions

A dual-quaternions comprises of a primary part, which is the quaternions rotation operator, and a secondary part, which is the product of a displacement pure quaternions and the primary part, as

$$\widehat{\boldsymbol{Q}} = \boldsymbol{Q} + \epsilon \boldsymbol{Q}_0 = \quad \boldsymbol{Q} + \epsilon\, \boldsymbol{Q}_{\boldsymbol{d}}\boldsymbol{Q}/2. \tag{3.50}$$

Where, $\boldsymbol{Q}_{\boldsymbol{d}} = [\boldsymbol{i} \quad \boldsymbol{j} \quad \boldsymbol{k}]\boldsymbol{d} = [\boldsymbol{i} \quad \boldsymbol{j} \quad \boldsymbol{k}][d_x \quad d_y \quad d_z]^{\mathrm{T}}$ and ϵ is the dual unit with $\epsilon^2 = 0$. In matrix form, the secondary part of eq. (3.50) is

$$\boldsymbol{Q}_0 = \frac{1}{2}[1 \quad \boldsymbol{i} \quad \boldsymbol{j} \quad \boldsymbol{k}]\begin{bmatrix} 0 & -d_x & -d_y & -d_z \\ d_x & 0 & -d_z & d_y \\ d_y & d_z & 0 & -d_x \\ d_z & -d_y & d_x & 0 \end{bmatrix}\begin{bmatrix} q_{20} \\ q_{21} \\ q_{22} \\ q_{23} \end{bmatrix}. \tag{3.51}$$

There are three forms of conjugates of a dual-quaternions, according to [3.11]

i. $\widehat{\boldsymbol{Q}}^{*} = \boldsymbol{Q} - \epsilon\boldsymbol{Q}_0$;

ii. $\widehat{\boldsymbol{Q}}^{\circ} = \boldsymbol{Q}^{*} + \epsilon\boldsymbol{Q}_0{}^{*}$;

iii. $\widehat{\boldsymbol{Q}}^{\sim} = \boldsymbol{Q}^{*} - \epsilon\boldsymbol{Q}_0{}^{*}$.

(3.52)

Each conjugate's conjugate is the dual-quaternion itself, however, only the third form represents the element of *SE*(3), whose adjoint action on a pure vector is

$$\boldsymbol{Q}_{\boldsymbol{V}'} = \quad \widehat{\boldsymbol{Q}}\boldsymbol{Q}_{\boldsymbol{V}} \quad \widehat{\boldsymbol{Q}}^{\sim}. \tag{3.53}$$

3.6 Chapter Summary and Discussion

In this chapter, some basic group theories and Lie algebra were retrospectively discussed, different representations of displacements operators were listed, and the exponential map of $se(3)$ were derived in a compact form, too.

A Lie group is a group composed of differentiable manifolds; all the group operations are smooth mappings between group elements. Lie algebra is a vector space formed by the tangential space near the identity element of its Lie group manifold. The conversion relations are given as the exponential mapping and differential mapping in this chapter.

The form of Lie action varies along the representation of its Lie algebra changes. For a pure quaternion Lie algebra element, the Lie group elements act as a conjugate operation of a unitary quaternions. If the Lie algebra element is represented as a matrix, the Lie action will be a conjugate operation of the Lie group element in matrix form. If the Lie algebra element is in vector form, the Lie action will be a left group action or, straightforwardly, left multiplication of matrix Lie group. Regardless of the representation form, the resultant Lie algebra element is the same. These properties were utilized in the formation of transformation operators in fields of CAD and computational graphics.

Some classical displacement operators were discussed in this chapter as well. Among the others, the quaternions operators will be focused in the following chapter. As one of the representations of $SO(3)$ elements, e.g. anti-Gimbal-lock, quaternions has lighter size than matrix and easier inversion. The inversion is the extraction of rotation information from a quaternions represented $SO(3)$ element. This ensures a more stable and effective trajectory planning, since the interpolation of the rotation will stay on the great circle and the interpolated variable will be the rotate angle, but not the rounded, interpolated rotation matrix.

Reference

[3.1] Rodrigues, Olinde. "Des lois géométriques qui régissent les déplacements d'un système solide dans l'espace, et de la variation des coordonnées provenant de ces déplacements considérés indépendamment des causes qui peuvent les produire." *Journal de mathématiques pures et appliquées* 5 (1840): 380-440.

[3.2] Bisshopp, K. E. "Rodrigues' formula and the screw matrix." (1969): 179-184.

[3.3] Bottema, Oene, and Bernard Roth. *Theoretical kinematics*. Vol. 24. Courier Corporation, 1990.

[3.4] Hamilton, William Rowan. "Ii. on quaternions; or on a new system of imaginaries in algebra." *The London, Edinburgh, and Dublin Philosophical Magazine and Journal of Science* 25.163 (1844): 10-13.

[3.5] Clifford. "Preliminary Sketch of Biquaternions." *Proceedings of The London Mathematical Society* (1871): 381-395.

[3.6] Scott, William Raymond. *Group theory*. Courier Corporation, 2012.

[3.7] Ado, I. D. "The representation of Lie algebras by matrices." *Uspekhi Matematicheskikh Nauk* 2.6 (1947): 159-173.

[3.8] Murray, Richard M., Zexiang Li, and S. Shankar Sastry. *A mathematical introduction to robotic manipulation*. CRC press, 2017.

[3.9] Bisshopp, K. E. "Rodrigues' formula and the screw matrix." (1969): 179-184.

[3.10] Bottema, Oene, and Bernard Roth. *Theoretical kinematics*. Vol. 24. Courier Corporation, 1990.

[3.11] Jia, Yan-Bin. "Dual quaternions." *Iowa State University: Ames, IA, USA* (2013).

Chapter 4
Kinematics of CENTAUROB

In this chapter, the kinematics model of CENTAUROB was built in a comprehensive manner, which refers to exponential matrix parameterization and quaternions in different modelling aspects. The robot CENTAUROB was derived from 6-SPS parallel kinematic mechanisms. Its kinematics was studied in both local coordinates of 6-SPS mechanisms and world coordinates.

The adoption of lead-screw actuators caused the length compensation problem, which induces destructive inner strains and control instabilities. This was originated by the inner relative rotation of the lead-screws. The problem was described and solved in a geometrical method.

To fulfil the demand for accurate controlling and autonomous operation, there derives a demand for end-effector pose recognition. By utilizing the modified 6-SPS mechanism, this FKP was solved by 1-dimensional searching process without losing working space.

4.1 State of the Art

A generalized parallel kinematic mechanism was defined by Merlet [4.1] as a closed-loop kinematic chain mechanism whose end-effector is linked to the base by several independent kinematic chains. Its modern utilization can trace back to 1928 by J. E. Gwinnett [4.2], for the purpose of entertainment. In 1947, Dr. Gough invented a six degree-of-freedom parallel kinematic mechanism [4.3] and put it into industrial use. The Gough platform was widely deemed to the first 6 DOF PKM which was successfully utilized in practice, e.g. in [4.1], [4.4],

[4.5]. In1965, Stewart [4.6] provided the scheme of a PKM served for an aircraft simulator. He has also played an important role in academic studies of Gough platform, which is thus also called Gough-Stewart platform. After decades of development, PKM were widely used in the field of testing rigs and simulators, such as aerospace testing rigs in [4.7], [4.8] and [4.9], vehicle testing rig [4.10], human joint load simulator [4.11]. PKMs are also widely used in medical scenarios, such as surgery platforms [4.12] and [4.13]. In the matter of walking robots, the PKMs are playing an important part, for example, Tian et al. [4.14] have developed the multi-mode walking robot which can move in different configurations. M. Almonacid, et al. in [4.15] have developed the trunk climbing robot based on Gough-Stewart platform.

Kinematics of a mechanical mechanism is the base of design, driving, kinematic and dynamic analysis, simulation and control of a robot system. Kinematics refers to rigid bodies without mass and forces, but only the dimensions, velocities and accelerations. As discussed in chapter 3, there are diverse methods of describing motions of a rigid bodies and no absolute advantages and disadvantages of them. The motion description methods should be weighed and applied according to application scenarios. The main trend of kinematic representations includes, e.g., most widely adopted Euler-Rodrigues equations and its derivation, rotation matrix expression. For example, rotation matrix method was used as basic of linearization dynamic study by Codourey, and Burdet [4.16], of inverse dynamics modelling by Staicu [4.17], of spherical rotation mechanisms by Enferadi and Shahi [4.18], by Chen, Wei-Hsi, et al [4.19], and so forth.

Besides, screw algebra expressions, Denavit-Hartenberg representation, quaternions expression based on Clifford algebra and etc. are also widely used in kinematic studies. For example, screw algebra was used to analyse the singularity of PKMs by Ben-Horin and Shoham in [4.20], by Hao and Ding in [4.21]. Comparing to kinematic analysis, screw theory was more often seen as an important approach for structure synthesis of parallel robots, such as, by Frisoli, et al in [4.22], by Kong and Gosselin in [4.23-24] among the others. Denavit-Hartenberg representation bases on four parameters and described the relations between connecting links. It was used to study the error model of a 3-DOF PKM in [4.25] and to analyse the kinematics in

[4.26]. Quaternions is used to express a rotation with a four-tuple number, a dual quaternions can be thus used to express the rotation and translation simultaneously. It was used for the structure synthesis of serial chain in [4.27], of a planar PKM in [4.28], and also used for the kinematic analysis of spatial PKMs in [4.29-31].

The forward kinematics can be roughly described as a mapping from joint variable space to the motion space of the end-effector, while the inverse kinematics does contrarily. For a parallel kinematics mechanism, the inverse kinematic problem (IKP) is in general more straightforward, while the forward kinematic problem (FKP) refers various dimensional searching problem, as mentioned in chapter 2. The study of FKP of PKMs is flourishing among researchers. Pott provided the FKP solutions based on Levenberg-Marquardt algorithm for a cable-driven PKM [4.32]. Yang, et al. provided a method based dual quaternions to solve the FKP of a class of 6-DOF PKMs [4.33]. Morell et al. have provided a method based on machine learning to solve the FKP of Gough-Stewart platforms [4.34]. Zhu and Zhang have developed the numerical method combining the artificial neural networks and Global Newton-Raphson with Monotonic Descent algorithm [4.35] and obtained accurate and efficient solutions.

In this chapter, the contents will be arranged as following. Section 4.2 will introduce the inverse kinematic model of the a modified 6-S<u>P</u>S. The coordinate system will be defined in a comprehensive manner, which gives consideration to both operating convenience and smoothness of rotations of platforms. Comparatively, the inverse kinematics in quaternions form will also be given in this section. In section 4.3, the inverse kinematic will be given in the spectrum of the whole robot. To be noticed, in both sections, the solutions of the double Cardan joints are given, for the sake of length compensation of linear actuators. This length compensation problem was proposed and solved in Section 4.4. Because of the adoption of PKM[6,3] mechanism, only 1-dimensional FKP process was discussed in Section 4.5. In Section 4.6, the simulation examples of IKP and FKP were given.

4.2 Inverse Kinematics Model of 6-SPSes in CENTAUROB

Inverse kinematic problem (IKP) for PKMs is normally obvious and straightforward. The IKP solution for PKMs is indeed to solve the motion of actuators from the motion of end effector. In other words, the main aim of IKP is to build the mapping relation from the end-effector to joint spaces. Especially, to thoroughly understand the kinematic properties of the mechanism and to compensate the length variation caused by linear actuators inner rotation, it is necessary to derive the inverse kinematic models for every rigid body in the structure. This means, not only the actuated joints, but also the passive joints should be studied.

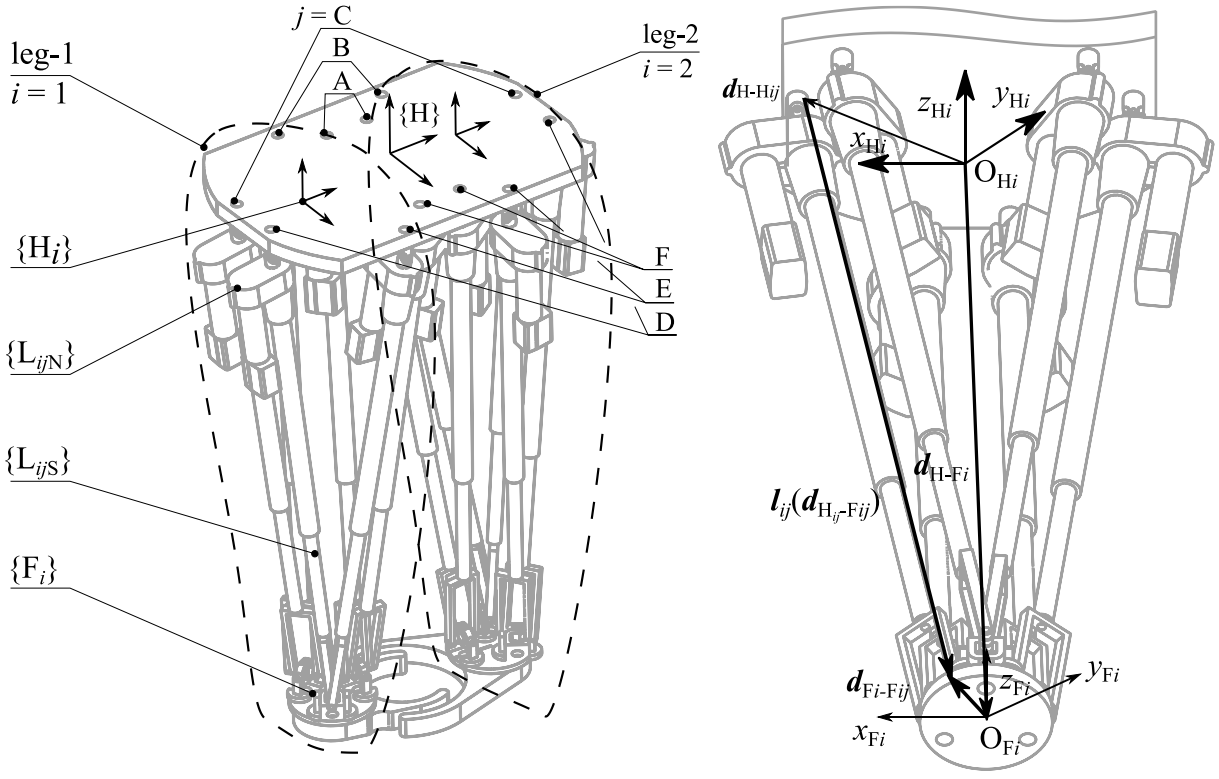

(a) (b)

Figure 4.1 Coordinates of the robot and one leg of it. (a) The coordinates assignment of CENTAUROB; (b) The coordinates in one leg. The foot platform was neglected.

The CENTAUTOB is in general composed of two PKM[6,3] mechanisms. As illustrated in fig. 4.1(a), the whole robot contains one hip platform and two foot platforms. The two coordinates on hips, $\{H_1\}$ and $\{H_2\}$, form two 6-SPS mechanisms with two foot platforms, $\{F_1\}$ and $\{F_2\}$, respectively. The two 6-SPS mechanisms are called leg-1 and leg-2. The 6 limbs of one leg was

noted as limb-*ij*, where *i* stands for 1 or 2, *j* stands for A, B, …, F. The upper and lower part of the limbs comprise of sleeves and shafts (screw nuts), noted as {L*ij*S} and {L*ij*N}.

4.2.1 Joint Variables and Generalized Coordinates

As mentioned in Chapter 2, the modified 6-S<u>P</u>S mechanism in fig. 4.1 (b) obtains the same topological properties as an original 6-S<u>P</u>S mechanism. Its moving platform {F$_i$} obtains 6 dimensional connectivity w.r.t. the base platform, {H$_i$}. Thus, the 6 prismatic joints are chosen as driving component. Their lengths are the joint variables.

$$\boldsymbol{q}_i = [l_{i\mathrm{A}} \quad l_{i\mathrm{B}} \quad l_{i\mathrm{C}} \quad l_{i\mathrm{D}} \quad l_{i\mathrm{E}} \quad l_{i\mathrm{F}}]^{\mathrm{T}} \quad i = 1, 2 \tag{4.1}$$

The generalized coordinates of {Fi} can be defined as

$$\boldsymbol{X}_i = [x_i \quad y_i \quad z_i \quad A_i \quad B_i \quad \Gamma_i]^{\mathrm{T}} \quad i = 1,2. \tag{4.2}$$

The first three entries in eq. (4.2) represent the translational displacement of the origin of {Fi}, while the last three entries represent the rotational motion of {Fi.}. The definition of them can be chosen arbitrarily base on different occasions. For instance, they can be Euler angles or any parameters of *SO*(3) group. For this reason, $\boldsymbol{X}_i$ can also be described in a dual-vector form.

$$\boldsymbol{X}_i = [\boldsymbol{t}_i^{\mathrm{T}} \quad \boldsymbol{r}_i^{\mathrm{T}}]^{\mathrm{T}} \quad i = 1,2. \tag{4.3}$$

For a screw algebra occasion, the definition of it is similar to eq. (2.7). For a quaternions form, $\boldsymbol{r}_i$ could denote the rotation axis and magnitude. For a matrix form, $\boldsymbol{r}_i$ stands for a tuple of Euler angles. In sum, the choice of coordinates is not unique, however, it must contain all the parameters of the *SE*(3) group.

Note that, the variables in leg-*i* are w.r.t. the base coordinates {H$_i$}. For convenience, their references are omitted. The variables w.r.t. other coordinates are written as ${}^{\{*\}}\boldsymbol{*}_i$, {*} represents the reference and $\boldsymbol{*}_i$ is the variable. For example, $\boldsymbol{X}_i$ referring to the inertial frame is ${}^{\{\mathrm{E}\}}\boldsymbol{X}_i$.

4.2.2 Inverse Kinematics with Matrix Form

1) Minimal Coordinates of Moving Platform

The position and pose of a rigid body is a member of *SE*(3) group. The *SE*(3) operator generated by motion of $\{F_i\}$ w.r.t. the *i*-th hip platform is

$$\boldsymbol{H}_{\mathrm{H-F}_i} = \begin{bmatrix} \boldsymbol{R}_{\mathrm{H-F}i} & \boldsymbol{d}_{\mathrm{H-F}i} \\ \boldsymbol{0} & 1 \end{bmatrix} \tag{4.4}$$

$\boldsymbol{R}_{\mathrm{H\text{-}F}i}$ is the *SO*(3) member in a matrix form, which is generated by pose parameter $\boldsymbol{r}_i$ in (4.3). Based on Euler-Rodrigues formulation,

$$\boldsymbol{R}_{\mathrm{H-F}i} = e^{\widetilde{\boldsymbol{\omega}}_{\mathrm{H-F}i}\gamma_{\mathrm{H-F}i}} = \boldsymbol{I} + \sin\gamma_{\mathrm{H-F}i}\,\widetilde{\boldsymbol{\omega}}_{\mathrm{H-F}i} + (1-\cos\gamma_{\mathrm{H-F}i})\widetilde{\boldsymbol{\omega}}_{\mathrm{H-F}i}\widetilde{\boldsymbol{\omega}}_{\mathrm{H-F}i}. \tag{4.5}$$

In which, $\gamma_{\mathrm{H\text{-}F}i}$ is the rotation angle of the *i*-th moving platform, $\widetilde{\boldsymbol{\omega}}_{\mathrm{H-F}i}$ is the cross product operator of $\boldsymbol{\omega}_{\mathrm{H-F}i}$, which is a unitary vetor representing the rotation axis. Thus, there are only two independent parameters of $\boldsymbol{\omega}_{\mathrm{H-F}i}$. It can also be written as

$$\begin{aligned} \boldsymbol{\omega}_{\mathrm{H-F}i} &= \begin{bmatrix} \omega_{\mathrm{H-F}ix} & \omega_{\mathrm{H-F}iy} & \omega_{\mathrm{H-F}iz} \end{bmatrix}^{\mathrm{T}} \\ &= [\cos\beta_{\mathrm{H-F}i}\cos\alpha_{\mathrm{H-F}i} \quad \cos\beta_{\mathrm{H-F}i}\sin\alpha_{\mathrm{H-F}i} \quad \sin\beta_{\mathrm{H-F}i}]^{\mathrm{T}}. \end{aligned} \tag{4.6}$$

Any pose of a rigid body can be equalized to a result of a rotation along one fixed axis. For this reason, the definition of $\boldsymbol{X}_i$ could be

$$\begin{aligned} \boldsymbol{X}_{\mathrm{H-F}i} &= \begin{bmatrix} \boldsymbol{d}_{\mathrm{H-F}i}{}^{\mathrm{T}} & \gamma_{\mathrm{H-F}i}\boldsymbol{\omega}_{\mathrm{H-F}i}{}^{\mathrm{T}} \end{bmatrix}^{\mathrm{T}} \\ &= [x_{\mathrm{H-F}i} \quad y_{\mathrm{H-F}i} \quad z_{\mathrm{H-F}i} \quad \gamma_{\mathrm{H-F}i}\omega_{\mathrm{H-F}ix} \quad \gamma_{\mathrm{H-F}i}\omega_{\mathrm{H-F}iy} \quad \gamma_{\mathrm{H-F}i}\omega_{\mathrm{H-F}iz}]^{\mathrm{T}}. \end{aligned} \tag{4.7}$$

This definition indicates that, any position and pose of $\{H_i\}$ is a combination of a translational displacement $\boldsymbol{d}_{\mathrm{H-F}i}$ and a fixed-axis rotation with angle $\gamma_{\mathrm{H-F}i}$ along axis $\boldsymbol{\omega}_{\mathrm{H-F}i}$. For a fixed axis rotation, $\boldsymbol{\omega}_{\mathrm{H-F}i}$ is a constant vetor. Thus, the time derivative of $\boldsymbol{X}_{\mathrm{H-F}i}$ should be

$$\dot{\boldsymbol{X}}_{\mathrm{H-F}i} = \begin{bmatrix} \dot{\boldsymbol{d}}_{\mathrm{H-F}i}{}^{\mathrm{T}} & \dot{\gamma}_{\mathrm{H-F}i}\boldsymbol{\omega}_{\mathrm{H-F}i}{}^{\mathrm{T}} \end{bmatrix}^{\mathrm{T}} = [\boldsymbol{v}_{\mathrm{H-F}i}{}^{\mathrm{T}} \quad \boldsymbol{\varpi}_{\mathrm{H-F}i}{}^{\mathrm{T}}]^{\mathrm{T}}. \tag{4.8}$$

Where, $\boldsymbol{v}_{\mathrm{F}i}$ is the translational velocity of the origin of the moving platform and $\boldsymbol{\varpi}_{\mathrm{H-F}i}$ is the rotational velocity.

2) Inverse Jacobian of Linear Actuators

The main task of IKP of this 6-SPS manipulator is to determine the length of vectors $\boldsymbol{l}_{ij}$. From the relation in fig. 4.1 (b),

$$\boldsymbol{d}_{\mathrm{H-H}ij} + \boldsymbol{l}_{ij} = \boldsymbol{d}_{\mathrm{H-F}i} + \boldsymbol{d}_{\mathrm{F}i-\mathrm{F}ij}. \tag{4.9}$$

It derives

$$\bar{\boldsymbol{l}}_{ij} = \boldsymbol{H}_{\mathrm{H-F}_i}{}^{\{\mathrm{F}_i\}}\bar{\boldsymbol{d}}_{\mathrm{F}i-\mathrm{F}ij} - \bar{\boldsymbol{d}}_{\mathrm{H-H}ij}. \tag{4.10}$$

$\bar{\boldsymbol{l}}_{ij} = \begin{bmatrix}\boldsymbol{l}_{ij}{}^{\mathrm{T}} & 0\end{bmatrix}^{\mathrm{T}}$, is the homogeneous form of $\boldsymbol{l}_{ij}$, which is a pure vector representing the difference of two points. $\bar{\boldsymbol{d}}_{*} = \begin{bmatrix}\boldsymbol{d}_{*}{}^{\mathrm{T}} & 1\end{bmatrix}^{\mathrm{T}}$ is the homogeneous form of $\boldsymbol{d}_{*}$, which is a position vector representing the position of a point in the reference frame. The time differential of $\boldsymbol{l}_{ij}$ is

$$\bar{\boldsymbol{v}}_{\mathrm{H}ij-\mathrm{F}ij} = \dot{\bar{\boldsymbol{l}}}_{ij} = \dot{\boldsymbol{H}}_{\mathrm{H-F}_i}{}^{\{\mathrm{F}_i\}}\bar{\boldsymbol{d}}_{\mathrm{F}i-\mathrm{F}ij} = \begin{bmatrix}\dot{\boldsymbol{R}}_{\mathrm{H-F}_i} & \boldsymbol{v}_{\mathrm{H-F}_i} \\ \boldsymbol{0} & 0\end{bmatrix}{}^{\{\mathrm{F}_i\}}\bar{\boldsymbol{d}}_{\mathrm{F}i-\mathrm{F}ij}. \tag{4.11}$$

Based on equation (4.5)

$$\dot{\boldsymbol{R}}_{\mathrm{H-F}_i} = \dot{\gamma}_{\mathrm{H-F}i}\tilde{\boldsymbol{\omega}}_{\mathrm{H-F}i}e^{\tilde{\omega}_{\mathrm{H-F}i}\gamma_{\mathrm{H-F}i}} = \dot{\gamma}_{\mathrm{H-F}i}\tilde{\boldsymbol{\omega}}_{\mathrm{H-F}i}\boldsymbol{R}_{\mathrm{F}i} \tag{4.12}$$

$$\boldsymbol{v}_{\mathrm{H}ij-\mathrm{F}ij} = \dot{\gamma}_{\mathrm{H-F}i}\tilde{\boldsymbol{\omega}}_{\mathrm{H-F}i}\boldsymbol{R}_{\mathrm{F}i}{}^{\{\mathrm{F}_i\}}\boldsymbol{d}_{\mathrm{F}i-\mathrm{F}ij} + \boldsymbol{v}_{\mathrm{H-F}_i} \tag{4.13}$$

The time derivative of length of linear actuator should be the projection of $\dot{\boldsymbol{l}}_{ij}$.

$$\dot{l}_{ij} = \boldsymbol{v}_{\mathrm{H}ij-\mathrm{F}ij}{}^{\mathrm{T}}\boldsymbol{e}_{ij} \tag{4.14}$$

Where, $\boldsymbol{e}_{ij}$ is the unit vector of $\boldsymbol{l}_{ij}$. Equation (4.14) is obvious a function of $\dot{\boldsymbol{X}}_{\mathrm{H-F}i}$, the inverse Jacobian on one linear actuator should be obtained from

$$\dot{l}_{ij} = J_{ij}{}^{-1}(\boldsymbol{X}_{\mathrm{H-F}i})\dot{\boldsymbol{X}}_{\mathrm{H-F}i}. \tag{4.15}$$

Which is equivalent to (4.14). The inverse Jacobian of the mechanism should be

$$\dot{\boldsymbol{q}}_i = \boldsymbol{J}_i{}^{-1}\dot{\boldsymbol{X}}_{\mathrm{H-F}i} = \begin{bmatrix}J_{i\mathrm{A}}{}^{-1}(\boldsymbol{X}_{\mathrm{H-F}i}) \\ \vdots \\ J_{i\mathrm{F}}{}^{-1}(\boldsymbol{X}_{\mathrm{H-F}i})\end{bmatrix}\begin{bmatrix}\boldsymbol{v}_{\mathrm{H-F}i} \\ \boldsymbol{\varpi}_{\mathrm{H-F}i}\end{bmatrix}. \tag{4.16}$$

It is not difficult to find that, the inverse Jacobian, as a set of functions of $\boldsymbol{X}_{\mathrm{H-F}i}$, is highly coupled and non-linear.

3) Inverse Jacobian of Shafts of Linear Actuators

For different designs of 6-SPS mechanisms, the methods to derive the motion description of the upper part (sleeves, $\{\mathrm{L}_{ij\mathrm{N}}\}$) and lower part (shafts, $\{\mathrm{L}_{ij\mathrm{S}}\}$) are different. It highly depends on the joints used to connect the linear actuators and platforms. The difference takes place on the rotational motion of them and mainly about the circumferential motion of them. Here, the method is based on the design with Cardan joints and double Cardan joints.

Geometrics

For the reading convenience, all the vectors are expressed in the coordinates of joints bases, the reference superscripts are omitted. As illustrated in fig. 4.2(a), for example, the common axis $\boldsymbol{x}_{i\mathrm{AF}}$ of the double Cardan joint connecting limbs-A and -F can be obtained as

$$\boldsymbol{x}_{i\mathrm{AF}} = [x_{xi\mathrm{AF}} \quad y_{xi\mathrm{AF}} \quad z_{xi\mathrm{AF}}]^{\mathrm{T}} = |\tilde{\boldsymbol{e}}_{i\mathrm{F}}\boldsymbol{e}_{i\mathrm{A}}|^{-1}\tilde{\boldsymbol{e}}_{i\mathrm{F}}\boldsymbol{e}_{i\mathrm{A}}. \tag{4.17}$$

The rotation matrix of the shaft-A can be obtained as

$$\boldsymbol{R}_{\mathrm{L}i\mathrm{AS}} = [\boldsymbol{x}_{i\mathrm{A-shaft}} \quad \boldsymbol{y}_{i\mathrm{A-shaft}} \quad \boldsymbol{z}_{i\mathrm{A-shaft}}] = [\boldsymbol{x}_{i\mathrm{AF}} \quad \tilde{\boldsymbol{e}}_{i\mathrm{A}}\boldsymbol{x}_{i\mathrm{AF}} \quad -\boldsymbol{e}_{i\mathrm{A}}] \tag{4.18}$$

The orientation of $\boldsymbol{x}_{i\mathrm{AF}}$ reveals the orientation of axis-1 and -2 on the same joint. Its orientation is a combination of them,

$$\boldsymbol{x}_{i\mathrm{AF}} = \boldsymbol{R}(y, \gamma_y)\boldsymbol{R}(z, \gamma_z)[1 \quad 0 \quad 0]^{\mathrm{T}} = [\cos\gamma_y \cos\gamma_z \quad \sin\gamma_z \quad -\sin\gamma_y \cos\gamma_z]^{\mathrm{T}} \tag{4.19}$$

$\boldsymbol{R}(*_1,*_2)$ indicates a rotation around axis $*_1$ with an angle $*_2$. Through this equation and eq. (4.17), the rotation angle of axis -3, -1 and -2 can be solved.

$$\begin{cases} \gamma_x = -\sin^{-1}\dfrac{e_{i\mathrm{A}y}}{\sqrt{1-{y_{xi\mathrm{AF}}}^2}} \\ \gamma_y = -\tan^{-1}\left(\dfrac{z_{xi\mathrm{AF}}}{x_{xi\mathrm{AF}}}\right) \\ \gamma_z = \sin^{-1} y_{xi\mathrm{AF}} \end{cases} \qquad \gamma_x, \gamma_y, \gamma_z \in \left[-\frac{\pi}{2} \quad \frac{\pi}{2}\right] \tag{4.20}$$

Where, $e_{i\mathrm{A}y}$ is the 2nd entry of $\boldsymbol{e}_{i\mathrm{A}}$. The angle of axis-3 is obtained through the relation $\boldsymbol{R}(y,\gamma_y)\boldsymbol{R}(z,\gamma_z)\boldsymbol{R}(x,\gamma_x)[0 \quad 0 \quad 1]^{\mathrm{T}} = \boldsymbol{e}_{i\mathrm{A}}$. Limited by the working space of joint and whole structure, the joint variables are limited in the range of [-π/2, π/2]. The detailed workspace analysis of double Cardan joints will be performed in Chapter 5.

Velocities

The rotation velocity of a shaft can be seen as a combination of two velocities: the rotation of its *x*-axis, $\boldsymbol{\varpi}_{i\mathrm{AF}yz}$, and the rotation around its *x*-axis, $\boldsymbol{\varpi}_{i\mathrm{A-sleeve}x}$, as illustrated in fig. 4.2 (b),

$$\boldsymbol{\varpi}_{i\mathrm{A-shaft}} = \boldsymbol{\varpi}_{i\mathrm{A-shaft}x} + \boldsymbol{\varpi}_{i\mathrm{AF}yz}. \tag{4.21}$$

For the reading convenience, we use $\boldsymbol{v}_{i\mathrm{A}}$ as a substitute for $\boldsymbol{v}_{\mathrm{H}i\mathrm{A-F}i\mathrm{A}}$ in this part. The velocity component of shaft-A caused by the rotational velocity around its *x* axis is then

$$\boldsymbol{v}_{i\mathrm{A}y} = -\tilde{\boldsymbol{l}}_{i\mathrm{A}}\boldsymbol{\varpi}_{i\mathrm{A-shaft}x}. \tag{4.22}$$

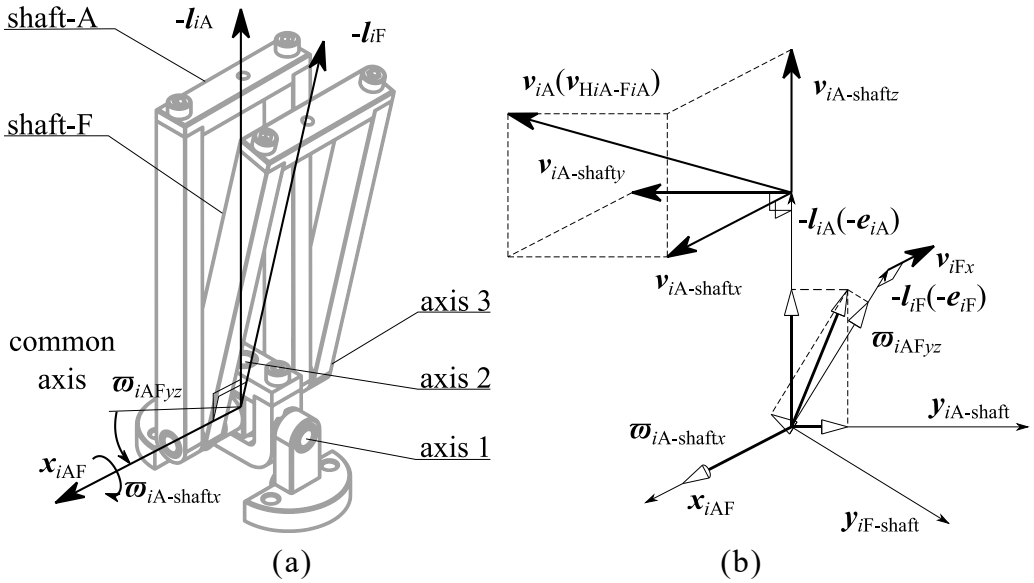

Figure 4.2 Velocity analysis of a double Cardan joint. (a) Mechanical scheme of double Cardan joint and (b) its velocities relations on the foot platform.

At the same time, it is the projection of the translational velocity, $\boldsymbol{v}_{i\mathrm{A}}$, on $\boldsymbol{y}_{i\mathrm{A-sleeve}}$.

$$\boldsymbol{v}_{i\mathrm{A}y} = (\boldsymbol{v}_{i\mathrm{A}}{}^{\mathrm{T}}\boldsymbol{y}_{i\mathrm{A-shaft}})\boldsymbol{y}_{i\mathrm{A-shaft}} \tag{4.23}$$

It derives

$$\boldsymbol{\varpi}_{i\mathrm{A-shaft}x} = -\frac{1}{|\boldsymbol{l}_{i\mathrm{A}}|}(\boldsymbol{v}_{i\mathrm{A}}{}^{\mathrm{T}}\boldsymbol{y}_{i\mathrm{A-shaft}})\boldsymbol{x}_{i\mathrm{AF}} = -\frac{1}{|\boldsymbol{l}_{i\mathrm{A}}||\tilde{\boldsymbol{e}}_{i\mathrm{F}}\boldsymbol{e}_{i\mathrm{A}}|^2}(\boldsymbol{v}_{i\mathrm{A}}{}^{\mathrm{T}}\tilde{\boldsymbol{e}}_{i\mathrm{A}}\tilde{\boldsymbol{e}}_{i\mathrm{F}}\boldsymbol{e}_{i\mathrm{A}})\tilde{\boldsymbol{e}}_{i\mathrm{F}}\boldsymbol{e}_{i\mathrm{A}}. \tag{4.24}$$

The other rotational velocity, $\boldsymbol{\varpi}_{i\mathrm{AF}yz}$, causes the translation of the end of linear actuators along the common axis. Seeing fig. 4.2 (b), there are

$$\begin{cases} \boldsymbol{v}_{i\mathrm{A}x} = -(\boldsymbol{\varpi}_{i\mathrm{AF}yz}{}^{\mathrm{T}}\boldsymbol{y}_{i\mathrm{A-shaft}})\tilde{\boldsymbol{l}}_{i\mathrm{A}}\boldsymbol{y}_{i\mathrm{A-shaft}}, \\ \boldsymbol{v}_{i\mathrm{F}x} = -(\boldsymbol{\varpi}_{i\mathrm{AF}yz}{}^{\mathrm{T}}\boldsymbol{y}_{i\mathrm{F-shaft}})\tilde{\boldsymbol{l}}_{i\mathrm{F}}\boldsymbol{y}_{i\mathrm{F-shaft}}. \end{cases} \tag{4.25}$$

Through coordinates transferring, the following equations stand.

$$\begin{cases} {}^{\{i\mathrm{A-shaft}\}}\boldsymbol{\varpi}_{i\mathrm{AF}yz}{}^{\mathrm{T}}{}^{\{i\mathrm{A-shaft}\}}\boldsymbol{y}_{i\mathrm{A-shaft}} = |\boldsymbol{l}_{i\mathrm{A}}|^{-1}\boldsymbol{v}_{i\mathrm{A}}{}^{\mathrm{T}}\boldsymbol{x}_{i\mathrm{AF}} \\ {}^{\{i\mathrm{A-shaft}\}}\boldsymbol{\varpi}_{i\mathrm{AF}yz}{}^{\mathrm{T}}{}^{\{i\mathrm{A-shaft}\}}\boldsymbol{y}_{i\mathrm{F-shaft}} = |\boldsymbol{l}_{i\mathrm{F}}|^{-1}\boldsymbol{v}_{i\mathrm{F}}{}^{\mathrm{T}}\boldsymbol{x}_{i\mathrm{AF}} \end{cases} \tag{4.26}$$

Where,

$${}^{\{i\mathrm{A-shaft}\}}\boldsymbol{y}_{i\mathrm{F-shaft}} = \boldsymbol{R}_{i\mathrm{A-shaft}}{}^{-1}\boldsymbol{y}_{i\mathrm{F-shaft}} = \boldsymbol{R}(x, -\gamma_{i\widehat{\mathrm{AF}}})[0 \quad 1 \quad 0]^{\mathrm{T}} = \begin{bmatrix} 0 \\ \boldsymbol{e}_{i\mathrm{F}}{}^{\mathrm{T}}\boldsymbol{e}_{i\mathrm{A}} \\ -|\tilde{\boldsymbol{e}}_{i\mathrm{F}}\boldsymbol{e}_{i\mathrm{A}}| \end{bmatrix}. \tag{4.27}$$

$\gamma_{i\widehat{\mathrm{AF}}}$ is the angle from $\boldsymbol{l}_{i\mathrm{A}}$ to $\boldsymbol{l}_{i\mathrm{F}}$ and there exists $\sin\gamma_{i\widehat{\mathrm{AF}}} = |\tilde{\boldsymbol{e}}_{i\mathrm{F}}\boldsymbol{e}_{i\mathrm{A}}|$. Constrained by the mechanical structure, $\boldsymbol{l}_{i\mathrm{F}}$ always locates on the right side (seeing fig. 4.2(a)) of $\boldsymbol{l}_{i\mathrm{A}}$, $\gamma_{i\widehat{\mathrm{AB}}}$ is thus always positive. Let ${}^{\{i\mathrm{A-shaft}\}}\boldsymbol{\varpi}_{i\mathrm{AF}yz} = [0 \quad w_{i\mathrm{AF}yzy} \quad w_{i\mathrm{AF}yzz}]^{\mathrm{T}}$, equation (4.26) turns to

$$\begin{cases} w_{i\mathrm{AF}yzy} = \dfrac{1}{|\boldsymbol{l}_{i\mathrm{A}}|}\boldsymbol{v}_{i\mathrm{A}}{}^{\mathrm{T}}\boldsymbol{x}_{i\mathrm{AF}}, \\ w_{i\mathrm{AF}yzz} = \dfrac{1}{|\tilde{\boldsymbol{e}}_{i\mathrm{F}}\boldsymbol{e}_{i\mathrm{A}}|}\left(\dfrac{1}{|\boldsymbol{l}_{i\mathrm{A}}|}\boldsymbol{e}_{i\mathrm{F}}{}^{\mathrm{T}}\boldsymbol{e}_{i\mathrm{A}}\boldsymbol{v}_{i\mathrm{A}}{}^{\mathrm{T}} - \dfrac{1}{|\boldsymbol{l}_{i\mathrm{F}}|}\boldsymbol{v}_{i\mathrm{F}}{}^{\mathrm{T}}\right)\boldsymbol{x}_{i\mathrm{AF}}. \end{cases} \tag{4.28}$$

Based on last section, all the variables are functions of $\dot{\boldsymbol{X}}_i$ and $\boldsymbol{X}_i$, including $\boldsymbol{e}_{i\mathrm{A}}$, $\boldsymbol{e}_{i\mathrm{F}}$, $|\boldsymbol{l}_{i\mathrm{A}}|$, $|\boldsymbol{l}_{i\mathrm{A}}|$ $\boldsymbol{v}_{i\mathrm{A}}$, and $\boldsymbol{v}_{i\mathrm{A}}$. Then, the rotational velocity of the common x-axis is

$$\boldsymbol{\varpi}_{i\mathrm{AF}yz} = \boldsymbol{R}_{i\mathrm{A-shaft}}{}^{-1}[0 \quad w_{i\mathrm{AB}yzy} \quad w_{i\mathrm{AF}yzz}]^{\mathrm{T}}. \tag{4.29}$$

The rotational velocity of sleeve-A is the combination of (4.29) and (4.24).

$$\boldsymbol{\varpi}_{\mathrm{L}i\mathrm{AS}} = \boldsymbol{\varpi}_{i\mathrm{A-shaft}x} + \boldsymbol{\varpi}_{i\mathrm{AF}yz} \tag{4.30}$$

The two components are obvious functions of $\dot{\boldsymbol{X}}_i$, since $\boldsymbol{v}_{i\mathrm{A}x}$ and $\boldsymbol{v}_{i\mathrm{B}x}$ are also functions of $\dot{\boldsymbol{X}}_i$. Note that, rotation $\boldsymbol{\varpi}_{i\mathrm{AB}yz}$ is not the rotation of output end of axis-2 in fig. 4.2(a). There is a Cardan angle along the common axis, however, it was compensated by the kinematic pairs $\mathrm{R}_{3\mathrm{A}}$ and $\mathrm{R}_{4\mathrm{B}}$. The velocity of shaft-A can be expressed as

$$\dot{\boldsymbol{q}}_{\mathrm{L}i\mathrm{AS}} = [\boldsymbol{v}_{\mathrm{F}i\mathrm{A}}{}^{\mathrm{T}} \quad \boldsymbol{\varpi}_{\mathrm{L}i\mathrm{AS}}{}^{\mathrm{T}}]^{\mathrm{T}} = \boldsymbol{J}_{\mathrm{L}i\mathrm{AS}}{}^{-1}(\dot{\boldsymbol{X}}_i). \tag{4.31}$$

$\boldsymbol{v}_{\mathrm{F}i\mathrm{A}}$ is the velocity of joint centre of double Cardan joint-*i*A and $\boldsymbol{J}_{\mathrm{L}i\mathrm{AS}}{}^{-1}$ is the inverse Jacobian of shaft of linear actuator-*i*A. The corresponding $\boldsymbol{J}_{\mathrm{L}i\mathrm{FS}}{}^{-1}$ can be obtained similarly. The complete form of inverse Jacobians can be found in Chapter 6.

4) Inverse Jacobian of Sleeves

The motion of sleeve on linear actuators is simpler, since they are mounted on the Cardan joints, as illustrated in fig. 4.3.

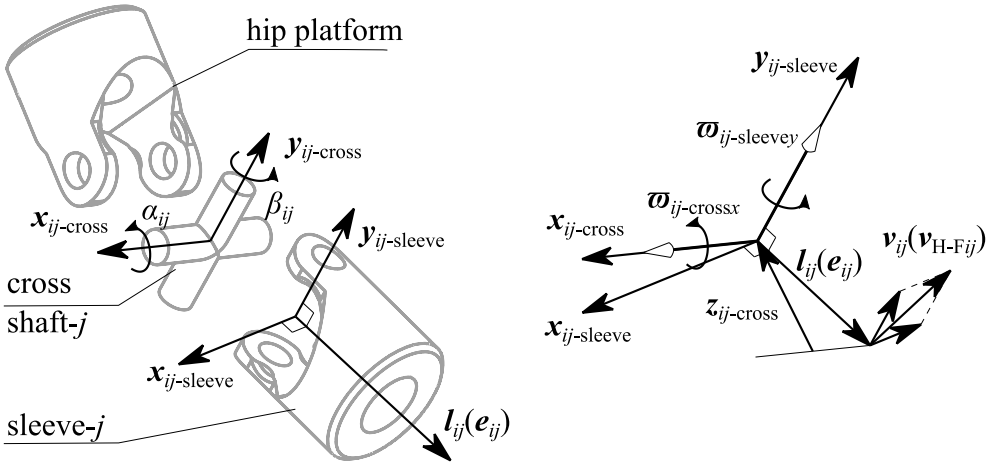

(a) (b)

Figure 4.3 Velocity analysis of a Cardan joint. (a) The mechanical scheme of a Cardan joint and (b) its velocities relations on the hip platform.

The coordinates of the sleeve of linear actuator -*ij* is

$$\boldsymbol{R}_{\mathrm{L}ij\mathrm{N}} = \quad \boldsymbol{R}(x,\alpha_{ij})\boldsymbol{R}(y,\beta_{ij}) = \begin{bmatrix} \cos\beta_{ij} & 0 & \sin\beta_{ij} \\ \sin\alpha_{ij}\sin\beta_{ij} & \cos\alpha_{ij} & -\sin\alpha_{ij}\cos\beta_{ij} \\ -\cos\alpha_{ij}\sin\beta_{ij} & \sin\alpha_{ij} & \cos\alpha_{ij}\cos\beta_{ij} \end{bmatrix}. \tag{4.32}$$

The unitary vector of linear actuator $\boldsymbol{l}_{ij}$ can thus be written as

$$\boldsymbol{e}_{ij} = \boldsymbol{R}(x,\alpha_{ij})\boldsymbol{R}(y,\beta_{ij})[0 \quad 0 \quad -1]^{\mathrm{T}} = [-\sin\beta_{ij} \quad \sin\alpha_{ij}\cos\beta_{ij} \quad -\cos\alpha_{ij}\cos\beta_{ij}]^{\mathrm{T}}. \tag{4.33}$$

Bring in $\boldsymbol{e}_{ij} = [e_{ijx} \quad e_{ijy} \quad e_{ijz}]^{\mathrm{T}}$,

$$\begin{bmatrix} -\sin\beta_{ij} \\ \sin\alpha_{ij}\cos\beta_{ij} \\ -\cos\alpha_{ij}\cos\beta_{ij} \end{bmatrix} = \begin{bmatrix} e_{ijx} \\ e_{ijy} \\ e_{ijz} \end{bmatrix}. \tag{4.34}$$

The two rotation angles of a Cardan joint can be expressed as following.

$$\begin{cases} \sin\beta_{ij} = -e_{ijx} & \cos\beta_{ij} = \sqrt{1-{e_{ijx}}^2} \\ \sin\alpha_{ij} = \dfrac{e_{ijy}}{\cos\beta_{ij}} & \cos\alpha_{ij} = -\dfrac{e_{ijz}}{\cos\beta_{ij}} \end{cases} \tag{4.35}$$

The orientation of the lead screw sleeve is solved as

$$\boldsymbol{R}_{\mathrm{L}ij\mathrm{N}} = \boldsymbol{R}(x,\alpha_{ij})\boldsymbol{R}(y,\beta_{ij}) = [\boldsymbol{x}_{ij-\mathrm{sleeve}} \quad \boldsymbol{y}_{ij-\mathrm{sleeve}} \quad \boldsymbol{z}_{ij-\mathrm{sleeve}}]$$

$$= \begin{bmatrix} \sqrt{1-{e_{ijx}}^2} & 0 & -e_{ijx} \\ -\dfrac{e_{ijy}e_{ijx}}{\sqrt{1-{e_{ijx}}^2}} & -\dfrac{e_{ijz}}{\sqrt{1-{e_{ijx}}^2}} & -e_{ijy} \\ -\dfrac{e_{ijz}e_{ijx}}{\sqrt{1-{e_{ijx}}^2}} & \dfrac{e_{ijy}}{\sqrt{1-{e_{ijx}}^2}} & -e_{ijz} \end{bmatrix}. \tag{4.36}$$

The angular velocity of {L*ij*N} is composed by two components around two axes of cross shaft, as illustrated in fig.4.3 (b), they can be written as

$$\begin{cases} \boldsymbol{\varpi}_{ij-\text{cross}x} & = \varpi_{ij-\text{cross}x}\boldsymbol{x}_{ij-\text{cross}}, \\ \boldsymbol{\varpi}_{ij-\text{sleeve}y} & = \varpi_{ij-\text{sleeve}y}\boldsymbol{y}_{ij-\text{sleeve}}. \end{cases} \tag{4.37}$$

The amplitude $\varpi_{ij-\text{cross}x}$ and $\varpi_{ij-\text{sleeve}y}$ can be derived if the velocity on the other end of linear actuators are known. Letting it be $\boldsymbol{v}_{ij}$, there are relations

$$\begin{cases} \widetilde{\boldsymbol{\varpi}}_{ij-\text{cross}x}\boldsymbol{l}_{ij} & = \left(\boldsymbol{v}_{ij}{}^{\mathrm{T}}\boldsymbol{y}_{ij-\text{sleeve}}\right)\boldsymbol{y}_{ij-\text{sleeve}}/\cos\beta_{ij}, \\ \widetilde{\boldsymbol{\varpi}}_{ij-\text{sleeve}y}\boldsymbol{l}_{ij} & = \left(\boldsymbol{v}_{ij}{}^{\mathrm{T}}\boldsymbol{x}_{ij-\text{sleeve}}\right)\boldsymbol{x}_{ij-\text{sleeve}}. \end{cases} \tag{4.38}$$

Considering $\boldsymbol{l}_{ij} = l_{ij}[e_{ijx} \quad e_{ijy} \quad e_{ijz}]^{\mathrm{T}}$ and eq. (4.36), the amplitudes are derived,

$$\begin{cases} \varpi_{ij-\text{cross}x} & = \dfrac{\left(\boldsymbol{v}_{ij}{}^{\mathrm{T}}\boldsymbol{y}_{ij-\text{sleeve}}\right)}{\left(1-e_{ijx}{}^{2}\right)l_{ij}}, \\ \varpi_{ij-\text{sleeve}y} & = -\dfrac{\left(\boldsymbol{v}_{ij}{}^{\mathrm{T}}\boldsymbol{x}_{ij-\text{sleeve}}\right)}{l_{ij}}. \end{cases} \tag{4.39}$$

Thus, the rotational velocity of sleeve is

$$\boldsymbol{\varpi}_{\mathrm{L}ij\mathrm{N}} = \boldsymbol{\varpi}_{ij-\text{cross}x} + \boldsymbol{\varpi}_{ij-\text{sleeve}y} = \frac{\left(\boldsymbol{v}_{ij}{}^{\mathrm{T}}\boldsymbol{y}_{ij-\text{sleeve}}\right)}{\left(1-e_{ijx}{}^{2}\right)l_{ij}}\boldsymbol{x}_{ij-\text{cross}} - \frac{\left(\boldsymbol{v}_{ij}{}^{\mathrm{T}}\boldsymbol{x}_{ij-\text{sleeve}}\right)}{l_{ij}}\boldsymbol{y}_{ij-\text{sleeve}}. \tag{4.40}$$

The velocity of linear actuator sleeve w.r.t. the hip platform can be written as

$$\dot{\boldsymbol{q}}_{\mathrm{L}ij\mathrm{N}} = \left[\boldsymbol{0}^{\mathrm{T}} \quad \widetilde{\boldsymbol{\varpi}}_{ij-\text{sleeve}}{}^{\mathrm{T}}\right]^{\mathrm{T}} = \boldsymbol{J}_{\mathrm{L}ij\mathrm{N}}{}^{-1}\left(\dot{\boldsymbol{X}}_{i}\right). \tag{4.41}$$

$\boldsymbol{J}_{\mathrm{L}ij\mathrm{N}}{}^{-1}$ is the inverse Jacobian and its complete form can be found in Chapter 6.

5) Summary of Linear Actuators

Till here, the inverse kinematics of all main parts of a modified 6-SPS mechanism with spherical-equivalent double Cardan joints were discussed. The rotation of double Cardan joints depends not only on the relative motion of both ends of a linear actuator, but also on the relation with the neighbour linear actuator. For the designs with other rotational joints, the rotational velocities are obtained differently. This will be discussed in Chapter 5.

Based on [4.39], the rotation around the linear actuator are not vital in kinetic analysis, since the its moment of inertia along limb axis is tiny compare to that along the radial directions (see table 6.3 and 6.4). However, the relative rotation between the sleeve and shaft will cause the length variation of lead screws. This is a common problem for most of designs with mechanical linear actuators. The length variation compensation problem will be discussed in Section 4.4.

4.2.3 Inverse Kinematics with Quaternions Form

As discussed in Chapter 3, there are some advantages of the using quaternions to describe the motions of rigid bodies. The inverse kinematics of a 6-SPS mechanism will be discussed. All the variables in quaternions form will be written as $\boldsymbol{Q}$. Where, its dual quaternion form is $\widehat{\boldsymbol{Q}}$.

1) Minimal Coordinates of Moving Platforms

Based on equation (4.4), the *SE*(3) operator generated by motion of $\{\mathrm{F}_i\}$ can be written as

$$\begin{cases} \widehat{\boldsymbol{Q}}_{\mathrm{H-F}_i} = \boldsymbol{Q}_{\boldsymbol{R}\mathrm{H-F}_i} + \epsilon\dfrac{1}{2}\boldsymbol{Q}_{\boldsymbol{d}\mathrm{H-F}_i}\boldsymbol{Q}_{\boldsymbol{R}\mathrm{H-F}_i}, \\ \widehat{\boldsymbol{Q}}_{\mathrm{H-F}_i}{}^{\sim} = \boldsymbol{Q}_{\boldsymbol{R}\mathrm{H-F}_i}{}^{*} - \epsilon\dfrac{1}{2}\boldsymbol{Q}_{\boldsymbol{R}\mathrm{H-F}_i}{}^{*}\boldsymbol{Q}_{\boldsymbol{d}\mathrm{H-F}_i}{}^{*}. \end{cases} \tag{4.42}$$

In which, ϵ is the dual operator and there exists $\epsilon^2 = 0$, $\widehat{\boldsymbol{Q}}_{\mathrm{H-F}_i}{}^{\sim}$ is its third conjugate form (seeing Chapter 3). The quaternions representing the rotation of $\{\mathrm{F}_i\}$ is

$$\begin{aligned} \boldsymbol{Q}_{\boldsymbol{R}\mathrm{H-F}_i} &= \cos\frac{\gamma_{\mathrm{H-F}i}}{2} + \sin\frac{\gamma_{\mathrm{H-F}i}}{2}\boldsymbol{\omega}_{\mathrm{H-F}i}{}^{\mathrm{T}}\boldsymbol{C}_{\mathrm{H}} \\ &= \cos\frac{\gamma_{\mathrm{H-F}i}}{2} + \sin\frac{\gamma_{\mathrm{H-F}i}}{2}\left(\boldsymbol{i}\omega_{\mathrm{H-F}ix} + \boldsymbol{j}\omega_{\mathrm{H-F}iy} + \boldsymbol{k}\omega_{\mathrm{H-F}iz}\right). \end{aligned} \tag{4.43}$$

$\boldsymbol{C}_{\mathrm{H}} = [\boldsymbol{i} \quad \boldsymbol{j} \quad \boldsymbol{k}]^{\mathrm{T}}$ is a set of orthogonal basis in a three dimensional space. The product of basis obeys cross production and their self-product equals to -1. The quaternions representing the translational displacement of $\{\mathrm{F}_i\}$ is

$$\boldsymbol{Q}_{\boldsymbol{d}\mathrm{H-F}_i} = \boldsymbol{d}_{\mathrm{H-F}_i}{}^{\mathrm{T}}\boldsymbol{C}_{\mathrm{H}} = \boldsymbol{i}x_{\mathrm{H-F}_i} + \boldsymbol{j}y_{\mathrm{H-F}_i} + \boldsymbol{k}z_{\mathrm{H-F}_i}. \tag{4.44}$$

Thus, the generalized coordinates of $\{F_i\}$ can still be defined as equation (4.7).

$$\boldsymbol{X}_i = [\boldsymbol{d}_{\mathrm{F}i} \quad \gamma_i \boldsymbol{\omega}_i{}^{\mathrm{T}}]^{\mathrm{T}} = [x_i \quad y_i \quad z_i \quad \gamma_i \omega_{ix} \quad \gamma_i \omega_{iy} \quad \gamma_i \omega_{iz}]^{\mathrm{T}} \tag{4.45}$$

The configuration of $\{F_i\}$ can be described by two 3-dimensinoal vectors. They are the entries of the *SE*(3) operator in dual quaternions form $\widehat{\boldsymbol{Q}}_{\mathrm{F}_i}$.

2) Inverse Jacobian of Linear Actuators

In context of quaternions, there exists

$$\widehat{\boldsymbol{Q}}_{\mathrm{F}_i}{}^{\{\mathrm{F}_i\}} \widehat{\boldsymbol{Q}}_{\boldsymbol{p}_{ij}} \widehat{\boldsymbol{Q}}_{\mathrm{F}_i}{}^{\sim} = \widehat{\boldsymbol{Q}}_{\boldsymbol{d}\mathrm{H}ij} \widehat{\boldsymbol{Q}}_{\boldsymbol{l}_{ij}} \widehat{\boldsymbol{Q}}_{\boldsymbol{d}\mathrm{H}ij}{}^{\sim}. \tag{4.46}$$

Where, $\widehat{\boldsymbol{Q}}_{\boldsymbol{d}\mathrm{H}ij} = 1 + \epsilon\, \boldsymbol{Q}_{\boldsymbol{d}\mathrm{H}ij}/2$, is the location quaternions of joint on hip platform. The quaternions form of $\boldsymbol{l}_{ij}$ is derived as

$$\boldsymbol{Q}_{\boldsymbol{l}_{ij}} = \boldsymbol{Q}_{\boldsymbol{R}\mathrm{F}_i}{}^{\{\mathrm{F}_i\}} \boldsymbol{Q}_{\boldsymbol{p}_{ij}} \boldsymbol{Q}_{\boldsymbol{R}\mathrm{F}_i}{}^{*} + \boldsymbol{Q}_{\boldsymbol{d}\mathrm{F}_i} - \boldsymbol{Q}_{\boldsymbol{d}\mathrm{H}ij}. \tag{4.47}$$

Thus, the linear actuator length is

$$q_{ij} = \left\| \boldsymbol{Q}_{\boldsymbol{l}_{ij}} \right\|. \tag{4.48}$$

The time differential of $\boldsymbol{Q}_{\boldsymbol{l}_{ij}}$ is

$$\boldsymbol{Q}_{\boldsymbol{v}_{ij}} = \frac{d}{dt} \boldsymbol{Q}_{\boldsymbol{l}_{ij}} = \frac{1}{2} \left(\boldsymbol{Q}_{\boldsymbol{\varpi}_i \mathrm{H}-\mathrm{F}_i} \boldsymbol{Q}_{\boldsymbol{p}_{ij}} + \boldsymbol{Q}_{\boldsymbol{p}_{ij}} \boldsymbol{Q}_{\boldsymbol{\varpi}_i \mathrm{H}-\mathrm{F}_i}{}^{*} \right) + \boldsymbol{Q}_{\boldsymbol{v}\mathrm{F}_i} = \mathrm{Im} \left(\boldsymbol{Q}_{\boldsymbol{\varpi}_i \mathrm{H}-\mathrm{F}_i} \boldsymbol{Q}_{\boldsymbol{p}_{ij}} \right) + \boldsymbol{Q}_{\boldsymbol{v}\mathrm{H}-\mathrm{F}_i} \tag{4.49}$$

Its projection on linear actuator is

$$\dot{q}_{ij} = \boldsymbol{v}_{ij}{}^{\mathrm{T}} \boldsymbol{e}_{ij} = -\,\mathrm{Re} \left(\boldsymbol{Q}_{\boldsymbol{v}_{ij}} \boldsymbol{Q}_{\boldsymbol{e}_{ij}} \right). \tag{4.50}$$

$\boldsymbol{Q}_{\boldsymbol{e}_{ij}}$ is the quaternion form of $\boldsymbol{e}_{ij}$, its definition is as in eq. (4.14).

3) Inverse Jacobian of Sleeves and Shafts

Here, the mechanism with Cardan joints and double Cardan joints are taken as example.

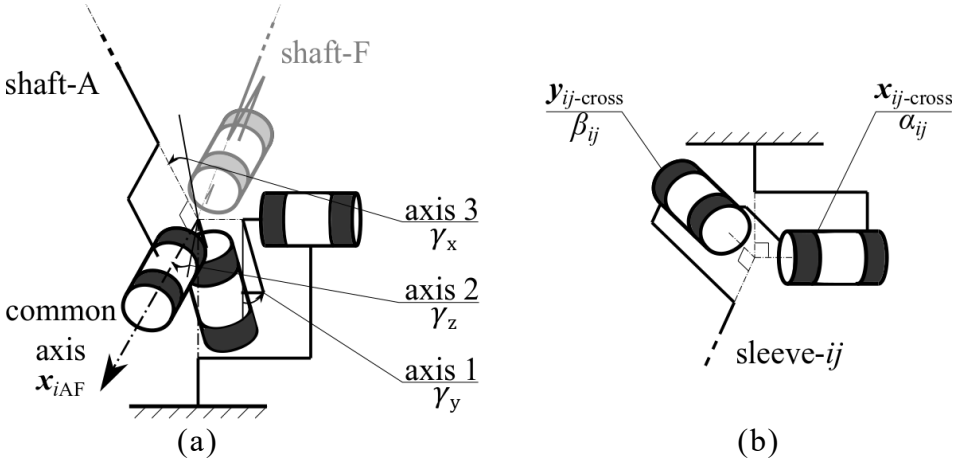

Figure 4.4 Geometric definitions of (a) double Cardan joints on foot platform and (b) Cardan joints on hip platform.

Shafts

There are varies methods to obtain quaternions from a rotation matrix like equation (4.18), such as Shepperds' method in Chapter 3. Here a method with Euler angles was used. The common axis between limb-A and limb-F can be obtained as

$$\boldsymbol{Q}_{\boldsymbol{x}_{i\mathrm{AF}}} = \boldsymbol{i}x_{\boldsymbol{x}i\mathrm{AF}} + \boldsymbol{j}y_{\boldsymbol{x}i\mathrm{AF}} + \boldsymbol{k}z_{\boldsymbol{x}i\mathrm{AF}} = \mathrm{Im}\left(\boldsymbol{Q}_{\boldsymbol{e}_{i\mathrm{F}}}\boldsymbol{Q}_{\boldsymbol{e}_{i\mathrm{A}}}\right) \tag{4.51}$$

Based on eq. (4.19), the pose of axis-3 is determined by two rotations and their angular displacement (seeing fig. 4.4(a)) can be obtained through eq. (4.20).

$$\begin{aligned}\boldsymbol{z}_{i\mathrm{AF}} &= \boldsymbol{R}\left(y,\gamma_y\right)\boldsymbol{R}(z,\gamma_z)[0 \quad 0 \quad 1]^{\mathrm{T}} = [\sin\gamma_y \quad 0 \quad \cos\gamma_y]^{\mathrm{T}} \\ &= \left[-\frac{z_{\boldsymbol{x}i\mathrm{AF}}}{\sqrt{1-{y_{\boldsymbol{x}i\mathrm{AF}}}^2}} \quad 0 \quad \frac{x_{\boldsymbol{x}i\mathrm{AF}}}{\sqrt{1-{y_{\boldsymbol{x}i\mathrm{AF}}}^2}}\right]^{\mathrm{T}}\end{aligned} \tag{4.52}$$

The rotation of linear actuators around their common axis can be obtained as

$$\begin{cases}\cos\gamma_x = {\boldsymbol{z}_{i\mathrm{AF}}}^{\mathrm{T}}\boldsymbol{e}_{i\mathrm{A}} \\ \sin\gamma_x = {\boldsymbol{x}_{i\mathrm{AF}}}^{\mathrm{T}}\tilde{\boldsymbol{z}}_{i\mathrm{AF}}\boldsymbol{e}_{i\mathrm{A}}\end{cases} \Rightarrow \begin{cases}\cos\dfrac{\gamma_x}{2} = \sqrt{\dfrac{1+{\boldsymbol{z}_{i\mathrm{AF}}}^{\mathrm{T}}\boldsymbol{e}_{i\mathrm{A}}}{2}} \\ \sin\dfrac{\gamma_x}{2} = \mathrm{sign}\left(\sin\gamma_{\boldsymbol{z}_{i\mathrm{A}}}\right)\sqrt{\dfrac{1-{\boldsymbol{z}_{i\mathrm{AF}}}^{\mathrm{T}}\boldsymbol{e}_{i\mathrm{A}}}{2}}\end{cases} \quad \gamma_x \in [-\pi \quad \pi]. \tag{4.53}$$

$\cos(\gamma_{z_{iA}}/2)$ is determined as positive, since the working space of the joint was limited. Similarly, the angular displacements of axis-1 and -2 can be obtained as

$$\begin{cases}\cos\gamma_y = \dfrac{x_{xi\mathrm{AF}}}{\sqrt{1-y_{xi\mathrm{AF}}{}^2}} \\ \sin\gamma_y = -\dfrac{z_{xi\mathrm{AF}}}{\sqrt{1-y_{xi\mathrm{AF}}{}^2}}\end{cases} \Rightarrow \begin{cases}\cos\dfrac{\gamma_y}{2} = \sqrt{\dfrac{\sqrt{1-y_{xi\mathrm{AF}}{}^2}+x_{xi\mathrm{AF}}}{2\sqrt{1-y_{xi\mathrm{AF}}{}^2}}} \\ \sin\dfrac{\gamma_y}{2} = \mathrm{sign}(\sin\gamma_y)\sqrt{\dfrac{\sqrt{1-y_{xi\mathrm{AF}}{}^2}-x_{xi\mathrm{AF}}}{2\sqrt{1-y_{xi\mathrm{AF}}{}^2}}}\end{cases} \quad \gamma_y \in \left[-\frac{\pi}{2} \quad \frac{\pi}{2}\right], \tag{4.54-1}$$

$$\begin{cases}\cos\gamma_z = \sqrt{1-y_{xi\mathrm{AF}}{}^2} \\ \sin\gamma_z = y_{xi\mathrm{AF}}\end{cases} \Rightarrow \begin{cases}\cos\dfrac{\gamma_z}{2} = \sqrt{\dfrac{1+\sqrt{1-y_{xi\mathrm{AF}}{}^2}}{2}} \\ \sin\dfrac{\gamma_z}{2} = \mathrm{sign}(\sin\gamma_z)\sqrt{\dfrac{1-\sqrt{1-y_{xi\mathrm{AF}}{}^2}}{2}}\end{cases} \quad \gamma_z \in \left[-\frac{\pi}{2} \quad \frac{\pi}{2}\right]. \tag{4.54-2}$$

Till here, the rotation of the shaft-A can be expressed in quaternions form as

$$\boldsymbol{Q}_{\boldsymbol{R}\mathrm{L1AS}} = \boldsymbol{Q}_{(y,\gamma_y)}\boldsymbol{Q}_{(z,\gamma_z)}\boldsymbol{Q}_{(x,\gamma_x)} = \left(\cos\frac{\gamma_y}{2} + \boldsymbol{j}\sin\frac{\gamma_y}{2}\right)\left(\cos\frac{\gamma_z}{2} + \boldsymbol{k}\sin\frac{\gamma_z}{2}\right)\left(\cos\frac{\gamma_x}{2} + \boldsymbol{i}\sin\frac{\gamma_x}{2}\right). \tag{4.55}$$

The velocity vectors can be seen in last section. The final rotational velocity results in eq. (4.28) are succinct and refers only vector multiplications, thus, the rotational velocity in quaternions form are given as

$$\boldsymbol{Q}_{\boldsymbol{\varpi}_{\mathrm{L1AS}}} = \boldsymbol{Q}_{\boldsymbol{\varpi}_{i\mathrm{A-shaft}x}} + \boldsymbol{Q}_{\boldsymbol{\varpi}_{i\mathrm{AB}yz}}. \tag{4.56}$$

Where, $\begin{cases}\boldsymbol{Q}_{\boldsymbol{\varpi}_{i\mathrm{A-shaft}x}} = \boldsymbol{\varpi}_{i\mathrm{A-shaft}x}{}^{\mathrm{T}}\boldsymbol{C}_{\mathrm{H}} \\ \boldsymbol{Q}_{\boldsymbol{\varpi}_{i\mathrm{AF}yz}} = \boldsymbol{Q}_{\boldsymbol{R}\mathrm{L1AS}}{}^{*}([0 \quad w_{i\mathrm{AF}yzy} \quad w_{i\mathrm{AF}yzz}]\boldsymbol{C}_{\mathrm{H}})\boldsymbol{Q}_{\boldsymbol{R}\mathrm{L1AS}}\end{cases}$.

Sleeves

The sleeve-*ij* is connected to the Cardan joints, thus, its rotation in quaternions form is

$$\boldsymbol{Q}_{\boldsymbol{R}i\mathrm{A-shaft}} = \boldsymbol{Q}_{(x,\alpha_{ij})}\boldsymbol{Q}_{(y,\beta_{ij})} = \left(\cos\frac{\alpha_{ij}}{2} + \boldsymbol{i}\sin\frac{\alpha_{ij}}{2}\right)\left(\cos\frac{\beta_{ij}}{2} + \boldsymbol{j}\sin\frac{\beta_{ij}}{2}\right). \tag{4.57}$$

Similarly, the rotation angles of two axes must be obtained by performing half angle equations or inverse trigonometric on eq. (4.35). Here the half angle equations are used.

$$\begin{cases} \cos\dfrac{\alpha_{ij}}{2} = \dfrac{\sqrt{1 - e_{ijz}/\sqrt{1 - e_{ijx}{}^2}}}{2} & \sin\dfrac{\alpha_{ij}}{2} = \operatorname{sign}(\sin\alpha_{ij})\dfrac{\sqrt{1 + e_{ijz}/\sqrt{1 - e_{ijx}{}^2}}}{2} \\ \cos\dfrac{\beta_{ij}}{2} = \dfrac{\sqrt{1 + \sqrt{1 - e_{ijx}{}^2}}}{2} & \sin\dfrac{\beta_{ij}}{2} = \operatorname{sign}(\sin\beta_{ij})\dfrac{\sqrt{1 - \sqrt{1 - e_{ijx}{}^2}}}{2} \end{cases} \tag{4.58}$$

The orientation of sleeves in quaternions form is thus derived. The rotational velocity should still be obtained by vector operations as eq. (4.40), in quaternions form, it should be

$$\boldsymbol{Q}_{\boldsymbol{\varpi}\mathrm{L}ij\mathrm{N}} = \frac{\left(\boldsymbol{v}_{ij}{}^{\mathrm{T}}\boldsymbol{y}_{ij-\mathrm{sleeve}}\right)}{\left(1 - e_{ijx}{}^2\right)l_{ij}}\boldsymbol{Q}_{\boldsymbol{x}ij-\mathrm{cross}} - \frac{\left(\boldsymbol{v}_{ij}{}^{\mathrm{T}}\boldsymbol{x}_{ij-\mathrm{sleeve}}\right)}{l_{ij}}\boldsymbol{Q}_{\boldsymbol{y}ij-\mathrm{sleeve}}. \tag{4.59}$$

Where, $\begin{cases} \boldsymbol{Q}_{\boldsymbol{x}ij-\mathrm{cross}} = \boldsymbol{x}_{ij-\mathrm{cross}}{}^{\mathrm{T}}\boldsymbol{C}_{\mathrm{H}} \\ \boldsymbol{Q}_{\boldsymbol{y}ij-\mathrm{sleeve}} = \boldsymbol{y}_{ij-\mathrm{sleeve}}{}^{\mathrm{T}}\boldsymbol{C}_{\mathrm{H}} \end{cases}$.

4) Summary of Quaterinons Form

The quaternions representation of *SO*(3) members shows advantages in coordinates transferring and trajectory planning of rigid bodies. However, during solving the passive joint variables of a serial mechanism, it is not showing the expecting computational efficiency. For example, in eq. (4.54) and (4.58), either square roots or inverse trigonometric must be operated to obtain the half value of the angular displacements. These introduced transcendental functions will hinder the computation speed and introduce computation errors. Thus, computation method in part *3*) and *4*) of section 4.4.2 should be more reasonable for these particular elements computation.

4.3 Inverse Kinematics of the Biped CENTAUROB

CENTAUROB equips two 6-DOF PKMs as two legs to form a biped walking mechanism. The modified 6-SPS with double Cardan joints is utilized in this case. The coordinates are designed as shown in fig. 4.5. Frame {H} is assigned at the geometric centre of hip platform. The two sets of hip joints are assigned symmetrically on both sides of centre of {H}. Thus, there are three

platforms, {H}, {F_1} and {F_2}, should be described and controlled. During the walking and the switch of standing foot platforms, the computation of actuators efforts varies. However, in the view of kinematics, the displacements of actuating joints depend only on the relative pose and location of three platforms. As formerly notified, the left-superscript indicates the reference frame of this vector or matrix and will be omitted inside one modified 6-SPS.

4.3.1 Minimal Coordinates of CENTAUROB

During the walking of the biped robot, the trajectories and positions of platforms, {H} {F_1} and {F_2}, should be designed and controlled in real-time, in order to keep the stability and fulfil the transportation tasks. Here, the pose and position of the platforms are given though double 3-tuples, similar to eq. (4.7). The coordinates are given referred to world coordinates {E}. The motion coordinates of hip platform is

$$\begin{aligned} {}^{\{E\}}\boldsymbol{X}_{E-H} &= \left[{}^{\{E\}}\boldsymbol{d}_{E-H}{}^{T} \quad \gamma_{E-H}{}^{\{E\}}\boldsymbol{\omega}_{E-H}{}^{T}\right]^{T} \\ &= \left[{}^{\{E\}}x_{E-H} \quad {}^{\{E\}}y_{E-H} \quad {}^{\{E\}}z_{E-H} \quad \gamma_{E-H}{}^{\{E\}}\omega_{E-Hx} \quad \gamma_{E-H}{}^{\{E\}}\omega_{E-Hy} \quad \gamma_{E-H}{}^{\{E\}}\omega_{E-Hz}\right]^{T}. \end{aligned} \tag{4.60}$$

The motion of foot platforms is

$$\begin{aligned} {}^{\{E\}}\boldsymbol{X}_{H-Fi} &= \left[{}^{\{E\}}\boldsymbol{d}_{H-Fi}{}^{T} \quad \gamma_{H-Fi}{}^{\{E\}}\boldsymbol{\omega}_{H-Fi}{}^{T}\right]^{T} \\ &= \left[{}^{\{E\}}x_{H-Fi} \quad {}^{\{E\}}y_{H-Fi} \quad {}^{\{E\}}z_{H-Fi} \quad \gamma_{H-Fi}{}^{\{E\}}\omega_{H-Fix} \quad \gamma_{H-Fi}{}^{\{E\}}\omega_{H-Fiy} \quad \gamma_{H-Fi}{}^{\{E\}}\omega_{H-Fiz}\right]^{T}. \end{aligned} \tag{4.61}$$

Their time-derivatives are

$$\begin{cases} {}^{\{E\}}\dot{\boldsymbol{X}}_{E-H} = \left[{}^{\{E\}}\boldsymbol{v}_{E-H}{}^{T} \quad \dot{\gamma}_{E-H}{}^{\{E\}}\boldsymbol{\omega}_{E-H}{}^{T}\right]^{T}, \\ {}^{\{E\}}\dot{\boldsymbol{X}}_{H-Fi} = \left[{}^{\{E\}}\boldsymbol{v}_{H-Fi}{}^{T} \quad \dot{\gamma}_{H-Fi}{}^{\{E\}}\boldsymbol{\omega}_{H-Fi}{}^{T}\right]^{T}. \end{cases} \tag{4.62}$$

The joint variables are the same as defined in eq. (4.1). The whole mechanism realizes biped walking through driving and controlling the 12 linear actuators. The motion of hip platform can be described by an *SE*(3) operator as

$${}^{\{E\}}\boldsymbol{H}_{E-H} = \begin{bmatrix} {}^{\{E\}}\boldsymbol{R}_{E-H} & {}^{\{E\}}\boldsymbol{d}_{E-H} \\ \boldsymbol{0} & 1 \end{bmatrix}. \tag{4.63}$$

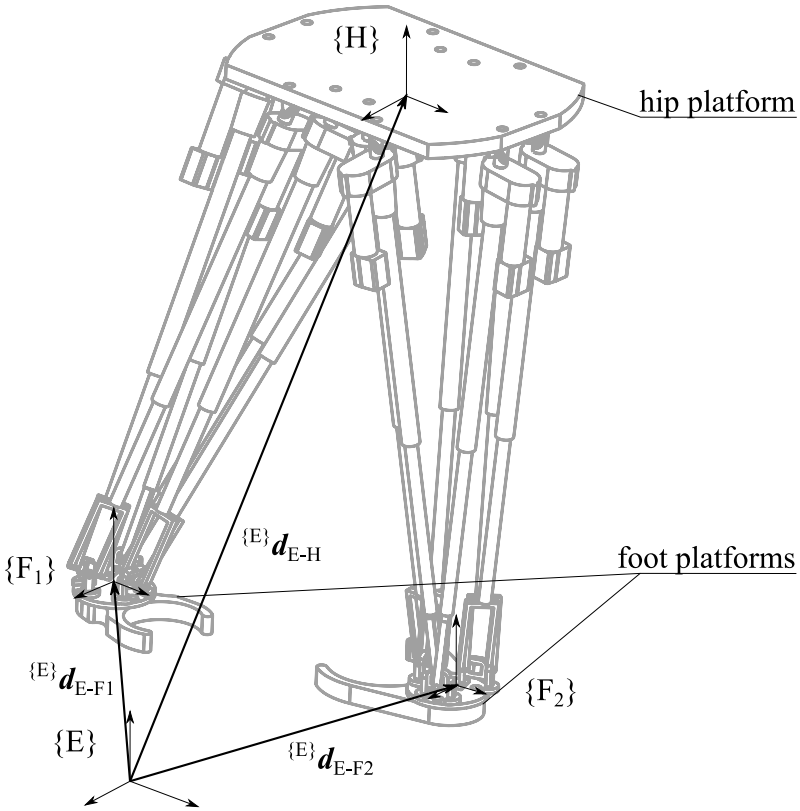

Figure 4.5 The coordinates arrangement of three platforms of CENTAUROB.

${}^{\{E\}}\boldsymbol{R}_{E-H}$ is the rotation matrix of the hip platform, {H}, w.r.t. the world frame. Based on Euler-Rodrigues formulation,

$$ {}^{\{E\}}\boldsymbol{R}_{E-H} = e^{\gamma_{E-H}\,{}^{\{E\}}\tilde{\boldsymbol{\omega}}_{E-H}} = \boldsymbol{I} + \sin\gamma_{E-H}\,{}^{\{E\}}\tilde{\boldsymbol{\omega}}_{E-H} + (1-\cos\gamma_{E-H})\,{}^{\{E\}}\tilde{\boldsymbol{\omega}}_{E-H}\,{}^{\{E\}}\tilde{\boldsymbol{\omega}}_{E-H}. \tag{4.64} $$

The *se*(3) operator of it should be

$$ {}^{\{E\}}\dot{\boldsymbol{H}}_{E-H} = \begin{bmatrix} \dot{\gamma}_{E-H}\,{}^{\{E\}}\tilde{\boldsymbol{\omega}}_{E-H}\,{}^{\{E\}}\boldsymbol{R}_{E-H} & {}^{\{E\}}\dot{\boldsymbol{d}}_{E-H} \\ \boldsymbol{0} & 0 \end{bmatrix}. \tag{4.65} $$

The motions of foot platforms are

$$ {}^{\{E\}}\boldsymbol{H}_{E-F_i} = \begin{bmatrix} {}^{\{E\}}\boldsymbol{R}_{E-Fi} & {}^{\{E\}}\boldsymbol{d}_{E-Fi} \\ \boldsymbol{0} & 1 \end{bmatrix}. \tag{4.66} $$

Correspondingly, ${}^{\{E\}}\boldsymbol{R}_{E-Fi}$ is the rotation matrix of $\{F_i\}$ w.r.t the world frame {E}.

$$ {}^{\{E\}}\boldsymbol{R}_{E-Fi} = e^{\gamma_{E-Fi}\,{}^{\{E\}}\tilde{\boldsymbol{\omega}}_{E-Fi}} = \boldsymbol{I} + \sin\gamma_{E-Fi}\,{}^{\{E\}}\tilde{\boldsymbol{\omega}}_{E-Fi} + (1-\cos\gamma_{E-Fi})\,{}^{\{E\}}\tilde{\boldsymbol{\omega}}_{E-Fi}\,{}^{\{E\}}\tilde{\boldsymbol{\omega}}_{E-Fi} \tag{4.67} $$

The relative motions of foot platforms w.r.t their own base can be derived as

$$\boldsymbol{H}_{\mathrm{H-F}_i} = {}^{\{\mathrm{E}\}}\boldsymbol{H}_{\mathrm{E-H}}{}^{-1}{}^{\{\mathrm{E}\}}\boldsymbol{H}_{\mathrm{E-F}_i} = \begin{bmatrix} {}^{\{\mathrm{E}\}}\boldsymbol{R}_{\mathrm{E-H}}{}^{\mathrm{T}}{}^{\{\mathrm{E}\}}\boldsymbol{R}_{\mathrm{E-F}i} & {}^{\{\mathrm{E}\}}\boldsymbol{R}_{\mathrm{E-H}}{}^{\mathrm{T}}{}^{\{\mathrm{E}\}}\boldsymbol{d}_{\mathrm{E-F}i} - {}^{\{\mathrm{E}\}}\boldsymbol{R}_{\mathrm{E-H}}{}^{\mathrm{T}}{}^{\{\mathrm{E}\}}\boldsymbol{d}_{\mathrm{E-H}} \\ \boldsymbol{0} & 1 \end{bmatrix}. \tag{4.68}$$

Note that, the reference coordinates of $\boldsymbol{H}_{\mathrm{H-F}_i}$ was omitted as mentioned in Sub-section 4.2.1.

4.3.2 Inverse Jacobian of Linear Actuators

Bring equation (4.68) into equation (4.10), the linear actuators are obtained as

$${}^{\{\mathrm{E}\}}\bar{\boldsymbol{l}}_{ij} = {}^{\{\mathrm{E}\}}\boldsymbol{H}_{\mathrm{E-H}}\bar{\boldsymbol{l}}_{ij} = {}^{\{\mathrm{E}\}}\boldsymbol{H}_{\mathrm{E-F}_i}{}^{\{\mathrm{F}_i\}}\bar{\boldsymbol{d}}_{\mathrm{F}i-\mathrm{F}ij} - {}^{\{\mathrm{E}\}}\boldsymbol{H}_{\mathrm{E-H}}\bar{\boldsymbol{d}}_{\mathrm{H-H}ij} \tag{4.69}$$

The lengths of linear actuators are obtained as the norm of ${}^{\{\mathrm{E}\}}\boldsymbol{l}_{ij}$, i.e. $|{}^{\{\mathrm{E}\}}\boldsymbol{l}_{ij}|$. Its unit vector is ${}^{\{\mathrm{E}\}}\boldsymbol{e}_{ij} = {}^{\{\mathrm{E}\}}\boldsymbol{l}_{ij}/|{}^{\{\mathrm{E}\}}\boldsymbol{l}_{ij}|$.

The time differential of ${}^{\{\mathrm{E}\}}\bar{\boldsymbol{l}}_{ij}$ is the relative veloctiy between the joints center, as

$$\begin{aligned} {}^{\{\mathrm{E}\}}\bar{\boldsymbol{v}}_{\mathrm{H}ij-\mathrm{F}ij} = {}^{\{\mathrm{E}\}}\dot{\bar{\boldsymbol{l}}}_{ij} &= {}^{\{\mathrm{E}\}}\dot{\boldsymbol{H}}_{\mathrm{E-F}_i}{}^{\{\mathrm{F}_i\}}\bar{\boldsymbol{d}}_{\mathrm{F}i-\mathrm{F}ij} - {}^{\{\mathrm{E}\}}\dot{\boldsymbol{H}}_{\mathrm{E-H}}\bar{\boldsymbol{d}}_{\mathrm{H-H}ij} \\ &= \begin{bmatrix} {}^{\{\mathrm{E}\}}\dot{\boldsymbol{R}}_{\mathrm{E-F}i} & {}^{\{\mathrm{E}\}}\dot{\boldsymbol{d}}_{\mathrm{E-F}i} \\ \boldsymbol{0} & 0 \end{bmatrix}{}^{\{\mathrm{F}_i\}}\bar{\boldsymbol{d}}_{\mathrm{F}i-\mathrm{F}ij} - \begin{bmatrix} {}^{\{\mathrm{E}\}}\dot{\boldsymbol{R}}_{\mathrm{E-H}} & {}^{\{\mathrm{E}\}}\dot{\boldsymbol{d}}_{\mathrm{E-H}} \\ \boldsymbol{0} & 0 \end{bmatrix}\bar{\boldsymbol{d}}_{\mathrm{H-H}ij}. \end{aligned} \tag{4.70}$$

Where, ${}^{\{\mathrm{E}\}}\dot{\boldsymbol{R}}_{\mathrm{E-F}i} = \dot{\gamma}_{\mathrm{E-F}i}{}^{\{\mathrm{E}\}}\widetilde{\boldsymbol{\omega}}_{\mathrm{E-F}i}{}^{\{\mathrm{E}\}}\boldsymbol{R}_{\mathrm{E-F}i}$ and ${}^{\{\mathrm{E}\}}\dot{\boldsymbol{R}}_{\mathrm{E-H}} = \dot{\gamma}_{\mathrm{E-H}}{}^{\{\mathrm{E}\}}\widetilde{\boldsymbol{\omega}}_{\mathrm{E-H}}{}^{\{\mathrm{E}\}}\boldsymbol{R}_{\mathrm{E-H}}$.

Thus, the length variation velocities of linear actuators are

$$\dot{l}_{ij} = {}^{\{\mathrm{E}\}}\boldsymbol{v}_{\mathrm{H}ij-\mathrm{F}ij}{}^{\mathrm{T}}{}^{\{\mathrm{E}\}}\boldsymbol{e}_{ij} = {}^{\{*\}}\boldsymbol{v}_{\mathrm{H}ij-\mathrm{F}ij}{}^{\mathrm{T}}{}^{\{*\}}\boldsymbol{e}_{ij}. \tag{4.71}$$

The control variables, $|{}^{\{\mathrm{E}\}}\boldsymbol{l}_{ij}|$ and $\dot{l}_{ij}$, depend only on the relative velocity between platforms, but not on the reference frame. The inverse Jacobian of the whole mechanism is a function of the relative motion of the three platforms, which is in the same form with eq. (4.16).

4.3.3 Inverse Jacobian of Sleeves and Shafts

From Sub-section 4.3.2, it is not difficult to find that the configurations of the sleeves and shafts

are derived only from pure vectors, their motion in homogenous forms are directly given as

$$\begin{cases} {}^{\{E\}}\boldsymbol{H}_{\mathrm{E}-i\mathrm{A}-\mathrm{sleeve}} = {}^{\{E\}}\boldsymbol{H}_{\mathrm{E}-\mathrm{H}}\boldsymbol{H}_{i\mathrm{A}-\mathrm{sleeve}}, \\ {}^{\{E\}}\boldsymbol{H}_{\mathrm{E}-i\mathrm{B}-\mathrm{shaft}} = {}^{\{E\}}\boldsymbol{H}_{\mathrm{E}-\mathrm{H}}\boldsymbol{H}_{i\mathrm{B}-\mathrm{shaft}}. \end{cases} \tag{4.72}$$

Based on equation (4.31) and (4.63), the velocity of sleeves is given as

$$\begin{aligned} {}^{\{E\}}\dot{\boldsymbol{q}}_{\mathrm{H}-i\mathrm{A}-\mathrm{sleeve}} &= \begin{bmatrix} {}^{\{E\}}\dot{\boldsymbol{d}}_{\mathrm{E}-\mathrm{H}} + \dot{\gamma}_{\mathrm{E}-\mathrm{H}}\,{}^{\{E\}}\tilde{\boldsymbol{\omega}}_{\mathrm{E}-\mathrm{H}}\boldsymbol{d}_{\mathrm{H}-\mathrm{H}ij} \\ \dot{\gamma}_{\mathrm{E}-\mathrm{H}}\,{}^{\{E\}}\boldsymbol{\omega}_{\mathrm{E}-\mathrm{H}} + {}^{\{E\}}\boldsymbol{R}_{\mathrm{E}-\mathrm{H}}\boldsymbol{\varpi}_{\mathrm{H}-i\mathrm{A}-\mathrm{sleeve}} \end{bmatrix} \\ &= \boldsymbol{J}_{\mathrm{E}-i\mathrm{A}-\mathrm{sleeve}}{}^{-1}\left({}^{\{E\}}\dot{\boldsymbol{X}}_{\mathrm{E}-\mathrm{H}}, {}^{\{E\}}\dot{\boldsymbol{X}}_{\mathrm{H}-\mathrm{F}i}\right). \end{aligned} \tag{4.73}$$

The velocity of shafts is given as

$${}^{\{E\}}\dot{\boldsymbol{q}}_{\mathrm{H}-i\mathrm{A}-\mathrm{shaft}} = \begin{bmatrix} {}^{\{E\}}\dot{\boldsymbol{d}}_{\mathrm{E}-\mathrm{H}} + {}^{\{E\}}\boldsymbol{R}_{\mathrm{E}-\mathrm{H}}\boldsymbol{v}_{i\mathrm{B}} \\ \dot{\gamma}_{\mathrm{E}-\mathrm{H}}\,{}^{\{E\}}\boldsymbol{\omega}_{\mathrm{E}-\mathrm{H}} + {}^{\{E\}}\boldsymbol{R}_{\mathrm{E}-\mathrm{H}}\boldsymbol{\varpi}_{i\mathrm{B}-\mathrm{shaft}}{}^{\mathrm{T}} \end{bmatrix} = \boldsymbol{J}_{\mathrm{E}-i\mathrm{A}-\mathrm{shaft}}{}^{-1}\left({}^{\{E\}}\dot{\boldsymbol{X}}_{\mathrm{E}-\mathrm{H}}, {}^{\{E\}}\dot{\boldsymbol{X}}_{\mathrm{H}-\mathrm{F}i}\right). \tag{4.74}$$

Till here, the motion descriptions of all the main parts in CENTAUROB w.r.t world frame were given in matrix form.

4.3.4. The Inverse Kinematics in Quaternions Form

Derived from eq. (4.60) to (4.62), the motion quaternions of the hip platform w.r.t {E} is

$$\begin{cases} {}^{\{E\}}\widehat{\boldsymbol{Q}}_{\mathrm{E}-\mathrm{H}} = {}^{\{E\}}\boldsymbol{Q}_{\boldsymbol{R}\mathrm{E}-\mathrm{H}} + \epsilon\frac{1}{2}\,{}^{\{E\}}\boldsymbol{Q}_{\boldsymbol{d}\mathrm{E}-\mathrm{H}}\,{}^{\{E\}}\boldsymbol{Q}_{\boldsymbol{R}\mathrm{E}-\mathrm{H}}, \\ {}^{\{E\}}\widehat{\boldsymbol{Q}}_{\mathrm{E}-\mathrm{H}}{}^{\sim} = {}^{\{E\}}\boldsymbol{Q}_{\boldsymbol{R}\mathrm{E}-\mathrm{H}}{}^{*} - \epsilon\frac{1}{2}\,{}^{\{E\}}\boldsymbol{Q}_{\boldsymbol{d}\mathrm{E}-\mathrm{H}}{}^{*}\,{}^{\{E\}}\boldsymbol{Q}_{\boldsymbol{R}\mathrm{E}-\mathrm{H}}.{}^{*} \end{cases} \tag{4.75}$$

In which, according to eq. (4.64), $\begin{cases} {}^{\{E\}}\boldsymbol{Q}_{\boldsymbol{d}\mathrm{E}-\mathrm{H}} = {}^{\{E\}}\boldsymbol{d}_{\mathrm{E}-\mathrm{H}}{}^{\mathrm{T}}\boldsymbol{C}_{\mathrm{H}}, \\ {}^{\{E\}}\boldsymbol{Q}_{\boldsymbol{R}\mathrm{E}-\mathrm{H}} = \cos\frac{\gamma_{\mathrm{E}-\mathrm{H}}}{2} + \sin\frac{\gamma_{\mathrm{E}-\mathrm{H}}}{2}\,{}^{\{E\}}\boldsymbol{\omega}_{\mathrm{E}-\mathrm{H}}{}^{\mathrm{T}}\boldsymbol{C}_{\mathrm{H}}. \end{cases}$

The motion quaternions of foot platforms w.r.t {E} is

$$\begin{cases} {}^{\{\mathrm{E}\}}\widehat{\boldsymbol{Q}}_{\mathrm{E-F}_i} = {}^{\{\mathrm{E}\}}\boldsymbol{Q}_{\boldsymbol{R}\mathrm{E-F}_i} + \epsilon\, {}^{\{\mathrm{E}\}}\boldsymbol{Q}_{\boldsymbol{d}\mathrm{E-F}_i}\, {}^{\{\mathrm{E}\}}\boldsymbol{Q}_{\boldsymbol{R}\mathrm{E-F}_i}/2\,, \\ {}^{\{\mathrm{E}\}}\widehat{\boldsymbol{Q}}_{\mathrm{E-F}_i}{}^{\sim} = {}^{\{\mathrm{E}\}}\boldsymbol{Q}_{\boldsymbol{R}\mathrm{E-F}_i}{}^{*} - \epsilon\, {}^{\{\mathrm{E}\}}\boldsymbol{Q}_{\boldsymbol{d}\mathrm{E-F}_i}{}^{*}\, {}^{\{\mathrm{E}\}}\boldsymbol{Q}_{\boldsymbol{R}\mathrm{E-F}_i}/2^{*} \end{cases} \tag{4.76}$$

Where, according to eq. (4.67), $\begin{cases} {}^{\{\mathrm{E}\}}\boldsymbol{Q}_{\boldsymbol{d}\mathrm{E-F}_i} = {}^{\{\mathrm{E}\}}\boldsymbol{d}_{\mathrm{E-F}_i}{}^{\mathrm{T}}\boldsymbol{C}_{\mathrm{H}}, \\ {}^{\{\mathrm{E}\}}\boldsymbol{Q}_{\boldsymbol{R}\mathrm{E-F}_i} = \cos\frac{\gamma_{\mathrm{E-F}i}}{2} + \sin\frac{\gamma_{\mathrm{E-F}i}}{2}\, {}^{\{\mathrm{E}\}}\boldsymbol{\omega}_{\mathrm{E-F}i}{}^{\mathrm{T}}\boldsymbol{C}_{\mathrm{H}}. \end{cases}$

Thus, the motion quaternions of platforms are given. Based on eq. (4.69) and (4.47), there is

$${}^{\{\mathrm{E}\}}\widehat{\boldsymbol{Q}}_{\boldsymbol{l}_{ij}} = {}^{\{\mathrm{E}\}}\widehat{\boldsymbol{Q}}_{\mathrm{E-F}_i}\, {}^{\{\mathrm{F}\}}\widehat{\boldsymbol{Q}}_{\boldsymbol{d}\mathrm{F-F}ij}\, {}^{\{\mathrm{E}\}}\widehat{\boldsymbol{Q}}_{\mathrm{E-F}_i}{}^{\sim} - {}^{\{\mathrm{E}\}}\widehat{\boldsymbol{Q}}_{\mathrm{E-H}}\, {}^{\{\mathrm{H}\}}\widehat{\boldsymbol{Q}}_{\boldsymbol{d}\mathrm{H-H}ij}\, {}^{\{\mathrm{E}\}}\widehat{\boldsymbol{Q}}_{\mathrm{E-H}}{}^{\sim}. \tag{4.77}$$

It derives

$$\begin{aligned} {}^{\{\mathrm{E}\}}\boldsymbol{Q}_{\boldsymbol{l}_{ij}} = {}^{\{\mathrm{E}\}}\boldsymbol{Q}_{\boldsymbol{R}\mathrm{E-F}_i}\, {}^{\{\mathrm{F}\}}\boldsymbol{Q}_{\boldsymbol{d}\mathrm{F-F}ij}\, {}^{\{\mathrm{E}\}}\boldsymbol{Q}_{\boldsymbol{R}\mathrm{E-F}_i}{}^{*} - {}^{\{\mathrm{E}\}}\boldsymbol{Q}_{\boldsymbol{R}\mathrm{E-H}}\, {}^{\{\mathrm{F}\}}\boldsymbol{Q}_{\boldsymbol{d}\mathrm{H-H}ij}\, {}^{\{\mathrm{E}\}}\boldsymbol{Q}_{\boldsymbol{R}\mathrm{E-H}}{}^{*} + {}^{\{\mathrm{E}\}}\boldsymbol{Q}_{\boldsymbol{d}\mathrm{E-F}_i} \\ - {}^{\{\mathrm{E}\}}\boldsymbol{Q}_{\boldsymbol{d}\mathrm{E-H}} \end{aligned} \tag{4.78}$$

Similar to eq. (4.49), its time differential is

$$\begin{aligned} {}^{\{\mathrm{E}\}}\boldsymbol{Q}_{\boldsymbol{v}\mathrm{H}ij-\mathrm{F}ij} &= \frac{d}{dt}\, {}^{\{\mathrm{E}\}}\boldsymbol{Q}_{\boldsymbol{l}_{ij}} \\ &= \mathrm{Im}\left({}^{\{\mathrm{E}\}}\boldsymbol{Q}_{\boldsymbol{\varpi}\mathrm{E-F}_i}\, {}^{\{\mathrm{E}\}}\boldsymbol{Q}_{\boldsymbol{d}\mathrm{F}_i-\mathrm{F}ij} - {}^{\{\mathrm{E}\}}\boldsymbol{Q}_{\boldsymbol{\varpi}\mathrm{E-H}}\, {}^{\{\mathrm{E}\}}\boldsymbol{Q}_{\boldsymbol{d}\mathrm{H-H}ij} + {}^{\{\mathrm{E}\}}\boldsymbol{Q}_{\boldsymbol{v}\mathrm{E-F}_i} - {}^{\{\mathrm{E}\}}\boldsymbol{Q}_{\boldsymbol{v}\mathrm{E-H}} \right) \end{aligned} \tag{4.79}$$

Its projection on linear actuator is same as (4.71), in quaternions form is

$$\dot{l}_{ij} = -\,\mathrm{Re}\left({}^{\{\mathrm{E}\}}\boldsymbol{Q}_{\boldsymbol{v}\mathrm{H}ij-\mathrm{F}ij}\, {}^{\{\mathrm{E}\}}\boldsymbol{Q}_{\boldsymbol{e}_{ij}} \right). \tag{4.80}$$

Where, ${}^{\{\mathrm{E}\}}\boldsymbol{Q}_{\boldsymbol{e}_{ij}}$ is the quaternions form of unit vector ${}^{\{\mathrm{E}\}}\boldsymbol{e}_{ij}$.

As discussed in Sub-section 4.2.2, there is barely any obvious advantage of computing the motions of sleeves and shafts in quaternions form. Therefore, their computations rest on the matrix form, as part *3)* of Sub-section 4.2.4.

4.4 Passive Rotation Problem

During the modelling of the linear actuators, they were usually treated as a combination of one prismatic pair and one revolute pair, as mentioned in Chapter 2. Nevertheless, the most ball lead screws should be treated as a combination of one helical joint and one prismatic joint, seeing fig. 4.6(a). It was caused by the mechanical driving approach of balls as illustrated in fig. 4.6(b). When the sleeves stay angularly still and the balls are driven by the motor in the screw groove and return groove, the sleeves will be pushed linearly. When the screw sleeve rotates and the balls stay, the sleeve will move along the axis, as illustrated in fig. 4.6(b). This phenomenon was discussed in several former publications [4.36-38].

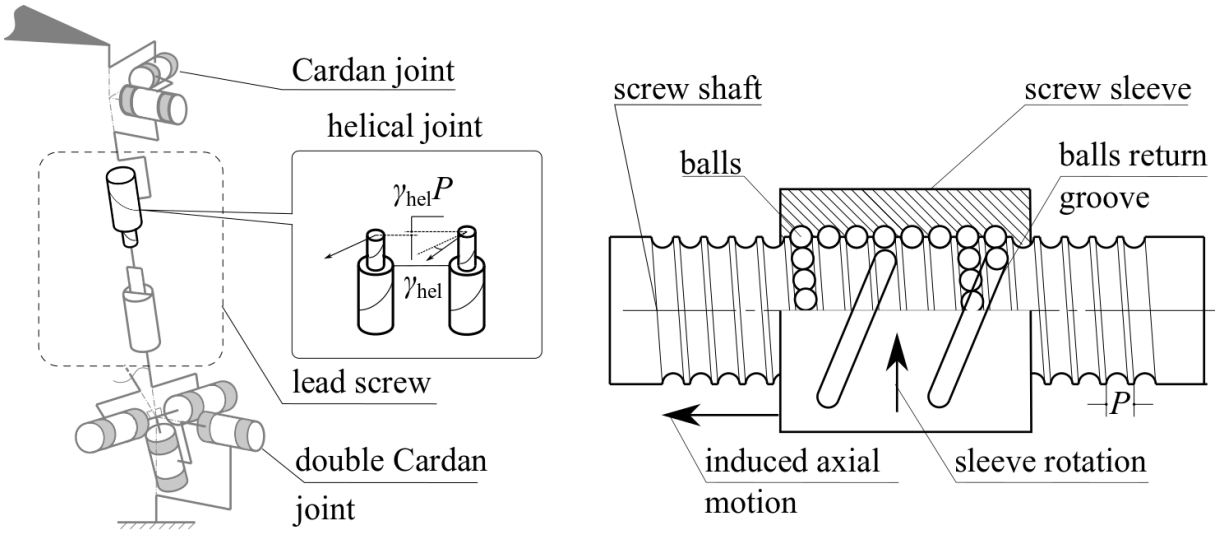

Figure 4.6 Analysis of a lead screw. (a) The topological modelling of lead screw as a combination of helical and prismatic joint. (b) Mechanical scheme of a ball lead screw.

The relative axial rotation between sleeve and shaft will cause a length variation of a lead screw. This length variation will cause inner stress or strain and will further reduce the control accuracy. Therefore, this length variation must be compensated through the adjustment of control efforts. Since the length variation is introduced by the relative rotation of the two structural parts of a lead screw, it can be obtained as,

$$l_{\mathrm{P}ij} = \gamma_{\mathrm{hel}ij}P \tag{4.81}$$

In which, P stands for the screw pitch and $\gamma_{\mathrm{hel}ij}$ is the realtive rotation angle between the shaft and sleeve of a lead screw. At the same time, since the common z-axis for the shaft and sleeve of one lead screw, there exists the following relation about the relative rotation.

$$\boldsymbol{R}\left(z,\gamma_{\mathrm{hel}ij}\right) = {}^{\{ij-\mathrm{sleeve}\}}\boldsymbol{R}_{ij-(\mathrm{sleeve}-\mathrm{shaft})} = {}^{\{ij-\mathrm{sleeve}\}}\boldsymbol{R}_{(ij-\mathrm{sleeve})-\mathrm{E}}\,{}^{\{\mathrm{E}\}}\boldsymbol{R}_{\mathrm{E}-(ij-\mathrm{shaft})} \tag{4.82}$$

E stands for inertial coordinates system. From which, it is obvious, $\gamma_{\mathrm{hel}ij}$ is in fact the angle between the x-axes or y-axes of two frames fixed on sleeve and shaft. Introducing equation (4.18) and (4.36),

$$\sin\gamma_{\mathrm{hel}ij} = \boldsymbol{e}_{ij}{}^{\mathrm{T}}\tilde{\boldsymbol{x}}_{ij-\mathrm{sleeve}}\boldsymbol{x}_{ij-\mathrm{shaft}} \tag{4.83}$$

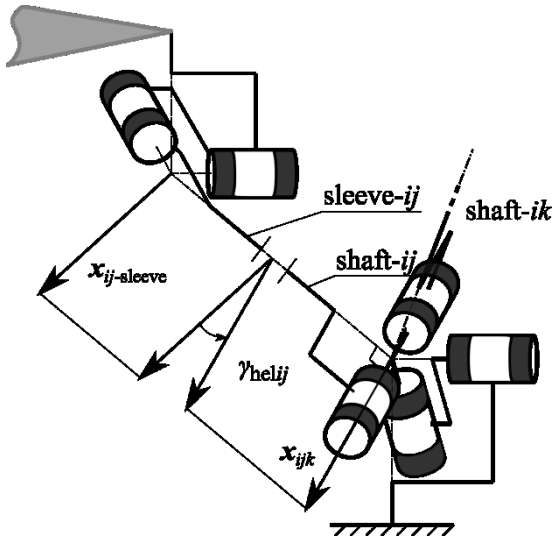

Figure 4.7 The solution of passive rotation problem. The relative rotation can be solved by calculating the angular difference between the x-axes of sleeve and shaft of one linear actuator, e.g., $\boldsymbol{x}_{ij-\mathrm{sleeve}}$ and $\boldsymbol{x}_{ijk}$.

Seeing limbs-ij in fig. 4.7, the relative motion can be obtained by

$$\gamma_{\mathrm{hel}ij} = \sin^{-1}\left(\boldsymbol{e}_{ij}{}^{\mathrm{T}}\tilde{\boldsymbol{x}}_{ij-\mathrm{sleeve}}\boldsymbol{x}_{ij-\mathrm{shaft}}\right). \tag{4.84}$$

The velocity of this length variation caused by passive rotation could be obtained through time differential of $l_{\mathrm{P}ij}$.

$$\dot{l}_{\mathrm{P}ij} = \dot{\gamma}_{\mathrm{hel}ij}P. \tag{4.85}$$

$\dot{\gamma}_{\mathrm{hel}ij}$ is indeed the axial rotation velocity difference between sleeve and shaft. From fig. 4.2, fig. 4.3, eq. (4.30) and (4.40), this rotational velocity can be obtained as the rotational velocity projection on the linear actuator. For limb-*ij*, there is

$$\dot{\gamma}_{\mathrm{hel}ij} = \left(\boldsymbol{\varpi}_{\mathrm{L}ij\mathrm{S}} - \boldsymbol{\varpi}_{\mathrm{L}ij\mathrm{N}}\right)^{\mathrm{T}} \boldsymbol{e}_{ij}. \tag{4.86}$$

The variables above should be in the same coordinates frame.

4.5 Forward Kinematics Problem

4.5.1 Problem Statement

As discussed in Chapter 2, the FKP of a 6-SPS formed PKM[6,3] mechanism will involve to a 1-dimensional searching problem. As illustrated in fig. 2.8(b), knowing the lengths of 6 linear actuators, the mechanism can be transformed to a determination of 2-RS+RSR FKP. It can also be described as a geometrical problem in fig. 2.10(b).

As shown in fig. 4.8(b), the problem is abstracted to finding the configurations of R_1, R_2 and R_3, by which the bars $\boldsymbol{l}_4$ and $\boldsymbol{l}_3$ intersect. Alternatively, it can be expressed in the following form.

Conditions: $C_{\mathrm{S}1}: \boldsymbol{H}_{\mathrm{R}1-\mathrm{S}1}\bar{\boldsymbol{l}}_1, \quad C_{\mathrm{S}2}: \boldsymbol{H}_{\mathrm{R}2-\mathrm{S}2}\bar{\boldsymbol{l}}_2, \quad C_{\mathrm{S}3}: \boldsymbol{H}_{\mathrm{R}3-\mathrm{S}3}\bar{\boldsymbol{l}}_3, \quad C_{\mathrm{S}3'}: \boldsymbol{H}_{\mathrm{R}1-2-\mathrm{S}3}\bar{\boldsymbol{l}}_4$

Constraint: $\|\boldsymbol{S}_1 - \boldsymbol{S}_2\| = l_{1-2}, \quad C_{\mathrm{S}3'} \cap C_{\mathrm{S}3} \neq \emptyset.$

Where, $\begin{cases} \boldsymbol{H}_{\mathrm{R}i-\mathrm{S}i} = \begin{bmatrix} \boldsymbol{R}_{\mathrm{R}i-\mathrm{S}i} & \boldsymbol{d}_{\mathrm{R}i} \\ \boldsymbol{0} & 1 \end{bmatrix} = \begin{bmatrix} \boldsymbol{R}(z,\alpha_{\mathrm{R}i})\boldsymbol{R}(x,\gamma_{\mathrm{R}i}) & \boldsymbol{d}_{\mathrm{R}i} \\ \boldsymbol{0} & 1 \end{bmatrix} \\ \boldsymbol{H}_{\mathrm{R}1-2-\mathrm{S}3} = \begin{bmatrix} \boldsymbol{R}_{\mathrm{R}1-2-\mathrm{S}3} & \boldsymbol{d}_{\mathrm{R}1-2} \\ \boldsymbol{0} & 1 \end{bmatrix} \end{cases}$.

From the first condition, the location of S_1 S_2 and S_3 can be derived

$$\bar{\boldsymbol{S}}_i = \boldsymbol{H}_{\mathrm{R}i-\mathrm{S}i}\bar{\boldsymbol{l}}_i = \begin{bmatrix} l_i\boldsymbol{R}(z,\alpha_{\mathrm{R}i})\boldsymbol{R}(x,\gamma_{\mathrm{R}i})\boldsymbol{z} + \boldsymbol{d}_{\mathrm{R}i} \\ 1 \end{bmatrix} = \begin{bmatrix} l_i \sin\alpha_{\mathrm{R}i} \sin\gamma_{\mathrm{R}i} + x_{\mathrm{R}i} \\ -l_i \cos\alpha_{\mathrm{R}i} \sin\gamma_{\mathrm{R}i} + y_{\mathrm{R}i} \\ l_i \cos\gamma_{\mathrm{R}i} \\ 1 \end{bmatrix}, \quad i = 1,2,3. \tag{4.87}$$

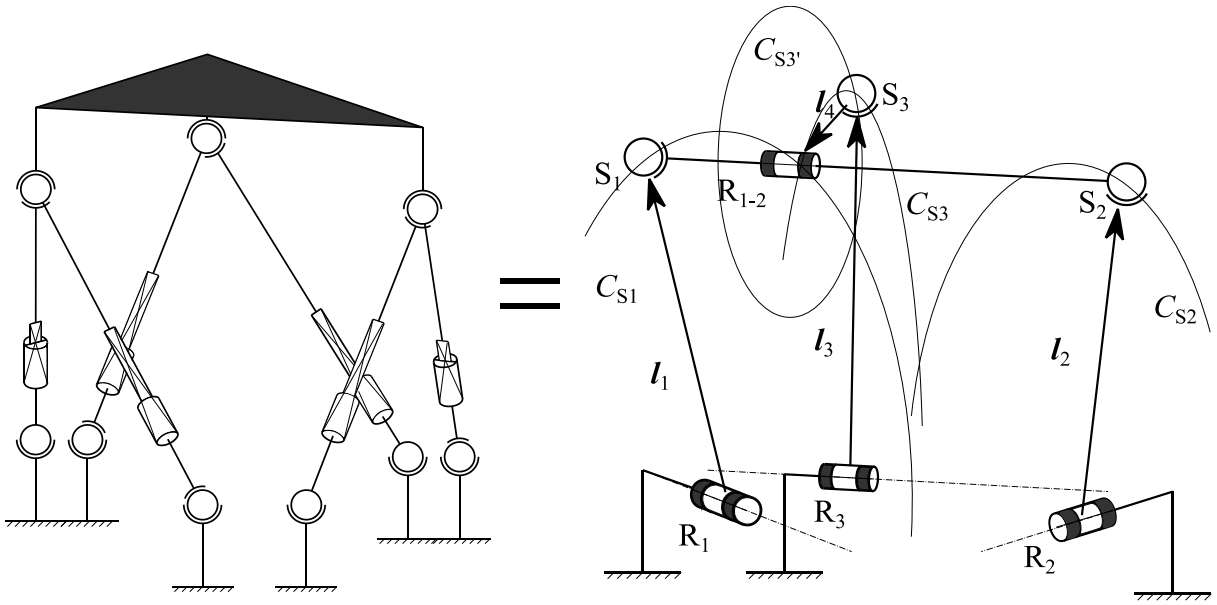

(a) (b)

Figure 4.8 The solving method of FKP of a PKM [6,3]. (a) A typical 6-S<u>P</u>S PKM with locked actuators and (b) its equivalent 2-RS+RSR PKM.

4.5.2 Solution of S_1 and S_2

Seeing fig. 4.8(b), the trajectories of S_1 and S_2 are two circles in 3D space, the constraint is the length between them, which depends on the installation dimensions of the joints, as l_{1-2}. If the S_1 is too far from the plane of C_{S2}, there will be no solution. The location of $R_{1\text{-}2}$ is confirmed once the line $\overline{S_1S_2}$ was confirmed. The location of S_2 should be the intersections of C_{S2} and a sphere surface, $S_{S2'}$, centric to S_1. Thus, as illustrated in fig. 4.9, there will be at most 2 solutions of S_2, despite the singular positions, for example, when S_1 locates along the axis of R_2.

Introducing eq. (4.87), the first constraint, $\|\boldsymbol{S}_1 - \boldsymbol{S}_2\| = l_{1-2}$, turns to

$$\begin{aligned}(l_1 \sin\alpha_{R1} \sin\gamma_{R1} - l_2 \sin\alpha_{R2} \sin\gamma_{R2} + x_{R1} - x_{R2})^2 \\ + (l_2 \cos\alpha_{R2} \sin\gamma_{R2} - l_1 \cos\alpha_{R1} \sin\gamma_{R1} + y_{R1} - y_{R2})^2 \\ + (l_1 \cos\gamma_{R1} - l_2 \cos\gamma_{R2})^2 = {l_{1-2}}^2.\end{aligned} \tag{4.88}$$

It derives

$$A_1 \cos\gamma_{R2} + B_1 \sin\gamma_{R2} = \left({l_{1-2}}^2 - C_1\right)/2. \tag{4.89}$$

In which,

$$\begin{cases} A_1 = -l_1 l_2 \cos\gamma_{\mathrm{R1}}\,, \\ B_1 = l_2[(y_{\mathrm{R1}} - y_{\mathrm{R2}})\cos\alpha_{\mathrm{R2}} - (x_1 - x_{\mathrm{R2}})\sin\alpha_{\mathrm{R2}}] - l_1 l_2 \cos(\alpha_{\mathrm{R1}} - \alpha_{\mathrm{R2}})\sin\gamma_{\mathrm{R1}} \\ C_1 = {l_1}^2 + {l_2}^2 + (x_{\mathrm{R1}} - x_{\mathrm{R2}})^2 + (y_{\mathrm{R1}} - y_{\mathrm{R2}})^2 \\ \qquad\qquad +2l_1[(x_{\mathrm{R1}} - x_{\mathrm{R2}})\sin\alpha_{\mathrm{R1}} - (y_{\mathrm{R1}} - y_{\mathrm{R2}})\cos\alpha_{\mathrm{R1}}]\sin\gamma_{\mathrm{R1}}\,. \end{cases}$$

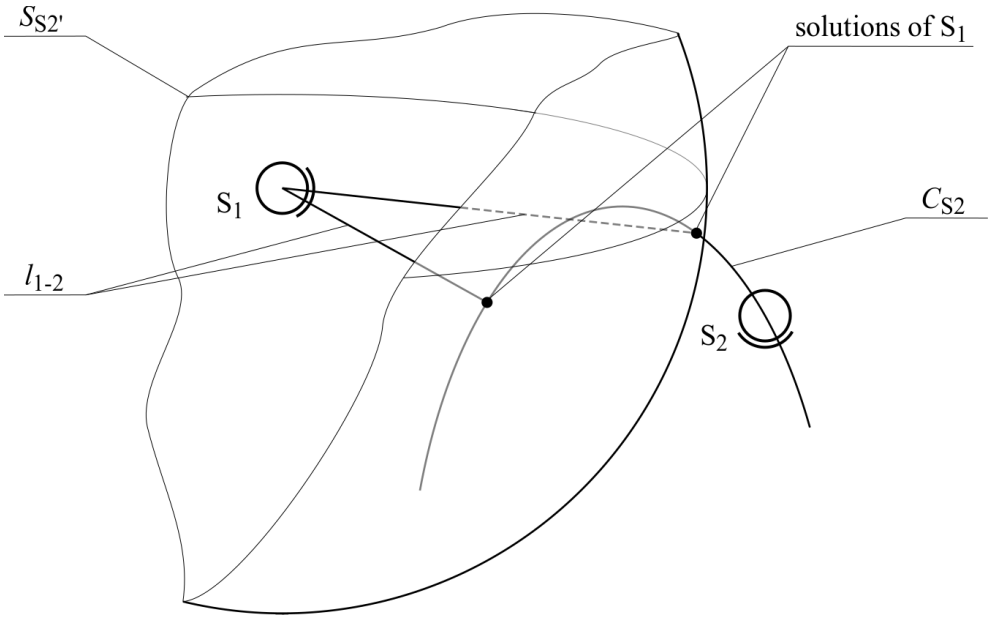

Figure 4.9 Solutions of S_2 position based on the position of S_1.

Thus, the position of S_2 can be confirmed by

$$\gamma_{\mathrm{R2}} = E_1 \pm \cos^{-1}\left[\left({l_{1-2}}^2 - C_1\right)/2D_1\right] \tag{4.90}$$

Where, $D_1 = \sqrt{{A_1}^2 + {B_1}^2}$ and $E_1 = \tan^{-1}\frac{B_1}{A_1} + \begin{cases} 0 & A_1 > 0 \\ \pi & A_1 \le 0 \ \ and \ \ B_1 \ge 0. \\ -\pi & A_1 \le 0 \ \ and \ \ B_1 < 0 \end{cases}$

Note that, in eq. (4.90), the quadrant of E_1 is determined by the polarity of A_1 and B_1.

4.5.3 Solution of S_3

Seeing figure 4.10(a), the trajectory of S_3 around joint $R_{1\text{-}2}$ is a circle with the norm vector along $R_{1\text{-}2}$ and co-centric with $R_{1\text{-}2}$. If the search result stands or not, relies on if $C_{S3'}$ and C_{S3} intersect or not. The intersections of two circles must be on the intersections line, $L_{3'\text{-}3}$, of the two planes, $P_{S3'}$ and P_{S3}, where the two circles locate. If the two planes' intersection line is too far from one of two circle centres, there will be no intersection of two circles, seeing fig. 4.10(c). Otherwise, if the intersections of one circle with the intersection line are also the point on the other circle,

this configuration stands, as fig. 4.10(a) and (b).

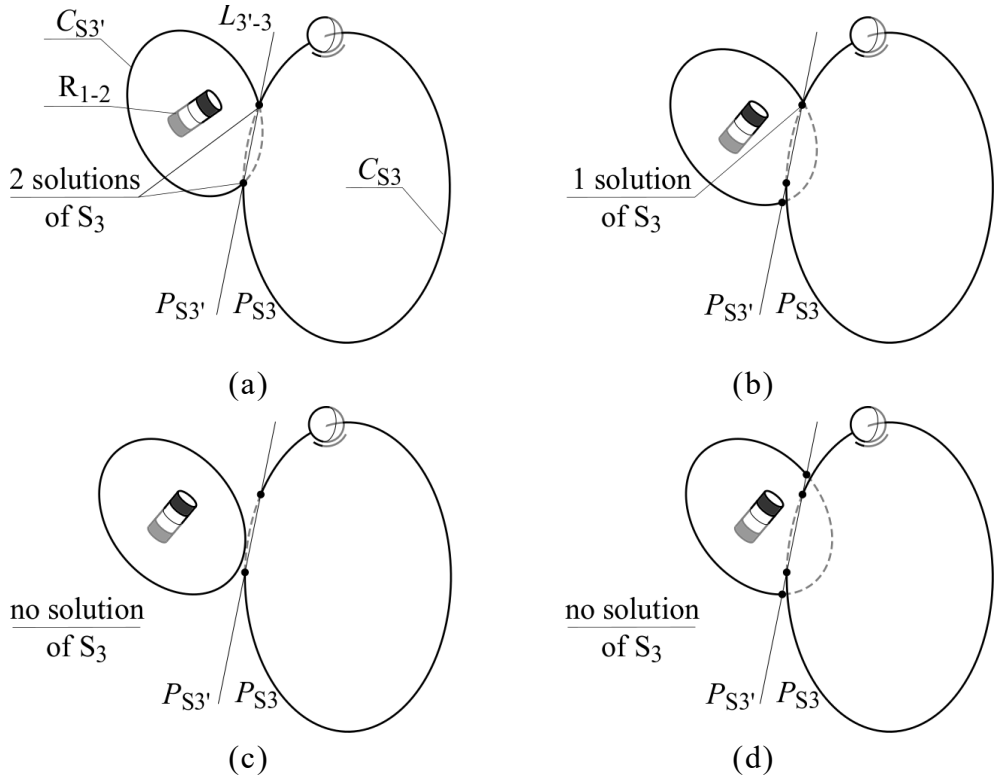

Figure 4.10 Four cases during solving S_3: (a) 2 intersections between C_{S3} and $C_{S3'}$; (b) 1 intersection between C_{S3} and $C_{S3'}$; (c) no intersections between C_{S3} and $C_{S3'}$ and no intersections between $C_{S3'}$ and $L_{3'-3}$; (d) no intersections between C_{S3} and $C_{S3'}$ but there exist intersections between $C_{S3'}$ and $L_{3'-3}$.

Based on the shape of moving platform, the position and orientation of R_{1-2} is thus confirmed. Let the position and orientation of R_{1-2} and R_3 be $\boldsymbol{r}_{1-2}$, $\boldsymbol{r}_3$ and $\boldsymbol{\omega}_{1-2}$, $\boldsymbol{\omega}_3$, there are

$$\begin{cases} \boldsymbol{d}_{R1-2} = [x_{1-2} \quad y_{1-2} \quad z_{1-2}]^T, & \boldsymbol{d}_{R3} = [x_3 \quad y_3 \quad 0]^T; \\ \boldsymbol{\omega}_{R1-2} = [\omega_{1-2x} \quad \omega_{1-2y} \quad \omega_{1-2z}]^T, & \boldsymbol{\omega}_{R3} = [\omega_{3x} \quad \omega_{3y} \quad 0]^T. \end{cases} \tag{4.91}$$

The planes, where $C_{S3'}$ and C_{S3} locate, intersect at

$$L_{3'-3}: \begin{cases} P_{S3'}: \omega_{1-2x}x + \omega_{1-2y}y + \omega_{1-2z}z = D_{1-2}, \\ P_{S3}: \omega_{3x}x + \omega_{3y}y = D_3. \end{cases} \tag{4.92}$$

Where, $\begin{cases} D_{1-2} = \omega_{1-2x}x_{1-2} + \omega_{1-2y}y_{1-2} + \omega_{1-2z}z_{1-2}, \\ D_3 = \omega_{3x}x_3 + \omega_{3y}y_3. \end{cases}$

Thus, the intersection line of $P_{S3'}$ and P_{S3} is $L_{3'-3} = P_{S3'} \cap P_{S3}$. The distances between R_{1-2}, R_3 and $L_{3'-3}$, named as d_{1-2I} and d_{3I}, should be smaller than their own radius, otherwise, the

case in figure 4.10(c) happens. Given two arbitrary points on $L_{3'-3}$, named as $\boldsymbol{p}_{3'-3-1}$and $\boldsymbol{p}_{3'-3-2}$, the distance can be calculated as

$$d_{*\mathrm{I}} = \frac{|(\widetilde{\boldsymbol{p}}_{3'-3-1} - \widetilde{\boldsymbol{p}}_{3'-3-2})(\boldsymbol{p}_{3'-3-1} - \boldsymbol{d}_{*})|}{|\boldsymbol{p}_{3'-3-1} - \boldsymbol{p}_{3'-3-2}|} \leq l_{*} \quad *= 1-2 \ \ or \ \ 3. \tag{4.93}$$

From eq. (4.87) and (4.92).The intersection of C_{S3} and the line $L_{3'-3}$ should fulfil

$$A_2 \cos\gamma_{\mathrm{R3}} + B_2 \sin\gamma_{\mathrm{R3}} = C_2. \tag{4.94}$$

Where, $\begin{cases} A_2 = l_3\omega_{1-2z}, \\ B_2 = l_3\omega_{1-2x}\sin\alpha_{\mathrm{R3}} - l_3\omega_{1-2y}\cos\alpha_{\mathrm{R3}}, \\ C_2 = -\left(\omega_{1-2x}x_{\mathrm{R3}} + \omega_{1-2y}y_{\mathrm{R3}} + D_{1-2}\right). \end{cases}$

It derives

$$\gamma_{\mathrm{R3}} = E_2 \pm \cos^{-1}(C_2/D_2). \tag{4.95}$$

In which, $\begin{cases} D_2 = \sqrt{{A_2}^2 + {B_2}^2}, \\ E_2 = \tan^{-1}\frac{B_2}{A_2} + \begin{cases} 0 & A_2 > 0 \\ \pi & A_2 \leq 0 \ \ and \ \ B_2 \geq 0 \\ -\pi & A_2 \leq 0 \ \ and \ \ B_2 < 0 \end{cases}. \end{cases}$

Thus, the 2 possible locations of the joint S_3 can be confirmed as

$$\boldsymbol{S}_3 = \begin{bmatrix} \sin\alpha_{\mathrm{R3}}\sin\gamma_{\mathrm{R3}} + x_{\mathrm{R3}} \\ -\cos\alpha_{\mathrm{R3}}\sin\gamma_{\mathrm{R3}} + y_{\mathrm{R3}} \\ \cos\gamma_{\mathrm{R3}} \end{bmatrix} \tag{4.96}$$

If the distance from S_3 to $R_{1\text{-}2}$, as d_{II}, is equal to the radius of $C_{S3'}$, the configurations stands, otherwise not.

$$d_{\mathrm{II}} = \|\boldsymbol{S}_3 - \boldsymbol{d}_{\mathrm{R1-2}}\|. \tag{4.97}$$

Notice that, if the two planes, P_{S3} and $P_{S3'}$, coincide, it turns to a 2 dimensional geometric problem. The searching aim will be to find the intersections of two circles on one plane.

4.5.4 Solution Searching Process

The searching process can be described in the following flow chart. As shown in fig. 4.11, there

will be four sets of possible solutions of S_3. These four sets of solutions are corresponding to the signs of cosine terms in equation (4.90) and (4.95). The search step length $\Delta\gamma_{R1}$ will be decreased in the neighbourhood of $\gamma_{R1}|_{\min(d_{II})}$ to do more iterations of searching. Then, four solutions with minimum d_{II} will be adopted. Based on the former pose and location of moving platform or other peripheral approaches (sensors, prior knowledge, etc.), only one solution will be confirmed.

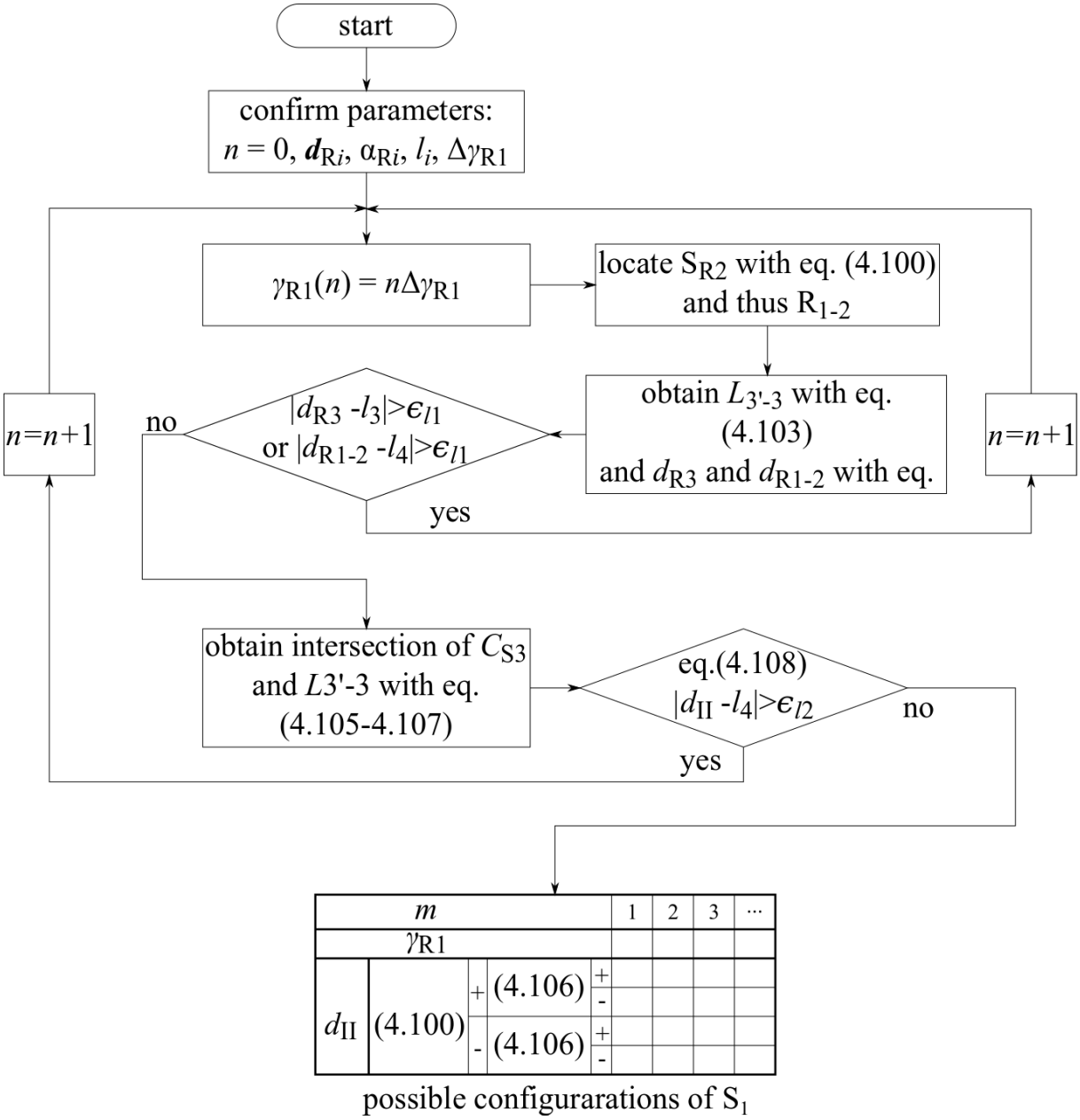

Figure 4.11 Flow chart of FKP solution searching algorithm of a PKM-[6,3].

4.6 Simulation Results

The inverse kinematic solution is known as the essential topic for various subjects during the design and operating a parallel kinematic mechanism. The kinematics of CENTAUROB was simulated under a MATLAB environment. All joint variables and control contributions are calculated with different trajectories of three platforms, {H}, {F_1} and {F_2}. The position and velocities will be given referred to the fixed coordinates {E}. It should be noticed, that the length compensation of linear actuators caused by the passive relative rotation are also simulated and studied. Since the algebra symmetry of PKMs, the motion of the hip w.r.t the feet is in fact a symmetry of converse motion. This fact allows a simulation of hip motion to represent all kinds of relative motion of feet w.r.t. hip.

4.6.1 IKP Simulation

In the kinematic simulation, the hip platform was abstracted as a blue hexagon in fig. 4.12, the foot joints are illustrated as two red triangles and linear actuators as 12 blue lines. The velocities are noted in the figure as arrows, the rotational as cyan and translational as red.

Since the symmetry of the two feet w.r.t. the hip, the simulation result for foot-1 was shown in fig. 4.13. The motion of hip was defined as a sine wave rotation with amplitude of 0.1π around its z-axis. The period of rotation is 2 seconds. Correspondingly, its rotational velocity is a cosine wave with same period. The lengths of linear actuators are illustrated as different curves. The length variation velocities are in a range of ±26.65mm/s. The relative rotations between the sleeves and shafts cause length variations in a range of ±0.518mm. The corresponding length variation velocity compensation is in a range of ±1.73mm/s.

In fig. 4.14, the result of a motion of the hip along the *x*-axis with sine wave was shown. The amplitude of translational motion was 200mm and the period was 2 seconds. The length variation velocity is in a range of ±151.63mm/s. The length compensation was in a range of ±0.13mm and with a velocity between ±0.91mm/s.

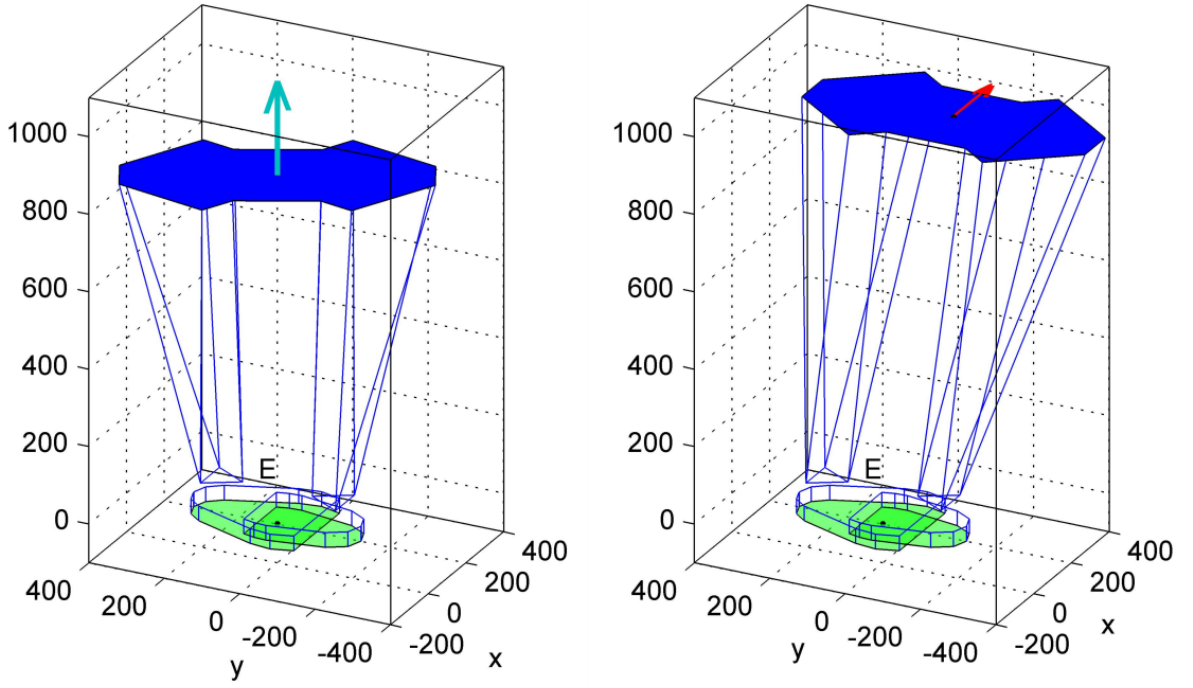

(a) (b)

Figure 4.12 Two simulations of CENTAUROB when:

(a): ${}^{\{E\}}\boldsymbol{X}_{E-H} = [0 \quad 0 \quad 0 \quad 0 \quad 0 \quad \mathrm{Amp}_6 \sin(t/T_6)]^T$ and (b): ${}^{\{E\}}\boldsymbol{X}_{E-H} = [\mathrm{Amp}_6 \sin(t/T_1) \quad 0 \quad 0 \quad 0 \quad 0 \quad 0]^T$

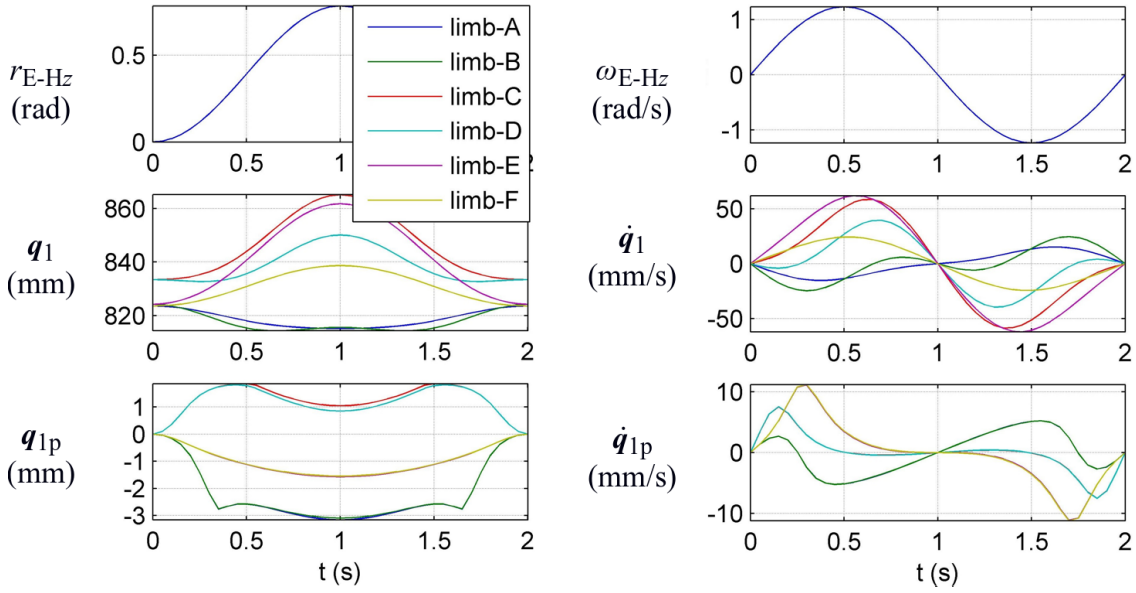

Figure 4.13 Simulation result of fig. 4.12(a). The position (top left) and velocity (top right) of hip were given. The lengths (middle left) and velocities (middle right) of linear actuators were given. The length compensations (bottom left) and their variation velocities (bottom right) were shown.

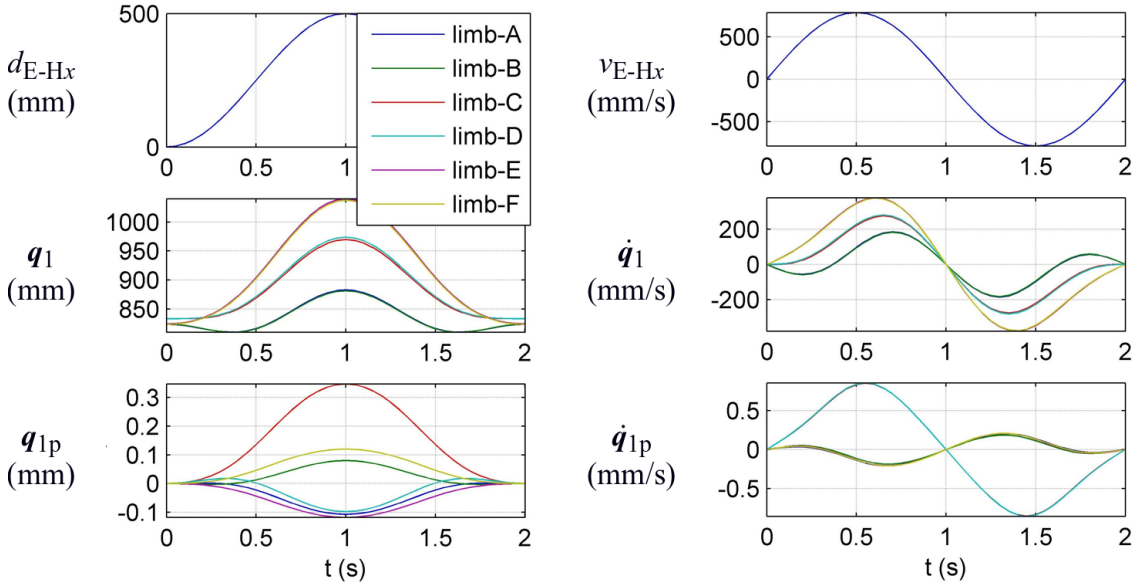

Figure 4.14 Simulation result of fig. 4.12(b). The position (top left) and velocity (top right) of hip were given. The lengths of linear actuators (middle left) and their velocities (middle right) were given. The length compensations (bottom left) and variation velocities (bottom right) were shown.

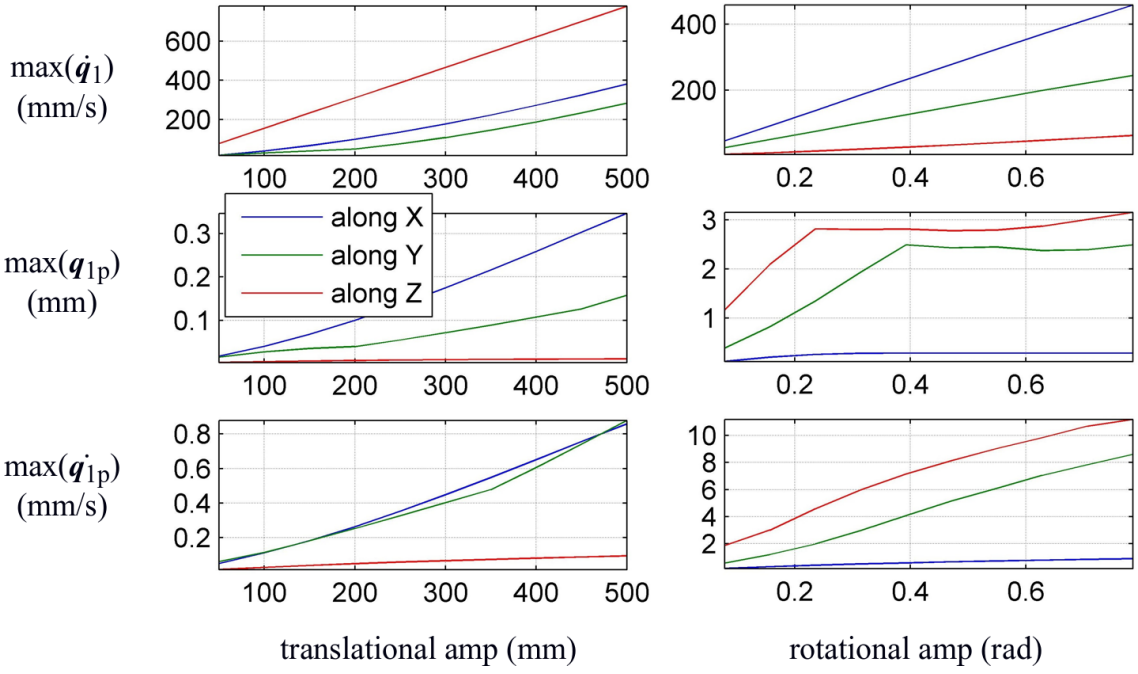

Figure 4.15 Simulation results of different amplitudes. There are translational (left column) and rotational (right column) displacements of hip platform. The maximum length variation velocity (first row), maximum passive rotation compensation quantities (second row) and maximum passive rotation compensation velocities (third row) are shown. The motions are in three directions: along *x*- (blue), *y*- (red) and along *z*-axis (green).

As shown in fig. 4.15, some key variables' maximum values were computed for different motion amplitudes along different directions. For translational displacements, the motion along *z*-axis caused greater control efforts, comparing with the same motion range along *x*- and *y*- axis. Contrarily, translational motion along *x*- and *y*-axis caused similar velocity demanding, though *y* direction motion (side way movement) caused higher velocity than *x* direction motion (fore-backward movement). The rotational motion along *x*-axis caused the highest velocity demand, while the rotation along *z*-axis caused the lowest. From the graphs of the 2nd and 3rd row of the left column in fig. 4.15, the amount of compensation of passive rotations are limited in a small range, comparing to the length demanding of linear actuators. It is worth to be noticed, that compensation quantities in translational motion along *z*- axis showed more obvious non-linear properties, while along the other two directions it showed more linear properties, both in displacement and velocity aspects. For rotations, it shows contrarily linearity.

4.6.2 Numerical FKP Examples

As discussed in section 4.3, the forward kinematic problem of a 6-SPS formed PKM[6,3] can be solved after a 1-dimensional searching process. The motions of the moving platform were defined in two examples as table 4.1. The mechanism will then be transferred to an equivalent 2-RS+RSR mechanism (see fig. 4.8(c)) and be solved. Based on eq. (4.87), the result variables of equivalent rotational joints R_1, R_2 and R_3 are given in table 4.2. In which, γ_{R2+} and γ_{R2-} are cooresponding to two solutions of eq. (4.90), γ_{R3+} and γ_{R3-} are cooresponding to two solutions of eq. (4.95). The searching error was defined as $\epsilon_{l1} = 1mm$ and $\epsilon_{l2} = 0.5mm$ (referring fig. 4.11). In each example, four solutions are illustrated in fig. 4.16.

In the first example, the 4th solution coincidences the real position of the moving platform. The errors of three points of the platform are 0.187mm, 0.025mm and 0.125mm. It can be observed and calculated that, the solution-4 and solution-1 are symmetric about the plane formed by S_1, S_2 and R_3. It is the same case for solution-2 and -3 about the same plane. On the other side, the solution-1 and -2 are symmetric about the *x*-*y* plane, so are the solution-3 and -4.

Table 4.1 Motion parameters of moving platform of a 6-SPS PKM

${}^{\{H\}}\boldsymbol{X}_{H-Fi}$	Example 1.	Example 2.
${}^{\{H\}}\boldsymbol{d}_{H-Fi}$	$\begin{bmatrix} 0 \\ 300 \\ 200 \end{bmatrix}$	$\begin{bmatrix} -100 \\ 100 \\ 200 \end{bmatrix}$
$\gamma_{H-Fi}{}^{\{H\}}\boldsymbol{\omega}_{H-Fi}$	$\begin{bmatrix} 36^\circ \\ 0 \\ 18^\circ \end{bmatrix}$	$\begin{bmatrix} -18^\circ \\ -36^\circ \\ 0 \end{bmatrix}$

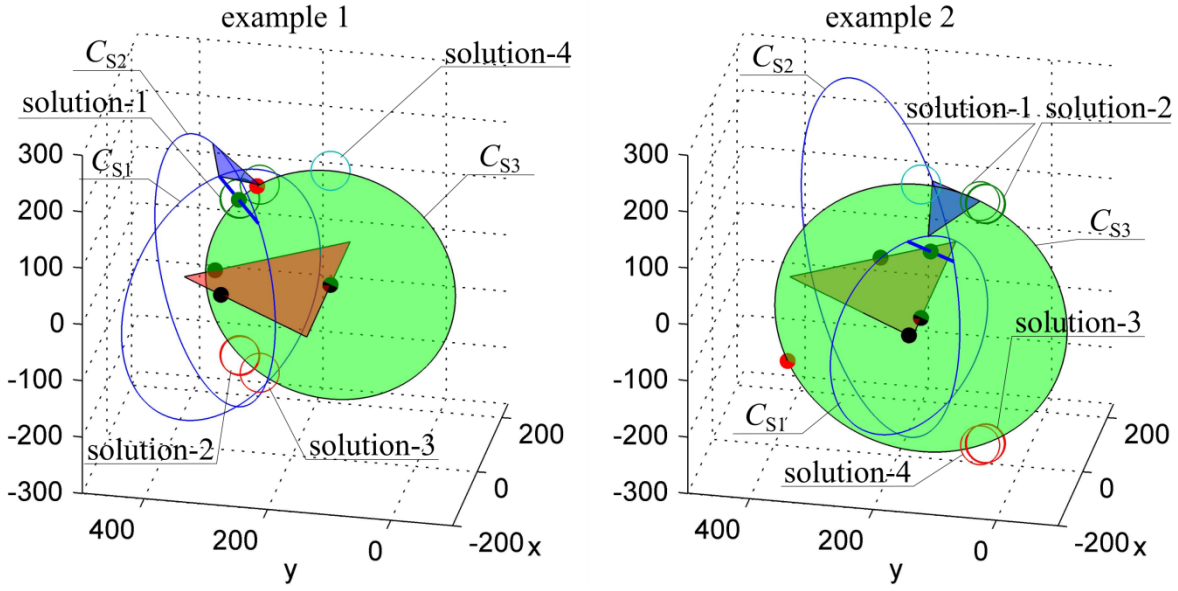

(a) (b)

Figure 4.16 Two numerical examples of 1-dimentional searching process for the location of joint S_3 in a 6-SPS PKM[6,3]. The definitions of curves and figures referred to fig. 4.10. (a) solutions of example 1, (b) solutions of example 2.

In the second example, the first solution coincidences the real position of the moving platform. The errors of the three points of the platform are 0.080mm, 0.010mm and 0.050mm. Similar to the first example, the 1st and 4th solutions, the 2nd and 3rd solutions are symmetric about the *x*-*y* plane, respectively. The 1st and 2nd solutions, the 3rd and 4th solutions are symmetric about the plane formed by S_1, S_2 and R_3, respectively.

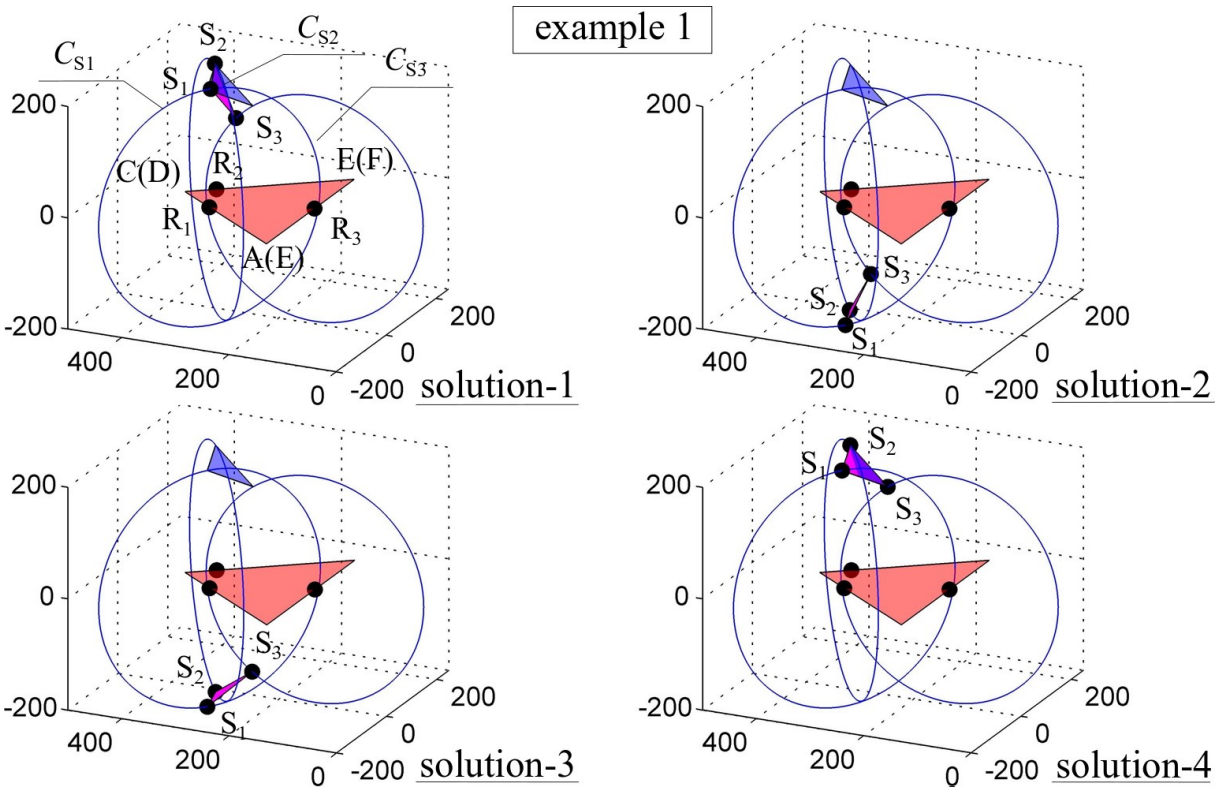

Figure 4.17 Four solutions of the location of the moving platform in numerical example 1. Solutions were shown as purple triangles.

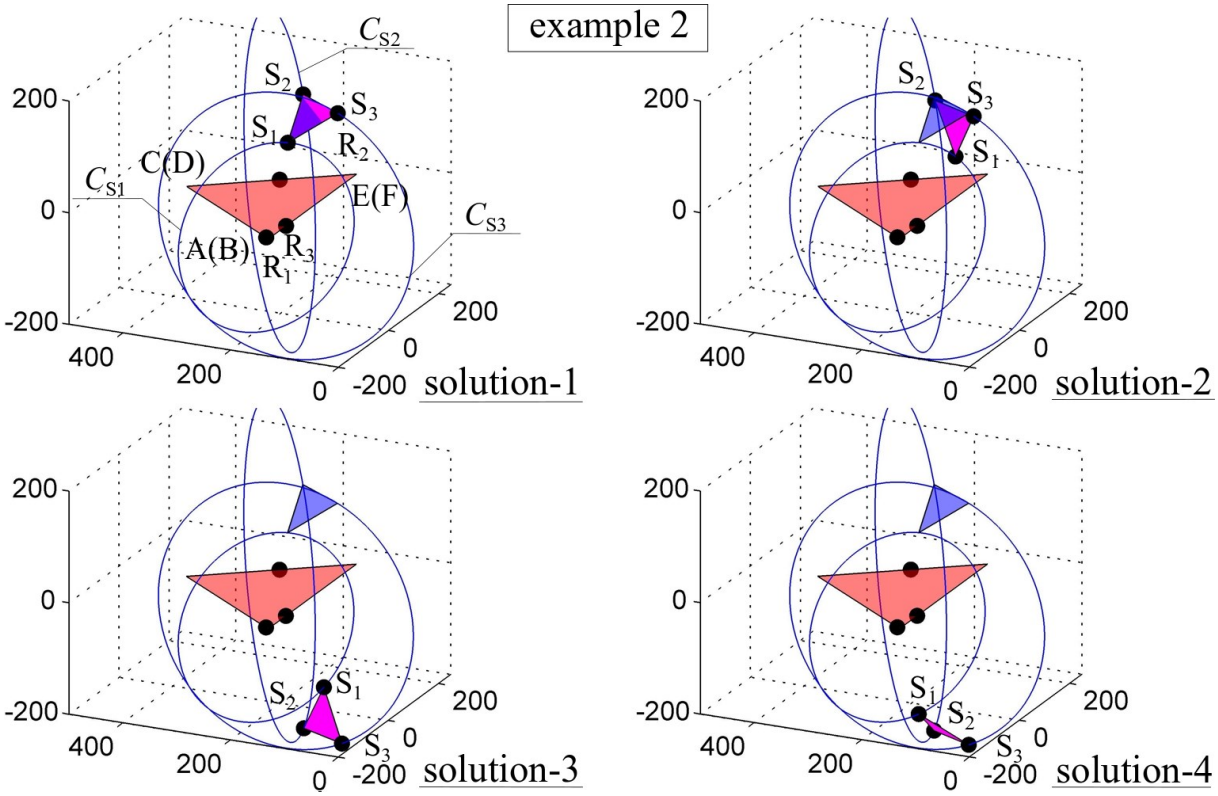

Figure 4.18 Four solutions of the location of the moving platform in numerical example 2. Solutions were shown as purple triangles.

Table 4.2. Four sets of joint variable solutions of an equivalent 2-RS+RSR mechanism.

Example 1					
Variables(◦)		Solution-1.	Solution-2.	Solution-3.	Solution-4.
γ_{R1}		0.722	179.314	181.157	358.860
γ_{R2+}		-3.255	-	-	-2.185
γ_{R2+}	γ_{R3+}	-	-	-	-
	γ_{R3-}	46.249	-	-	34.612
γ_{R2-}		-	-176.745	-177.767	-
γ_{R2-}	γ_{R3+}	-	133.751	144.776	-
	γ_{R3-}	-	-	-	-
Example 2					
Variables(◦)		Solution-1.	Solution-2.	Solution-3.	Solution-4.
γ_{R1}		14.221	41.457	138.802	165.871
γ_{R2+}		40.875	43.132	-	-
γ_{R2+}	γ_{R3+}	-	-	-	-
	γ_{R3-}	-23.885	-26.278	-	-
γ_{R2-}		-	-	-223.047	-220.875
γ_{R2-}	γ_{R3+}	-	-	206.104	203.885
	γ_{R3-}	-	-	-	-

4.7 Chapter Summary and Discussions

In this chapter, the complete kinematic model of CENTAUROB was given. The kinematic relations between every part of links were thoroughly described, including the relation between two parts of linear actuators and the relations between one input and two output ends of a double Cardan joint. These will be the foundation of further kinematic analysis in following

chapters, for example, working space, singularities and agility analysis.

The kinematic model was built in two manners: exponential matrix parameterization and quaternions. Quaternions representation will increase the computation speed as a result of less uses of transcendental functions. Thereby, the real-time capabilities of controller can be strengthened. For rotation matrices, regardless generated by Euler angles, exponential parameterization or others, the regeneration of rotation parameters is always a challenge. This is to say, knowing the rotation matrix, only the pose of the rigid body is recognized, while it is difficult to generate a trajectory along the great circle centric to the rotation centre. In practice, however, the quaternions representation showed its disadvantages during solving the angles of sleeves and shafts of linear actuators. It introduced even more transcendental functions that will thereby decrease the computation speed and reduce the computation accuracy.

The passive rotation problem was discussed in Section 4.4. It is the relative rotation between the sleeve and shaft of a lead screw and will cause the length deviation of the linear actuators. From the simulation result, the deviation was limited in a very small range. In general, the rotation of platforms causes more obvious length compensation demanding than translational motions.

In this chapter, the 1-dimensional FKP solution of 6-SPS mechanism was given and operated in two numerical examples. In each example, 4 solutions were obtained. All these solutions are symmetric to base platform and R_3-S_1-S_2 plane, respectively. All the correct solutions obtained an acceptable error range, from 0.01mm to 0.19mm. This result can be further optimized by decrease the error thresholds and increase iteration cycles.

Reference

[4.1] Merlet, Jean-Pierre. *Parallel robots*. Vol. 128. Springer Science & Business Media, 2005.

[4.2] Gwinnett J.E. Amusement device, January, 20, 1931. United States Patent no 1,789,680.

[4.3] V. E. Gough and S. G. Whitehall, “Universal Tyre Test Machine,” Proceedings of 9th

International Congress FISITA, May 1962, pp. 117-137

[4.4] Zhang, Dan. *Parallel robotic machine tools*. Springer Science & Business Media, 2009.

[4.5] Siciliano, Bruno, Oussama Khatib, and Torsten Kröger, eds. *Springer handbook of robotics*. Vol. 200. Berlin: springer, 2008.

[4.6] Stewart D. A platform with 6 degrees of freedom. *Proc. of the Institution of mechanical engineers*, 180(Part 1, 15):371–386, 1965.

[4.7] Hahn, Hubert. "Mathematical modeling, control, computer simulation and laboratory experiments of a spatial servopneumatic parallel robot." *Nonlinear Dynamics* 40.4 (2005): 387-417.

[4.8] Akima, Toshifumi, Susumu Tarao, and Masaru Uchiyama. "Hybrid micro-gravity simulator consisting of a high-speed parallel robot." Proceedings *1999 IEEE International Conference on Robotics and Automation (Cat. No. 99CH36288C)*. Vol. 2. IEEE, 1999.

[4.9] Asif, Umar. "Design of a parallel robot with a large workspace for the functional evaluation of aircraft dynamics beyond the nominal flight envelope." *International Journal of Advanced Robotic Systems* 9.2 (2012): 51.

[4.10] Huang, Jiung-yao, and Chung-yun Gau. "A PC cluster high-fidelity mobile crane simulator." *Journal of Applied Science and Engineering* 5.1 (2002): 7-20.

[4.11] Howard, R. A., Rosvold, J. M., Darcy, S. P., Corr, D. T., Shrive, N. G., Tapper, J. E., Ronsky, J. L., Beveridge, J. E., Marchuk, L. L., and Frank, C. B. (May 1, 2007). "Reproduction of In Vivo Motion Using a Parallel Robot." ASME. J Biomech Eng. October 2007; 129(5): 743–749.

[4.12] Carbone, Giuseppe, and Marco Ceccarelli. "A serial-parallel robotic architecture for surgical tasks." *Robotica* 23.3 (2005): 345-354.

[4.13] Li, Temei, and Shahram Payandeh. "Design of spherical parallel mechanisms for

application to laparoscopic surgery." *Robotica* 20.2 (2002): 133-138.

[4.14] Tian, Yaobin, et al. "A reconfigurable multi-mode mobile parallel robot." *Mechanism and Machine Theory* 111 (2017): 39-65.

[4.15] Almonacid, Miguel, et al. "Motion planning of a climbing parallel robot." *IEEE transactions on robotics and automation* 19.3 (2003): 485-489.

[4.16] A. Codourey, and E. Burdet. "A body-oriented method for finding a linear form of the dynamic equation of fully parallel robots." *Proceedings of international conference on robotics and automation*. Vol. 2. IEEE, 1997.

[4.17] Staicu, Stefan. "Matrix modeling of inverse dynamics of spatial and planar parallel robots." *Multibody System Dynamics* 27.2 (2012): 239-265.

[4.18] Enferadi, Javad, and Amir Shahi. "On the position analysis of a new spherical parallel robot with orientation applications." *Robotics and Computer-Integrated Manufacturing* 37 (2016): 151-161.

[4.19] Chen, Wei-Hsi, et al. "Design and implementation of an omnidirectional spherical robot Omnicron." *2012 IEEE/ASME International Conference on Advanced Intelligent Mechatronics (AIM)*. IEEE, 2012.

[4.20] Ben-Horin, Patricia, and Moshe Shoham. "Singularity condition of six-degree-of-freedom three-legged parallel robots based on grassmann-cayley algebra." *IEEE transactions on robotics* 22.4 (2006): 577-590.

[4.21] Hao, Kuangrong, and Yongsheng Ding. "Screw theory and singularity analysis of parallel robots." *2006 International Conference on Mechatronics and Automation*. IEEE, 2006.]

[4.22] Frisoli, A., et al. "Synthesis by screw algebra of translating in-parallel actuated mechanisms." *Advances in robot kinematics*. Springer, Dordrecht, 2000. 433-440.

[4.23] Kong, Xianwen, and Clément M. Gosselin. "1. Generation of parallel manipulators with three translational degrees of freedom based on screw theory." *Proc. 2001 CCToMM Symposium on Mechanisms, Machines and Mechatronics, Saint-Hubert, Montreal. See webpage: http://www. cim. mcgill. ca/∼alexvit/SM3/Content. htm*. 2001.

[4.24] Kong, Xianwen, and Cle´ ment M. Gosselin. "Type synthesis of 3-DOF translational parallel manipulators based on screw theory." *J. Mech. Des.* 126.1 (2004): 83-92.

[4.25] Lee, Sungcheul, Qiang Zeng, and Kornel F. Ehmann. "Error modeling for sensitivity analysis and calibration of the tri-pyramid parallel robot." *The International Journal of Advanced Manufacturing Technology* 93.1 (2017): 1319-1332.

[4.26] Cui, Hongliang, et al. "Kinematic analysis and error modeling of TAU parallel robot." *Robotics and Computer-Integrated Manufacturing* 21.6 (2005): 497-505.

[4.27] Perez, Alba, and J. Michael McCarthy. "Dual quaternion synthesis of constrained robotic systems." *J. Mech. Des.* 126.3 (2004): 425-435.

[4.28] Murray, Andrew P., et al. "A planar quaternion approach to the kinematic synthesis of a parallel manipulator." *Robotica* 15.4 (1997): 361-365.

[4,29] Chablat, Damien, et al. "Workspace and joint space analysis of the 3-RPS parallel robot." *International Design Engineering Technical Conferences and Computers and Information in Engineering Conference*. Vol. 46360. American Society of Mechanical Engineers, 2014.

[4.30] Pisla, Doina, et al. "Algebraic modeling of kinematics and singularities for a prostate biopsy parallel robot." *Proceedings of the Romanian Academy, series A* 19.3 (2018): 489-497.

[4.31] Fu, Jianxun, et al. "Kinematic accuracy research of a novel six-degree-of-freedom parallel robot with three legs." *Mechanism and Machine Theory* 102 (2016): 86-102.

[4.32] Pott, Andreas. "An algorithm for real-time forward kinematics of cable-driven parallel robots." *Advances in Robot Kinematics: Motion in man and machine*. Springer, Dordrecht, 2010. 529-538.

[4.33] Morell, Antonio, Mahmoud Tarokh, and Leopoldo Acosta. "Solving the forward kinematics problem in parallel robots using Support Vector Regression." *Engineering Applications of Artificial Intelligence* 26.7 (2013): 1698-1706.

[4.34] Yang, XiaoLong, et al. "A dual quaternion solution to the forward kinematics of a class of six-DOF parallel robots with full or reductant actuation." *Mechanism and Machine Theory* 107 (2017): 27-36.

[4.35] Zhu, Qidan, and Zheng Zhang. "An efficient numerical method for forward kinematics of parallel robots." *IEEE Access* 7 (2019): 128758-128766.

[4.36] Du, Shucen, et al. "Passive rotation compensation in parallel kinematics using quaternions." *PAMM* 16.1 (2016): 51-52.

[4.37] Du, Shucen, et al. "On the origin of passive rotation in rotational joints, and how to calculate it." *PAMM* 19.1 (2019): e201900298.

[4.38] Du, Shucen, et al. "Passive rotation of rotational joints and its computation method." *IFToMM World Congress on Mechanism and Machine Science*. Springer, Cham, 2019.

[4.39] Guo, HongBo, et al. "Cascade control of a hydraulically driven 6-DOF parallel robot manipulator based on a sliding mode." *Control Engineering Practice* 16.9 (2008): 1055-1068.

Chapter 5
Kinematics Analysis of CENTAUROB

In this chapter, the kinematic performance of CENTAUROB will be studied based on its main component, 6-SPS PKM. The kinematic analysis includes divers aspects such as, workspace analysis, manipulability and singularity. Through the kinematic model, the configuration, velocity and acceleration characteristics will be exhibited. By introducing collision conditions and working range of various joints, the workspace with different demanding will be obtained. The velocity manipulability will be illustrated as velocity ellipsoid as well. The singularity will be concerned by means of a special screw indicator for different application scenarios.

5.1 State of the Art

Kinematic analysis is an important aspect of robot investigations. It plays a vital role from the design phase, simulation to robot diagnosis, motion planning and control phase of a robot development. The basis of kinematic analysis is the foundation of Jacobian or inverse Jacobian of a robot system, which is a mapping from joint velocity space to the operational space and has been dissected in the last chapter. There are many considerations of analysing the kinematic, e.g. workspace, manipulability, accuracy, singularity, decoupling, dexterity etc. In this chapter, the main focus will be placed on the former four aspects.

The workspace is an assemble of configurations that the end effector can reach. It is normally constrained by the working ranges of joints, regardless of passive or active ones. According to the definition made by Merlet in [5.1], the workspace can be classified as constant-orientation

workspace, reachable workspace, inclusive workspace, dexterous workspace and total orientation workspace. The manners to obtain workspace include normally geometrical, discrete numerical and non-discrete numerical methods. The main approach of geometrical method to obtain a workspace is by the intersections of boundaries of each limb. This method was explicitly announced by Gosselin in 1989 for the first time ([5.2]) and widely used in earlier workspace researches. Then Merlet has studied the rotational workspace of a 6-DOF PKM in his earlier work [5.3]. Later, Kim and others have provided the workspace of a 6-DOF Gough-Stewart platform. Bonev, et. al. have studied the constant-orientation workspace of a 6-PRRS PKM through geometrical approach in [5.5]. The discrete numerical method is to search the possible positions of a PKM in a specific space under different constraints. The discrete numerical method is to mapping the positions into the joint space through inverse kinematics and to test if the joints are constrained or not. This method is the most intuitionistic and widely used in the workspace studies for present PKMs. With this method, Bonev and Ryu have studied the rotation workspace of a 6-DOF PKM at a fixed position ([5.6]), Lee and Park have given the workspace analysis of a double PKM in [5.7]. In the field of novel PKM development, Gagliardini, et al provided the workspace analysis of a cable-driven PKM ([5.8]), Antonov and Glazunov analysed the workspace of a PKM with limbs penetrating the base platform in [5.9].

There are many error recourses affecting the kinematic accuracy of a PKM, e.g. actuator errors, geometrical errors, thermal errors, computational errors, etc. Among them, the actuator error is the determinant operational error ([5.1]). The interest of accuracy research was initially emphasized on methods based on Jacobian condition numbers. The condition number can be used to represent the upper and lower boundary of the ratio of operational velocity error over actuator velocity error. Further, the Jacobian matrix can be replaced by other matrix to transform other error sources to operational error space, as Ryu et al mentioned in [5.10]. Besides condition numbers, there are some later introduced accuracy indices. In [5.11], Xu and Li introduced error amplification index (EAI), which is a weighted combination of

maximum singular value and the condition number. No matter which method, the condition number should be homogenized, since the different unit of translational and rotational motion can cause fierce change of the norms of a Jacobian matrix.

Manipulability is the ability of velocity and force amplifications, while, sometime, it is used as the positioning error measurement ([5.12]). It reflects not only the amplitude of transmissions, but also the isotropy. The manipulability can often be represented as velocity or force ellipsoid. The principle axes of the ellipsoids illustrate the directional characteristic of the amplification. There are various practices of manipulability ellipsoid in the research of PKMs. For example, Li and Xu have optimized the design of a 3-PSR PKM through the maximum and minimum lengths of the velocity ellipsoid in [5.13]. Withal, Choi et al. have applied manipulability ellipsoid on the optimization of a 4-DOF PKM ([5.14]). Prattichizzo, et al. have analysed the velocity and force ellipsoid of a robotic hand ([5.15]), which was handled as under-actuated PKM while grasping objects.

The singularity of a PKM is a configuration where the mechanism turns instantaneous dysfunctional. Thus, it is a crucial drawback in workspace and should be attentively studied and avoided in the design stage. Gosselin and Angeles have developed the method of determining the singularity by observing the Jacobian matrix in [5.16]. Depending on the direct Jacobian, inverse Jacobian and both, the singularity was classified as type-1, type-2 and type-3. At type-1 singular configurations, the end effector will not move if the actuators move at an infinitesimal scale. If type-2 singularity happens, the end effector can move even the actuators are locked. While both conditions can happen at type-3 singularity. Merlet has studied the singularity problem with help of Grassmann line geometry in [5.17], which can express all the singular configurations with distinct kinematic meaning. Although there are manifold measures of determining and classifying the singularity problem, it is always a predicament to find the global closed-form solution of a PKM with more than 3-DOF. For example, the singularity of a 6-DOF PKM was analytically solved by introducing extra sensors and local structuration method (LSM) in [5.18], a subset of singularities of a 4-DOF

PKM was analytically presented by using Jacobian deficiency in [5.19]. Moreover, a method depending not on Jacobian matrix but on geometric constraint of 6-3 Gough-Stewart platform was developed by Cao et al in [5.21]. In virtue of this method, the analytical solutions of a series special poses (e.g. with z-rotations of$\pm 30^{o}$, $\pm 90^{o}$, and $\pm 150^{o}$ for an equiangular triangle moving platform) were represented. Although this method is not giving the global solutions of singularity of 6-3 Gough-Stewart platform, a new necessary and sufficient condition was proposed and could fulfil the demanding of the singularity analysis of CENTAUROB.

This chapter will be arranged as following: in Section 5.2, the working range of active and passive joints will be analysed in detail and the workspace of one leg of CENTAUROB will be given as consequence; based on different application scenarios, the kinematic performance will be evaluated in two aspects, namely the manipulability and accuracy, through velocity ellipsoids and condition number in Section 5.3; in Section 5.4, the singularity will be analysed, based on four applications scenarios; in Section 5.5., a conclusion will be made.

5.2 Workspace Analysis

Workspace is one of the most important kinematic indices for diverse mechanical mechanisms, including serial and parallel mechanisms. The workspace of a robot is affected by various factors, such as, working range of the actuators, mechanical limits of passive joints, self-collisions of main and auxiliary parts, and also, the split caused by singularities. In this section, the workspace of the passive joints, limitation of actuators and collisions between actuators will be analysed to form workspaces of the whole structure.

5.2.1 Workspace Analysis of Double Cardan Joints

The constraints of a double Cardan joint comprise collisions between axis-3 and the frame of axis-2, between the joint column and limb coupling, between two limb couplings (or between following limbs), and between the vertices of limb couplings and base surface. Due to the

special one-in-two-out structure, the workspace of single output will be firstly considered, followed by the constraint between the two outputs. The workspace of this joint will be divided into 3 sections, and will be described as the ranges of displacements of each axis. Also, only the most rigorous conditions are considered; e.g., if only one limb coupling can reach one certain position while the other one cannot, the position will be excluded from the workspace of both. In addition, inside workspace sections, all the axes should move symmetrically in both directions, and the sections should be wide enough to accommodate the specific tolerances. Otherwise, if the symmetrical characteristic of axes motion is lost, the workspace must be discussed in 4 or 8 quadrants, which increases the computation quantity without significant expansion of workspace.

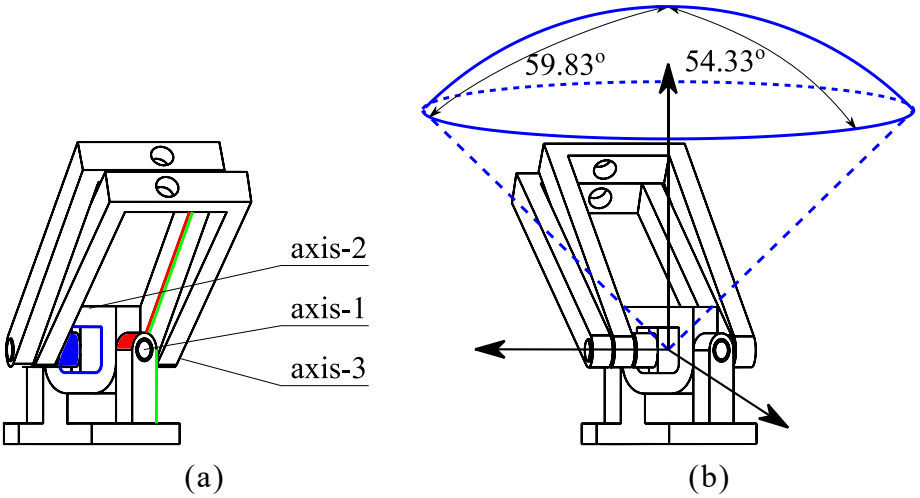

Figure 5.1 (a) The first group of collision conditions of a double Cardan joint on extreme positions and (b) its corresponding workspace section.

1) Workspace Section-1

The limb couplings are allowed to revolve around axis-3 until they collide with the ground or other entities. The first collision takes place when their inner edge meets the upper boundary surface of the holding column, coloured as red in fig. 5.1(a). At this position, axis-2 reaches its extreme displacement, since the collision happens between axis-3 and the frame inner edge of axis-2, coloured blue in the figure. If axis-1 rotates so that the red edge slides along the red surface until the it meets the vertical edge of the holding column, coloured green, the extreme displacement of axis-1 will be reached. This section can be roughly described as an oval cone

with a sphere cap, as illustrated in fig. 5.1(b), which obtains a half major angle of 59.83° and a half minor angle of 54.33°.

2) Workspace Section-2

Fig. 5.2(a) illustrates another extreme position outside of workspace section-1. If the displacement of axis-3 exceeds the range of ±54.33°, the inner edge of limb coupling could collide with the vertical edge of holding column before the *blue* collision in fig. 5.1(a) took place. Thus, under this condition, the working range of axis-2 is reduced to ±7.99°, and the collision is coloured green. The motion of axis-3 will not cease until the apex of this limb coupling, or its neighbour, collides with the ground. For this extreme position, the working range of axis-3 is ±37.19°. The workspace section-2 of one output shaft of double Cardan joint can be illustrated in fig. 5.2(b) as the cladding area formed by blue lines.

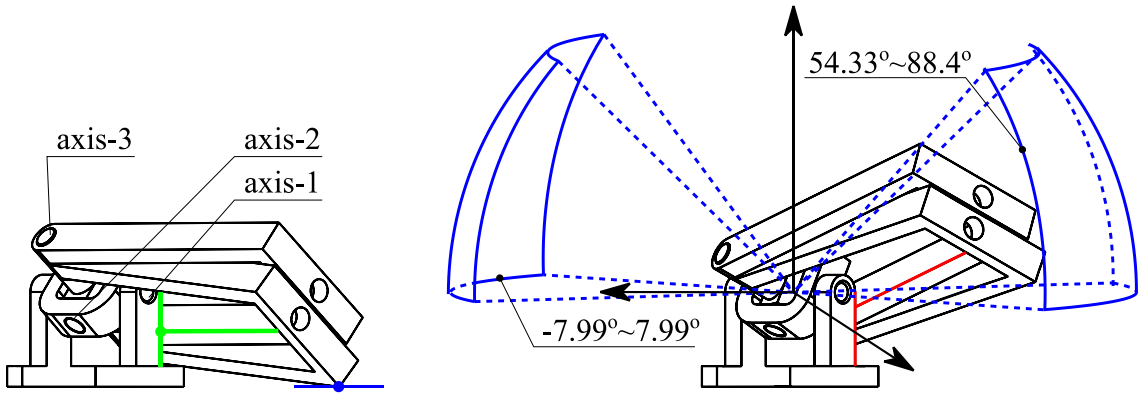

Figure 5.2 (a) The second group of collision conditions of a double Cardan joint on extreme positions and (b) its corresponding workspace section.

3) Workspace Section-3

From the architecture of the joint, the motion ranges of axis-1 and axis-3 are obviously wider than that of axis-2. Thus, it is more reasonable to limit the range of axis-1 and -3 to avoid collisions. If the displacement of axis-1 exceeds the aforementioned two ranges and is over 70.13° or under -70.13°, axis-3 will be limited inside the space between the two vertical surfaces formed by two holding columns, seeing fig. 5.3(a). In this case, axis-2 can move between ±26.08°, while axis-3 can move only between 2.16° and 6.52°. Otherwise, the limb

coupling vertex and the ground, or the outer edge of limb coupling and inner vertical surface of holding column will collide. If the motion of axis-1 is limited inside ±68.13°, the range of axis-3 will be extended to at least ±40.79°. Outside this range, the *blue* or *green* collision in fig. 5.3(a) could take place. Thus, the workspace of this section can be abstracted as two symmetric sphere parts, as shown in fig. 5.3(b).

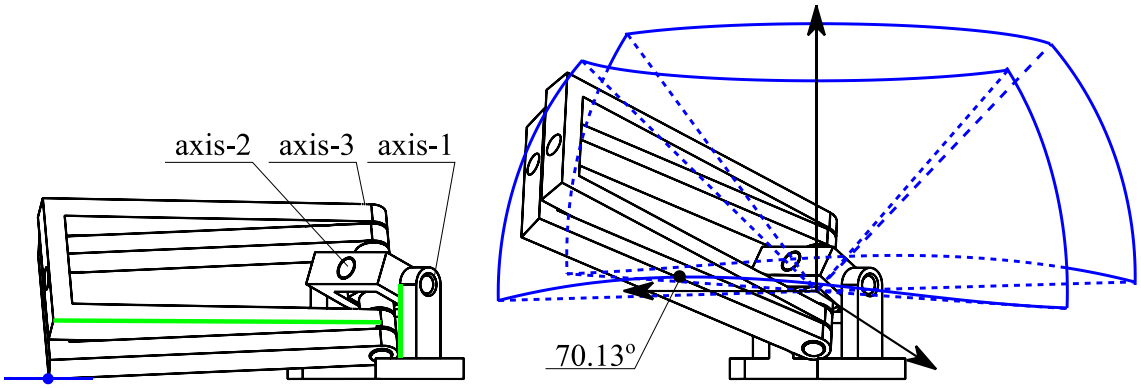

Figure 5.3 (a) The third group of collision conditions of a double Cardan joint on extreme positions and (b) its corresponding workspace section.

Table 5.1 Three workspace sections of double Cardan joints and their corresponding joint parameters.

	Axis-3	Aixs-2	Axis-1
Section 1	[-54.33°, 54.33°]	[-30.04°, 30.04°]	[-59.83°, 59.83°]
Section 2	[-88.40°, -54.33°]∪ [54.33°, 88.40°]	[-7.99°, 7.99°]	[-37.19°, 37.19°]
Section 3	[-40.79°, 40.79°]	[-26.08°, 26.08°]	[-70.13°, -59.83°] ∪[59.83°, 70.13°]

4) Workspace Summary for Double Cardan Joint

From the former analysis, 3 sections of workspace are given and listed in table 5.1. There exist overlaps between sections, which ensures the motion continuity of joints. The three

sections can be merged as a part spherical shown in fig. 5.4. The boundary of the workspace is marked as a red curve. This area was obtained under the design above. Through optimization of its mechanical components, the workspace could be further extended.

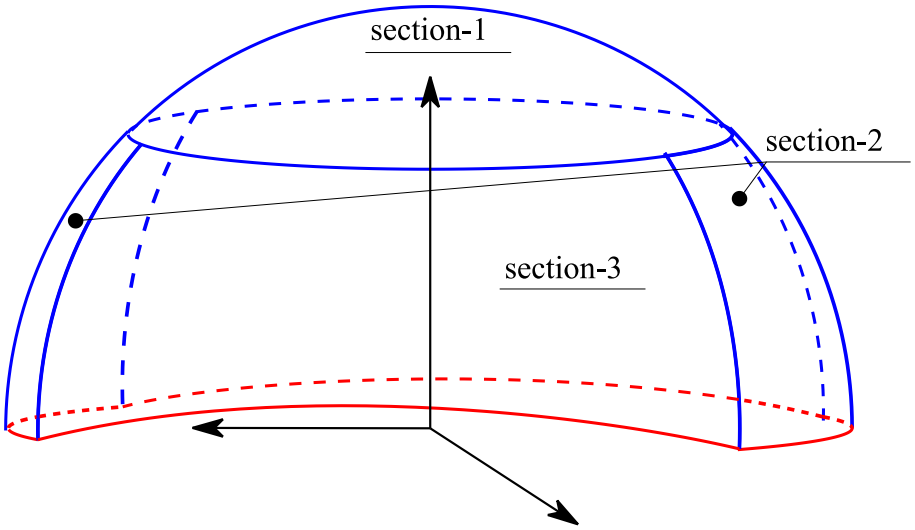

Figure 5.4 The whole workspace of a double Cardan joint as a part sphere range formed by three workspace sections.

Except the listed areas, there exist divers aspects of possible configurations. For example, in fig. 5.5(a), axis-2 was limited in a narrower range, and the motion range of axis-3 lost its symmetrical characteristic without obviously expanding workspace. The blue and red areas on the sphere represent different workspaces under different positions of axis-2. These areas were thus neglected. Another workspace was excluded for the same reason and is shown in fig. 5.5(b). Besides the asymmetries, the possible collision between the following limbs and the ground should also be taken into account, thus, the workspace of the joint should not exceed the north semi-sphere w.r.t the present coordinates. It should be noted that the workspace was originated for only one of the two output ends of the joint. The output orientations of the two ends belong to a 4-dimensional space and could be challenging to illustrate it in a 3 dimensional figure. The motions of asxis-1 and -2 were determined by orientation of two output ends. Despite this, the workspace constraints in table 5.1 still stand, since they are the necessary conditions for a collision free motion.

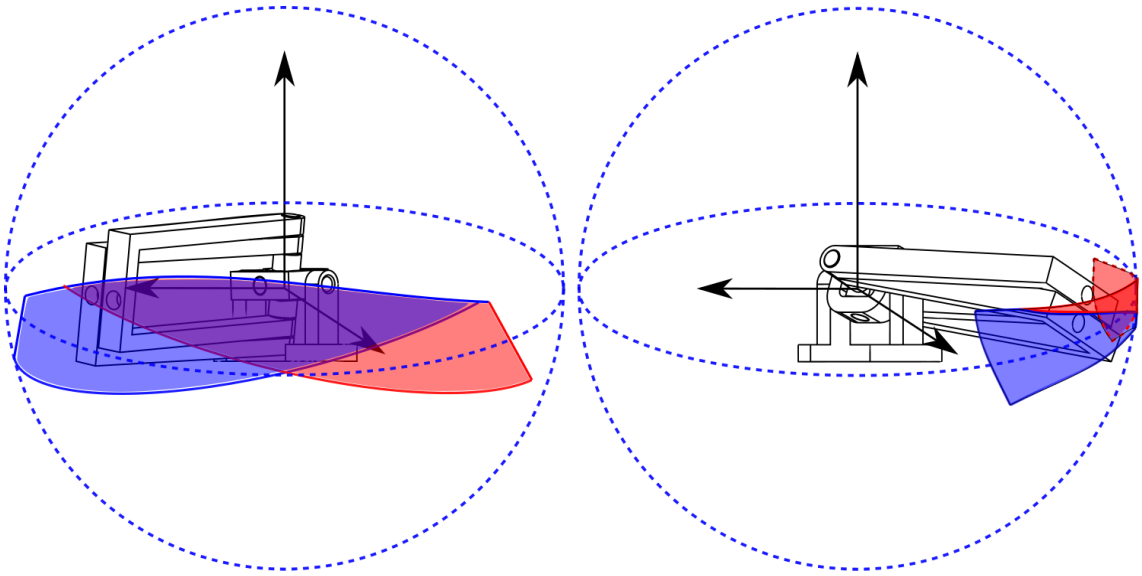

(a) (b)

Figure 5.5 The excluded working areas of the double Cardan joint. The red and blue zones illustrate the positions where the axis-3 can reach under different displacement of axis-2. The overlapped purple area can be reached for two configurations of axis-2, however, they are not connected since the two configurations are not continuous.

5.2.2 Workspace Analysis of Cardan Joints

The universal joint is also known as Cardan joint, named after its inventor. It is a typical non-constant velocity joint and formed by three parts: input and output hinges, and one cross shaft. To compromise the dilemma of structural strength and workspace of a Cardan joint, the profile of it should be optimized. In this case, the Cardan joint in fig. 5.6(a) was adopted. Its topological structure is straightforward and obtains two orthogonal axes, named as axis-1 and axis-2. For the present design, working range of axis-2 should be equal to the displacement of axis-1. The working space of this Cardan joint is illustrated by the blue area in fig. 5.6(a) and the real measurement can be found in fig. 5.6(b).

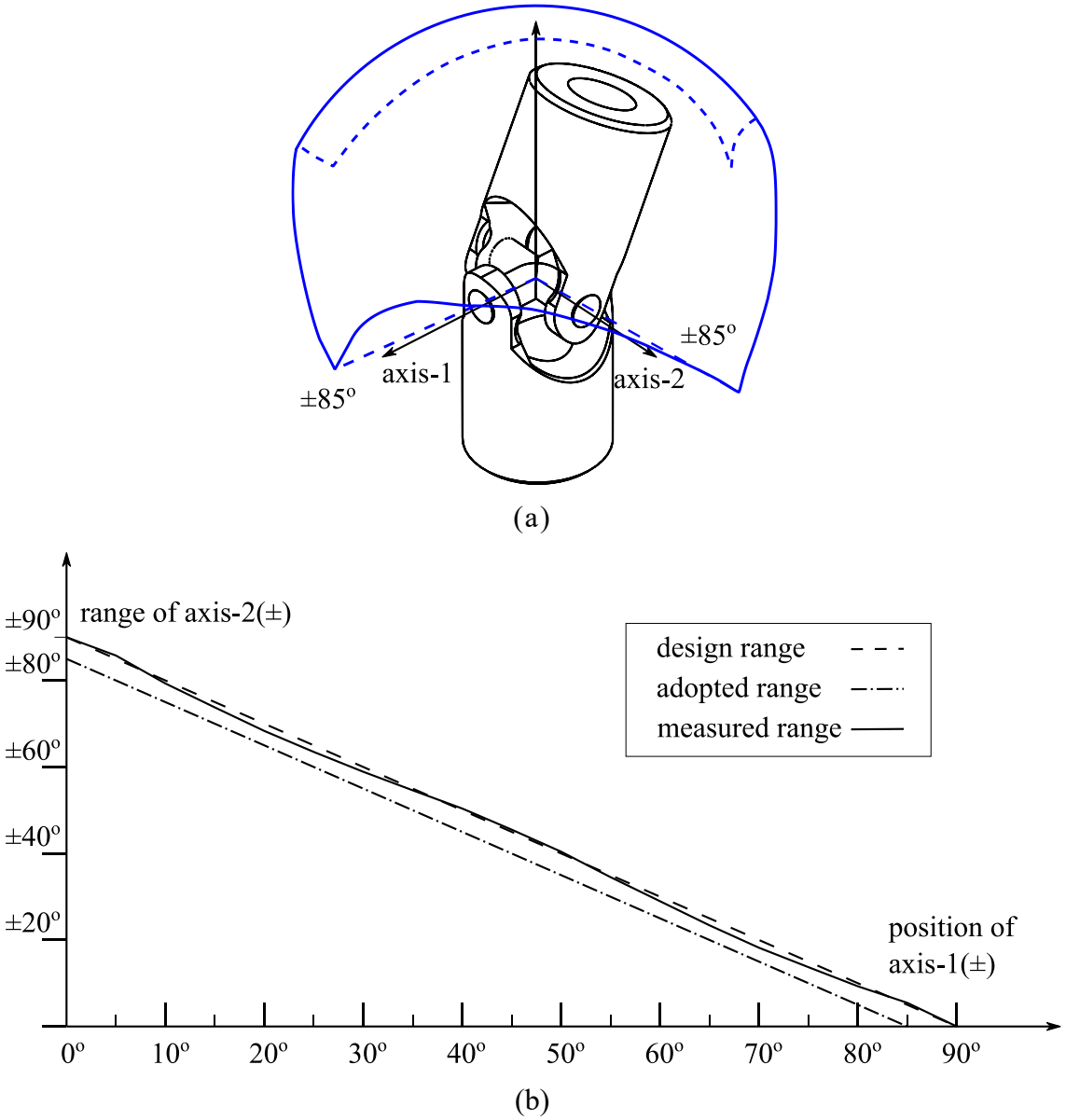

Figure 5.6 The workspace of a Cardan joint (a) in 3-dimensional space. (b) The measured, design and fitted working range of axis-2 over axis-1.

5.2.3 Working Range and Profile Constraints of Actuators

1) Workspace on Sleeve Ends

In this design, the lead screw linear actuators were used. The overall dimensions of it can be found in fig. 5.8. For the convenience of kinematic analysis, it is the most instinctive strategy to arrange the 6-SPS mechanism as a 3-3 PKM form. That will ease the computational burden for singularity analysis and increase the installation precision. Unfortunately, considering the

installation dimension of solidary lead screws, utilization of double Cardan joint on the sleeve side could be troublesome. A 6-3 PKM deployment with Cardan + double Cardan was adopted in this case, as illustrated in fig. 5.7.

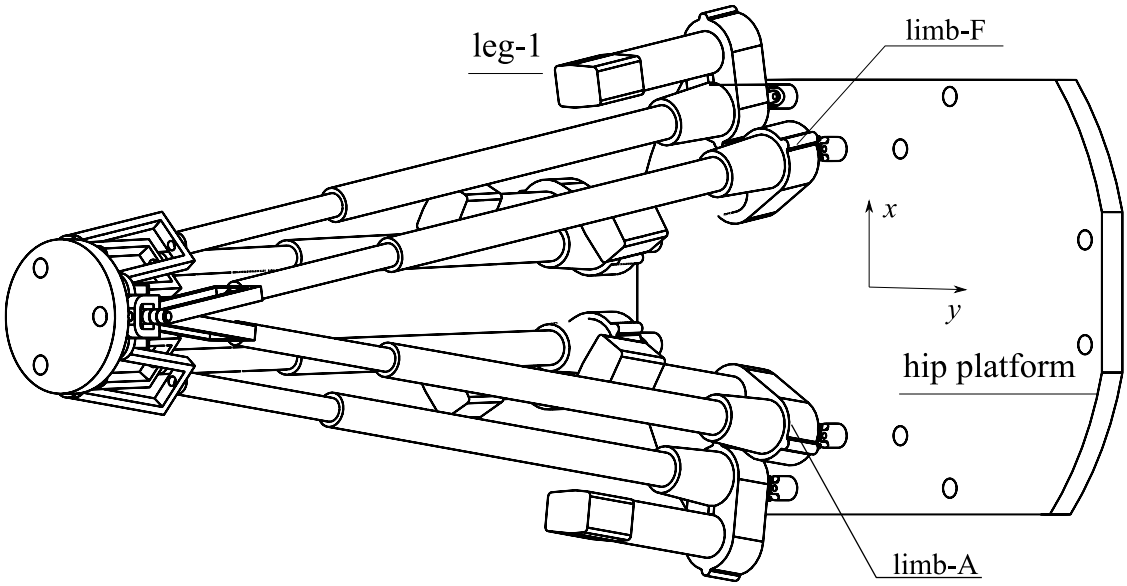

Figure 5.7 The possible joints deployment of a 6-3 PKM. To avoid the collision between two legs, limb-A and –F should be mounted oppositely.

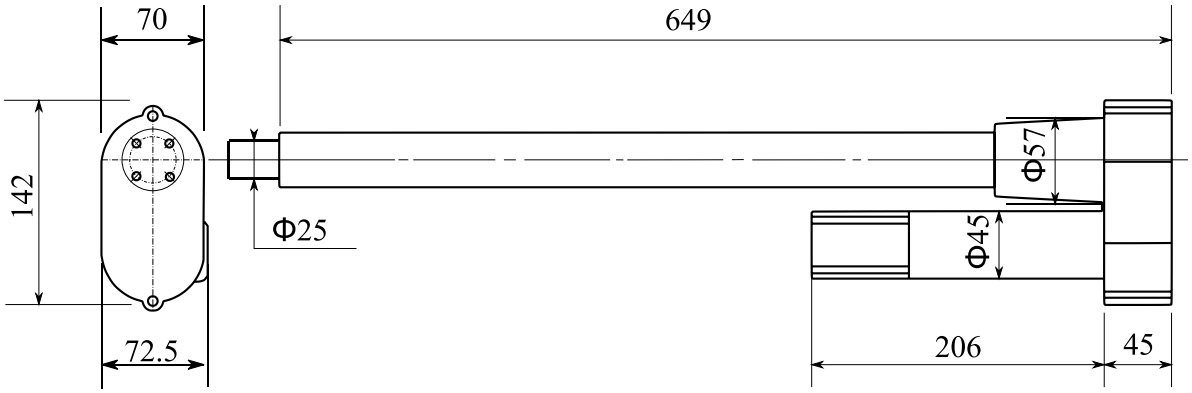

Figure 5.8 Overall dimension of linear actuators (UBA0).

The installation of double Cardan joint on the sleeve side is invalid. In fig. 5.9(a), for example, the angle is limited bigger than 27.14^{o}, and the minimum distance of the two ends of lead screws is 335mm. That is obvious an invalid design to form a reasonable moving platform on the shaft side of lead screws. Even if considering a linearly mounted motor, its smallest profile size is still more than 36mm, this permits a confined workspace for the two output ends. In fact, no matter parallel or linearly arranged motors, the angle between two output

ends of a joint will be limited in a big range. For a workspace up to 1000mm, the minimum angle between two output ends will reach 5.756°, as illustrated in fig. 5.9(b). This requires a lead screw, which obtains a maximum profile smaller than 42.05mm on its narrowest side.

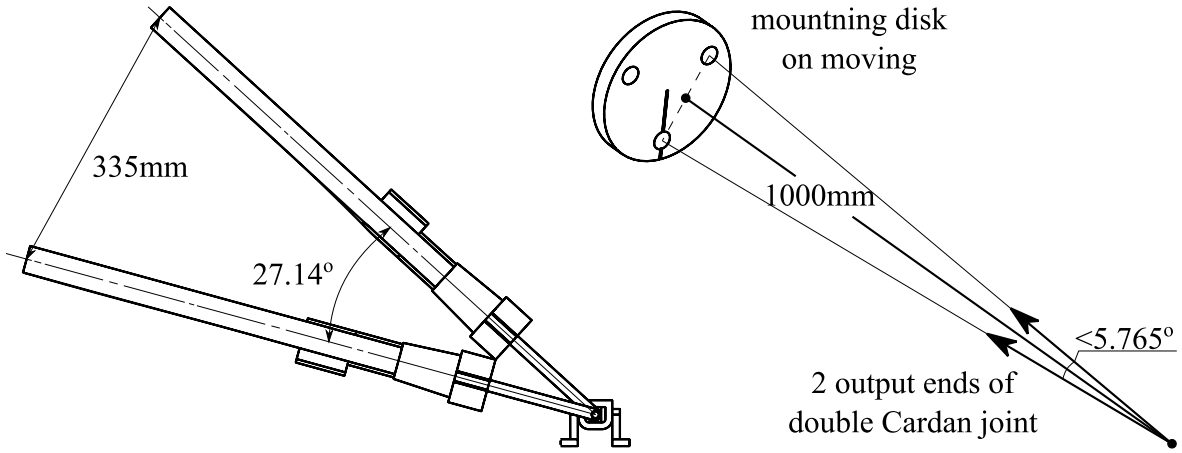

Figure 5.9 An invalid design of joints on sleeve ends of linear actuator: (a) the minimum flare angle is up to 27.14°; (b) the minimum flare angle of a 3-3 PKM design must be smaller than 5.765°.

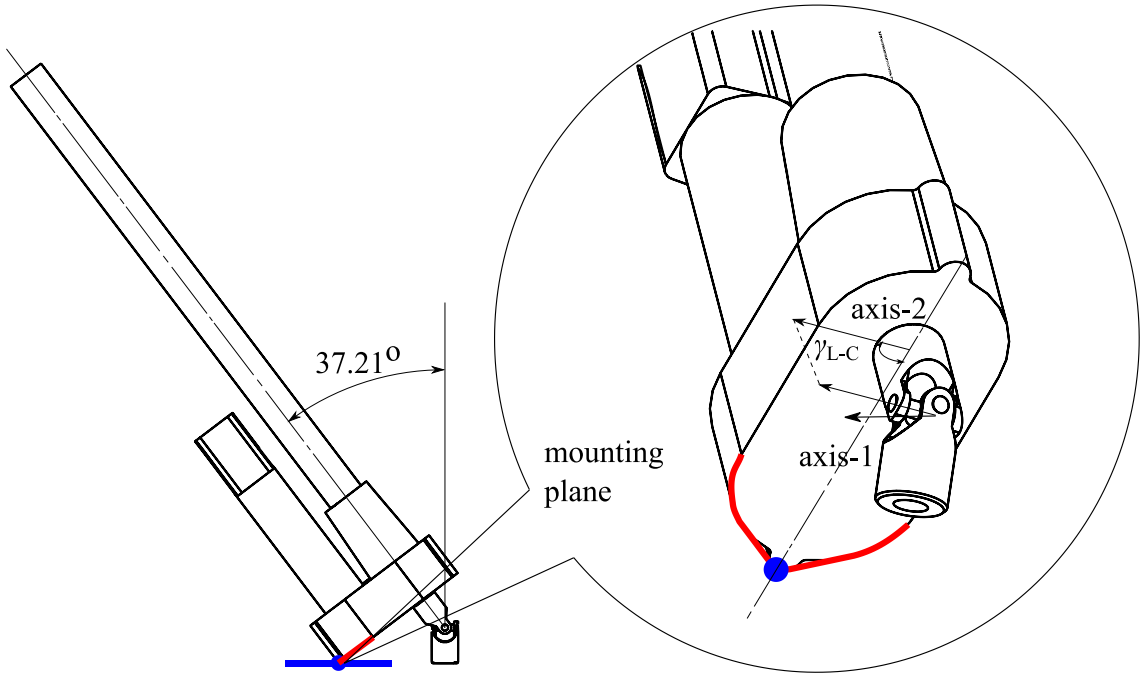

Figure 5.10 The collision condition and colliding profile of sleeve end with hip platform when $\gamma_{L\text{-}C} = 0°$.

For a PKM[6,3] deployment, to ensure the maximum motion range along x and y direction of the lead screws, the Cardan joints are so installed that their axis-1s are along the x-direction of

the hip platform. Due to the size of parallel mounted motor, the part of the profile, coloured as red, could collide with the ground surface, coloured as blue in fig. 5.10. These collisions happen only on limb -A and -F. The mounting angle, $\gamma_{L\text{-}C}$, is the determinant parameter to the decreasing of workspace shown in fig. 5.6.

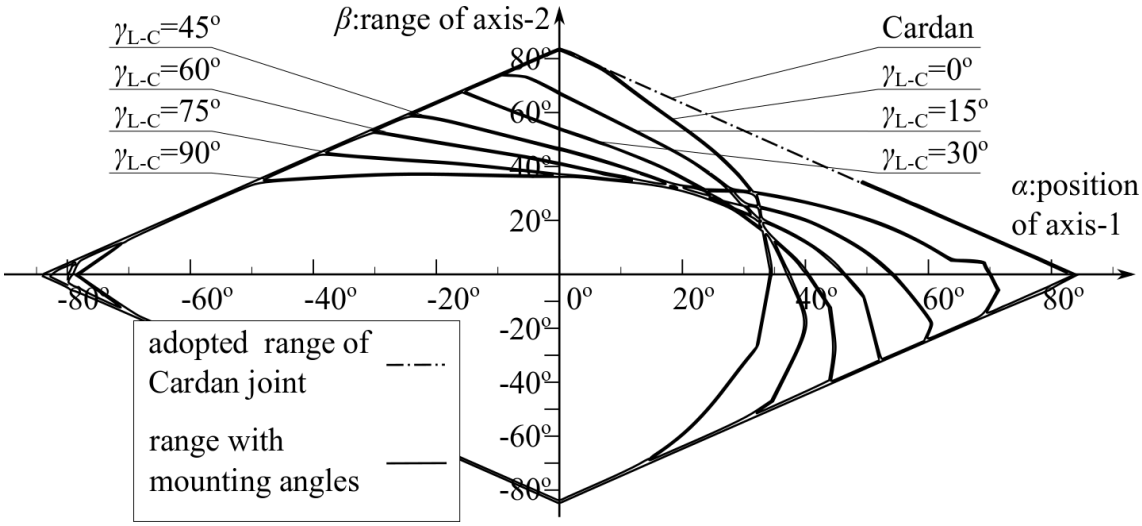

Figure 5.11 The working ranges of axes-2 over axes-1 under different $\gamma_{L\text{-}C}$.

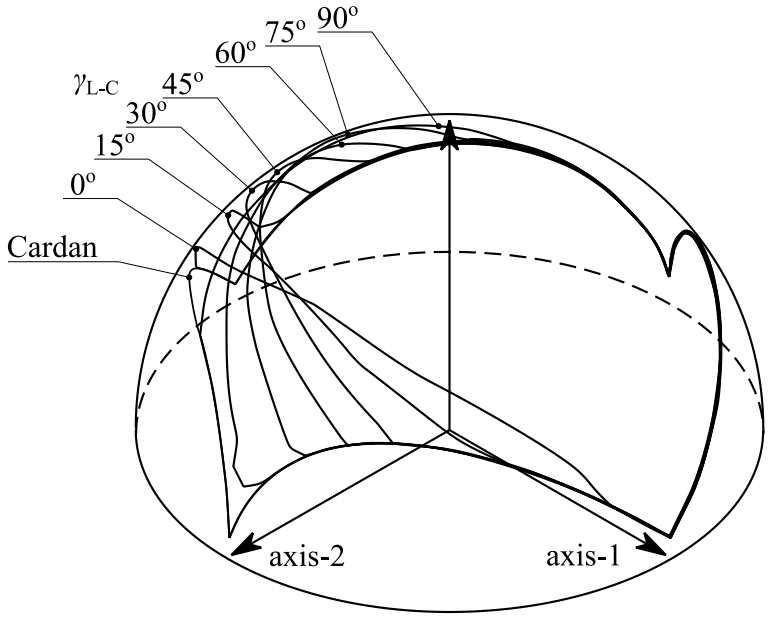

Figure 5.12 the representational working ranges of Cardan joints with angularly different mounted linear actuator sleeves.

Fig. 5.11 shows the detailed work ranges of two axes of a Cardan joint under different mounting angles. These ranges were obtained considering the red profile in fig. 5.10. The working ranges are given in fig. 5.12. Both illustrations show that the mounting angle will

cause loss of working range either in axis-1 or -2 direction, depending on the required working area. To avoid the collision between limbs and between legs, the linear actuators on limb -C and -D are mounted with $\gamma_{L\text{-}C}$= 60º and 120º, while axis-1 are along the *y* direction of the hip platform, as shown in fig 5.7. The working range of a Cardan joint with lead screw can be fitted as shown in fig 5.13(a) and expressed in eq. (5.1). For the computation efficiency, the fitted curve was limited in maximum 2nd order. For limb -A and -F, due to the difference of installation angle, the working ranges of corresponding Cardan joints are reversed. Taking leg-1 as example, the installation angles are $\gamma_{L\text{-}C1A}$ and $\gamma_{L\text{-}C1F}$. Their working ranges can be found in fig. 5.13 (b, c).

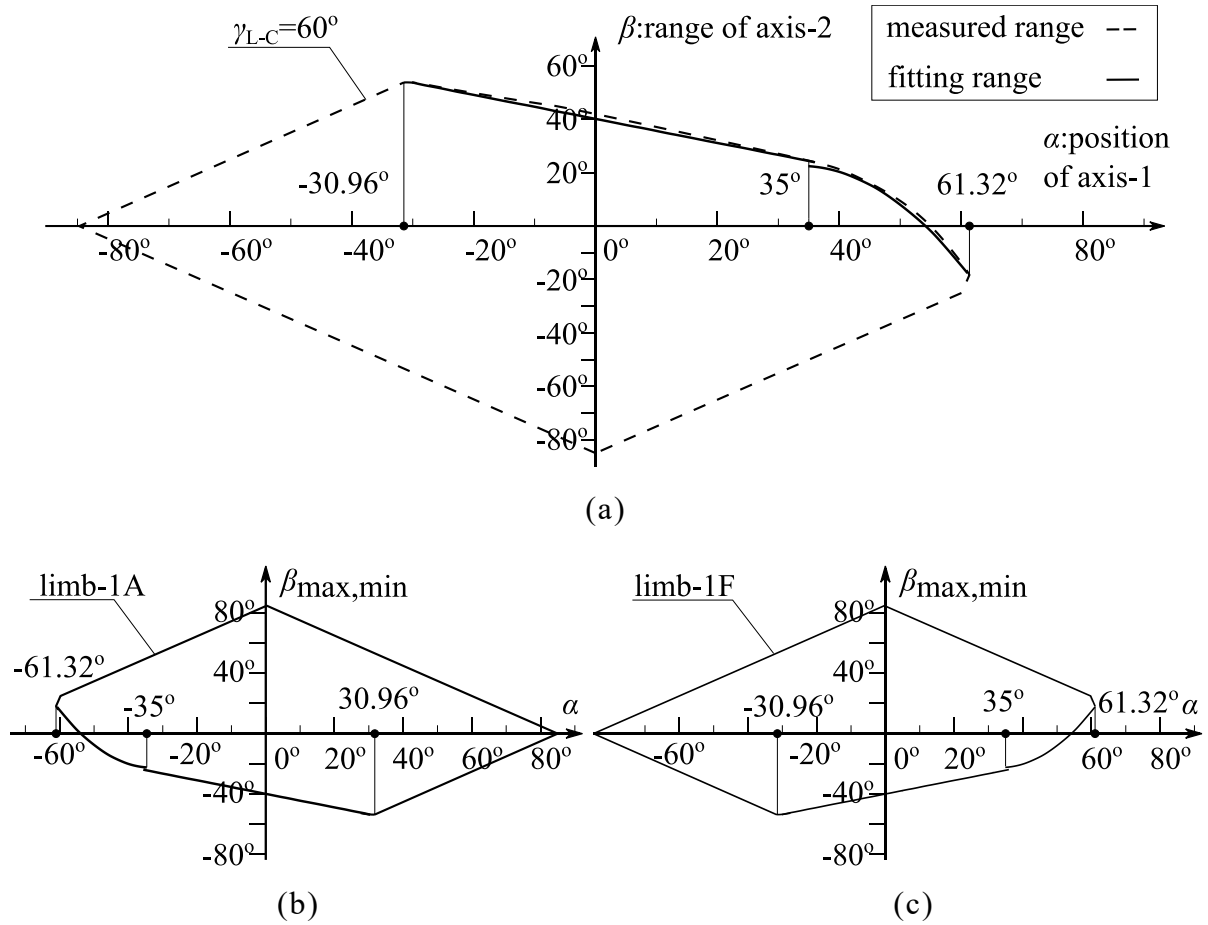

Figure 5.13 The general fitted working range curve of Cardan joints with linear actuators (a) under 60º mounting angle and its projections on (b) limb-1A and (c) limb-1F.

$$\beta \begin{cases} \geq \begin{cases} -85^\circ - \alpha & [-85^\circ, 0^\circ], \\ \alpha - 85^\circ & (0^\circ, 85^\circ]; \end{cases} \\ \leq \begin{cases} \alpha + 85^\circ & [-85^\circ, -30.96^\circ], \\ 40^\circ - 0.45\alpha & (-30.96^\circ, 35^\circ], \\ -\frac{1}{19}\alpha^2 + 3.516\alpha - 36.23 & (35^\circ, 61.32^\circ] \end{cases} \end{cases} \tag{5.1}$$

2) Workspace on Shaft Ends

Contrarily to the sleeve ends of lead screws, the shaft ends are much narrower and obtain isotropy on different directions. Thus, they were connected to the moving platform with double Cardan joints, as illustrated in fig. 5.7. Seeing fig. 5.14, the minimum angle of the two output ends should be bigger than 9.85º. In the workspace of double Cardan joint in fig. 5.4, there will be no collisions between lead screw shaft and the moving platform.

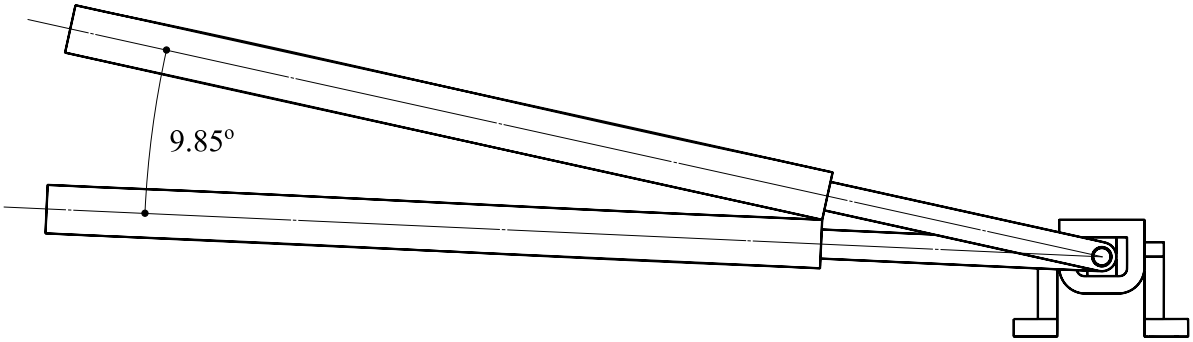

Figure 5.14 The minimum flare angle of shaft ends on double Cardan joint.

3) Workspace of Lead Screws

The nominal stroke of a lead screw is 400mm, however, the practical measurement is around 440mm. Here, the stroke was adopted as 420mm. The rest shaft part outside the sleeve is 32mm. Including the length of Cardan joint and the frame of double Cardan joint, the working space of a lead screw is between 860mm~1280mm.

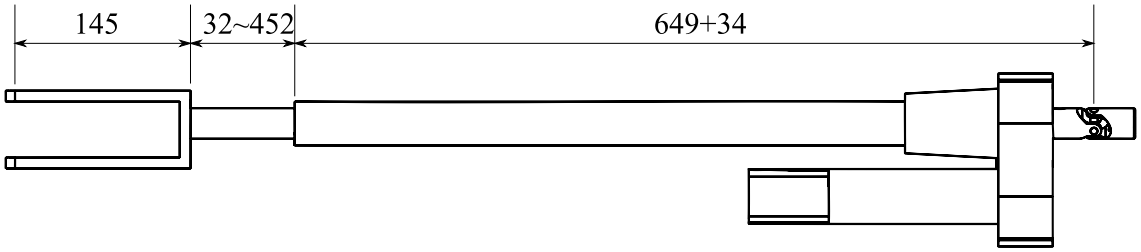

Figure 5.15 The dimensional working range of lead screws.

5.2.4 Workspace of One Leg

The workspace analysis is a vital aspect of kinematic analysis and the precondition of gait patterning of walking mechanisms. As former discussed, the collision conditions for different joints are also different. The biped walking mechanism, CENTAUROB, comprises of two legs. Each leg contains two platforms, 6 linear actuators, 6 Cardan joints and 3 double Cardan joints. The workspaces of the main parts were analysed in last subsections. In this subsection, the workspaces will be summarized as one leg. A discrete searching method will be used and the whole workspace will be sliced in a series of sub-workspaces.

1) Workspace Requirements

Based on the mission properties, namely, pace transporting with ability of slope-climbing and turning, the workspace of one leg should meet following demands:

1) The moving platform should obtain lengthy move ability in x direction (forward and backward).

2) The moving platform should obtain certain move ability in y direction (side direction).

3) The moving platform should obtain certain rotation ability in its own x-y surface to adapt various terrains with different inclination degrees.

4) The turning of robot will take place only when the robot stays standing. This means the relative rotations between two platforms along z direction will happen only when the two platforms obtain an identical x-y location.

5) Any collisions should be avoided, referring the aforementioned subsections.

Thus, the 6-dimensional workspace of the moving platform can be divided into 3 modes: standing, agile reachable and constant-orientation reachable. In the standing mode, the z-rotation ability will be verified for different height. For an agile reachable mode, the x-y rotation ability of the moving platform at different locations will be studied. A constant-orientation reachable workspace is a space including all the locations where the

moving platform can reach with some certain poses. Concerning the practical demands in this case, the constant-orientation reachable mode is limited to a horizontal pose of the moving platform, corresponding for a walking process on a flat surface.

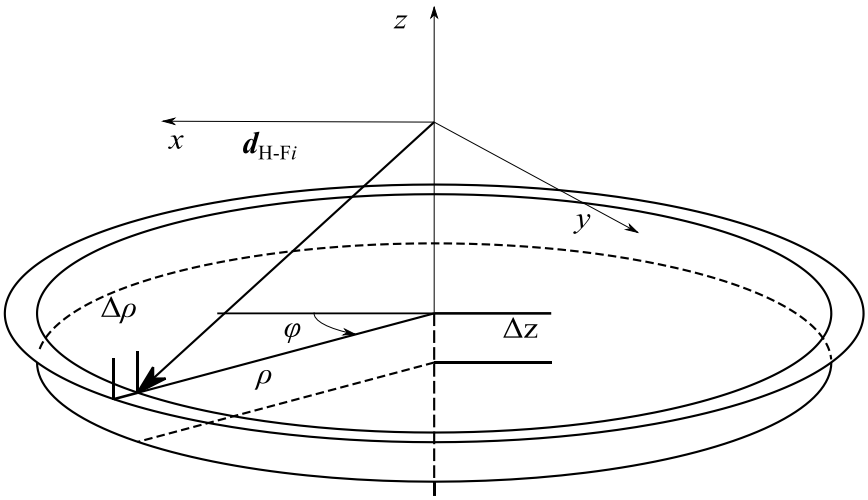

Figure 5.16 The searching algorithm in a 3-dimensional space defined by the translational displacement of moving platform. The displacement is $\boldsymbol{d}_{\text{H}-\text{F}i} = [\rho\cos\varphi \quad \rho\sin\varphi \quad z]$.

Through the inverse kinematics, the pose and position points will be converted to axis rotation angles for each joint. The angles will be checked according to joints working ranges listed in last subsections. For a Cardan joint, the axis motion can be calculated through equation (4.18), hereby, it is recalled as

$$\begin{cases} \beta_{\text{H}-\text{sleeve}ij} = \sin^{-1}{}^{\{\text{C}\}}l_{ijy}, \\ \alpha_{\text{H}-\text{sleeve}ij} = \tan^{-1}\left(\dfrac{{}^{\{\text{C}\}}l_{ijx}}{{}^{\{\text{C}\}}l_{ijz}}\right). \end{cases} \tag{5.2}$$

${}^{\{\text{C}\}}l_{ijx}$ ${}^{\{\text{C}\}}l_{ijy}$ and ${}^{\{\text{C}\}}l_{ijz}$ are the entries of ${}^{\{\text{C}\}}\boldsymbol{l}_{ij}$, its definition can be found in equation (4.10) and with respect to the Cardan joints' coordinates, {C}. The axis motions of axis-3, -1 and -2 of double Cardan joint A-F can be obtained through equation (4.20). Here, it was recalled as

$$\begin{cases} \gamma_x = \sin^{-1} \dfrac{e_{iAy}}{\sqrt{1 - {y_{xi\mathrm{AF}}}^2}} \\ \gamma_y = -\tan^{-1}\left(\dfrac{z_{xi\mathrm{AF}}}{x_{xi\mathrm{AF}}}\right) \\ \gamma_z = \sin^{-1} y_{xi\mathrm{AF}} \end{cases} \tag{5.3}$$

2) Workspace Searching Algorithm

Hereby, the eq. (4.3) and (4.4) will be retrospect. The translational displacement, $\boldsymbol{d}_{\mathrm{H-F}i}$, will be surveyed in different heights, z_i. For each height, circular searching ranges with increasing radius, ρ, will be analysed. The searching variable, φ, is in a range between 0 to 2π. At the end, a boundary at this height will be generated. In the neighbourhood of this boundary, the searching step length, $\Delta\rho$, will be decreased to refine the boundary curve. This process is illustrated in fig. 5.16.

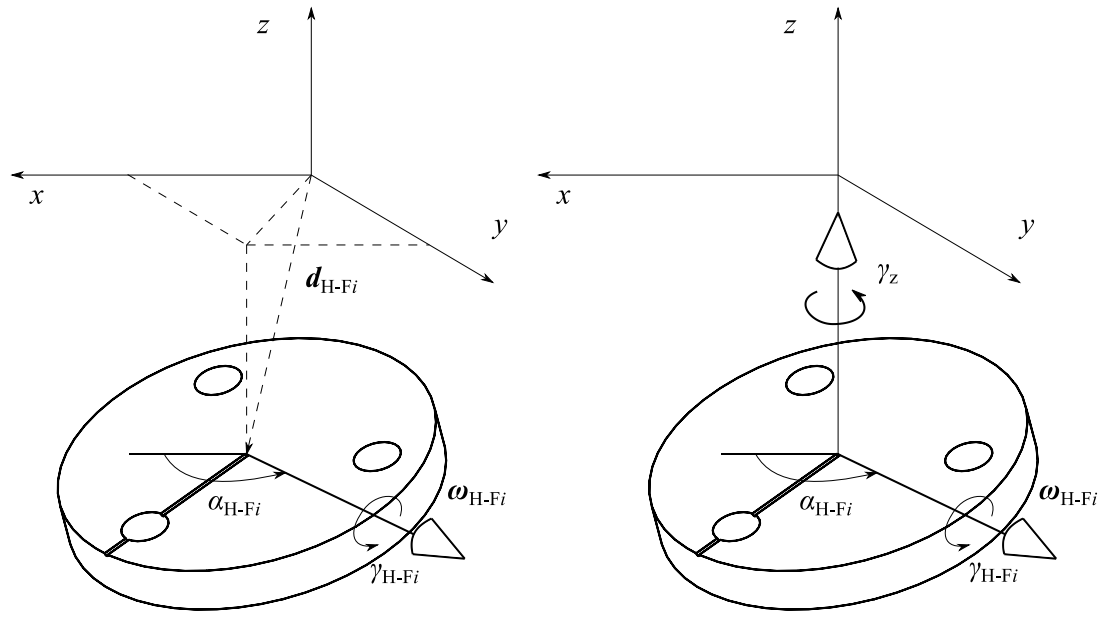

Figure 5.17 The agile workspace searching algorithm of rotational displacements around axis (a) on *x*-*y* plane (e.g. swinging and landing of moving platform) and (b) in 3-dimensional space (e.g. standing spinning).

For an agile reachable workspace, at each position in fig. 5.17(a), the moving platform should operate rotations around an axis on *x*-*y* plane. Referring eq. (4.6), it corresponds to rotations

with $\beta_{\mathrm{H-F}i} = 0$, while for a constant-orientation reachable workspace, $\boldsymbol{\omega}_{\mathrm{H-F}i} = \mathbf{0}$. In a standing mode, the moving platform should be able to rotate around z-axis for different pose of the moving platform, as shown in fig. 5.17(b).

In summary, the boundary searching process starts with a height, $z_{\min}$. The points at this height will be checked for the collision conditions in a circular sequence. All the points, at which the moving platform can operate certain rotations, belong to an agile workspace, otherwise, they belong to a constant-orientation workspace. The process is described as a flowchart in fig. 5.18.

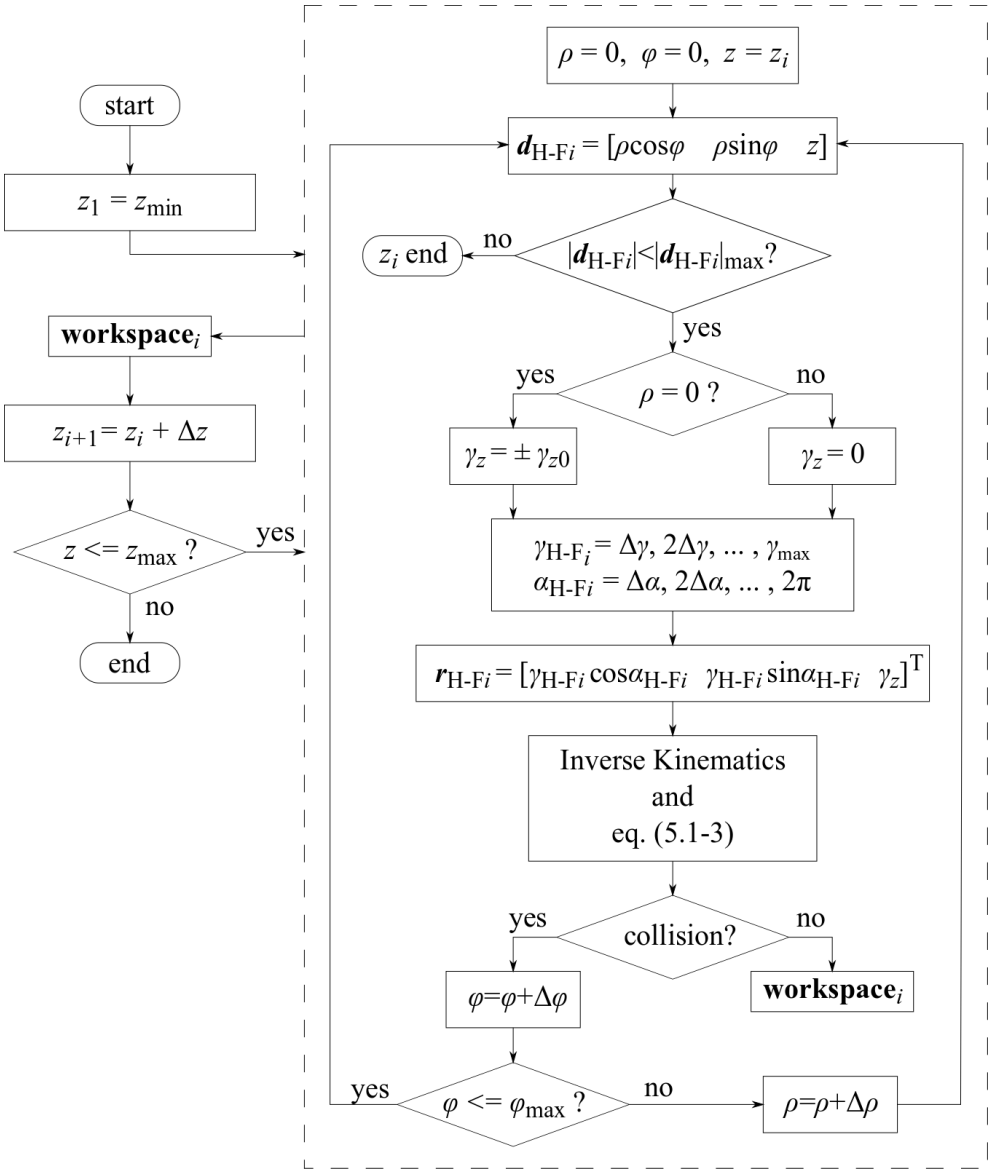

Figure 5.18 The flowchart of the workspace searching process.

3) Collision Conditions

As described in advance, the workspace was constrained by the collision conditions inside one leg. Besides, the collision between legs is not referred in this part and will be concerned in the trajectory planning parts. The necessary conditions can be summarized as three parts:

1) The length of one limb should not exceed the range between 860mm and 1280mm.

2) The axis angles of Cardan joints should not exceed the range shown in fig. 5.6, especially for limbs -A and -F, the axis angles should obey the constraint shown in fig. 5.13 and eq. (5.1).

3) the axis angles of double Cardan joints should in the range of table 5.1 and the angle between two ends should be bigger than. 9.85°.

For each pose and position, when one or more conditions were not fulfilled, this point will be excluded from the workspace.

4) Case Study of Workspace

For an acknowledgment of the workspace of one foot in general, a case study in the whole possible space was made. The ranges of searching parameters can be found in table 5.2. Due to the limitation of the length of linear actuators, the searching radius was limited less than 1280mm.

Table 5.2 The workspace searching variables of one leg of CENTAUROB.

$\boldsymbol{d}_{\mathrm{H-F}i}$			$\boldsymbol{r}_{\mathrm{H-F}i}$		
z	ρ	φ	$\max(\alpha_{\mathrm{H-F}i})$	$\max(\gamma_{\mathrm{H-F}i})$	$\max(\gamma_z)$
$[-1280 \quad -860]$	$[0 \quad 1280]$	$[0^\circ \quad 360^\circ]$	$360^\circ \quad (agile)$ $0^\circ \quad (const.)$	$30^\circ \quad (agile)$ $0^\circ \quad (const.)$	$30^\circ \quad (\rho = 0)$ $0^\circ \quad (\rho \neq 0)$

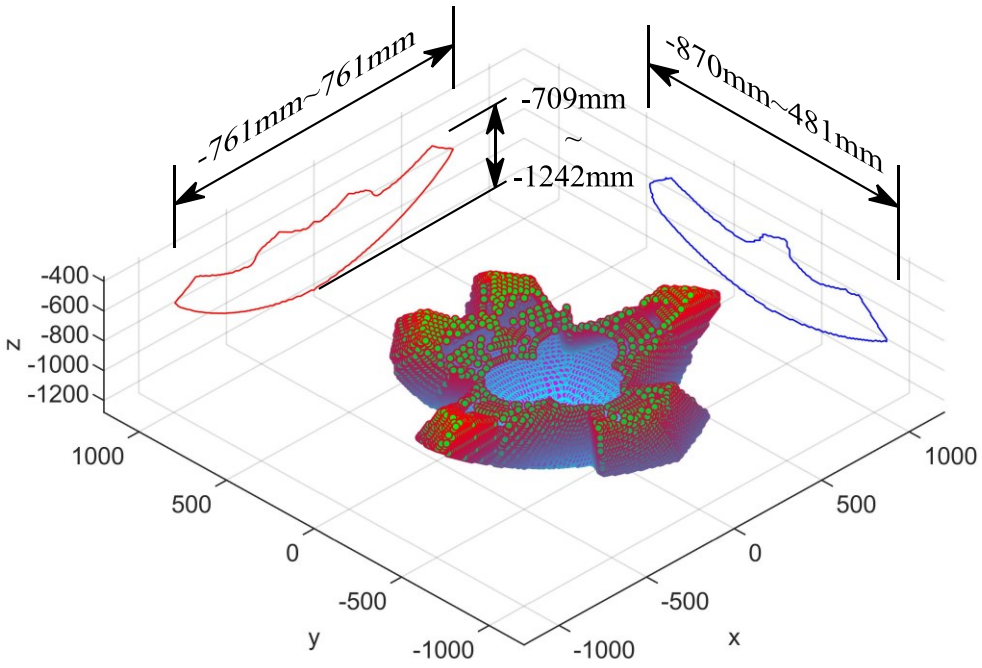

(a)

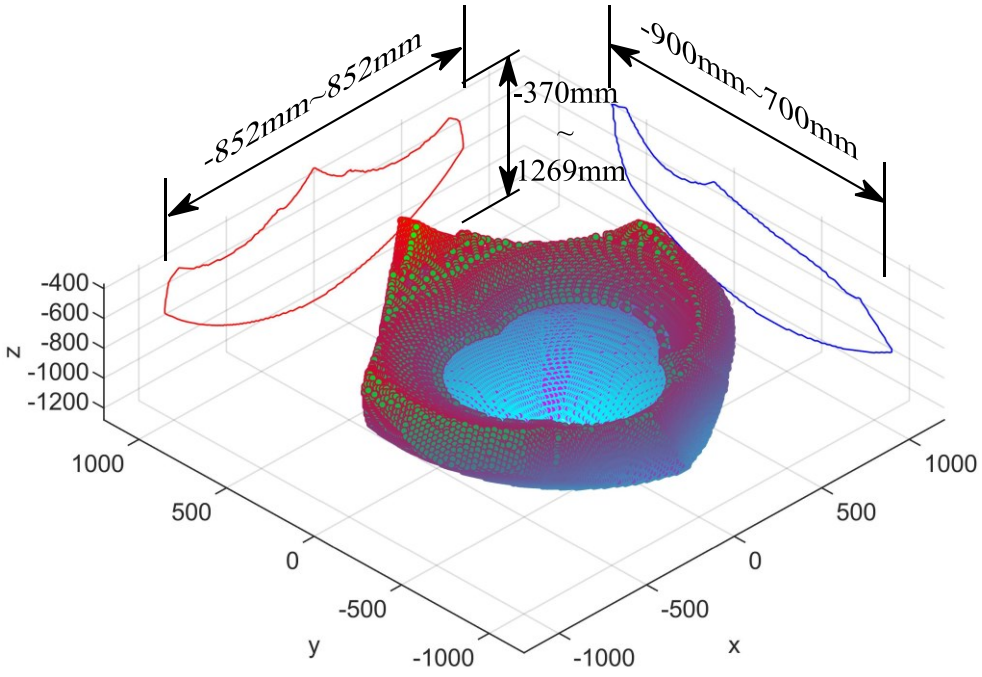

(b)

Figure 5.19 (a-b) The workspaces under two classifications: (a) agile reachable workspace, (b) constant-orientation workspace with $\boldsymbol{\omega}_{\mathrm{H-F}i} = \mathbf{0}$.

The workspaces in two conditions, namely agile and constant-orientation, are shown in fig. 5.19(a) and (b), respectively. The two graphs show the boundary of the workspaces. The extreme range in *x*-direction of a leg with demanded rotation is ±761mm, while a

constant-orientation reachable range is ±852mm. In *y*-direction, the moving platform can reach from -870mm to 481mm with rotations, and can reach from -900mm to 700mm without rotations. In *z*-direction, there is a 27mm maximum depth loss if compare agile and constant-orientation workspaces. The result shows, the quantity of constant-orientation workspace is obviously larger than an agile one. Due to the constraints, there are different gap spaces where the rotations in table 5.2 are not entirely allowed. The projections of two workspaces on *x*-*z* and *y*-*z* planes show distinct difference, seeing fig. 5.19(c, d). However, the main difference exists above -800mm altitude, because the moving platform can move higher on the *y*-plus side. This implies that the loss of agility in forward and sideway directions (*x* and *y*-minus directions) is not conspicuous.

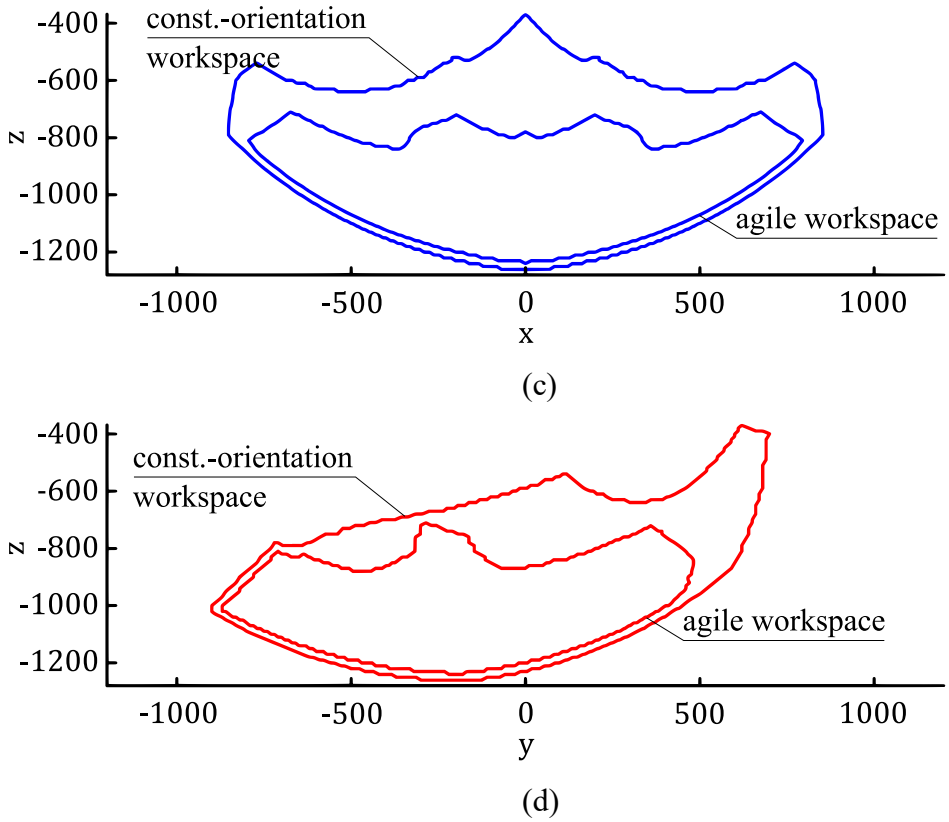

Figure 5.19 (c-d) The projections of agile-reachable and constant-orientation workspaces on *x*-*z* plane(c) and *y*-*z* plane (d).

Two remarks should be noted in this case. Firstly, since the main aim of the robot is the transportation of objects mainly on flat terrain, the reachable workspace, where the moving platform can reach with at least one orientation, was not studied, but the positions where can

be reached with only a horizontal orientation. Secondly, the searching object is the workspace of leg-1 of the robot, which was mounted on the right side (y-minus) according to the coordinates in fig. 5.19. Thus, the left half (y-plus) workspace must be cut off in the later research of trajectory planning phase. For the same reason, the side way motion range of the whole robot is in fact smaller than the for-backward motion range.

5.2.5 Section Summary of Workspace Analysis

In this section, the workspace of one leg of CENTAUROB was analysed in detail. The working ranges of all the passive and active joints were modelled and provided as well. Various collision conditions were given for Cardan joints and double Cardan joints. The working ranges of Cardan joint were studied combining the dimensions of linear actuators with different installation angles. At the same time, the workspace of a double Cardan joint was divided into 3 sections, and the joint parameters of each section were listed. Based on these collision conditions, the workspace of one leg of the biped robot was represented as constant-orientation workspace and agile reachable workspace.

5.3 Manipulability and Accuracy

Manipulability provides more information than condition number, since the former represents not only the isotropy scale, but also the isotropic magnitude after each direction. However, condition number plays an important role of kinematic design, especially, when the general kinematic performances in whole workspace with different design parameters should be compared. In this section, the manipulability and accuracy will be analysed in forms of velocity ellipsoid and condition numbers, respectively.

5.3.1 Velocity Ellipsoids

Velocity ellipsoid is a hyper geometric entity, which describes the motion performance of a

robot. According to the ratio relations between principle axes, the motion ability along different directions can be determined. The boundary of the ellipsoid shows in fact the maximum velocity in the corresponding direction.

1) Definition of Velocity Ellipsoid

The inverse Jacobian of one leg of the robot can be found in eq. (4.16), which is a mapping from the operational space to the joint space. The entries were listed in vector forms but not in matrix form. Hereby, the velocity relations of one joint and of one leg are respectively recalled and listed in matrix form as eq. (5.4) and eq. (5.5).

$$\begin{aligned}\dot{l}_{ij} &= \boldsymbol{J}_{ij}{}^{-1}(\boldsymbol{X}_{\mathrm{H-F}i})\dot{\boldsymbol{X}}_{\mathrm{H-F}i} = \boldsymbol{e}_{ij}{}^{\mathrm{T}}\boldsymbol{v}_{\mathrm{H-F}_i} - \boldsymbol{e}_{ij}{}^{\mathrm{T}\{\mathrm{H}_i\}}\tilde{\boldsymbol{d}}_{\mathrm{F}i-\mathrm{F}ij}\boldsymbol{\varpi}_{\mathrm{H-F}i} \\ &= \begin{bmatrix} e_{ijx} \\ e_{ijy} \\ e_{ijz} \end{bmatrix}^{\mathrm{T}} \dot{\boldsymbol{t}}_{\mathrm{H-F}_i} + \begin{bmatrix} e_{ijz}{}^{\{\mathrm{H}_i\}}d_{\mathrm{F}i-\mathrm{F}ijy} - e_{ijy}{}^{\{\mathrm{H}_i\}}d_{\mathrm{F}i-\mathrm{F}ijz} \\ e_{ijx}{}^{\{\mathrm{H}_i\}}d_{\mathrm{F}i-\mathrm{F}ijz} - e_{ijz}{}^{\{\mathrm{H}_i\}}d_{\mathrm{F}i-\mathrm{F}ijx} \\ e_{ijy}{}^{\{\mathrm{H}_i\}}d_{\mathrm{F}i-\mathrm{F}ijx} - e_{ijx}{}^{\{\mathrm{H}_i\}}d_{\mathrm{F}i-\mathrm{F}ijy} \end{bmatrix}^{\mathrm{T}} \dot{\boldsymbol{r}}_{\mathrm{H-F}_i} \\ &= \boldsymbol{J}_{tij}^{-1}\dot{\boldsymbol{t}}_{\mathrm{H-F}_i} + \boldsymbol{J}_{rij}^{-1}\dot{\boldsymbol{r}}_{\mathrm{H-F}_i}\end{aligned} \tag{5.4}$$

$$\dot{\boldsymbol{q}}_i = \begin{bmatrix} \boldsymbol{J}_{ti\mathrm{A}}^{-1} & \boldsymbol{J}_{ri\mathrm{A}}^{-1} \\ \vdots & \vdots \\ \boldsymbol{J}_{ti\mathrm{F}}^{-1} & \boldsymbol{J}_{ri\mathrm{F}}^{-1} \end{bmatrix} \dot{\boldsymbol{X}}_{\mathrm{H-F}_i} = \boldsymbol{J}_i^{-1}\dot{\boldsymbol{X}}_{\mathrm{H-F}_i} \tag{5.5}$$

Note that, the reference coordinates frame is $\{\mathrm{H}_i\}$ in this case and the definition of $\dot{\boldsymbol{X}}_{\mathrm{H-F}_i}$ can be found in eq. (4.16). Let the maximum velocity of each joint be $\dot{q}_{max}$, the bounded Euclidean norms of the joint velocities are bounded by

$$|\dot{\boldsymbol{q}}_i|^2 = \dot{q}_{i\mathrm{A}}^2 + \dot{q}_{i\mathrm{B}}^2 + \cdots + \dot{q}_{i\mathrm{F}}^2 \leq 6\dot{q}_{max}{}^2 \tag{5.6}$$

The inverse Jacobian $\boldsymbol{J}_i^{-1}$ can map this relation into operational space of the moving platform, so that it will form a 6-dimensional hyper ellipsoid expressed in following form.

$$|\dot{\boldsymbol{q}}_i|^2 = \dot{\boldsymbol{q}}_i{}^{\mathrm{T}}\dot{\boldsymbol{q}}_i = \dot{\boldsymbol{X}}_{\mathrm{H-F}_i}{}^{\mathrm{T}}\left(\boldsymbol{J}_i^{-1\mathrm{T}}\boldsymbol{J}_i^{-1}\right)\dot{\boldsymbol{X}}_{\mathrm{H-F}_i} = \dot{\boldsymbol{X}}_{\mathrm{H-F}_i}{}^{\mathrm{T}}\boldsymbol{P}\dot{\boldsymbol{X}}_{\mathrm{H-F}_i} \leq 6\dot{q}_{max}{}^2 \tag{5.7}$$

The matrix, $\boldsymbol{P}$, must be positive definite, this is to say, $\boldsymbol{J}_i$ must be full rank. The matrix $\boldsymbol{P}$ is

symmetric and contains 6 eigenvectors, $\boldsymbol{v}_{ik}$, and 6 eigenvalues, λ_{ik}, where, $k = 1,2,\ldots,6$. Each eigenvector represents the orientation of the semi-axis with respect to the basis formed by $\dot{\boldsymbol{X}}_{\mathrm{H-F}_i}$ and the length of semi-axes are represented by $1/\sqrt{\lambda_{ik}}$. The projections of eigenvectors on each component of $\dot{\boldsymbol{X}}_{\mathrm{H-F}_i}$ represent how the $\dot{\boldsymbol{q}}_i$ is amplified on this direction in the operational space. Through the illustrated ellipsoid on each position, the moving ability, or manipulability, can be shown and analysed in the whole workspace.

The velocity ellipsoid brings two information. The first one is that the motion can be operated faster along the major axis. The second one is that the velocity errors of actuators can be more easily amplified on that same direction. If the length of one axis is approaching infinity, this position is approaching a singularity of the mechanism and any disturbance on actuators can cause a huge motion on the end effector.

It is worth to notice, that the boundary of velocity ellipsoids is based on the limitation of the active joints, namely the linear actuators, but not on the velocity limitation of passive joints, such as Cardan joints or double Cardan joints. The maximum velocity of passive joints is considered as infinity.

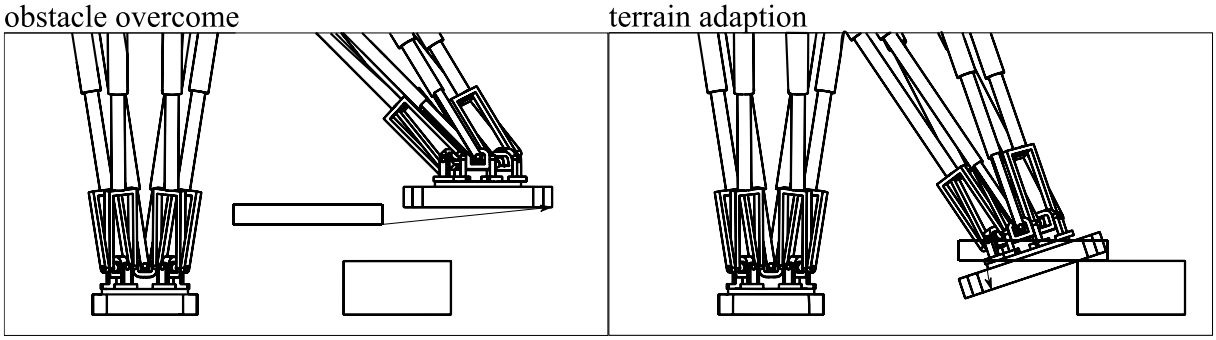

Figure 5.20 Two cases in which the translational velocity demanding (e.g. obstacle overcoming) and rotational velocity demanding (e.g. terrain adaption) of the moving platform are higher.

2) Case Study of Velocity Ellipsoid of One 6-3 PKM

For most application scenarios with higher velocity requirement of biped walking mechanisms, for example, obstacle overcoming or stepping, the relative rotation between hip platform and foot platform is minor, thus, for a swing phase of one leg, the $\dot{\boldsymbol{r}}_{\mathrm{H-F}_i}$ in eq. (5.4)

can be disregarded. On the other hand, for cases, such as uneven terrain adaption, the rotation velocity is a major task, thus $\dot{\boldsymbol{t}}_{\mathrm{H-F}_i}$, can be thought as **0**, as shown in fig. 5.20. For the same reason, the velocity ellipsoids can be divided into two groups: *swing phase* and *landing phase*. Each group is corresponding to a series of 3-dimensional ellipsoids, which can be objectively shown in a 3-dimensional space. In the agile workspace shown in fig. 5.19, the velocity ellipsoids are plotted as fig. 5.21. For a finer reading experience, the terrain adaption ability was only analysed on the terrain height, which is at 1100mm.

In the translational velocity survey in fig. 5.21(a), ellipsoids show similar disc shapes. The shape parameters can be found in fig. 5.22(a). One disc-ellipsoid is given based on the square root mean values of all the samples. The deviation of λ_{i1} is in a range of ±15%, that of λ_{i2} is in a range of ±18%, and for λ_{i3}, it is between -0.2% to 0.3%. Although the values of eigenvalues, λ_{ik}, describes the velocity amplification effect, the ratios between them illustrate the anisotropy. The ratio of $\lambda_{i1}/\lambda_{i3}$ and $\lambda_{i2}/\lambda_{i3}$ show that all the samples obtain the same anisotropy properties. It can be concluded that the moving platform exhibits substantial velocity amplifying effect in the first and second direction of the ellipsoids and weak one in the third direction. The minor axes intersect near the origin of the leg on the hip platform. The angles between the third eigenvectors and the foot displacement vectors are in a range of 8.04° to 14.22°, the RMS value of all the samples is 11.36°. This fact suggests that the translational velocity can be intensively amplified in the near of the plane vertical to the orientation vector of the leg.

The rotational velocity amplifying effect on the ground surface is shown in fig. 5.21(b). The ellipsoids are fusiform, with their major axis pointing towards the leg origin on the hip platform, too. The deviation of the major axes from the position vector of moving platform is between 7.17° and 13.37°, while its RMS value is 10.52°. The shape parameters of the fusiform ellipsoids can also be found in the figure. The length deviation range of the major axis is -15.6% ~ 17.2%. The deviation ranges of the 2nd and minor axis are -9.1% ~18.2% and -2%~3%, respectively. The ratios of major axis to 2nd and minor axes are given in the graph.

There exists slight difference between the two ratios, but the shape of the ellipsoids is in general a fusiform. The ellipsoids illustrate that the rotation along the foot displacement vector can be easily amplified.

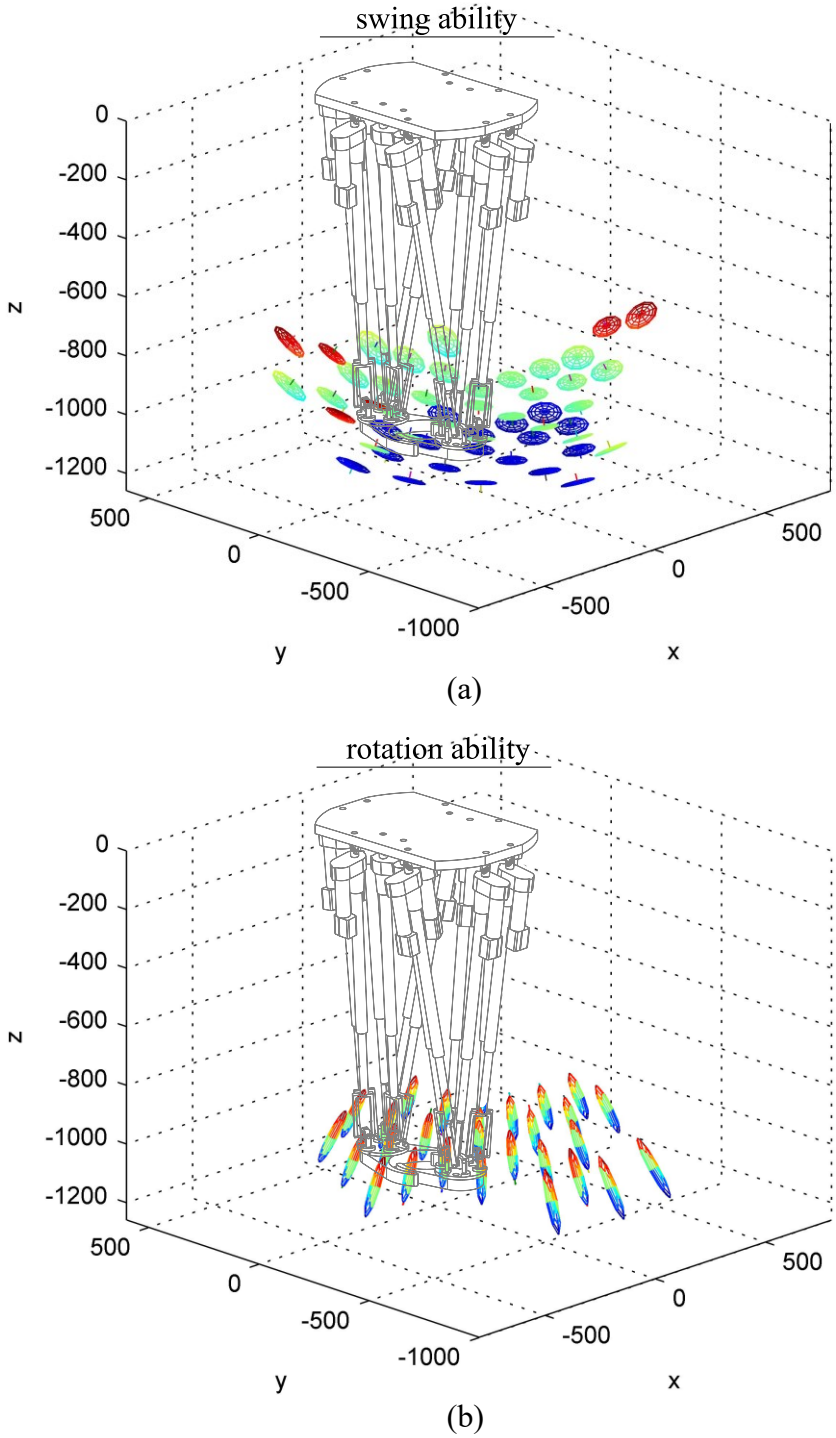

Figure 5.21 Velocity ellipsoids. (a) The translational velocity ellipsoids in the whole workspace; (b) the rotational velocity ellipsoids on the ground plane (-1100mm) of the workspace.

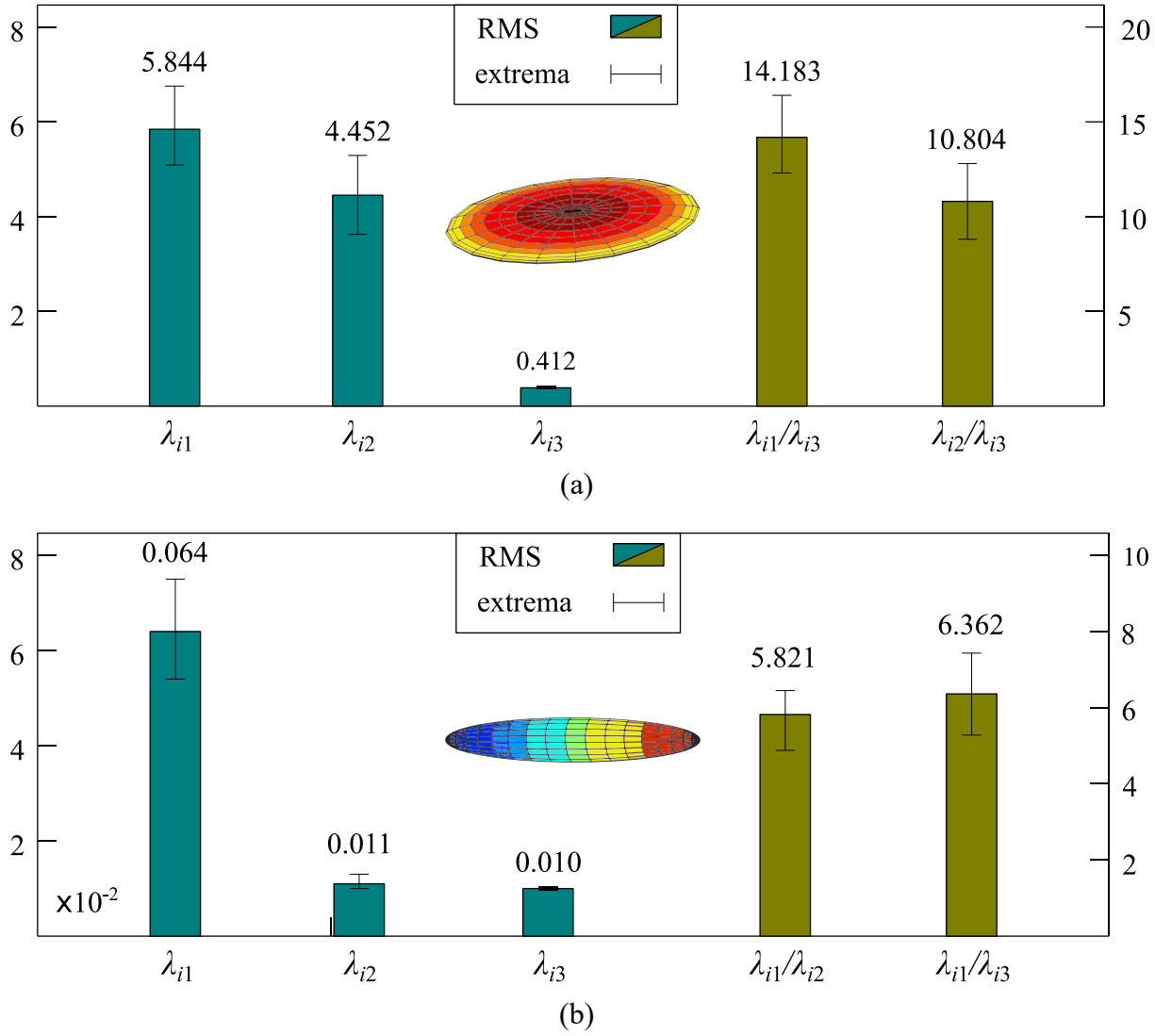

Figure 5.22 The shape parameters of velocity ellipsoid were given as statistic. (a) The ellipsoids for translational velocity show obvious disc forms, while (b) the ones for rotational velocity are fusiform.

5.3.2 Condition Number

Except velocity ellipsoids analysis, there are other manipulability indices, such as condition numbers of a mechanism. The condition number is also a dexterity index based on the analysis of Jacobian matrix. It is an important accordance for the robust and sensitivity analysis, as well. As the condition number increases, the system tends to react more fiercely to a disturbance of the input end.

1) Definition of Condition Number

For a linear system described by eq. (5.5), the norm of $\dot{\boldsymbol{q}}_i = \boldsymbol{J}_i^{-1}\dot{\boldsymbol{X}}_{\mathrm{H-F}_i}$ can be defined as

$$\left\|\boldsymbol{J}_i^{-1}\right\| = \max_{\dot{\boldsymbol{X}}_{\mathrm{H-F}_i}} \frac{\left\|\boldsymbol{J}_i^{-1}\dot{\boldsymbol{X}}_{\mathrm{H-F}_i}\right\|}{\left\|\dot{\boldsymbol{X}}_{\mathrm{H-F}_i}\right\|}, \quad \|\boldsymbol{J}_i\| = \min_{\dot{\boldsymbol{X}}_{\mathrm{H-F}_i}} \frac{\left\|\dot{\boldsymbol{X}}_{\mathrm{H-F}_i}\right\|}{\left\|\boldsymbol{J}_i^{-1}\dot{\boldsymbol{X}}_{\mathrm{H-F}_i}\right\|}. \tag{5.8}$$

Defining the relation of disturbance, $\boldsymbol{J}_i^{-1}\delta\dot{\boldsymbol{X}}_{\mathrm{H-F}_i} = \delta\dot{\boldsymbol{q}}_i$, the following relations can be derived.

$$\frac{1}{\kappa(\boldsymbol{J}_i)}\frac{\|\delta\dot{\boldsymbol{q}}_i\|}{\|\dot{\boldsymbol{q}}_i\|} \le \frac{\left\|\delta\dot{\boldsymbol{X}}_{\mathrm{H-F}_i}\right\|}{\left\|\dot{\boldsymbol{X}}_{\mathrm{H-F}_i}\right\|} \le \kappa(\boldsymbol{J}_i)\frac{\|\delta\dot{\boldsymbol{q}}_i\|}{\|\dot{\boldsymbol{q}}_i\|} \tag{5.9}$$

Where the *condition number*, $\kappa(\boldsymbol{J}_i) = \left\|\boldsymbol{J}_i^{-1}\right\|\|\boldsymbol{J}_i\|$. $\boldsymbol{J}_i$ is a 6 by 6 matrix and should be semi-positive definite. This index expresses the upper and lower boundaries of the disturbances of end-effector caused by the disturbances of the linear actuators. Comparing to velocity ellipsoid, the condition number reflects the maximum and minimum amplifying effect of the control efforts of the actuators, but does not provide the specific direction of disturbance amplifying. For this reason, condition number is usually used as a standard for the stability of the mechanism at different positions.

2) Case Study of the Condition Number

Contrarily to velocity ellipsoids analysis, the condition number shows more considerable importance for low velocity and high load scenarios. This is due to the proportional relations shown in eq. (5.9). Assuming the overshoots or other disturbance of joint velocity controller is constant, if velocity demands decreases, the ratio of disturbance will increase proportionally. If the load on one joint increases, the assignable effects of external disturbances, such as friction and mechanical deformations, will emerge. The disturbance will hence reflect to the operational space of end effector, and condition number is the determinant factor of the upper and lower boundary of the disturbances on end effector. In general, one optimal design of a system should limit the condition number in the whole workspace, and the positions with

huge condition number should be excluded from the high load and low speed trajectories, even excluded from the workspace.

Based on the analysis above, there are some occasions should be especially treated carefully in a view of biped walking mechanism:

1. The starting and end phase of the hip platform moving (high load and low velocity);
2. Landing phase of one step (low velocity);
3. Rising phase of the hip (high load).
4. Spinning phase of the hip at place (high load and low velocity).

At but not only at these phases, the mechanism operates with a high load low speed mode, as shown in fig. 5.23. In some occasions, such as foot swinging phase, the standing leg obtains no velocity demand and the limbs can be locked by the brakes embedded in the motor units. Unlike the velocity ellipsoids, the condition number is a scalar number, thus there is no demand of visualization while distinguishing rotational and translational motions. However, the metric units of these two type motions are different, namely, the values of rotations are normally much smaller than that of translations. It is necessary to multiply a coefficient to the rotation columns of Jacobians, which is chosen as the inverse of the actual length of the leg.

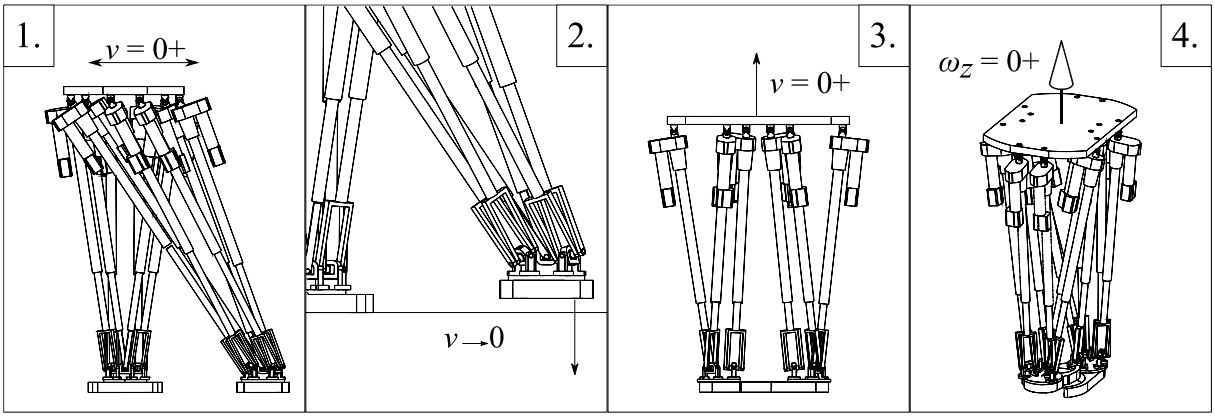

Figure 5.23 Four high load and/or low velocity scenarios: 1. the start/end moving of hip platform; 2. ground contacting. 3. hip lifting; 4. The start/end of a spinning.

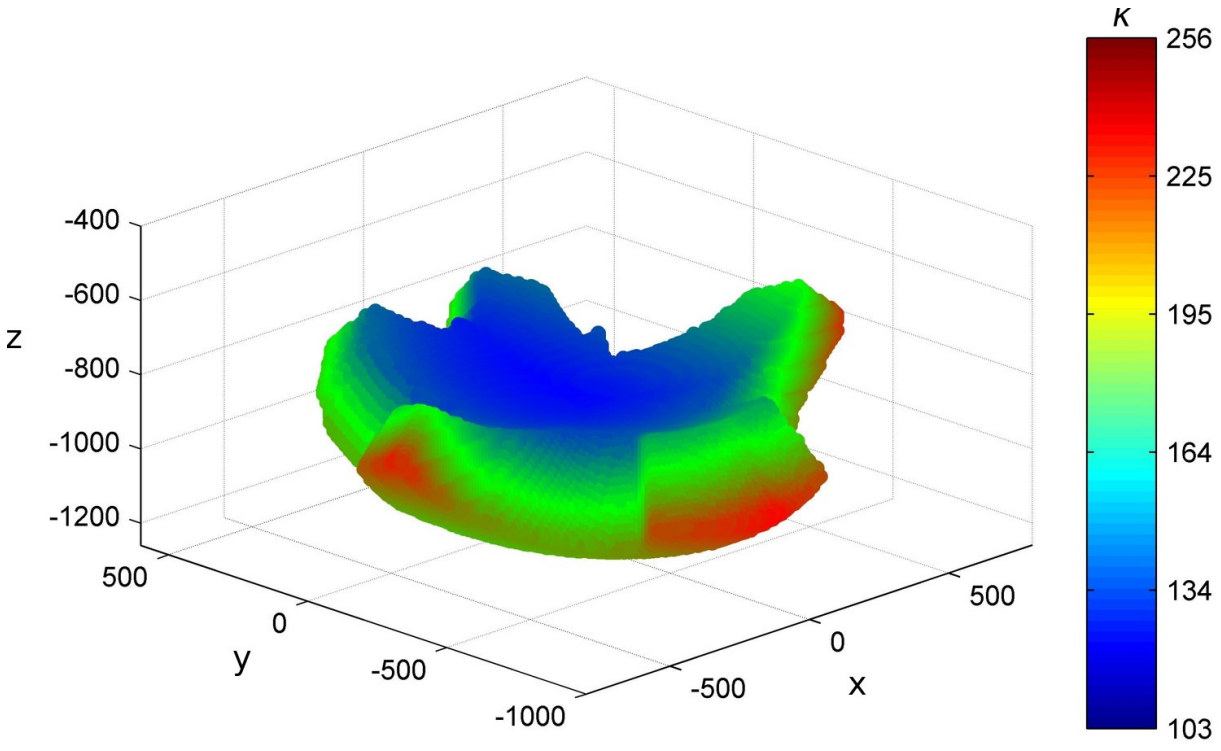

(a)

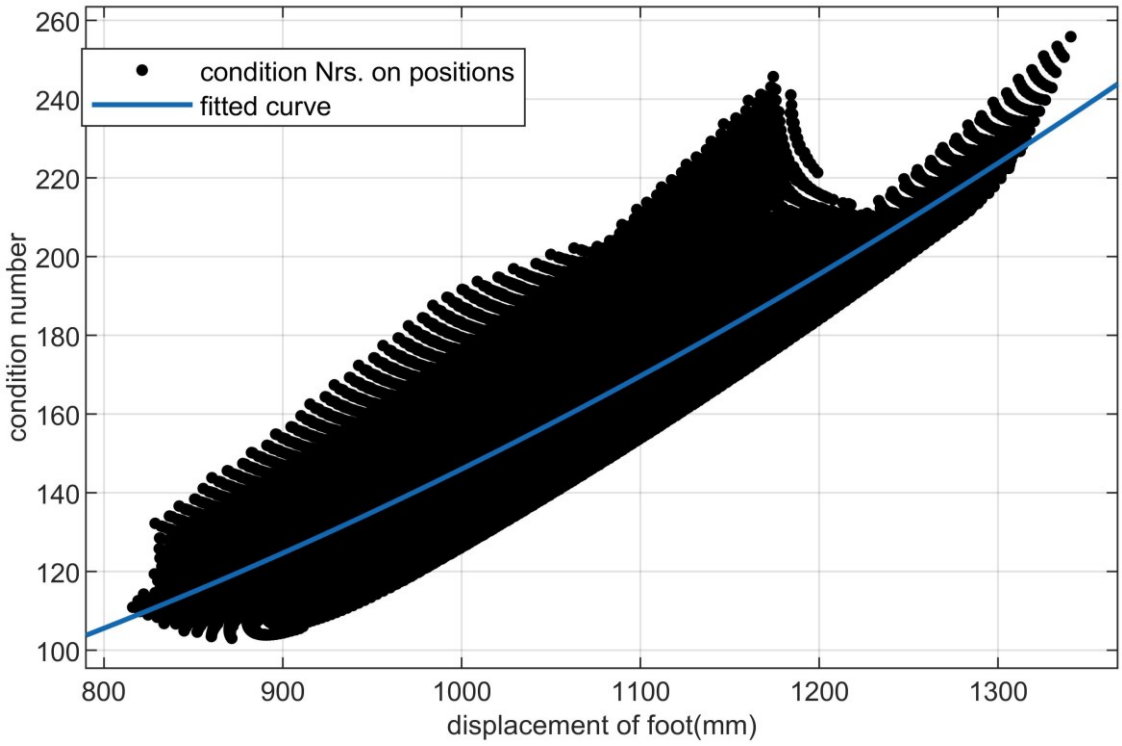

(b)

Figure 5.24 The 3-dimensional condition numbers distribution (a) in the whole agile workspace. (b) The condition numbers distribution over the displacement distance and its fitted curve.

As illustrated in fig. 5.24(a), the condition numbers distribution for an agile workspace is in a range of 103 to 256. It can be observed in fig. 5.24(b) that the condition number increases as the distance between the end effector and the hip increases. This relation is not definitively proportional, however, it can be concluded that the condition number is positively related to the displacement of end effector. In other words, the velocity accuracy is negatively related to the displacement of end effector. The most representative workspaces are the ones on the x=0 and y=0 planes, since the walking mechanism will work most frequently these two directions. Fig. 5.25 shows the condition number distributions on these two planes. On the x-direction (forward and backward), the maximum condition number is smaller than that on y-direction. The maximum condition number in the y-direction appears at the left vertex of the plot, corresponding to the right side of the robot in fig. 5.21.

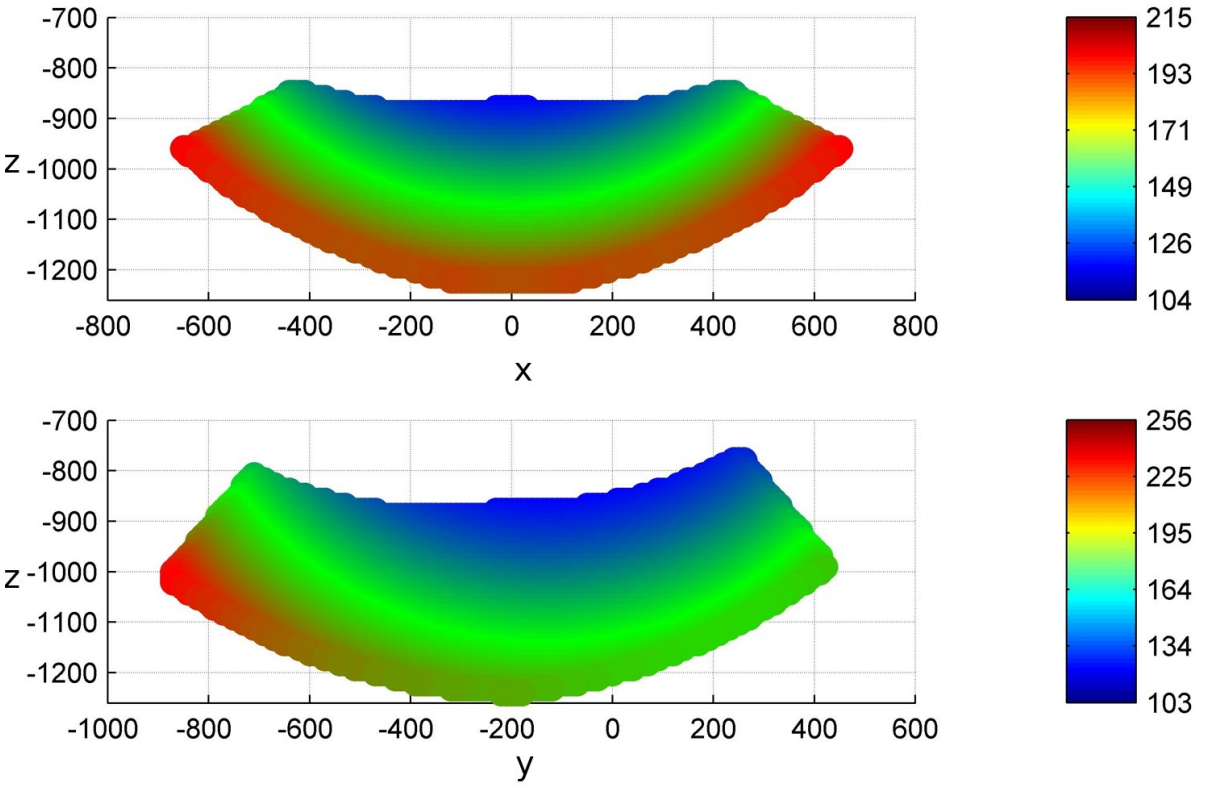

Figure 5.25 The condition numbers distributions projected on y=0 and x=0 planes. The values increase along the directions where the distance between moving platform and hip platform increases.

3) Design Optimisation Based on GCI

Referring to previous works of Tesfay Tesfu ([5.20]), the GCI (Global Condition Index) comparison based on the ratio of principal axes of hip platform joint assignments was made, the present design is already a compromise between workspace and condition number. The GCI is defined as the mean value of the condition numbers in the workspace.

$$GCI = \frac{\sum \kappa_i}{\max i} \tag{5.10}$$

Obviously, a smaller GCI means better response accuracy of the present workspace. Hereby, only several comparisons between different joint assignments are made. It can be seen in fig. 5.26, the mounting locations of the joints on hip can be described by two principal axes lengths, *a* and *b*, of an ellipse. The condition numbers of several *a*-*b* ratios under the present scale (b = 315.2mm) can be seen in fig. 5.27. At the present scale, as long as the *a*-*b* ratio increases, the condition number decreases. The fitted curve of the condition numbers is a line, whose slope rate decreases along the increasing of *a*-*b* ratio, too. This slope represents the relationship of the condition numbers distribution over the displacements of the end effector. A higher slope value indicates a more unstable velocity performance at the far ends in a workspace.

For an overview of the slope and GCI variations for different designs of hip joints, fig. 5.28 can be observed. In the figure, the slope is illustrated as scattered spheres and their colours represent the values of them. Disregarding the space limitation, the velocity performance will be optimal if the largest scale of dimensions was adopted. However, a larger hip platform will increase the weight and the size of the whole robot. Thus, the present design was adopted, in which *a* = 405.16mm and *b* = 315.2mm. The global condition index is 155.18, and the slope of condition number distribution is 0.2176. The velocity accuracy and the distance sensitivity are both in a relatively good range.

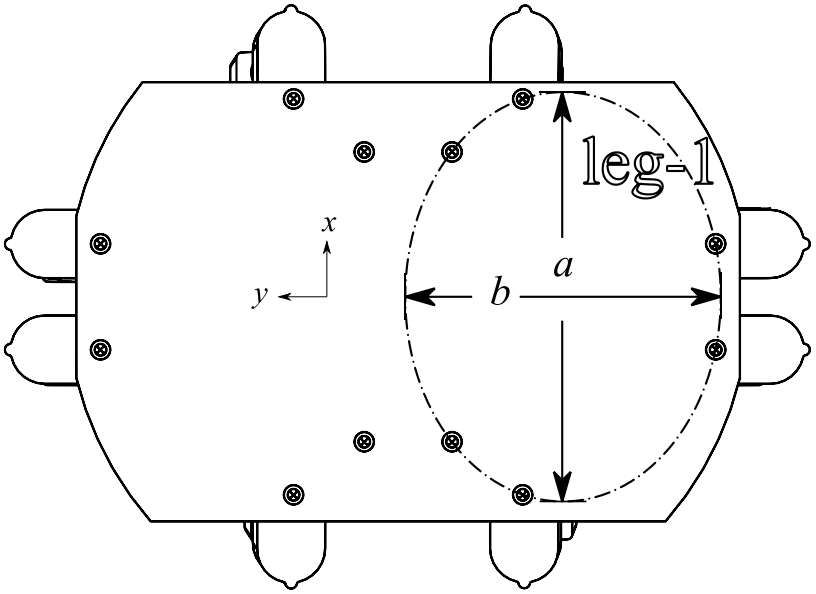

Figure 5.26 One design parameter: the joints assignment oval. The global condition number changes if the oval varies.

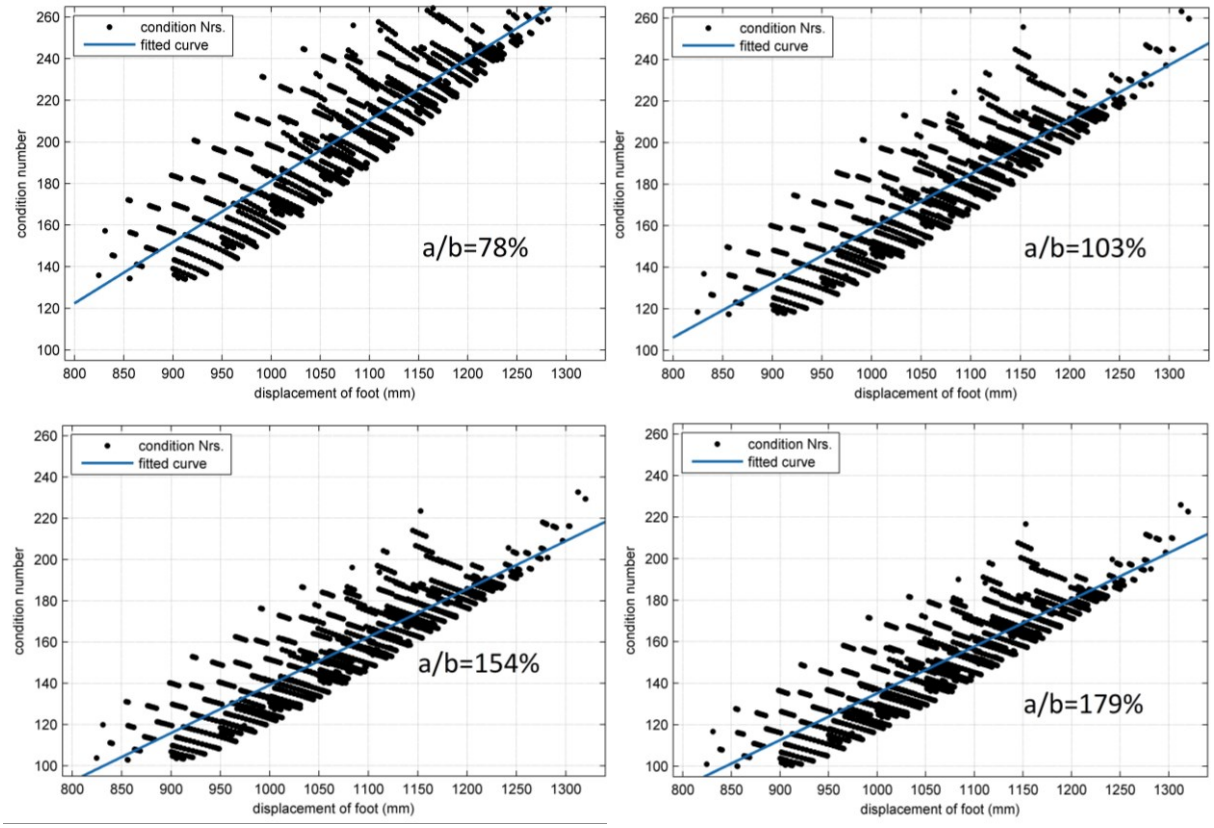

Figure 5.27 The condition numbers distribution over moving platform displacement under four typical joints oval shapes. The distributions were fitted as lines as that in fig. 5.24.

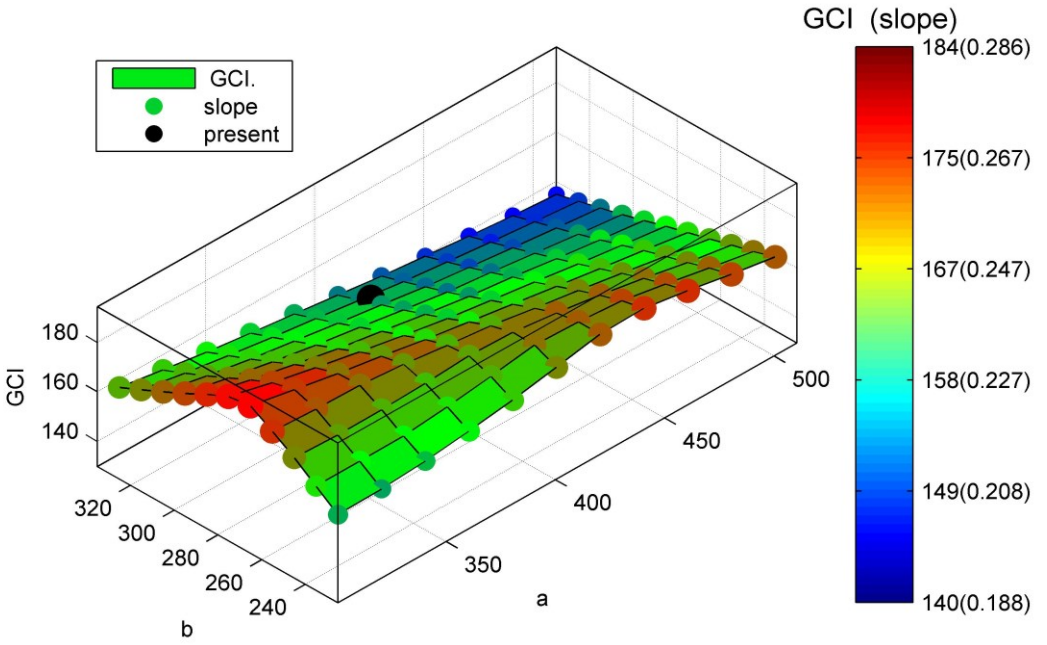

Figure 5.28 Hip joints assignment optimization after GCI variation and the condition distribution slope over displacement of moving platform.

5.3.3 Section Summary of Kinematic Performance

In this section, the kinematic performance of one leg of the robot was evaluated in two aspects, namely manipulability and accuracy. Through velocity ellipsoids, the translational manipulability was studied in the whole agile workspace and the rotational manipulability was studied on a hypothetical ground plane. It can be concluded that the translational motion ability will be enhanced in the directions approximately orthogonal to the displacement vector of the foot platform. Conversely, the rotational velocity is maximally amplified along the same vector direction. The translational velocity can be amplified slightly stronger on x-direction than on y-direction, while the rotational velocity can be amplified slightly stronger on y-direction than on x-direction.

The velocity accuracy was analysed through condition numbers. For the sake of a narrower limited velocity error, a smaller condition number is in general pursued. From the simulation results, it can be concluded that the value of condition number rises while the foot platform moves away from the hip platform. The joint assignment on the hip platform was analysed for a better condition number distribution. At last, a proper joint deployment was proposed.

5.4 Singularity Analysis

The singularity is an important drawback of both parallel and serial kinematic mechanisms. If the singularity happened, the whole mechanism will lack control, there could be extra unexpected DOF on the end effector, or, the end effector could lose some DOFs when the actuators move. During the motion planning, the singular configurations should be avoided, or, the mechanism should keep some 'distance' from singularities. There are various methods of singularity analysis, though, hereby, three methods will be introduced and the latter one is especially capable for the singularity analysis of PKM[6,3].

1) Determinant Analysis

The most straightforward method of studying the singularity problem is that to analyse the determinant of Jacobian matrix, $\det(\boldsymbol{J}_i^{-1})$, at each configuration. $\boldsymbol{J}_i^{-1}$ is singular if $\det(\boldsymbol{J}_i^{-1}) = 0$. One of the disadvantages of this method is the difficulty of constructing an analytical expression of the determinant. Moreover, using $\det(\boldsymbol{J}_i^{-1})$ can only judge the singularity of specific configurations, but cannot provide the kinematic information and type of singularity.

2) Grassmann Line Geometry

Grassmann line geometry provides clear kinematic and geometrical conditions of a parallel mechanism at a singular configuration. Since this computation method is based on the inner and outer product of Plücker vectors, its numerical stability is enhanced. There are some good applications of Grassmann line geometry on singularity studies. Nevertheless, due to the higher dimension of the singularity space, it is impractical to derive the analytical expression of singularities.

3) Screw Singularity Indicator for 6-3 Gough-Stewart PKM

For any rigid body obtains a definite velocity screw, there should be 3 random non-collinear points on it with three velocity vectors. The three nominal planes of these velocity vectors should intersect at a point on the plane formed by these 3 non-collinear points. Contrarily, if

the three nominal planes of velocity vectors intersect on the plane formed by the three points, there is a non-zero screw on the rigid body.

As discussed in Chapter 2, a PKM[6,3] obtains 4 BKCs and the velocities of the 3 joint locations totally determine the velocity of the moving platform (the foot platform). In this consequence, the first 3 BKCs are equivalent to 3 1-RS mechanical chains, referring fig. 2.8. If the actuators are locked, the velocities of S_{3BC}, S_{3DE} and S_{3FA} are orthogonal to the planes of 3 BKCs, respectively, and the connectivity of the whole mechanism should be zero. However, if the planes of the first 3 BKCs intersect, there will be at least one extra connectivity. According to the proof of Yi et. al. in [5.21], this principle can be used as the necessary and sufficient condition to determine the singularities of the 6-3 Gough-Stewart platform.

Since the continuity of the rigid body motion, the determinant of Jacobian matrix, $\det \boldsymbol{J}_i^{-1} = \left|\boldsymbol{J}_i^{-1}\right|$, will decrease during the value of $\Delta X = |X_{\mathrm{F}i} - X_{\mathrm{SF}i}|$ decreases, where, X_{SFi} is the singular configurations of moving platform and $X_{\mathrm{F}i}$ is the present configuration of moving platform. However, $\det \boldsymbol{J}_i^{-1}$ cannot express the quantization of the distance to a singularity loci. On the other hand, the distance of the intersection point of three normal planes and the plane formed by S_{3BC}, S_{3DE} and S_{3FA} can be geometrically measured.

5.4.1 Singularity Analysis Method

As shown in fig. 5.29, a PKM[6,3] can be abstracted as three planes, π_{BC} π_{DE} and π_{FA}, formed by three BKCs, and one plane where the moving platform lies in, as π_F. The intersection point of π_{BC}, π_{DE} and π_{FA} is P_π. The distance between P_π and π_F will be named as *Screw Singularity Indicator*, I_s, in the following text. For instance, the moving platform rotates after screw $\boldsymbol{X}_{\mathrm{H-F}_i} = [r_x \quad r_y \quad 0 \quad 0 \quad 0 \quad z_0]^{\mathrm{T}}$, as shown in fig. 5.30(a). The corresponding I_s distribution over $\boldsymbol{X}_{\mathrm{H-F}_i}$ can be seen in fig. 5.30(b). The value of I_s is in a range between -927mm to 100mm. The colour for positive value is between red and green, while the colour for negative is between yellow and blue. The borderline between red and yellow zones represents the value variations around positive zeros and negative zeros of I_s. Thus, it can be concluded that the

singular configurations lay in the near of the borderline, namely, the red yellow borderline is with high singular risks.

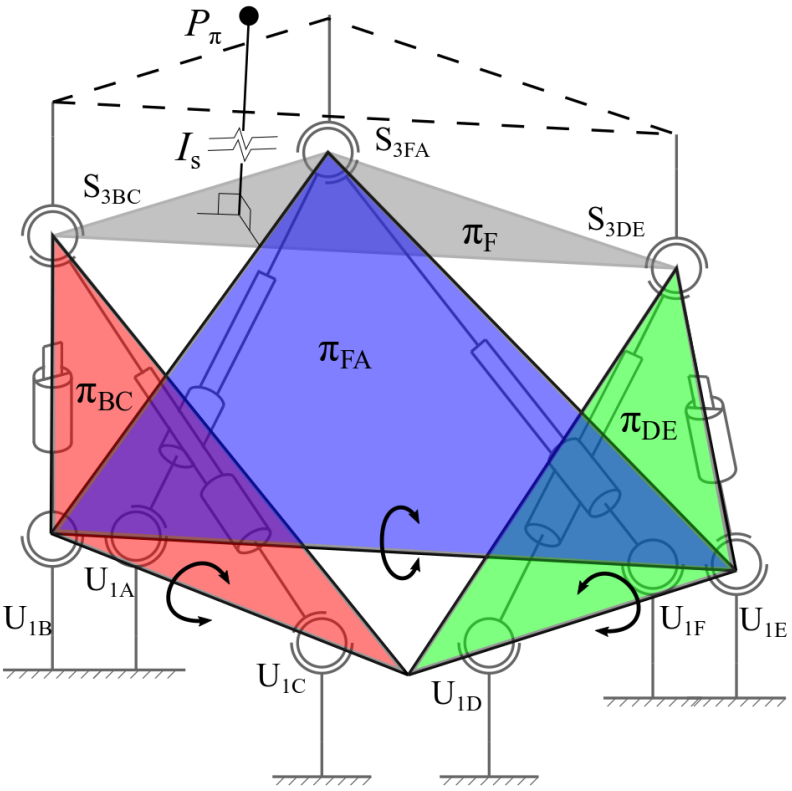

Figure 5.29 The definition of the screw singular indicator, I_s in a 6-3 Gough -Stewart platform. P_π is the intersection point of π_{BC} π_{DE} and π_{FA}.

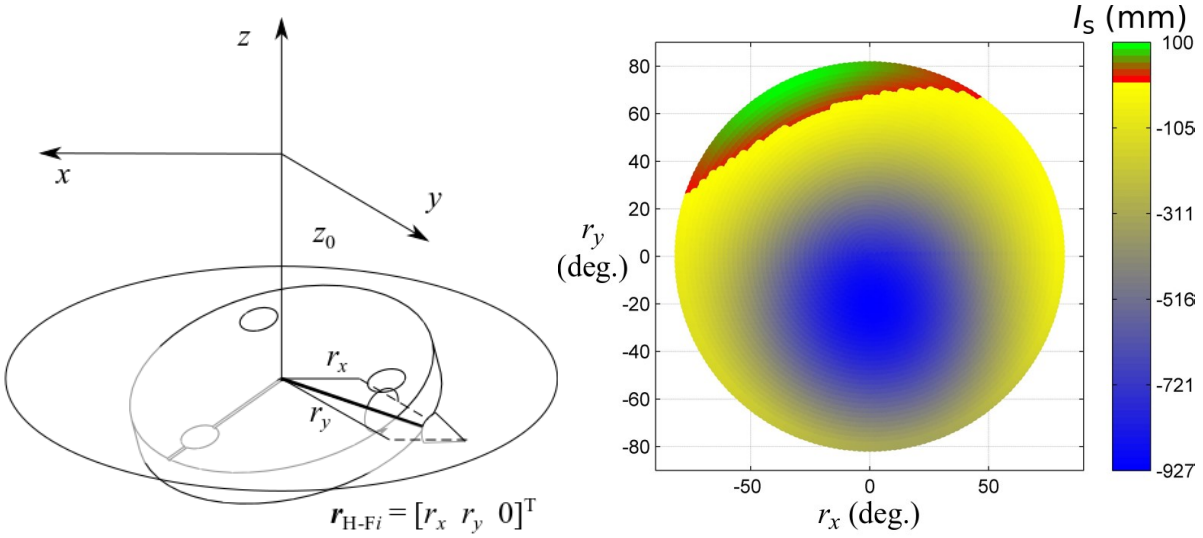

Figure 5.30 The singularity loci (b) of the rotations on the x-y plane (a). Yellow on (b) illustrate I_s = -0 and red illustrate I_s = +0, thus the red-yellow borderline indicates the singularities.

5.4.2 Singularity Analysis with Screw Singularity Indicator

Under screw singularity indicator principle, there will be no singular configurations if the moving platform does not rotate, i.e., $\boldsymbol{r}_{\mathrm{H-F}_i} = \mathbf{0}$. This is because that for this orientation, the three BKC planes will not intersect on the plane formed by joints on foot, until the foot joints plane coincides with the joints plane on the hip. Thus, the singularity analysis of present design can mainly focus on the application scenarios with rotation demands, such as spinning phases and terrain adaption cases. Similar to velocity ellipsoid analysis, the singularity analysis will be divided into four cases:

1) spinning phase: I_s values where $\boldsymbol{t}_{\mathrm{H-F}_i} = [0 \quad 0 \quad z_0]^{\mathrm{T}}$ $\boldsymbol{r}_{\mathrm{H-F}_i}(1) = [r_x \quad r_y \quad 0]^{\mathrm{T}}$ and $\boldsymbol{r}_{\mathrm{H-F}_i}(2) = [0 \quad 0 \quad r_z]^{\mathrm{T}}$, Note that, the rotations happen in sequence, the rotation matrix should be $e^{\boldsymbol{r}_{\mathrm{H-F}_i}(2)} e^{\boldsymbol{r}_{\mathrm{H-F}_i}(1)}$, but not $e^{\boldsymbol{r}_{\mathrm{H-F}_i}(2)+\boldsymbol{r}_{\mathrm{H-F}_i}(1)}$.;

2) rising phase: I_s values where $\boldsymbol{t}_{\mathrm{H-F}_i} = [0 \quad 0 \quad z_0 \sim z_0 + z_h]^{\mathrm{T}}$ and $\boldsymbol{r}_{\mathrm{H-F}_i} = [r_x \quad r_y \quad 0]^{\mathrm{T}}$, z_h is the rising height of the hip;

3) swinging phase: I_s values where $\boldsymbol{t}_{\mathrm{H-F}_i} \neq \mathbf{0}$ and $\boldsymbol{r}_{\mathrm{H-F}_i} = \mathbf{0}$;

4) terrain adaption phase: I_s values where $\boldsymbol{t}_{\mathrm{H-F}_i} = [x \quad 0 \quad z_0]^{\mathrm{T}}$ or $\boldsymbol{t}_{\mathrm{H-F}_i} = [0 \quad y \quad z_0]^{\mathrm{T}}$ and $\boldsymbol{r}_{\mathrm{H-F}_i} = [r_x \quad r_y \quad 0]^{\mathrm{T}}$.

1) Case 1 Study

For the 1st case, the hip rotates around the *z*-axis at its standing position. The rotation angle is between ±30°, corresponding to the rotation limitation of left and right spinning. The searching was made for different poses with a rotation on *x*-*y* plane, as shown in fig. 5.31(a). Fig. 5.31(b) illustrates the value distribution of the spinning I_s for different terrains. The I_s value always falls in a range between 774mm and 966mm. Concurrent, on every surveyed point, the value is continuous positive. This suggests that the intersection point, P_π, is always at the same side of the plane π_F, and the minimum distance between P_π and plane π_F is 774mm. During the observation of the colour scope of different layers of fig. 5.31(b), there is no keen variation of I_s between surveyed points. Thus, there is no singular configuration in case 1.

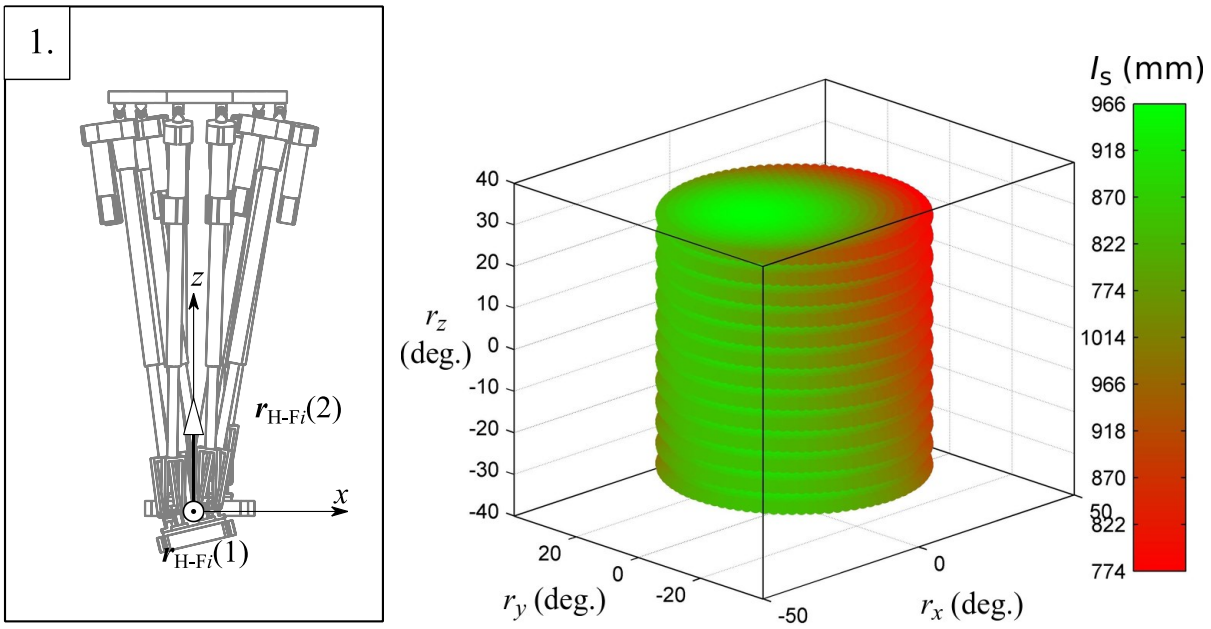

(a) (b)

Figure 5.31 (a) The robot spinning with a non-horizontal located standing foot platform and (b) its I_s distribution for different spinning angles.

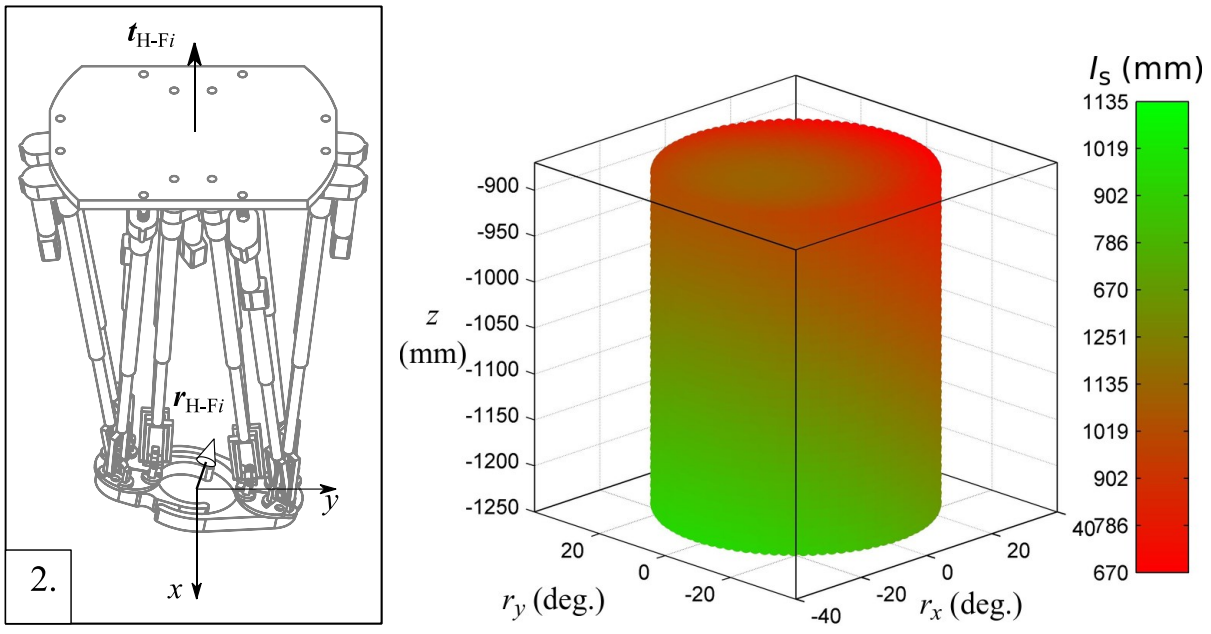

(a) (b)

Figure 5.32(a) The robot rising with a non-horizontal located standing foot platforms and (b) its I_s distribution for different rising distance.

2) Case 2 Study

In case 2, the hip platform will be lifted from 860mm to 1240mm with tilt foot platforms. The tilt angle is in a range of 0°~30° and the rotation angle stays in the *x*-*y* plane, as illustrated in

fig. 5.32(a). Similarly, in case 2, the I_s is always positive at all the surveyed points, P_π is consequently always at the same side of the plane π_F. The minimum value of I_s is 670mm, while the maximum value is 1135mm. From fig. 5.32(b), it can be seen that the singularity possibility will decrease if the height of hip platform increases. The colour changes gradually from green to red along the column radius expand. This implies a rising singular risk along the tilt angle increases. However, the I_s value shows no singularity in the surveyed workspace.

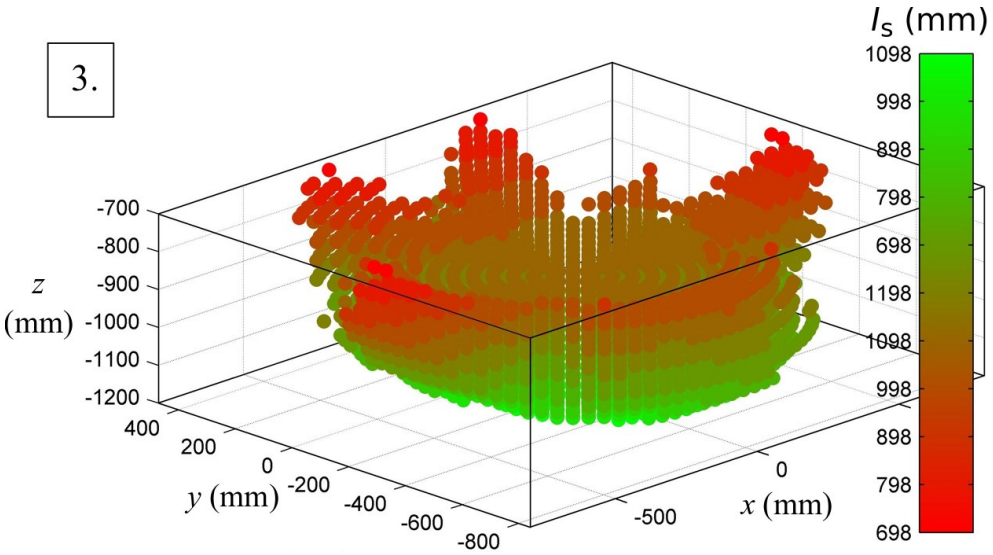

Figure 5.33 The I_s distribution for the whole agile reachable workspace.

3) Case 3 Study

The swinging phase was studied for its manipulability as velocity ellipsoid. Its motion mode can be found in fig. 5.20. As former analysed, there will be no singularity if the foot platform does not rotate until it coincides with the hip platform. However, it is still necessary to analyse the I_s distributions to understand the *distance* between the workspace and the singularity loci. In this part, the I_s was computed in the whole agile workspace and shown in fig. 5.32. The value of I_s stays in a range of 698mm~1098mm, and all the surveyed value are continuously positive. There is thus no proof that P_π passes through plane π_F. Note that, in this case, the foot platform is without any rotations. Therefore, the π_F tends to coincide with one or more planes of π_{BC} π_{DE} and π_{FA} if the foot platform was lifted. This is also the reason that the colour turns red at higher points in the workspace. From the range and gradual variation of the I_s

value, it can be concluded that there is no obvious risk of singularity in this case.

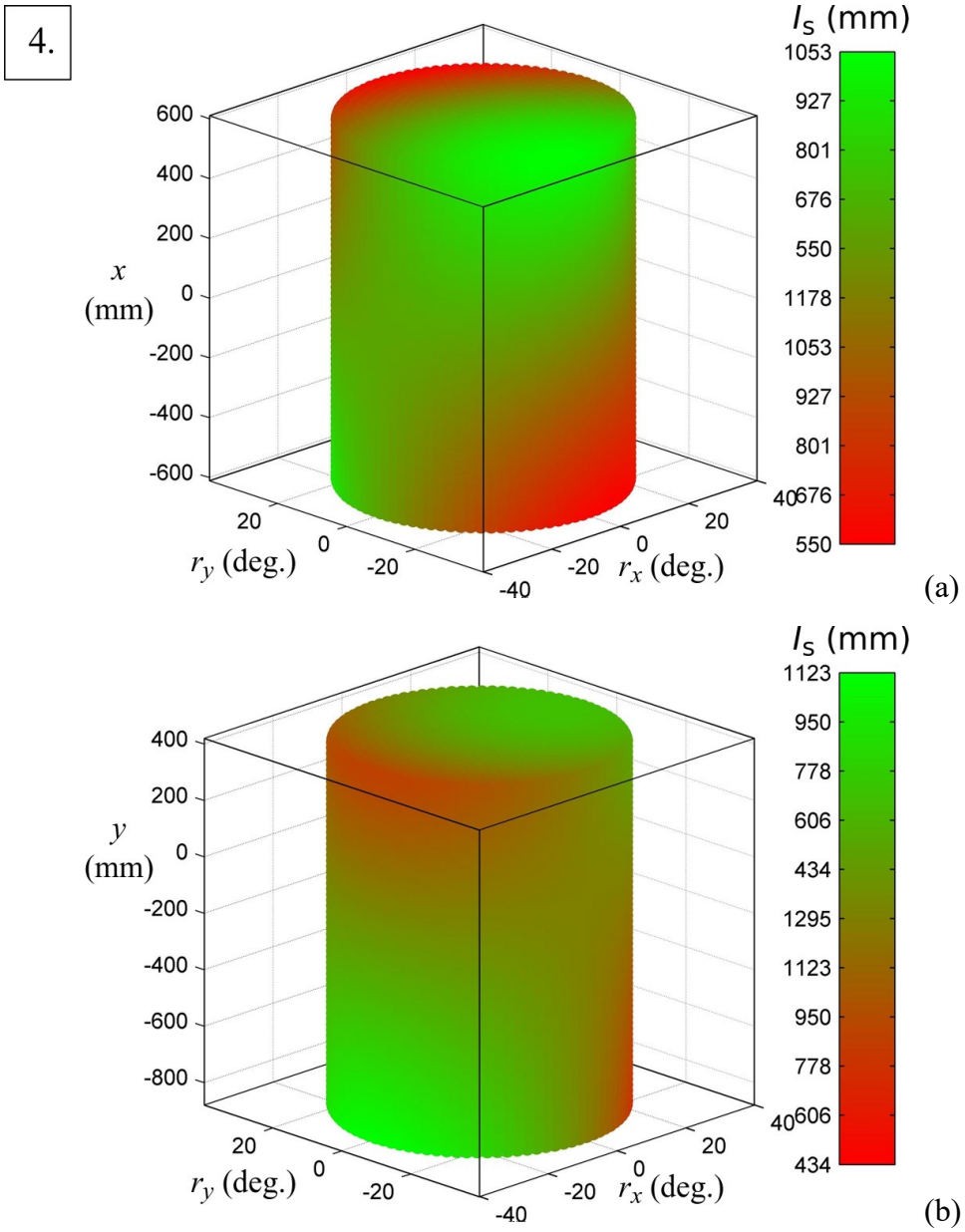

Figure 5.34 The I_s distribution with x-y rotations along (a) x- and (b) y-axis displacement.

4) Case 4 Study

Fig. 5.20 can be referred to as the motion mode of case 4; the results were shown in fig. 5.34. In this case, the foot platform will rotate on the x- and y- directions at the height z_0 = 1000mm. The rotation axis lays on the x-y plane, and the rotation angle is limited in ±30°. In the x-direction, the I_s stays in a range between +550mm and +1053mm. At the top left and bottom

right vertex of the column in fig. 5.34(a), the minimum values of I_s appears. At these two directions, π_F tends to coincide with one or more planes of π_{BC} π_{DE} and π_{FA}, similar to the highest points in case 3. This condition happens at the top vertexes and bottom vertexes (obscured) in fig. 5.34(b) for the same reason. The I_s value was limited inside +434mm to +1123mm. In the listed workspace, no risk of singularity was found.

5.4.3 Section Summary of Singularity Analysis

In this section, the singularity of CENTAUROB was studied with a novel screw singularity indicator. The distance of one configuration to a singular configuration was evaluated as the distance, labelled as I_s, of one plane intersection point, P_π, to the end effector plane, π_F. If P_π stays on π_F, this configuration can be determined as singular. If the distance, I_s, obtains continuity and stay on the same side of end effector plane, there will be no singularity.

Based on the application scenarios, the singularity analysis was divided into four cases, in each case the DOF was limited less than 4, whereby, the singularity 'distance' can be visualized. From the simulation results, it can be observed that in the workspace specified by application scenarios, the values of I_s are always continuous and the P_π is always at the same side of the π_F, which leads to no singularity risk.

5.5 Chapter Summary and Discussions

In this chapter, the kinematic performance was studied as three aspects: workspace, velocity performance and singularity. The formation and quantity of a workspace decide the configurations an end effector can reach. The velocity performance is highly related to the speed and quality of the control. Singularities are the configurations where the kinematic system lacks control and the machine should avoid. There is no unified performance index for PKMs under different application scenarios. Normally, the design of a machine in use of fine machining and finishing majorly emphasizes a dexterous angular reachable workspace, high

accuracy and repeatability, while less attention was paid to its workspace size. The design of a pick-and-place PKM requires a faster response to translational and limited rotational commands. The entertaining PKMs tend to realise higher dynamic responses but lower positioning and velocity accuracy. For a PKM utilized as legs of a biped locomotive machine, the size of workspace in specific directions (e.g. forward/backward and sideway) is pursued, as well as the velocity in these directions. Also, the rotation ability to fulfil the terrain adaption and spinning is needed.

The workspace of a kinematic mechanism depends not only on the synthesis realizations, but also highly on the joint adopted and their deployments. The Cardan joints are used as the passive joints on the hip platform and double Cardan joints on foot platforms. The relation of two axes of a Cardan joints are measured and adopted in a 1:1 linear range between ±85°. However, due to the connected linear actuators, the 1:1 relations distorted to various curves, depending on the mounting angle of the linear actuators. The collision conditions of a double Cardan joint are more complicated because of its 1-in-2-out design. Thus, its workspace was divided into 3 overlapped sections and finally merged as one semi-sphere like zone. Some non-continuous and non-symmetric workspace intervals were trimmed from its workspace. The workspace was obtained as the intersections of workspaces of all the joints. In the analysis, the agile and constant-orientation workspaces were represented.

The velocity performance was analysed through manipulability ellipsoids and condition number. From the manipulability analysis, it was shown that the translational velocity could be strongly amplified vertically to the foot displacement vector, while the rotational one along the same vector. The velocity accuracy was studied with help of condition numbers. The accuracy condition is better in the range near range of hip platform. By adjusting the hip joints deployment, different distributions of condition number value were obtained and different joints deployments were studied for an optimal GCI and condition number distribution.

The singularity was analysed by dint of a special screw singularity indicator. The value of this indicator expresses the 'distance' of the present configuration to a singular one. Through this

indicator, the closed-form solutions of 6-3 PKMs with some *z*-direction rotations can be derived. However, from a practical design perspective, the 'risk' of singularity was more concerned. By dissecting the application scenarios, the workspace was proven with no singularity risks.

Reference

[5.1] Merlet, Jean-Pierre. *Parallel robots*. Vol. 128. Springer Science & Business Media, 2006.

[5.2] Gosselin, Clement. "Determination of the workspace of 6-DOF parallel manipulators." *International Design Engineering Technical Conferences and Computers and Information in Engineering Conference*. Vol. 3691. American Society of Mechanical Engineers, 1989.

[5.3] Merlet, J -P. "Determination of the orientation workspace of parallel manipulators." *Journal of intelligent and robotic systems* 13 (1995): 143-160.

[5.4] Kim, D. J., Wan Kyun Chung, and Youngil Youm. "Geometrical approach for the workspace of 6-dof parallel manipulators." *Proceedings of International Conference on Robotics and Automation*. Vol. 4. IEEE, 1997.

[5.5] Bonev, Ilian A., and Jeha Ryu. "A geometrical method for computing the constant-orientation workspace of 6-PRRS parallel manipulators." *Mechanism and machine theory* 36.1 (2001): 1-13.

[5.6] Bonev, Ilian A., and Jeha Ryu. "A new approach to orientation workspace analysis of 6-DOF parallel manipulators." *Mechanism and machine theory* 36.1 (2001): 15-28.

[5.7] Lee, Min Ki, and Kun Woo Park. "Workspace and singularity analysis of a double parallel manipulator." *IEEE/ASME transactions on Mechatronics* 5.4 (2000): 367-375.

[5.8] Gagliardini, Lorenzo, et al. "Discrete reconfiguration planning for cable-driven parallel robots." *Mechanism and Machine Theory* 100 (2016): 313-337.

[5.9] Antonov, Anton, and Victor Glazunov. "Position, velocity, and workspace analysis of a novel 6-DOF parallel manipulator with “piercing” rods." *Mechanism and Machine Theory* 161 (2021): 104300.

[5.10] Ryu, Jeha, and Jongeun Cha. "Volumetric error analysis and architecture optimization for accuracy of HexaSlide type parallel manipulators." *Mechanism and Machine Theory* 38.3 (2003): 227-240.

[5.11] Xu, Qingsong, and Yangmin Li. "Error analysis and optimal design of a class of translational parallel kinematic machine using particle swarm optimization." *Robotica* 27.1 (2009): 67-78.

[5.12] Merlet, J. P. (June 20, 2005). "Jacobian, Manipulability, Condition Number, and Accuracy of Parallel Robots." ASME. *J. Mech. Des*. January 2006; 128(1): 199–206.

[5.13] Li, Yangmin, and Qingsong Xu. "Kinematic analysis of a 3-PRS parallel manipulator." *Robotics and Computer-Integrated Manufacturing* 23.4 (2007): 395-408.

[5.14] Choi, Hee-Byoung, Atsushi Konno, and Masaru Uchiyama. "Design, implementation, and performance evaluation of a 4-DOF parallel robot." *Robotica* 28.1 (2010): 107-118.

[5.15] Prattichizzo, Domenico, et al. "On the manipulability ellipsoids of underactuated robotic hands with compliance." *Robotics and Autonomous Systems* 60.3 (2012): 337-346.

[5.16] Gosselin, Clement, and Jorge Angeles. "Singularity analysis of closed-loop kinematic chains." *IEEE transactions on robotics and automation* 6.3 (1990): 281-290.

[5.17] Merlet, Jean-Pierre. "Singular configurations of parallel manipulators and Grassmann geometry." *The international journal of robotics research* 8.5 (1989): 45-56.

[5.18] Kim, Doik, and Wankyun Chung. "Analytic singularity equation and analysis of

six-DOF parallel manipulators using local structurization method." *IEEE Transactions on Robotics and Automation* 15.4 (1999): 612-622.

[5.19] Choi, Hee-Byoung, Atsushi Konno, and Masaru Uchiyama. "Analytic singularity analysis of a 4-DOF parallel robot based on Jacobian deficiencies." *International Journal of Control, Automation and Systems* 8 (2010): 378-384.

[5.20] Tesfu, Mekonnen Tesfay. Systematic development of a real-time motion control system for a coupled parallel kinematics robot. Der Andere Verlag, 2013.

[5.21] Cao, Yi, et al. "Singularity kinematics principle and position-singularity analyses of the 6-3 Stewart-Gough parallel manipulators." *Journal of mechanical science and technology* 25 (2011): 513-522.

Chapter 6
Dynamics Modelling of CENTAUROB

In this chapter, the acceleration states will be firstly analysed, then, the dynamic models will be built concerning the friction and inertial parameters of actuators and moving platforms. The latter is essential for a walking mechanism, since it refers to the balance control of the robot. The dynamic model will be built based on the virtual work principle and modified according to three motion modes. Through the simulation of dynamic models, the actuating forces will be predicted for four motion cases.

6.1 State of the Art

Inverse dynamic modelling (IDM) is of great significance in the motion control and planning of parallel mechanism and, especially, of biped walking mechanism. There are some aspects it mainly involves in: such as motion control, dynamic simulation, collision detection, safety control and dynamic optimization.

There are some common methods for IDM of PKMs. Müller has classified these methods as two groups in his work [6.2]: analytic and synthetic. The former uses Lagrange to obtain the energetic state of the mechanism and derive the equation of motion by differentiating it. The latter analyses the states of generalized forces applied on single rigid bodies and introduces constraints to obtain the equation of motion. Kalani et al ([6.3]) considered that all the dynamic modelling methods follow one of following three theories: Newton-Euler law, Euler-Lagrange formulations and virtual work principle.

Among these methods, Newton-Euler method is an inverse dynamics modelling method based on the principle of Lagrangian dynamics. By deriving the kinetic and potential energies of the robot system, the relationships between joint forces and actuating force and robot states are established. This method is suitable for parallel robots with complex structures, and a more accurate dynamic model can be obtained. Dasgupta and Mruthyunjaya ([6.1]) have developed and implemented a comprehensive and complete Newton-Euler formulation based IDM for the Gough-Stewart platform in 1998, concerning the friction and limbs inertia variations along the configuration changes. Based on Newton-Euler equations and introducing Lie group theory, Müller has also developed a systematic motion equation generation method for both PKM and SKM ([6.2]). Bi and Kang have built and surveyed the dynamic model of on over-constrained PKM and, further optimized its structure based on Newton-Euler formulations in [6.5].

Recursive inverse dynamics method is a commonly used and relatively intuitive inverse dynamics modelling method. First, starting from the end effector of the robot, the force/torque or driving torque of each joint is calculated step by step in a recursive manner. This method is suitable for some parallel robots with simple structures, but it may be complicated and time-consuming for robots with complex structures. Li and Staicu have built the velocity and acceleration relations of a 3-PRC mechanism through recursive matrices and solved the dynamic of it through virtual work method in [6.4]. Ibrahim and Khalil have developed the generalized recursive solution of the serially connected parallel mechanisms and implemented it on their proposed hybrid robot ([6.6], [6.7]). The dynamic model of a 7 DOF hybrid manipulator under space object capture scenario was also built in recursive form by He et al in their work ([6.8]). It might be worth to notice that, the CENTAUROB proposed by this dissertation can also be classified to this serially connected parallel mechanism group mentioned in above two examples.

The virtual work principle is a method based on Lagrange mechanics. The inverse dynamics model established by the virtual work method is called an approximate solution, because in

this method, certain simplifications and assumptions are usually used to obtain the kinetic equations. Due to the complexity and nonlinear characteristics of the robotic system, it is difficult to obtain an accurate analytical solution in practical applications, so the inverse dynamics model is obtained based on some approximation and linearization assumptions. For example, in [6.9], [6.10] and [6.11], there are some approximations of the inertial parameters. Note that, the [6.11] developed the generalized dynamic modelling method for serial-parallel hybrid mechanisms. There are also some modified applications of the dynamics modelling with virtual work principle, which, in some degrees, enhanced the accuracy of modelling. For instance, Li et al have reported their application of visual sensor-based model identification in [6.12]; Zhang, Ye and Li have utilized the so-called time-delay-estimation method in the control phase to optimize the dynamic model in [6.13]; or, some necessary correctness of dynamic model can be realized through multi-body dynamic software, as Arian, Isaksson and Gosselin have implemented in [6.14]; and so on.

Dynamic models can also be identified, verified or modified through different approaches, especially experiment-based ones. Rosyid and El-Khasawneh have identified the IDM with linear least square after observing a certain exciting trajectory in [6.15], as well as the utilization of the accompanied measurement instruments; Righettini et al ([6.16]) have built the dynamic model with help of sensors on joints and end-effecter.

Limited by the experimental conditions, in this work, the IDM will be built according to virtual work principle considering the friction model and be verified through simulations. This chapter will be arranged as following: in Section 6.2, the acceleration will be analysed in detail, concerning the actuators; at the end of this section, the simulation result of accelerations will be prohibited; in Section 6.3, the inverse dynamic models will be built and modified according to motion modes, the friction model and inertial parameters will be listed, too; in Section 6.4, a simulation of the IDM of CENTAUROB in four cases will be made, the results of with and without friction will be compared; the chapter will be summarized and discussed in Section 6.5.

6.2 Inverse Acceleration Analysis

The acceleration state is the basis of the analysis of dynamics of a PKM since it is the accordance of the general forces applied on a rigid body. To obtain the inverse acceleration of the mechanism is to find the second-order kinematic relation between the end-effecter and, not only the actuating kinematic pairs, but also the passive links. Unlike the velocity analysis, it would be more convenient to analyse the acceleration under the inertial frame, since the velocity of rigid body will affect the acceleration of mass points, too. During the derivation, it should be concerned that, due to the double Cardan joints on the foot platforms, the limbs are coupled in a degree.

6.2.1 Basic Definitions

The velocity relations between all the coordinates system, including the world frame, were discussed in Chapter 4. In this chapter, the accelerations will be analysed only in the world frame, namely the inertial frame. Except specially noted, the reference frame will be omitted. As a result, the acceleration of a single rigid body k can be described as

$$\ddot{\boldsymbol{X}}_k = [\ddot{\boldsymbol{t}}_k^{\mathrm{T}} \quad \ddot{\boldsymbol{r}}_k^{\mathrm{T}}]^{\mathrm{T}} \quad k = \{\mathrm{H}\}, \{\mathrm{C}_{ij\mathrm{C}}\}, \{\mathrm{L}_{ij\mathrm{N}}\}, \{\mathrm{L}_{ij\mathrm{S}}\}, \{\mathrm{D}_{ij2}\}, \{\mathrm{D}_{ij1}\} \ \textit{and} \ \{\mathrm{F}_i\}. \tag{6.1}$$

The parts represented by k are, hip platform, the cross shaft connected to the j-th linear actuator on the i-th foot, the sleeve and the shaft on the same linear actuator, the axis 2 and the axis 1 of the double Cardan joint, and the i-th foot platform, respectively. Thus, given the distance from $\boldsymbol{p}_0$ to $\boldsymbol{p}$, the acceleration of a point, $\boldsymbol{p}$ (rigidly or factitious), attached to rigid body, k, can be obtained as

$$\ddot{\boldsymbol{d}}_k(\boldsymbol{p}) = \ddot{\boldsymbol{t}}_k(\boldsymbol{p}_0) + \ddot{\boldsymbol{r}}_k \times \boldsymbol{d}_{\boldsymbol{p}_0-\boldsymbol{p}} + \dot{\boldsymbol{r}}_k \times \left(\dot{\boldsymbol{r}}_k \times \boldsymbol{d}_{\boldsymbol{p}_0-\boldsymbol{p}}\right). \tag{6.2}$$

6.2.2 Acceleration Analysis of Kinematic Pairs

One leg of CENTAUROB comprises of 4 BKCs, as discussed in Chapter 2. The motion of

limbs in first 3 BKCs are determined by the relative position of the three joints, namely, two Cardan joints on hip platform and one R-pair on the foot platform. The accelerations of Cardan joints, common axis and support of double Cardan joints, and P-R linear actuators will be dissected.

1) Cardan Joints

A Cardan joint comprises of an input end ({I}), an output end ({O}) and a cross shaft ({C}). The kinematic relations were analysed in Chapter 4. They are repetitively brought up as following, including the acceleration of one point on the output end. The vectors can be found in fig. 6.1.

$$\boldsymbol{d}_{\mathrm{O}}(\boldsymbol{p}_{\mathrm{O}}) = \boldsymbol{d}_{\mathrm{I}}(\boldsymbol{p}_{\mathrm{C}}) + e^{\tilde{\boldsymbol{r}}_{\mathrm{I}}} e^{\tilde{\boldsymbol{r}}_{\mathrm{C}x}} e^{\tilde{\boldsymbol{r}}_{\mathrm{C}y}\{\mathrm{O}\}} \boldsymbol{l}_{\mathrm{O}} \tag{6.3-1}$$

$$\dot{\boldsymbol{d}}_{\mathrm{O}}(\boldsymbol{p}_{\mathrm{O}}) = \dot{\boldsymbol{d}}_{\mathrm{I}}(\boldsymbol{p}_{\mathrm{C}}) + \tilde{\dot{\boldsymbol{r}}}_{\mathrm{O}} \boldsymbol{l}_{\mathrm{O}} \tag{6.3-2}$$

$$\ddot{\boldsymbol{d}}_{\mathrm{O}}(\boldsymbol{p}_{\mathrm{O}}) = \ddot{\boldsymbol{d}}_{\mathrm{I}}(\boldsymbol{p}_{\mathrm{C}}) + \left(\tilde{\ddot{\boldsymbol{r}}}_{\mathrm{O}} + \tilde{\dot{\boldsymbol{r}}}_{\mathrm{O}}^{\,2}\right) \boldsymbol{l}_{\mathrm{O}} \tag{6.3-3}$$

In which, $\ddot{\boldsymbol{r}}_{\mathrm{O}} = \ddot{\boldsymbol{r}}_{\mathrm{I}} + \ddot{\boldsymbol{r}}_{\mathrm{C}x} + \ddot{\boldsymbol{r}}_{\mathrm{O}y}$, $\dot{\boldsymbol{r}}_{\mathrm{O}} = \dot{\boldsymbol{r}}_{\mathrm{I}} + \dot{\boldsymbol{r}}_{\mathrm{C}x} + \dot{\boldsymbol{r}}_{\mathrm{O}y}$.

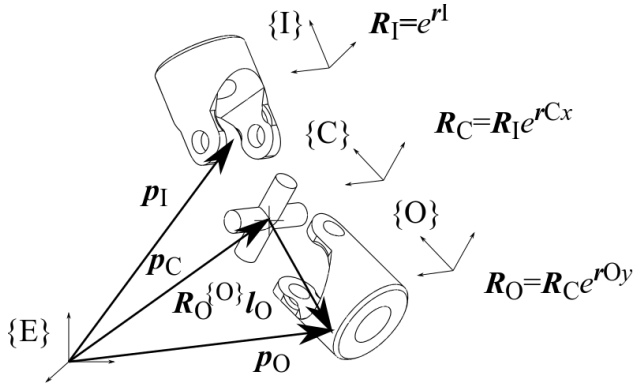

Figure 6.1 The composition and vectors of one Cardan joint.

$\ddot{\boldsymbol{r}}_{\mathrm{O}}$ is the full rotational acceleration expression of the output end of a Cardan joint. If the rotational acceleration of input end, $\ddot{\boldsymbol{r}}_{\mathrm{I}}$, and the velocities were known, the acceleration of cross shaft and output end must be solved to obtain the full acceleration expression of the output end and following solid connected linear actuator sleeve. From eq. (6.3-3), the

following relation in eq. (6.4) was derived.

$$\left(\tilde{\ddot{\boldsymbol{r}}}_{\mathrm{C}x} + \tilde{\ddot{\boldsymbol{r}}}_{\mathrm{O}y}\right)\boldsymbol{z}_{\mathrm{O}} = \boldsymbol{D}_{\mathrm{C}} \tag{6.4}$$

Where, $\boldsymbol{D}_{\mathrm{C}} = -l^{-1}\left[\ddot{\boldsymbol{d}}_{\mathrm{O}}(\boldsymbol{p}_{\mathrm{O}}) - \ddot{\boldsymbol{d}}_{\mathrm{I}}(\boldsymbol{p}_{\mathrm{C}}) - \left(\tilde{\ddot{\boldsymbol{r}}}_{\mathrm{I}} + \tilde{\dot{\boldsymbol{r}}}_{\mathrm{O}}{}^{2}\right)\boldsymbol{l}_{\mathrm{O}}\right]$.

Project eq. (6.4) to the *x*-axis and *y*-axis (also the *y*-axis of output end) of cross shaft, it can be solved. Taking the rotational acceleration of input end into account, there is

$$\ddot{\boldsymbol{r}}_{\mathrm{O}} = \ddot{\boldsymbol{r}}_{\mathrm{I}} - \cos^{-1}\gamma_y\,(\boldsymbol{y}_{\mathrm{O}}{}^{\mathrm{T}}\boldsymbol{D}_{\mathrm{C}})\boldsymbol{x}_{\mathrm{I}} + (\boldsymbol{x}_{\mathrm{O}}{}^{\mathrm{T}}\boldsymbol{D}_{\mathrm{C}})\boldsymbol{y}_{\mathrm{O}} \tag{6.5}$$

Where, $\ddot{\boldsymbol{d}}_{\mathrm{O}}(\boldsymbol{p}_{\mathrm{O}})$ can be obtained through eq. (6.8-1) as $\ddot{\boldsymbol{d}}_{\mathrm{N}}\left(\boldsymbol{p}_0|_{d_{\mathrm{N}}=0}\right)$. Thus, the acceleration of passive rotation should be the projection of $\ddot{\boldsymbol{r}}_{\mathrm{O}}$ in eq. (6.3-3) on the axis of output end, as

$$\ddot{\boldsymbol{r}}_{passive} = \ddot{\boldsymbol{r}}_{\mathrm{O}}{}^{\mathrm{T}}\boldsymbol{l}\boldsymbol{l}. \tag{6.6}$$

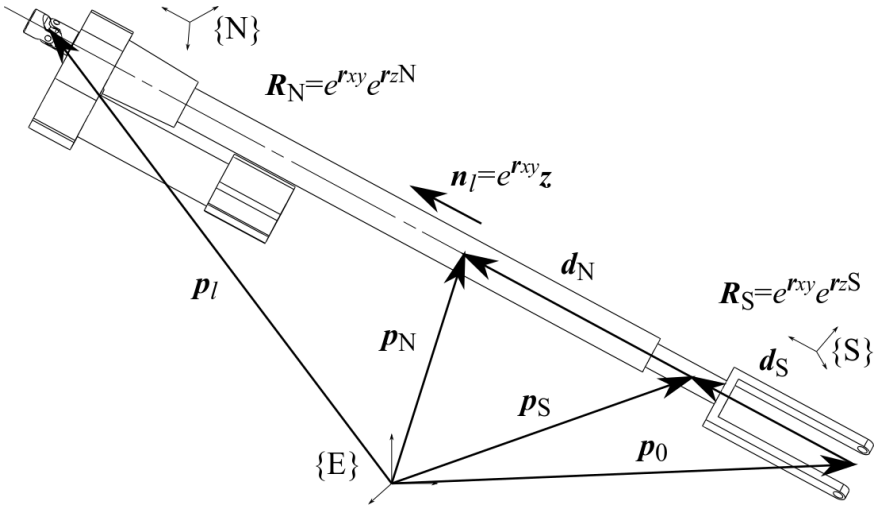

Figure 6.2 The vectors and kinematic constraints of on linear actuator.

2) Linear Actuators

The geometric and velocity relations of one linear actuator were analysed in Chapter 4. Hereby, they were repetitively brought up as following. The vectors are illustrated in fig. 6.2 and, for reading convenience, the names of vectors are simplified.

$$\begin{cases}\boldsymbol{d}_{\mathrm{N}}(\boldsymbol{p}_{\mathrm{N}}) = \boldsymbol{d}_{\mathrm{S}}(\boldsymbol{p}_0) + e^{\tilde{\boldsymbol{r}}_{\mathrm{L}xy}}\boldsymbol{z}d_{\mathrm{N}} \\ \boldsymbol{d}_{\mathrm{S}}(\boldsymbol{p}_{\mathrm{S}}) = \boldsymbol{d}_{\mathrm{S}}(\boldsymbol{p}_0) + e^{\tilde{\boldsymbol{r}}_{\mathrm{L}xy}}\boldsymbol{z}d_{\mathrm{S}}\end{cases} \tag{6.7-1}$$

$$\begin{cases}\dot{\boldsymbol{d}}_{\mathrm{N}}(\boldsymbol{p}_{\mathrm{N}}) = \dot{\boldsymbol{d}}_{\mathrm{S}}(\boldsymbol{p}_0) + \tilde{\dot{\boldsymbol{r}}}_{\mathrm{L}xy} e^{\tilde{\boldsymbol{r}}_{\mathrm{L}xy}} \boldsymbol{z} d_{\mathrm{N}} + e^{\tilde{\boldsymbol{r}}_{\mathrm{L}xy}} \boldsymbol{z} \dot{d}_{\mathrm{N}} \\ \dot{\boldsymbol{d}}_{\mathrm{S}}(\boldsymbol{p}_{\mathrm{S}}) = \dot{\boldsymbol{d}}_{\mathrm{S}}(\boldsymbol{p}_0) + \tilde{\dot{\boldsymbol{r}}}_{\mathrm{L}xy} e^{\tilde{\boldsymbol{r}}_{\mathrm{L}xy}} \boldsymbol{z} d_{\mathrm{S}}\end{cases} \tag{6.7-2}$$

$$\begin{cases}\ddot{\boldsymbol{d}}_{\mathrm{N}}(\boldsymbol{p}_{\mathrm{N}}) = \ddot{\boldsymbol{d}}_{\mathrm{S}}(\boldsymbol{p}_0) + \left(\ddot{d}_{\mathrm{N}} \boldsymbol{I} + d_{\mathrm{N}} \tilde{\ddot{\boldsymbol{r}}}_{\mathrm{L}xy} + 2\dot{d}_{\mathrm{N}} \tilde{\dot{\boldsymbol{r}}}_{\mathrm{L}xy} + d_{\mathrm{N}} \tilde{\dot{\boldsymbol{r}}}_{\mathrm{L}xy}{}^2\right) e^{\tilde{\boldsymbol{r}}_{\mathrm{L}xy}} \boldsymbol{z} \\ \ddot{\boldsymbol{d}}_{\mathrm{S}}(\boldsymbol{p}_{\mathrm{S}}) = \ddot{\boldsymbol{d}}_{\mathrm{S}}(\boldsymbol{p}_0) + d_{\mathrm{S}} \left(\tilde{\ddot{\boldsymbol{r}}}_{\mathrm{L}xy} + \tilde{\dot{\boldsymbol{r}}}_{\mathrm{L}xy}{}^2\right) e^{\tilde{\boldsymbol{r}}_{\mathrm{L}xy}} \boldsymbol{z}\end{cases} \tag{6.7-3}$$

Note that, in the equations above, the rotation vectors, $\tilde{\boldsymbol{r}}_{\mathrm{L}xy} = [r_x \quad r_y \quad 0]^{\mathrm{T}}$ and $\tilde{\boldsymbol{r}}_{\mathrm{L}z*} = [0 \quad 0 \quad r_{z*}]^{\mathrm{T}}$. These three equation groups express the kinematic states of the axial points on two rigid bodies that constrained by a rotational pair and a prismatic pair. At the point $\boldsymbol{p}_0$ and $\boldsymbol{p}_l$, there exist

$$\begin{cases}\ddot{\boldsymbol{d}}_{\mathrm{N}}(\boldsymbol{p}_0|_{d_{\mathrm{N}}=0}) = \ddot{\boldsymbol{d}}_{\mathrm{S}}(\boldsymbol{p}_0) + (\ddot{d}_{\mathrm{N}} \boldsymbol{I} + 2\dot{d}_{\mathrm{N}} \tilde{\dot{\boldsymbol{r}}}_{\mathrm{L}xy}) e^{\tilde{\boldsymbol{r}}_{\mathrm{L}xy}} \boldsymbol{z} \\ \ddot{\boldsymbol{d}}_{\mathrm{S}}(\boldsymbol{p}_0|_{d_{\mathrm{S}}=0}) = \ddot{\boldsymbol{d}}_{\mathrm{S}}(\boldsymbol{p}_0)\end{cases} \tag{6.8-1}$$

$$\begin{cases}\ddot{\boldsymbol{d}}_{\mathrm{N}}(\boldsymbol{p}_l|_{d_{\mathrm{N}}=l}) = \ddot{\boldsymbol{d}}_{\mathrm{S}}(\boldsymbol{p}_0) + \left(\ddot{d}_{\mathrm{N}} \boldsymbol{I} + l \tilde{\ddot{\boldsymbol{r}}}_{\mathrm{L}xy} + 2\dot{d}_{\mathrm{N}} \tilde{\dot{\boldsymbol{r}}}_{\mathrm{L}xy} + l \tilde{\dot{\boldsymbol{r}}}_{\mathrm{L}xy}{}^2\right) e^{\tilde{\boldsymbol{r}}_{\mathrm{L}xy}} \boldsymbol{z} \\ \ddot{\boldsymbol{d}}_{\mathrm{S}}(\boldsymbol{p}_l|_{d_{\mathrm{S}}=l}) = \ddot{\boldsymbol{d}}_{\mathrm{S}}(\boldsymbol{p}_0) + l \left(\tilde{\ddot{\boldsymbol{r}}}_{\mathrm{L}xy} + \tilde{\dot{\boldsymbol{r}}}_{\mathrm{L}xy}{}^2\right) e^{\tilde{\boldsymbol{r}}_{\mathrm{L}xy}} \boldsymbol{z}\end{cases} \tag{6.8-2}$$

From eq. (6.8-2), it can be derived that

$$(\ddot{d}_{\mathrm{N}} \boldsymbol{I} + l \tilde{\ddot{\boldsymbol{r}}}_{\mathrm{L}xy}) e^{\tilde{\boldsymbol{r}}_{\mathrm{L}xy}} \boldsymbol{z} = \boldsymbol{D}_{\mathrm{L}}. \tag{6.9}$$

Where $\boldsymbol{D}_{\mathrm{L}} = \ddot{\boldsymbol{d}}_{\mathrm{N}}(\boldsymbol{p}_l) - \ddot{\boldsymbol{d}}_{\mathrm{S}}(\boldsymbol{p}_0) - \left(2\dot{d}_{\mathrm{N}} \tilde{\dot{\boldsymbol{r}}}_{\mathrm{L}xy} + l \tilde{\dot{\boldsymbol{r}}}_{\mathrm{L}xy}{}^2\right) e^{\tilde{\boldsymbol{r}}_{\mathrm{L}xy}} \boldsymbol{z}$. In which, $\ddot{\boldsymbol{d}}_{\mathrm{S}}(\boldsymbol{p}_0)$ and $\ddot{\boldsymbol{d}}_{\mathrm{N}}(\boldsymbol{p}_l)$ can be obtained from eq. (6.23), $\tilde{\dot{\boldsymbol{r}}}_{xy}$ is the component of rotational velocity on the plane orthogonal to the linear actuator axis, $\dot{d}_{\mathrm{N}}$ is the length variation velocity of the linear actuator. If project eq. (6.9) to the *z*-axis and *x*-*y* plane of linear actuator,

$$\ddot{d}_{\mathrm{N}} = \boldsymbol{D}_{\mathrm{L}}{}^{\mathrm{T}} e^{\tilde{\boldsymbol{r}}_{\mathrm{L}xy}} \boldsymbol{z}, \tag{6.10}$$

$$l \tilde{\ddot{\boldsymbol{r}}}_{\mathrm{L}xy} \boldsymbol{z}_{\mathrm{L}xyn} = e^{\tilde{\boldsymbol{r}}_{\mathrm{L}n}} \begin{bmatrix} \boldsymbol{x}_{\mathrm{L}n}{}^{\mathrm{T}} \\ \boldsymbol{y}_{\mathrm{L}n}{}^{\mathrm{T}} \\ \boldsymbol{0} \end{bmatrix} \boldsymbol{D}_{\mathrm{L}} \tag{6.11}$$

$\ddot{d}_{\mathrm{N}}$ is the length variation acceleration of linear actuators. Eq. (6.11) represents the acceleration caused by the rotational acceleration on the *x*-*y* plane after a $e^{\tilde{r}_{xy}}$ rotation. Since

the cross product was done by two orthogonal vectors, $\ddot{\boldsymbol{r}}_{xy}$ can be solved, there is

$$\ddot{\boldsymbol{r}}_{\mathrm{L}xy} = l^{-1} e^{\tilde{\boldsymbol{r}}\mathrm{L}n} \begin{bmatrix} -\boldsymbol{y}_{\mathrm{L}n}{}^{\mathrm{T}} \\ \boldsymbol{x}_{\mathrm{L}n}{}^{\mathrm{T}} \\ \boldsymbol{0} \end{bmatrix} \boldsymbol{D}_{\mathrm{L}}. \tag{6.12}$$

The subscripts, n, stands for N or S, implies that $\boldsymbol{D}_{\mathrm{L}}$ can be projected either to sleeve or shaft and then inversely projected to the inertial frame. Bring eq. (6.10) and (6.12) to (6.8-1) and (6.8-2), the acceleration of the sleeve on $\boldsymbol{p}_0$ and the acceleration of shaft on $\boldsymbol{p}_l$ can be obtained. The former can be used to solve the full acceleration of the output end of the Cardan joints, while the latter will be used to solve the same elements of double Cardan joints.

3) Shafts of Linear Actuators

The kinematic pairs of linear actuators shafts are between shafts inter-limbs, besides between sleeve and shaft. These pairs are shown in fig. 6.3. The rotations of them can be assumed as the rotations around common x-axis and the rotation orthogonal to this axis, thus, the kinematic states can be listed in three following equation groups.

$$\begin{cases} \boldsymbol{d}_{1\mathrm{S}}(\boldsymbol{p}_{1\mathrm{S}}) = \boldsymbol{d}_{\mathrm{S}}(\boldsymbol{p}_0) + e^{\tilde{\boldsymbol{r}}\mathrm{L}yz\mathrm{S}} e^{\tilde{\boldsymbol{r}}\mathrm{L}1x\mathrm{S}} \boldsymbol{z} d_{\mathrm{S}} \\ \boldsymbol{d}_{2\mathrm{S}}(\boldsymbol{p}_{2\mathrm{S}}) = \boldsymbol{d}_{\mathrm{S}}(\boldsymbol{p}_0) + e^{\tilde{\boldsymbol{r}}\mathrm{L}yz\mathrm{S}} e^{\tilde{\boldsymbol{r}}\mathrm{L}2x\mathrm{S}} \boldsymbol{z} d_{\mathrm{S}} \end{cases} \tag{6.13-1}$$

$$\begin{cases} \dot{\boldsymbol{d}}_{1\mathrm{S}}(\boldsymbol{p}_{1\mathrm{S}}) = \dot{\boldsymbol{d}}_{\mathrm{S}}(\boldsymbol{p}_0) + \left(\tilde{\dot{\boldsymbol{r}}}_{\mathrm{L}yz\mathrm{S}} + \tilde{\dot{\boldsymbol{r}}}_{\mathrm{L}1x\mathrm{S}}\right) e^{\tilde{\boldsymbol{r}}\mathrm{L}yz\mathrm{S}} e^{\tilde{\boldsymbol{r}}\mathrm{L}1x\mathrm{S}} \boldsymbol{z} d_{\mathrm{S}} \\ \dot{\boldsymbol{d}}_{2\mathrm{S}}(\boldsymbol{p}_{2\mathrm{S}}) = \dot{\boldsymbol{d}}_{\mathrm{S}}(\boldsymbol{p}_0) + \left(\tilde{\dot{\boldsymbol{r}}}_{\mathrm{L}yz\mathrm{S}} + \tilde{\dot{\boldsymbol{r}}}_{\mathrm{L}2x\mathrm{S}}\right) e^{\tilde{\boldsymbol{r}}\mathrm{L}yz\mathrm{S}} e^{\tilde{\boldsymbol{r}}\mathrm{L}2x\mathrm{S}} \boldsymbol{z} d_{\mathrm{S}} \end{cases} \tag{6.13-2}$$

$$\begin{cases} \ddot{\boldsymbol{d}}_{1\mathrm{S}}(\boldsymbol{p}_{1\mathrm{S}}) = \ddot{\boldsymbol{d}}_{\mathrm{S}}(\boldsymbol{p}_0) + A_1 + \left(\tilde{\ddot{\boldsymbol{r}}}_{\mathrm{L}yz\mathrm{S}} + \tilde{\ddot{\boldsymbol{r}}}_{\mathrm{L}1x\mathrm{S}}\right) e^{\tilde{\boldsymbol{r}}\mathrm{L}yz\mathrm{S}} e^{\tilde{\boldsymbol{r}}\mathrm{L}1x\mathrm{S}} \boldsymbol{z} d_{\mathrm{S}} \\ \ddot{\boldsymbol{d}}_{2\mathrm{S}}(\boldsymbol{p}_{2\mathrm{S}}) = \ddot{\boldsymbol{d}}_{\mathrm{S}}(\boldsymbol{p}_0) + A_2 + \left(\tilde{\ddot{\boldsymbol{r}}}_{\mathrm{L}yz\mathrm{S}} + \tilde{\ddot{\boldsymbol{r}}}_{\mathrm{L}2x\mathrm{S}}\right) e^{\tilde{\boldsymbol{r}}\mathrm{L}yz\mathrm{S}} e^{\tilde{\boldsymbol{r}}\mathrm{L}2x\mathrm{S}} \boldsymbol{z} d_{\mathrm{S}} \end{cases} \tag{6.13-3}$$

In which, $A_j = \left(\tilde{\dot{\boldsymbol{r}}}_{\mathrm{L}yz\mathrm{S}} + \tilde{\dot{\boldsymbol{r}}}_{\mathrm{L}jx\mathrm{S}}\right)^2 e^{\tilde{\boldsymbol{r}}\mathrm{S}yz} e^{\tilde{\boldsymbol{r}}\mathrm{L}jx\mathrm{S}} \boldsymbol{z} d_{\mathrm{S}} = \tilde{\dot{\boldsymbol{r}}}_{\mathrm{L}j\mathrm{S}}{}^2 \boldsymbol{z}_{\mathrm{L}j\mathrm{S}} d_{\mathrm{S}}$, $j = 1,2$. The last two elements of eq. (6.13-3) are along the y-axis and x-axis of shafts, respectively. Thus, letting $d_{\mathrm{S}} = l$, they can be projected to these axes to eliminate each other, as

$$\begin{cases} \boldsymbol{x}_{\mathrm{L}j\mathrm{S}}{}^{\mathrm{T}} \tilde{\ddot{\boldsymbol{r}}}_{\mathrm{L}yz\mathrm{S}} \boldsymbol{z}_{\mathrm{L}j\mathrm{S}} = \dfrac{1}{l} \boldsymbol{x}_{\mathrm{L}j\mathrm{S}}{}^{\mathrm{T}} \left(\ddot{\boldsymbol{d}}_{j\mathrm{S}}(\boldsymbol{p}_{j\mathrm{S}}) - \ddot{\boldsymbol{d}}_{\mathrm{S}}(\boldsymbol{p}_0) - A_j\right) \\ \boldsymbol{y}_{\mathrm{L}j\mathrm{S}}{}^{\mathrm{T}} \tilde{\ddot{\boldsymbol{r}}}_{\mathrm{L}jx\mathrm{S}} \boldsymbol{z}_{\mathrm{L}j\mathrm{S}} = \dfrac{1}{l} \boldsymbol{y}_{\mathrm{L}j\mathrm{S}}{}^{\mathrm{T}} \left(\ddot{\boldsymbol{d}}_{j\mathrm{S}}(\boldsymbol{p}_{j\mathrm{S}}) - \ddot{\boldsymbol{d}}_{\mathrm{S}}(\boldsymbol{p}_0) - A_j\right) \end{cases} \tag{6.14}$$

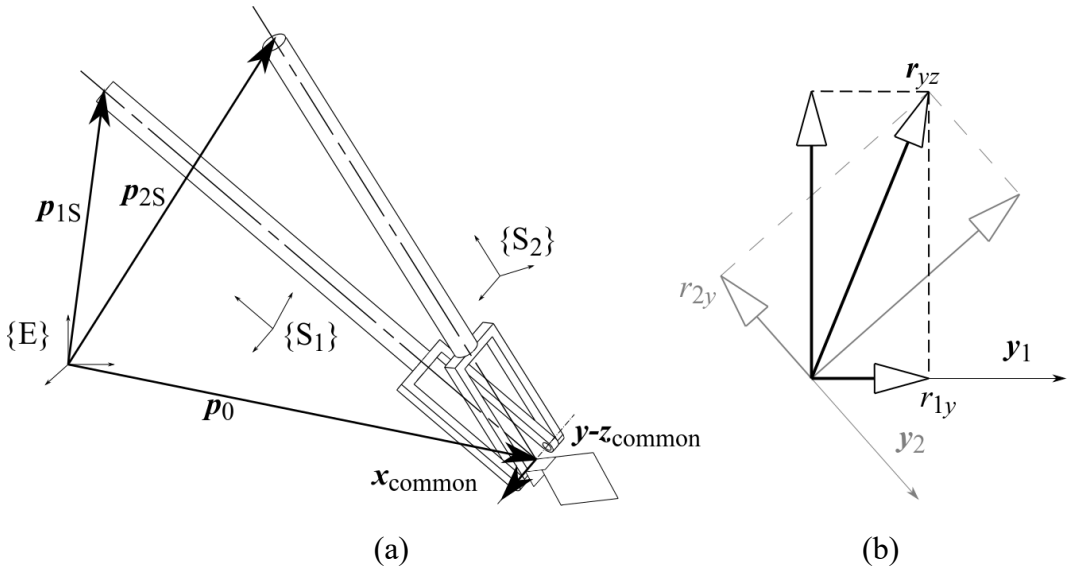

(a) (b)

Figure 6.3 (a) The rotational kinematic pair between two limbs and (b) the vector relations between two shafts of two linear actuators.

Similar to eq. (6.12), the rotational acceleration along $\boldsymbol{x}_{\text{common}}$ will be

$$\ddot{\boldsymbol{r}}_{\mathrm{L}jx\mathrm{S}} = -l^{-1}\left[\boldsymbol{y}_{\mathrm{L}j\mathrm{S}}{}^{\mathrm{T}}\left(\ddot{\boldsymbol{d}}_{j\mathrm{S}}(\boldsymbol{p}_{j\mathrm{S}}) - \ddot{\boldsymbol{d}}_{\mathrm{S}}(\boldsymbol{p}_0) - A_j\right)\right]\boldsymbol{x}_{\mathrm{L}j\mathrm{S}}. \tag{6.15}$$

As dissected in fig. 6.3 (b), the component of $\ddot{\boldsymbol{r}}_{yz}$ on two y-axes can be obtained, as

$$\ddot{\boldsymbol{r}}_{\mathrm{L}jy\mathrm{S}} = l^{-1}\left[\boldsymbol{x}_{\mathrm{L}j\mathrm{S}}{}^{\mathrm{T}}\left(\ddot{\boldsymbol{d}}_{j\mathrm{S}}(\boldsymbol{p}_{j\mathrm{S}}) - \ddot{\boldsymbol{d}}_{\mathrm{S}}(\boldsymbol{p}_0) - A_j\right)\right]\boldsymbol{y}_{\mathrm{L}jy\mathrm{S}}, \tag{6.16}$$

the component of $\ddot{\boldsymbol{r}}_{yz}$ on two z-axis of shaft-1 and can be obtained as

$$\begin{aligned}\ddot{\boldsymbol{r}}_{\mathrm{L1}z\mathrm{S}} = -\frac{1}{l\|\tilde{\boldsymbol{z}}_{\mathrm{L1S}}\boldsymbol{z}_{\mathrm{L2S}}\|}\Big[&\boldsymbol{x}_{\mathrm{L2S}}{}^{\mathrm{T}}\left(\ddot{\boldsymbol{d}}_{2\mathrm{S}}(\boldsymbol{p}_{2\mathrm{S}}) - \ddot{\boldsymbol{d}}_{\mathrm{S}}(\boldsymbol{p}_0) - A_2\right)\\ &- \boldsymbol{x}_{\mathrm{L1S}}{}^{\mathrm{T}}\left(\ddot{\boldsymbol{d}}_{1\mathrm{S}}(\boldsymbol{p}_{1\mathrm{S}}) - \ddot{\boldsymbol{d}}_{\mathrm{S}}(\boldsymbol{p}_0) - A_1\right)\left(\boldsymbol{y}_{\mathrm{L1S}}{}^{\mathrm{T}}\boldsymbol{y}_{\mathrm{L2S}}\right)\Big]\boldsymbol{z}_{\mathrm{L1S}}\end{aligned} \tag{6.17}$$

Note that, $\ddot{\boldsymbol{d}}_{\mathrm{S}}(\boldsymbol{p}_0)$ can be obtained through eq. (6.23) as $\ddot{\boldsymbol{d}}_{\mathrm{L}_{ij\mathrm{S}}}(\boldsymbol{p}_{\mathrm{F}ij})$, $\ddot{\boldsymbol{d}}_{j\mathrm{S}}(\boldsymbol{p}_{j\mathrm{S}})$ can be obtained through eq. (6.8-2) as $\ddot{\boldsymbol{d}}_{\mathrm{S}}(\boldsymbol{p}_l|_{d_{\mathrm{S}}=l})$. Since $\ddot{\boldsymbol{r}}_{\mathrm{L}yz\mathrm{S}} = \ddot{\boldsymbol{r}}_{\mathrm{L}jy\mathrm{S}} + \ddot{\boldsymbol{r}}_{\mathrm{L}jz\mathrm{S}}$, the acceleration component on the common y-z plane need to be calculated only once for two shafts. Thus, the acceleration of shafts is

$$\ddot{\boldsymbol{r}}_{\mathrm{L}j\mathrm{S}} = \ddot{\boldsymbol{r}}_{\mathrm{L}jx\mathrm{S}} + \ddot{\boldsymbol{r}}_{\mathrm{L}yz\mathrm{S}}. \tag{6.18}$$

4) Support of Double Cardan Joints

The couplings between a shaft of a linear actuator and the support of a double Cardan joint are purely rotational, as fig. 6.4. The rotation of the common axis of two limbs, $\{D_3\}$, depends only on the rotations of linear actuators. Since the constraint between $\{S\}$ and $\{D_3\}$ is a rotation vertical to $\boldsymbol{x}_{\text{common}}$ in fig.6.3, there exist following relations.

$$e^{\tilde{\boldsymbol{r}}\text{S}yz} = e^{\tilde{\boldsymbol{r}}\text{D1}}e^{\tilde{\boldsymbol{r}}\text{D2}y}e^{\tilde{\boldsymbol{r}}\text{D3}z} \tag{6.19-1}$$

$$e^{\tilde{\boldsymbol{r}}\text{S}yz}\tilde{\boldsymbol{r}}_{\text{S}yz} = \left(\tilde{\boldsymbol{r}}_{\text{D1}} + \tilde{\boldsymbol{r}}_{\text{D2}y} + \tilde{\boldsymbol{r}}_{\text{D3}z}\right)e^{\tilde{\boldsymbol{r}}\text{D1}}e^{\tilde{\boldsymbol{r}}\text{D2}y}e^{\tilde{\boldsymbol{r}}\text{D3}z} \tag{6.19-2}$$

$$e^{\tilde{\boldsymbol{r}}\text{S}yz}\ddot{\tilde{\boldsymbol{r}}}_{\text{S}yz} = e^{\tilde{\boldsymbol{r}}\text{D1}}\ddot{\tilde{\boldsymbol{r}}}_{\text{D1}}e^{\tilde{\boldsymbol{r}}\text{D2}y}e^{\tilde{\boldsymbol{r}}\text{D3}z} + e^{\tilde{\boldsymbol{r}}\text{D1}}e^{\tilde{\boldsymbol{r}}\text{D2}y}\ddot{\tilde{\boldsymbol{r}}}_{\text{D2}y}e^{\tilde{\boldsymbol{r}}\text{D3}z} + e^{\tilde{\boldsymbol{r}}\text{D1}}e^{\tilde{\boldsymbol{r}}\text{D2}y}e^{\tilde{\boldsymbol{r}}\text{D3}z}\ddot{\tilde{\boldsymbol{r}}}_{\text{D3}z} \tag{6.19-3}$$

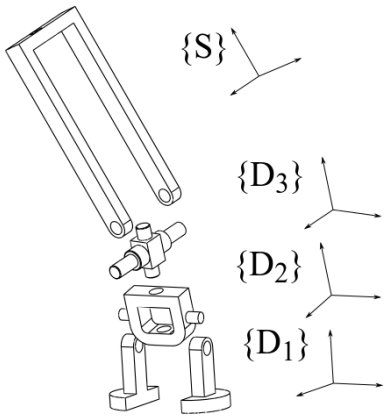

Figure 6.4 The composition of the support part and their coordinates of one double Cardan joint.

Applying the rotational acceleration to a z-vector, the rotational accelerations of rigid bodies $\{D_2\}$ will be,

$$\ddot{\boldsymbol{r}}_{\text{D2}y} = \tilde{\boldsymbol{z}}e^{-\tilde{\boldsymbol{r}}\text{D2}y}e^{-\tilde{\boldsymbol{r}}\text{D1}}\left(e^{\tilde{\boldsymbol{r}}\text{S}yz}\ddot{\tilde{\boldsymbol{r}}}_{\text{S}yz} - e^{\tilde{\boldsymbol{r}}\text{D1}}\ddot{\tilde{\boldsymbol{r}}}_{\text{D1}}e^{\tilde{\boldsymbol{r}}\text{D2}y}\right)\boldsymbol{z} \tag{6.20}$$

Bring it back to eq. (6.19-3), the rotational acceleration of $\{D_2\}$ in tensor form can be solved.

$$\ddot{\tilde{\boldsymbol{r}}}_{\text{D3}z} = e^{-\tilde{\boldsymbol{r}}\text{D3}z}e^{-\tilde{\boldsymbol{r}}\text{D2}y}\left(e^{-\tilde{\boldsymbol{r}}\text{D1}}e^{\tilde{\boldsymbol{r}}\text{S}yz}\ddot{\tilde{\boldsymbol{r}}}_{\text{S}yz} - \ddot{\tilde{\boldsymbol{r}}}_{\text{D1}}e^{\tilde{\boldsymbol{r}}\text{D2}y}e^{\tilde{\boldsymbol{r}}\text{D3}z}\right) - e^{-\tilde{\boldsymbol{r}}\text{D3}z}\ddot{\tilde{\boldsymbol{r}}}_{\text{D2}y}e^{\tilde{\boldsymbol{r}}\text{D3}z} \tag{6.21}$$

Thus, the rotational accelerations of all the parts of a double Cardan joint are

$$\begin{cases} \ddot{\boldsymbol{r}}_{\mathrm{D1}} = \ddot{\boldsymbol{r}}_{\mathrm{D1}} \\ \ddot{\boldsymbol{r}}_{\mathrm{D2}} = e^{\tilde{\boldsymbol{r}}_{\mathrm{D1}}} e^{\tilde{\boldsymbol{r}}_{\mathrm{D2}y}} \ddot{\boldsymbol{r}}_{\mathrm{D2}y} \\ \ddot{\boldsymbol{r}}_{\mathrm{D3}} = e^{\tilde{\boldsymbol{r}}_{\mathrm{D1}}} e^{\tilde{\boldsymbol{r}}_{\mathrm{D2}y}} e^{\tilde{\boldsymbol{r}}_{\mathrm{D3}z}} \ddot{\boldsymbol{r}}_{\mathrm{D3}z} \end{cases} \tag{6.22}$$

Where, $\ddot{\boldsymbol{r}}_{\mathrm{D1}}$ was obtained through the acceleration of foot platform.

6.2.3 Acceleration Integrations of the Complete Mechanism

The accelerations of all the parts of a parallel mechanism can be confirmed if the motion of end effector and base platforms are confirmed. The assembly of CENTAUROB are shown in fig. 6.5. The whole robot will be handled as three platforms, {H}, {F_1} and {F_2}, and 24 linear actuator parts, {L_{ijN}} and {L_{ijS}}, where i = 1,2, j = A, B, …, F. Since the inertia of shafts of Cardan joints are much smaller comparing to the platforms and linear actuators, their accelerations can be found in former parts but will not be discussed in this part.

The accelerations will be analysed according to some characteristic points, they are, $\boldsymbol{p}_{\mathrm{H0}}$, $\boldsymbol{p}_{\mathrm{F}i0}$, $\boldsymbol{p}_{\mathrm{H}ij}$ and $\boldsymbol{p}_{\mathrm{F}ij}$, which are defined at the geometric centres of hip and foot platforms, rotational centres of Cardan joints and double Cardan joints, respectively. Since all the kinematic pairs between the platforms and the linear actuators are concentrically rotational, all the parts of them (such as the cross shaft, input and output shafts of a Cardan joint, axis-1, -2 and -3 of a double Cardan joint) obtain the same translational acceleration at the rotational centre of them. The accelerations of two end points of one linear actuator can be obtained as

$$\begin{cases} \ddot{\boldsymbol{d}}_{\mathrm{L}_{ij\mathrm{N}}}(\boldsymbol{p}_{\mathrm{H}ij}) = \ddot{\boldsymbol{d}}_{\mathrm{H}}(\boldsymbol{p}_{\mathrm{H}ij}) = \ddot{\boldsymbol{t}}_{\mathrm{H}}(\boldsymbol{p}_{\mathrm{H0}}) + \ddot{\boldsymbol{r}}_{\mathrm{H}} \times \boldsymbol{d}_{\boldsymbol{p}_{\mathrm{H0}}-\boldsymbol{p}_{\mathrm{H}ij}} + \dot{\boldsymbol{r}}_{\mathrm{H}} \times \left(\dot{\boldsymbol{r}}_{\mathrm{H}} \times \boldsymbol{d}_{\boldsymbol{p}_{\mathrm{H0}}-\boldsymbol{p}_{\mathrm{H}ij}}\right) \\ \ddot{\boldsymbol{d}}_{\mathrm{L}_{ij\mathrm{S}}}(\boldsymbol{p}_{\mathrm{F}ij}) = \ddot{\boldsymbol{d}}_{\mathrm{F}_i}(\boldsymbol{p}_{\mathrm{F}ij}) = \ddot{\boldsymbol{t}}_{\mathrm{F}i}(\boldsymbol{p}_{\mathrm{F}i0}) + \ddot{\boldsymbol{r}}_{\mathrm{F}i} \times \boldsymbol{d}_{\boldsymbol{p}_{\mathrm{F}i0}-\boldsymbol{p}_{\mathrm{F}ij}} + \dot{\boldsymbol{r}}_{\mathrm{F}i} \times \left(\dot{\boldsymbol{r}}_{\mathrm{F}i} \times \boldsymbol{d}_{\boldsymbol{p}_{\mathrm{F}i0}-\boldsymbol{p}_{\mathrm{F}ij}}\right). \end{cases} \tag{6.23}$$

Based on the acceleration trajectories of three platforms, {H}, {F_1} and {F_2}, the acceleration of them on characteristic points can be derived through eq. (6.23). Bring eq. (6.23) to eq. (6.10) and eq. (6.12), the length variation acceleration of linear actuator, $\ddot{d}_{\mathrm{L}ij}$, and the rotational acceleration projection of linear actuator on x-y plane of it, $\ddot{\boldsymbol{r}}_{\mathrm{L}ijxy}$, can be obtained. Bringing $\ddot{d}_{\mathrm{L}ij}$ and $\ddot{\boldsymbol{d}}_{\mathrm{L}_{ij\mathrm{S}}}(\boldsymbol{p}_{\mathrm{F}ij})$ to eq. (6.8-1), the translational acceleration of rigid body

$\{L_{ijN}\}$ on point $\boldsymbol{p}_{Fij}$ is then obtained, as $\ddot{\boldsymbol{d}}_{L_{ijN}}(\boldsymbol{p}_{Fij})$. Bring it to eq. (6.4), (6.5) and (6.6), and replacing $\ddot{\boldsymbol{d}}_O(\boldsymbol{p}_O)$ and $\ddot{\boldsymbol{d}}_I(\boldsymbol{p}_C)$ with $\ddot{\boldsymbol{d}}_{L_{ijN}}(\boldsymbol{p}_{Fij})$ and $\ddot{\boldsymbol{d}}_{L_{ijN}}(\boldsymbol{p}_{Hij})$, the rotational acceleration of $\{L_{ijN}\}$, $\ddot{\boldsymbol{r}}_{LijN}$, can be derived as $\ddot{\boldsymbol{r}}_{LijN} = \ddot{\boldsymbol{r}}_{Lijxy} + \ddot{\boldsymbol{r}}_{LijNz}$.

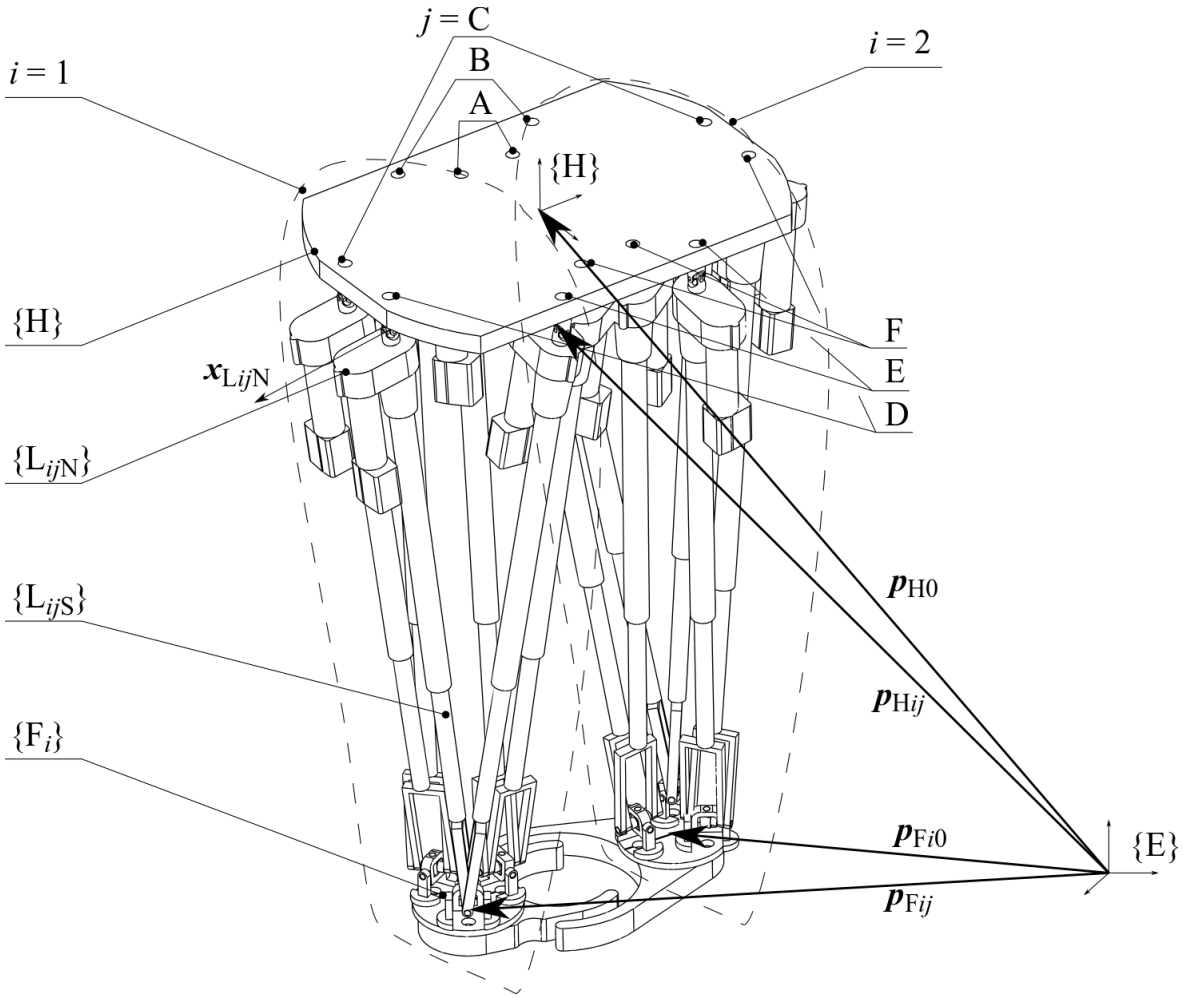

Figure 6.5 Assembly of CENTAUROB. The characteristic points in inertial frame and coordinates systems are also marked.

Introducing eq. (6.23) to eq. (6.8-2), the acceleration of rigid body $\{L_{ijS}\}$ on point $\boldsymbol{p}_{Hij}$ can be derived with corresponding subscripts, as $\ddot{\boldsymbol{d}}_{L_{ijS}}(\boldsymbol{p}_{Hij})$. Bring it to eq. (6.15), the rotational acceleration of $\{L_{ijS}\}$ along their common axis is $\ddot{\boldsymbol{r}}_{LijSx}$. Further, through eq. (6.16), (6.17) and (6.18), $\ddot{\boldsymbol{r}}_{L_{imS}}$ and $\ddot{\boldsymbol{r}}_{L_{inS}}$ can be obtained, where m = B, D, F and n = A, C, E.

Since the numerous subscripts of different components of each rigid body, the derivation of complete acceleration expressions will be given in the flowchart form, as fig 6.6.

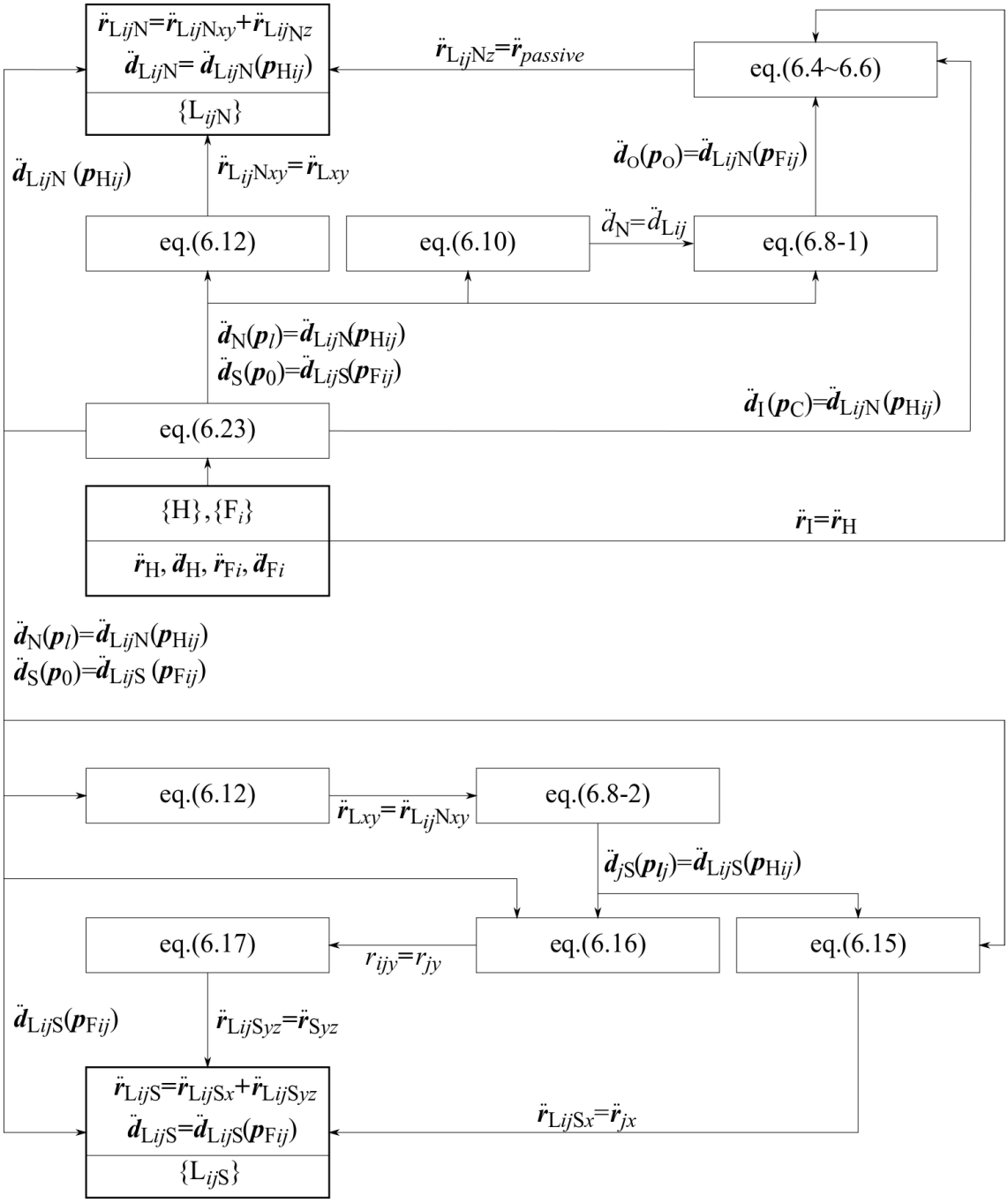

Figure 6.6 The equations introduction flowchart of accelerations.

6.2.4 Acceleration Simulations

Four motion cases will be simulated: the rotations around *z* and *y* –axes, and the translational along *x* and *z* –axes, as shown in fig. 6.7. The trajectory parameters are provided in table. 6.1. Since the symmetry of joint assignment of joints on the hip platform, the rotational accelerations of only three sleeves are shown in the results.

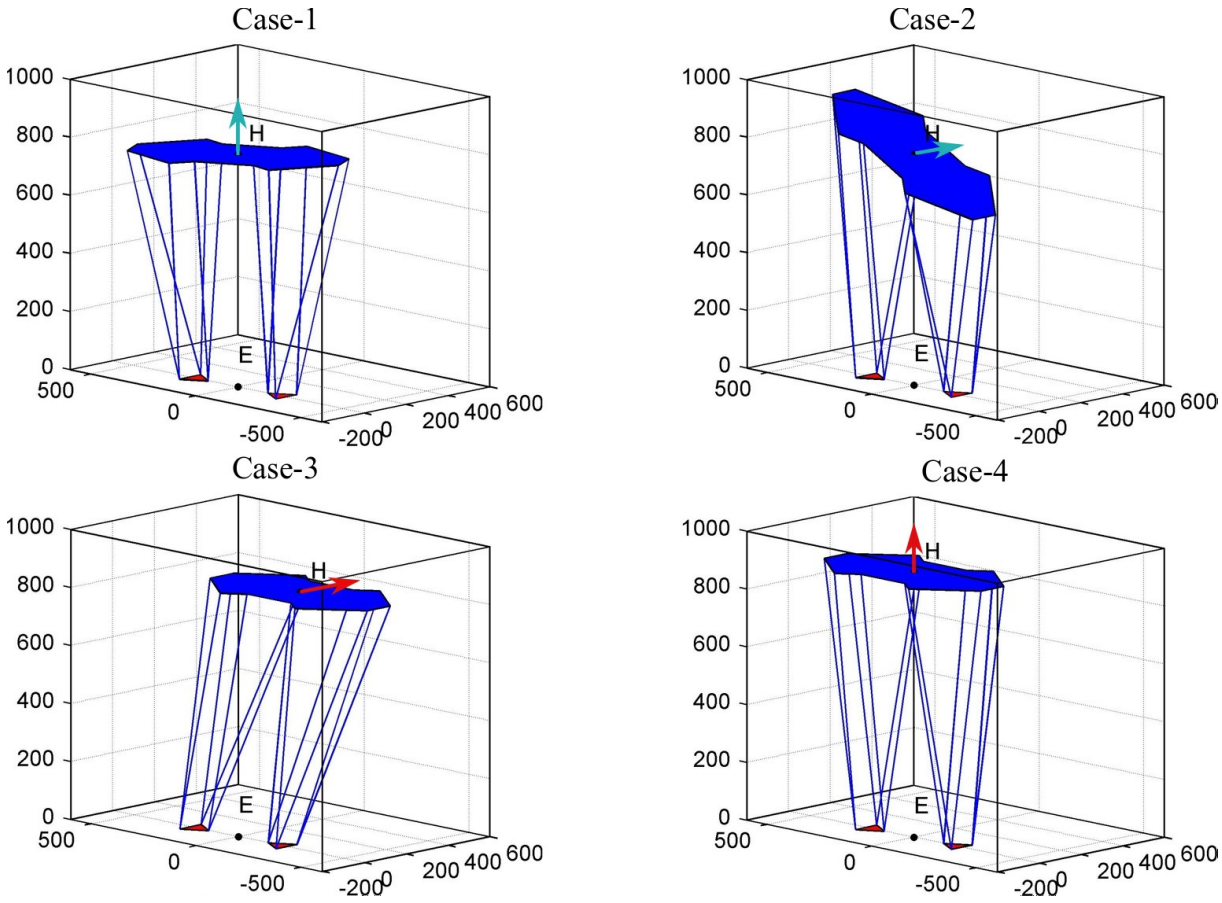

Figure 6.7 Four hip motion cases for acceleration simulation.

Table 6.1 Trajectories of four hip motion cases for acceleration simulation.

Cases	Trajectories (simulation time: T=2s)
1	$X_{\mathrm{H}}(t) = \left[0 \quad 0 \quad 0 \quad 0 \quad 0 \quad 0.25\pi \sin {}^{\pi t}/_{T}\right]^{\mathrm{T}}$
2	$X_{\mathrm{H}}(t) = \left[0 \quad 0 \quad 0 \quad 0.25\pi \sin {}^{\pi t}/_{T} \quad 0 \quad 0\right]^{\mathrm{T}}$
3	$X_{\mathrm{H}}(t) = \left[500 \sin {}^{\pi t}/_{T} \quad 0 \quad 0 \quad 0 \quad 0 \quad 0\right]^{\mathrm{T}}$
4	$X_{\mathrm{H}}(t) = \left[0 \quad 0 \quad 200 \sin {}^{\pi t}/_{T} \quad 0 \quad 0 \quad 0\right]^{\mathrm{T}}$

Case-1: In this case, the hip rotates along z-axis of the world coordinates, as shown in fig. 6.8-1. The accelerations are shown in fig. 6.8-2. The vectors of rotational acceleration of sleeves, $\ddot{\boldsymbol{r}}_{\mathrm{L}ij\mathrm{N}}$, are shown as scatters on a green unit sphere. The colour and size of scatters

are positively related to the norms of $\ddot{\boldsymbol{r}}_{\mathrm{L}ij\mathrm{N}}$. Besides, the norms of $\ddot{\boldsymbol{r}}_{\mathrm{L}ij\mathrm{N}}$ are shown as single curves. The result shows, the length variation accelerations, $\ddot{l}_{\mathrm{L}ij}$, of three limbs are similar. It is also notable that the accelerations are too small to observe when t = 0. Looking back upon eq. (6.3-3) and (6.4), the main component of $\ddot{\boldsymbol{r}}_{\mathrm{L}ij\mathrm{N}}$ is $\tilde{\dot{\boldsymbol{r}}}_{\mathrm{L}ij\mathrm{N}}{}^{2}\boldsymbol{l}_{\mathrm{L}ij}$ at t = 0. Compare to other cases, $\dot{\boldsymbol{r}}_{\mathrm{L}ij\mathrm{N}}$ is almost parallel to $\boldsymbol{l}_{\mathrm{L}ij\mathrm{N}}$, which leads to zero initial rotational acceleration. On the other hand, the rotation accelerations are rough-equally distributed between limbs.

Case-2: Here, the hip rotates along the *x*-axis w.r.t the world coordinates, as fig. 6.9-1. The vectors are illustrated inheriting the setups in Case-1, as fig. 6.9-2. Differ from Case-1, the rotational acceleration of limb increases along the distance increasing between the rotation centre to the joint centre. For same rotational amplitude and velocity, the maximum rotational accelerations are smaller than which in Case-1, while $\ddot{l}_{\mathrm{L1C}}$ locates in a bigger range.

Case-3: Here, the hip moves along the *x*-axis w.r.t the world coordinates, as fig. 6.10-1. The vectors are illustrated inheriting the setups in Case-1, as fig. 6.10-2. In this case, the rotational accelerations distributed equivalently among limbs and their directions were limited in a small zone on the unitary sphere, since all the limbs rotate steady towards the same direction. There is an obvious direction switching phase of the rotational acceleration when limb-A and -B are moving over the *y*-*z* plane of the world coordinates. This is not happening on the limb-C since its initial pose already exceeded the *x*=0 plane (seeing fig. 6.5).

Case-4: Here, the hip moves along the *z*-axis w.r.t the world coordinates, as shown in fig. 6.11-1. The vectors are illustrated inheriting the setups in Case-1, as fig. 6.11-2. The rotational accelerations are limited in a small range due to the limited change of their poses. However, the direction of them diverse along the distance increasing between the hip and hip joint centres, such as between limb-A and limb-C. In this case, the differences of $\ddot{l}_{\mathrm{L}ij}$ among limbs are not notable.

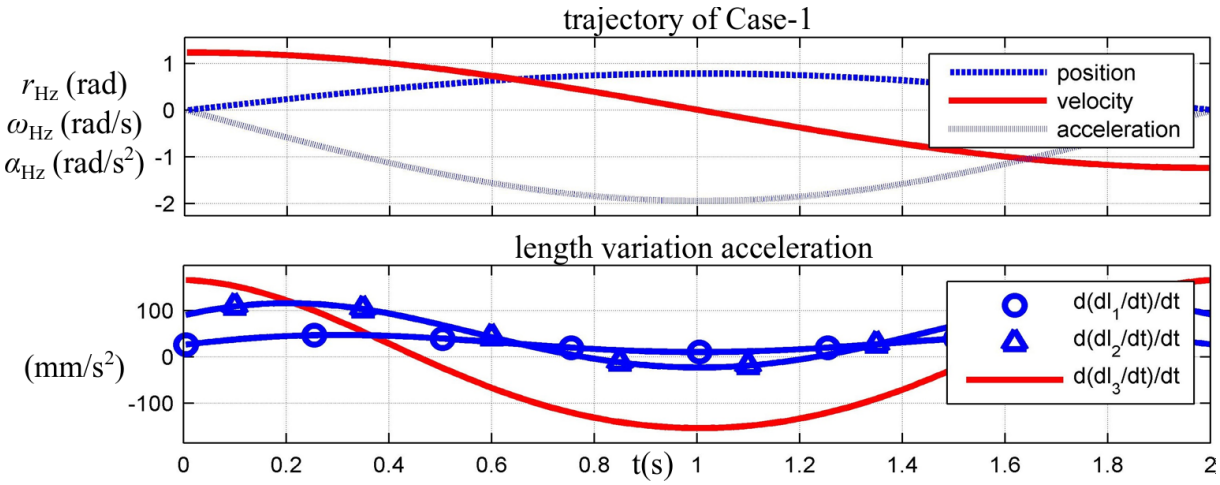

Figure 6.8-1 The trajectory of hip platform and linear actuator accelerations in Case-1.

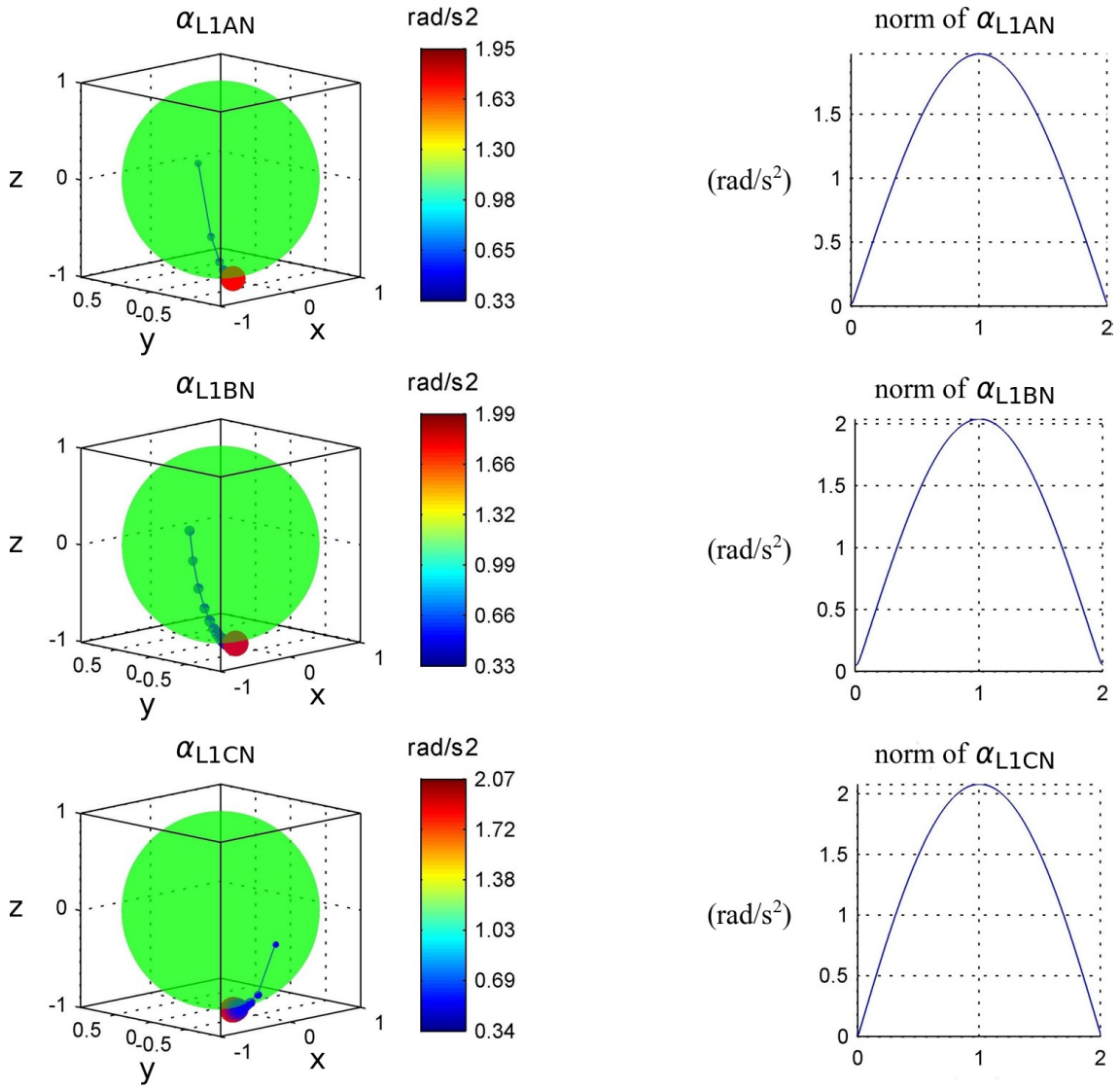

Figure 6.8-2 The rotational acceleration of sleeves in Case-1.

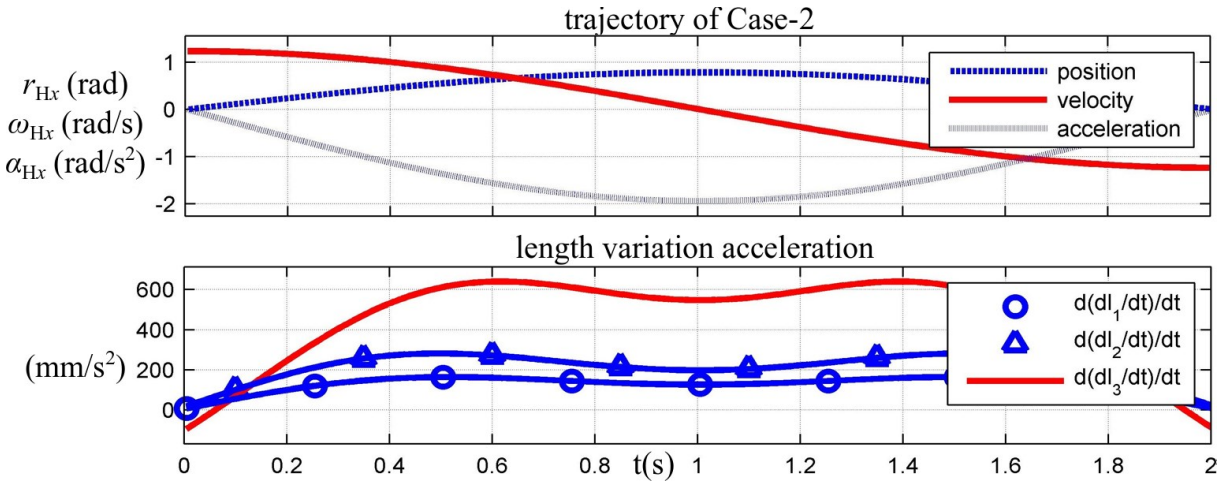

Figure 6.9-1 The trajectory of hip platform and linear actuator accelerations in Case-2.

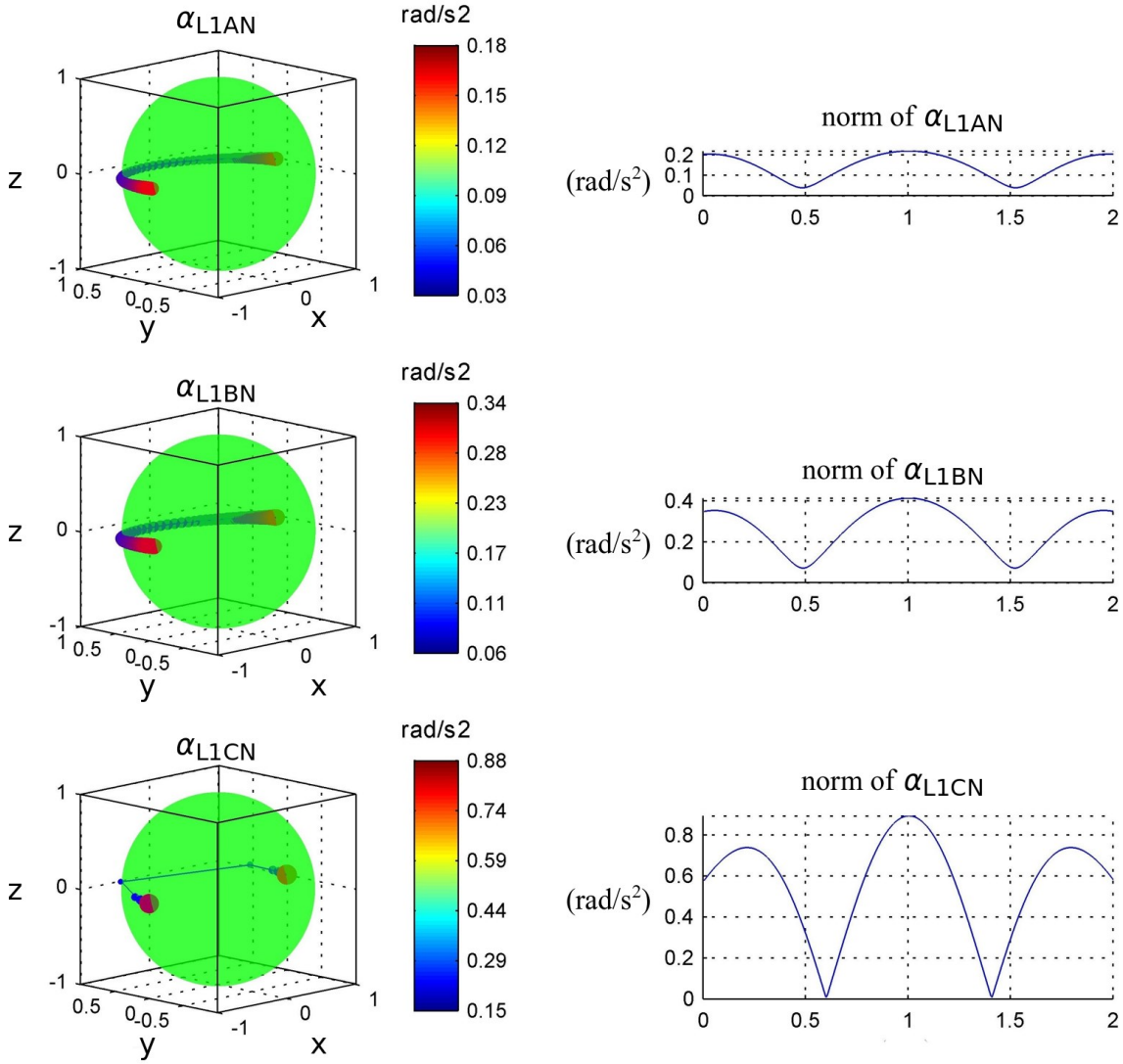

Figure 6.9-2 The rotational acceleration of sleeves in Case-2.

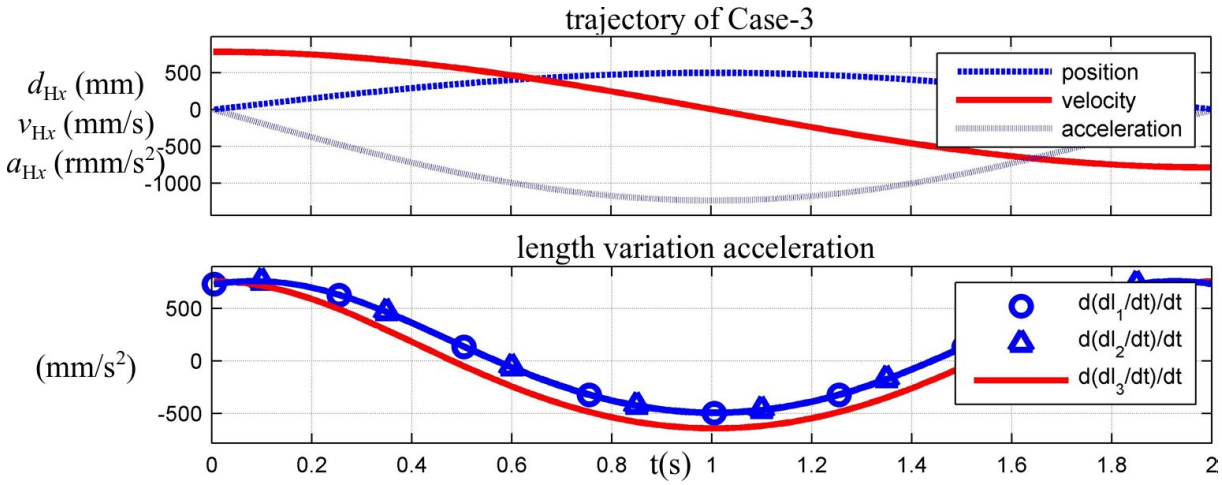

Figure 6.10-1 The trajectory of hip platform and linear actuator accelerations in Case-3.

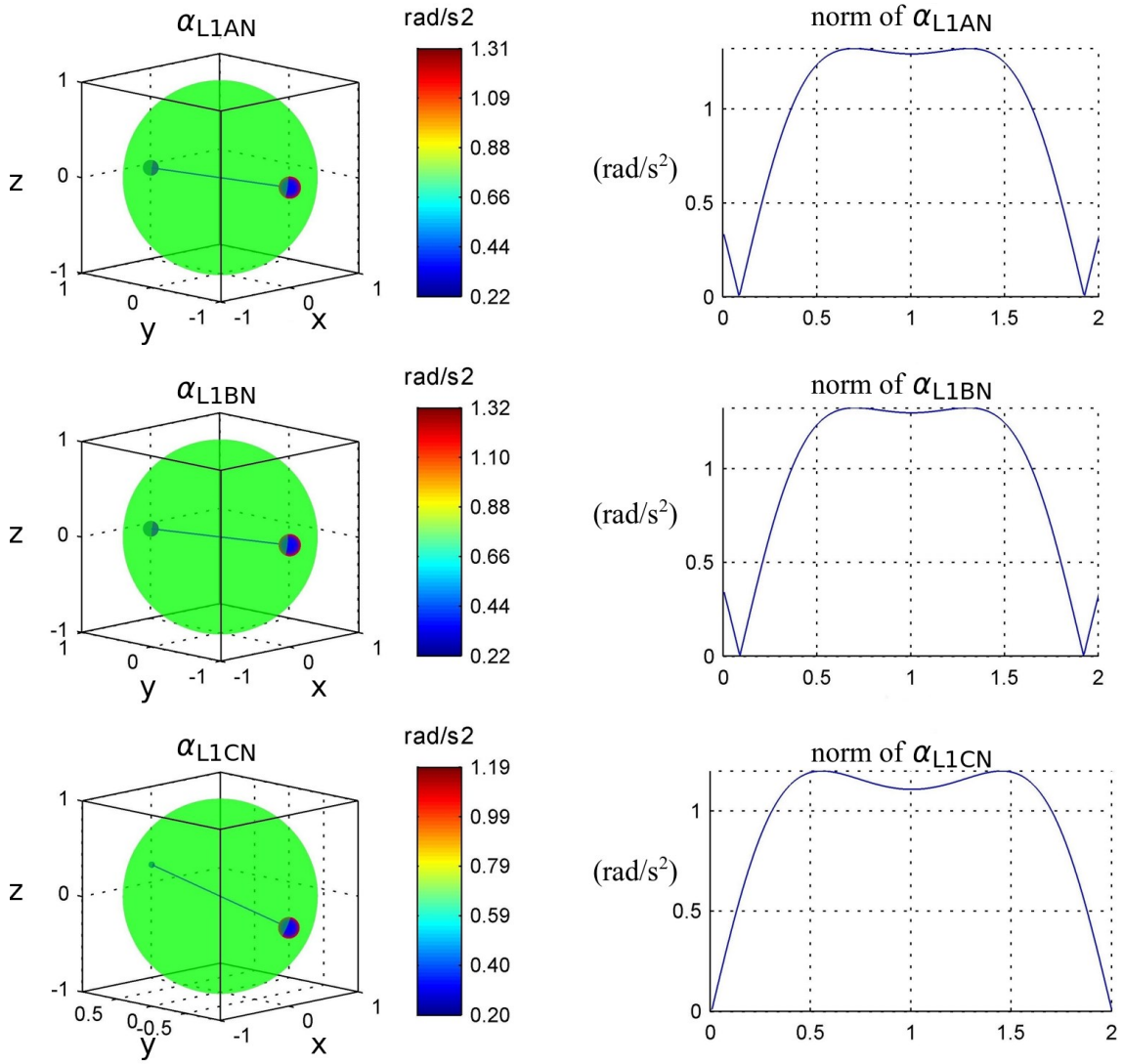

Figure 6.10-2 The rotational acceleration of sleeves in Case-3.

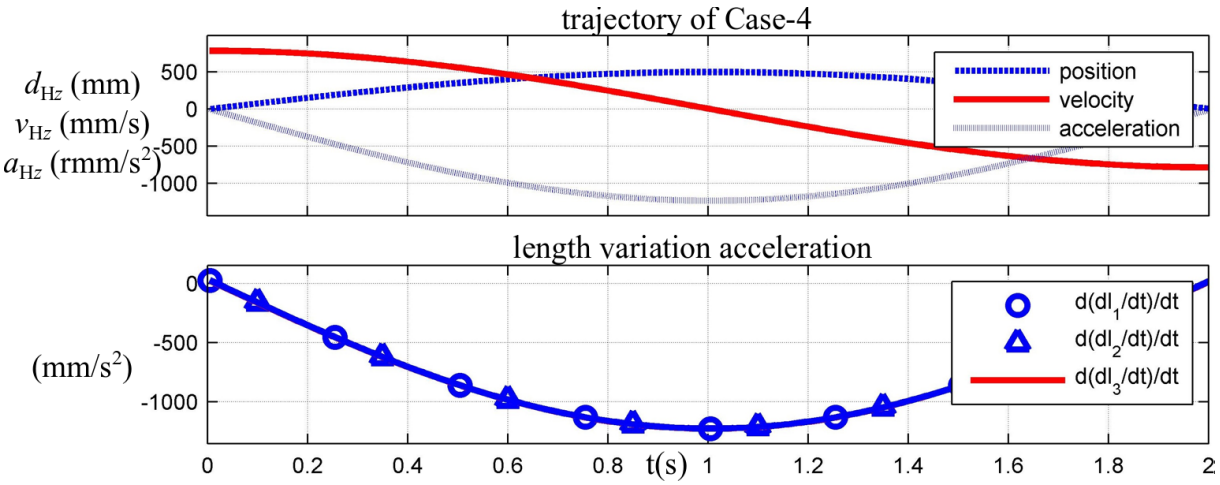

Figure 6.11-1 The trajectory of hip platform and linear actuator accelerations in Case-4.

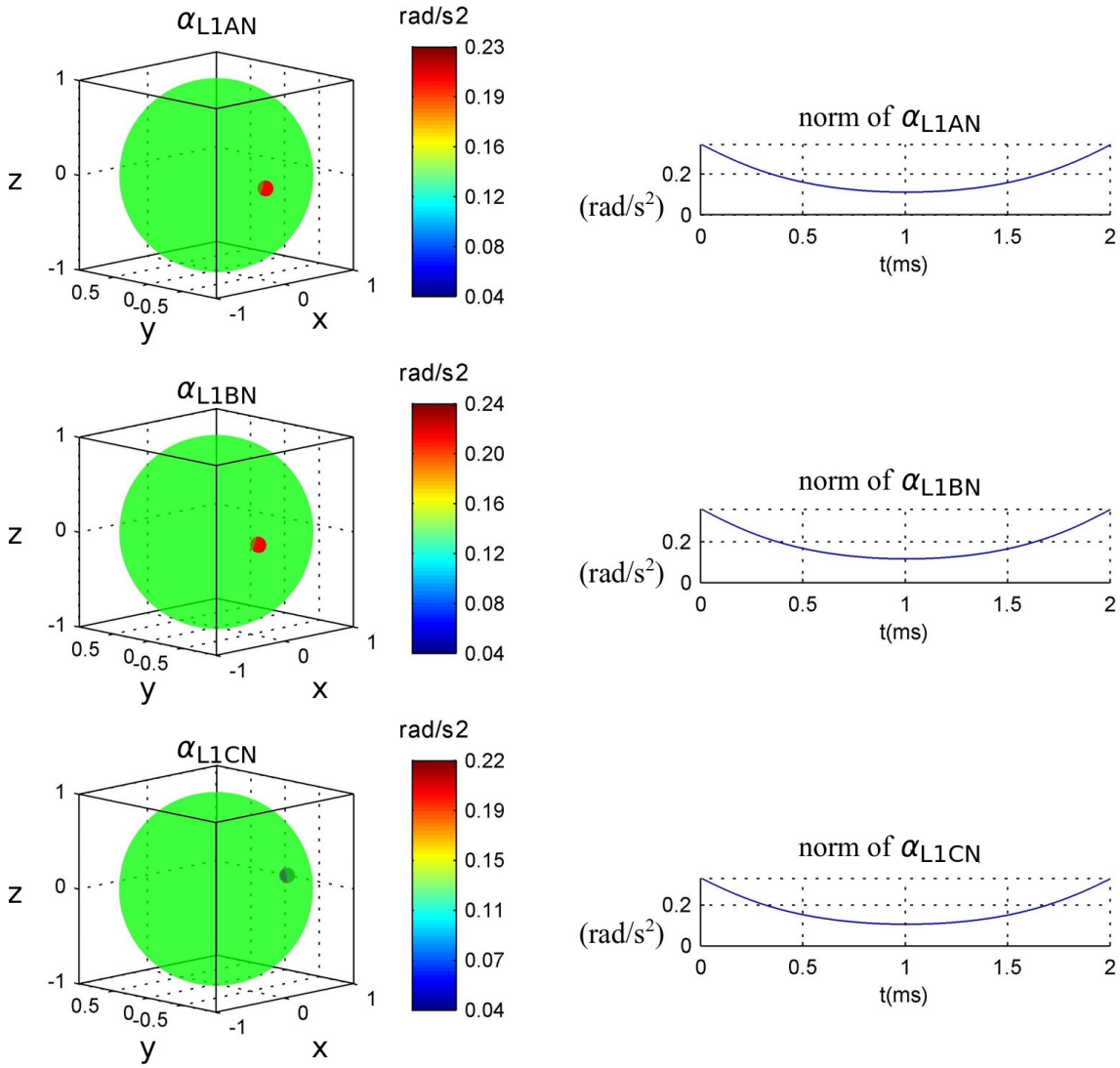

Figure 6.11-2 The rotational acceleration of sleeves in Case-4.

6.3 Inverse Dynamic Model

In this section, the inverse dynamic model (IDM) will be formulated following the virtual work principle, and the actuating forces will be predicted. As a biped walking mechanism, CENTAUROB obtains two motion phases: *leg swing* and *hip moving*. During the leg swing phase, the robot can be considered as a full-rank 6- or 12-dimensional system (depending on 1 or 2 actuated legs), while for a hip moving phase, the system will be involved into a semi-12 dimensional case. The so-called 'semi-' implies a case that the moving platform obtains only 6-dimensional motions, while it is driven by 12 actuators. Till the end of this chapter, the model will be limited in a full-rank 6 or 12 dimensional space, or in other words, only the swing phase will be analysed.

6.3.1 Methodology

Under *d' Alembert theory*, the accelerations applied on mass systems are taken as inertial forces, the dynamic system will be described in equivalent static equations, as

$$\sum \boldsymbol{F}_{\mathrm{ext}-i} + \sum \boldsymbol{F}_{\mathrm{inn}-i} + \int -\boldsymbol{a}(\boldsymbol{X})\, dm = \boldsymbol{0}. \tag{6.24}$$

In which, $\boldsymbol{F}_{\mathrm{ext}-i}$ is the i-th external force applied on the system, while $\boldsymbol{F}_{\mathrm{inn}-i}$ is the i-th inner force between mass points, $\boldsymbol{a}(\boldsymbol{X})$ is the acceleration of position $\boldsymbol{X}$. The inner, external and inertial forces in the equation are named as general force.

The *principle of virtual works* states that, for a static-definite system, if a virtual infinitesimal displacement was applied on the rigid bodies, the virtual work sum of all the forces should be 0, since the system is in fact static. If taking *d' Alembert theory* into consideration, this principle is also capable for system of general forces. For a multi-body system, the virtual work equation is

$$\delta \boldsymbol{q}^{\mathrm{T}} \boldsymbol{\tau} + \sum \delta \boldsymbol{X}_i{}^{\mathrm{T}} \boldsymbol{F}_i = 0. \tag{6.25}$$

Where, $\delta \boldsymbol{q}$ is the virtual displacement of action point of active forces, $\boldsymbol{\tau}$. $\delta \boldsymbol{X}_i$ is the virtual displacement vector of the mass centre of rigid body *i*. $\boldsymbol{F}_i$ is the general force applied on rigid body *i*. Due to that the sum of virtual works of inner forces is always 0, only the inertial forces of $\boldsymbol{F}_i$ will be considered. The virtual displacements obey the mechanical constraints of the system, given a virtual displacement of controlled body, $\delta \boldsymbol{X}_k$, there exist the following relations

$$\begin{cases} \delta \boldsymbol{q} &= \boldsymbol{J}_{\boldsymbol{q}} \delta \boldsymbol{X}_k, \\ \delta \boldsymbol{X}_i &= \boldsymbol{J}_i \delta \boldsymbol{X}_k. \end{cases} \tag{6.26}$$

In which, $\boldsymbol{J}_{\boldsymbol{q}}$ and $\boldsymbol{J}_i$ are the Jacobians between the velocity of controlled body, namely $\dot{\boldsymbol{q}} = \boldsymbol{J}_{\boldsymbol{q}} \dot{\boldsymbol{X}}_k$ and $\dot{\boldsymbol{X}}_i = \boldsymbol{J}_i \dot{\boldsymbol{X}}_k$. Bring eq. (6.26) to eq. (6.25), there is

$$\delta \boldsymbol{X}_k{}^{\mathrm{T}} \left(\boldsymbol{J}_{\boldsymbol{q}}{}^{\mathrm{T}} \boldsymbol{\tau} + \sum \boldsymbol{J}_i{}^{\mathrm{T}} \boldsymbol{F}_i \right) = 0. \tag{6.27}$$

Because of the universality of all virtual displacements, the active forces can be obtained through

$$\boldsymbol{J}_{\boldsymbol{q}}{}^{\mathrm{T}} \boldsymbol{\tau} = - \sum \boldsymbol{J}_i{}^{\mathrm{T}} \boldsymbol{F}_i \,. \tag{6.28}$$

Note that, the equation system represented by eq. (6.28) is not necessarily full rank in the dynamic point of view. If the rank of $\boldsymbol{J}_{\boldsymbol{q}}$ is smaller than the dimension of $\boldsymbol{\tau}$, there will be no unique solution, extra constraints should be introduced.

6.3.2 Expanded Inverse Jacobians on Mass Centres of Rigid Bodies

The kinematic problem of the main component of CENTAUROB was discussed in Chapter 4. However, the focus was laid on the solution of control variables and the compensation of passive rotation. During the discussion of dynamics, the motion of all the main parts must be fully expressed, such as rotational and translational velocities of hip, foot platforms and sleeves and shafts of linear actuators.

The rotational and translational velocities of different parts of were derived in Chapter 4. Hereby, the velocities will be transformed to the mass centres of all the parts and assembled as inverse Jacobians. Since the rotational velocity are irrelevant to the coordinates centre, only translational will be rewritten. Most Jacobians of rigid bodies depend on the relative positions of two platforms, the general coordinates for the whole mechanism are consequently defined as

$$\boldsymbol{X}_{\Sigma} = \begin{bmatrix} \boldsymbol{X}_{\mathrm{H}} \\ \boldsymbol{X}_{\mathrm{F1}} \\ \boldsymbol{X}_{\mathrm{F2}} \end{bmatrix}. \tag{6.29}$$

1) Velocity Transformation

As illustrated in fig. 6.12, the position of a point on one rigid body-*i* can be obtained by

$$\boldsymbol{d}_i(\boldsymbol{p}_{i\mathrm{C}}) = \boldsymbol{d}_i(\boldsymbol{p}_{i\mathrm{O}}) + e^{\tilde{\boldsymbol{r}}_i{}^{\{i\}}}\boldsymbol{p}_{i\mathrm{O-C}}. \tag{6.30}$$

Where, the subscript O denotes the coordinates origin of a rigid body. The first order differentiate of it over time is

$$\dot{\boldsymbol{d}}_i(\boldsymbol{p}_{i\mathrm{C}}) = \dot{\boldsymbol{d}}_i(\boldsymbol{p}_{i\mathrm{O}}) + e^{\tilde{\boldsymbol{r}}_i{}^{\{i\}}}\tilde{\dot{\boldsymbol{r}}}_i{}^{\{i\}}\boldsymbol{p}_{i\mathrm{O-C}} = \dot{\boldsymbol{t}}_i - \tilde{\boldsymbol{p}}_{i\mathrm{O-C}}\dot{\boldsymbol{r}}_i = \begin{bmatrix} \boldsymbol{I} & -\boldsymbol{R}_i{}^{\{i\}}\tilde{\boldsymbol{p}}_{i\mathrm{O-C}}\boldsymbol{R}_i{}^{\mathrm{T}} \end{bmatrix}\dot{\boldsymbol{X}}_i. \tag{6.31}$$

The second order differential of eq. (6.30) will be

$$\begin{aligned} \ddot{\boldsymbol{d}}_i(\boldsymbol{p}_{i\mathrm{C}}) &= \ddot{\boldsymbol{d}}_i(\boldsymbol{p}_{i\mathrm{O}}) + e^{\tilde{\boldsymbol{r}}_i{}^{\{i\}}}\tilde{\dot{\boldsymbol{r}}}_i{}^{2\{i\}}\boldsymbol{p}_{i\mathrm{O-C}} + e^{\tilde{\boldsymbol{r}}_i{}^{\{i\}}}\tilde{\ddot{\boldsymbol{r}}}_i{}^{\{i\}}\boldsymbol{p}_{i\mathrm{O-C}} \\ &= \begin{bmatrix} \boldsymbol{I} & -\boldsymbol{R}_i{}^{\{i\}}\tilde{\boldsymbol{p}}_{i\mathrm{O-C}}\boldsymbol{R}_i{}^{\mathrm{T}} \end{bmatrix}\ddot{\boldsymbol{X}}_i + \tilde{\dot{\boldsymbol{r}}}_i{}^{2}\boldsymbol{R}_i{}^{\{i\}}\boldsymbol{p}_{i\mathrm{O-C}} \end{aligned} \tag{6.32}$$

Substituting the subscripts with different parts of the whole mechanism, the translational accelerations of mass centres will be obtained, while the rotational velocity and acceleration are unchanged. For instance, the velocity and acceleration of the hip platform will be

$$\begin{cases} \dot{\boldsymbol{d}}_{\mathrm{H}}(\boldsymbol{p}_{\mathrm{HC}}) = \begin{bmatrix} \boldsymbol{I} & -\boldsymbol{R}_{\mathrm{H}}{}^{\{\mathrm{H}\}}\tilde{\boldsymbol{p}}_{\mathrm{HO-C}}\boldsymbol{R}_{\mathrm{H}}{}^{\mathrm{T}} \end{bmatrix}\dot{\boldsymbol{X}}_{\mathrm{H}}, \\ \ddot{\boldsymbol{d}}\ \ (\boldsymbol{p}_{\mathrm{C}}) = \begin{bmatrix} \boldsymbol{I} & -\boldsymbol{R}_{\mathrm{H}}{}^{\{\mathrm{H}\}}\tilde{\boldsymbol{p}}_{\mathrm{HO-C}}\boldsymbol{R}_{\mathrm{H}}{}^{\mathrm{T}} \end{bmatrix}\ddot{\boldsymbol{X}}_{\mathrm{H}} + \tilde{\dot{\boldsymbol{r}}}_{\mathrm{H}}{}^{2}\boldsymbol{R}_{\mathrm{H}}{}^{\{i\}}\boldsymbol{p}_{\mathrm{HO-C}}. \end{cases} \tag{6.33}$$

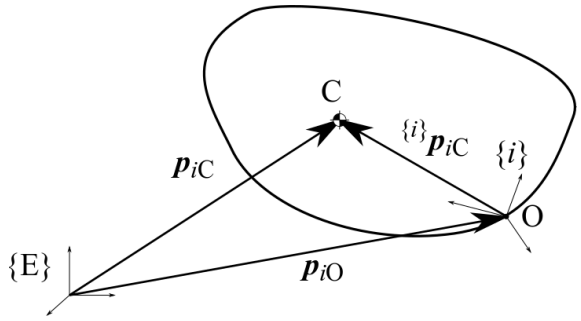

Figure 6.12 The transformation of vectors between different points.

2) Inverse Jacobians of Platforms

The velocities of hip and foot platforms on the mass centres are

$$\dot{\boldsymbol{d}}_k(\boldsymbol{p}_{k\mathrm{C}}) = \dot{\boldsymbol{d}}_k(\boldsymbol{p}_{k\mathrm{O}}) - \widetilde{\boldsymbol{p}}_{k\mathrm{O-C}}\dot{\boldsymbol{r}}_k = \dot{\boldsymbol{t}}_k - \boldsymbol{R}_k{}^{\{k\}}\widetilde{\boldsymbol{p}}_{k\mathrm{O-C}}\boldsymbol{R}_k{}^{\mathrm{T}}\dot{\boldsymbol{r}}_k. \tag{6.34}$$

Where, k stands for, H and F_i. Thus, the inverse Jacobians of platforms are

$$\dot{\boldsymbol{X}}_{k\mathrm{C}} = \begin{bmatrix}\dot{\boldsymbol{d}}_k(\boldsymbol{p}_{k\mathrm{C}}) \\ \dot{\boldsymbol{r}}_k\end{bmatrix} = \begin{bmatrix}\boldsymbol{I} & -\boldsymbol{R}_k{}^{\{k\}}\widetilde{\boldsymbol{p}}_{k\mathrm{O-C}}\boldsymbol{R}_k{}^{\mathrm{T}} \\ \boldsymbol{0} & \boldsymbol{I}\end{bmatrix}\begin{bmatrix}\dot{\boldsymbol{t}}_k \\ \dot{\boldsymbol{r}}_k\end{bmatrix} = \boldsymbol{J}_{k\mathrm{C}}^{inv}\dot{\boldsymbol{X}}_k \tag{6.35}$$

Respectively, the relations between platforms and general coordinates are

$$\begin{cases}\dot{\boldsymbol{X}}_{\mathrm{HC}} = [\boldsymbol{J}_{\mathrm{HC}}^{inv} \quad \boldsymbol{0} \quad \boldsymbol{0}]\dot{\boldsymbol{X}}_{\Sigma} = \bar{\boldsymbol{J}}_{\mathrm{HC}}^{inv}\dot{\boldsymbol{X}}_{\Sigma} \\ \dot{\boldsymbol{X}}_{\mathrm{F1C}} = [\boldsymbol{0} \quad \boldsymbol{J}_{\mathrm{F1C}}^{inv} \quad \boldsymbol{0}]\dot{\boldsymbol{X}}_{\Sigma} = \bar{\boldsymbol{J}}_{\mathrm{F1C}}^{inv}\dot{\boldsymbol{X}}_{\Sigma} \\ \dot{\boldsymbol{X}}_{\mathrm{F2C}} = [\boldsymbol{0} \quad \boldsymbol{0} \quad \boldsymbol{J}_{\mathrm{F2C}}^{inv}]\dot{\boldsymbol{X}}_{\Sigma} = \bar{\boldsymbol{J}}_{\mathrm{F2C}}^{inv}\dot{\boldsymbol{X}}_{\Sigma}\end{cases} \tag{6.36}$$

3) Inverse Jacobians of Linear Actuator Sleeves and Shafts

The velocities of linear actuator sleeves and shafts at mass centres are

$$\dot{\boldsymbol{d}}_{\mathrm{L}ijn}(\boldsymbol{p}_{\mathrm{L}ijn\mathrm{C}}) = \dot{\boldsymbol{d}}_{\mathrm{L}ijn}(\boldsymbol{p}_{\mathrm{L}ijn\mathrm{O}}) - \widetilde{\boldsymbol{p}}_{\mathrm{L}ijn\mathrm{O-C}}\dot{\boldsymbol{r}}_{\mathrm{L}ijn} = \dot{\boldsymbol{t}}_{\mathrm{L}ijn} - \boldsymbol{R}_{\mathrm{L}ijn}{}^{\{\mathrm{L}ijn\}}\widetilde{\boldsymbol{p}}_{\mathrm{L}ijn\mathrm{O-C}}\boldsymbol{R}_{\mathrm{L}ijn}{}^{\mathrm{T}}\dot{\boldsymbol{r}}_{\mathrm{L}ijn} \tag{6.37}$$

In matrix form, it will be

$$\begin{aligned}\dot{\boldsymbol{X}}_{\mathrm{L}ijn\mathrm{C}} &= \begin{bmatrix}\dot{\boldsymbol{d}}_{\mathrm{L}ijn}(\boldsymbol{p}_{\mathrm{L}ijn\mathrm{C}}) \\ \boldsymbol{\varpi}_{\mathrm{L}ijn}\end{bmatrix} = \begin{bmatrix}\boldsymbol{I} & -\boldsymbol{R}_{\mathrm{L}ijn}{}^{\{\mathrm{L}ijn\}}\widetilde{\boldsymbol{p}}_{\mathrm{L}ijn\mathrm{O-C}}\boldsymbol{R}_{\mathrm{L}ijn}{}^{\mathrm{T}} \\ \boldsymbol{0} & \boldsymbol{I}\end{bmatrix}\begin{bmatrix}\dot{\boldsymbol{t}}_{\mathrm{L}ijn} \\ \dot{\boldsymbol{r}}_{\mathrm{L}ijn}\end{bmatrix} \\ &= \boldsymbol{J}_{\mathrm{L}ijn\mathrm{C}}^{inv}\begin{bmatrix}\boldsymbol{J}_{\mathrm{L}ijn-\mathrm{H}}^{inv} & \boldsymbol{J}_{\mathrm{L}ijn-\mathrm{F}i}^{inv}\end{bmatrix}\begin{bmatrix}\dot{\boldsymbol{X}}_{\mathrm{H}} \\ \dot{\boldsymbol{X}}_{\mathrm{F}i}\end{bmatrix}\end{aligned} \tag{6.38}$$

Where, *n* stands for N or S, indicates the sleeve (screw nut) or shaft of linear actuators. Thus, for linear actuators of leg-1 and leg-2, there are

$$\begin{cases} \dot{\boldsymbol{X}}_{\mathrm{L1}jn\mathrm{C}} = \left[\boldsymbol{J}^{inv}_{\mathrm{L1}jn\mathrm{C}}\boldsymbol{J}^{inv}_{\mathrm{L1}jn-\mathrm{H}} \quad \boldsymbol{J}^{inv}_{\mathrm{L1}jn\mathrm{C}}\boldsymbol{J}^{inv}_{\mathrm{L1}jn-\mathrm{F1}} \quad \boldsymbol{0}\right]\dot{\boldsymbol{X}}_{\Sigma} = \bar{\boldsymbol{J}}^{inv}_{\mathrm{L1}jn\mathrm{C}}\dot{\boldsymbol{X}}_{\Sigma} \\ \dot{\boldsymbol{X}}_{\mathrm{L2}jn\mathrm{C}} = \left[\boldsymbol{J}^{inv}_{\mathrm{L2}jn\mathrm{C}}\boldsymbol{J}^{inv}_{\mathrm{L1}jn-\mathrm{H}} \quad \boldsymbol{0} \quad \boldsymbol{J}^{inv}_{\mathrm{L2}jn\mathrm{C}}\boldsymbol{J}^{inv}_{\mathrm{L2}jn-\mathrm{F2}}\right]\dot{\boldsymbol{X}}_{\Sigma} = \bar{\boldsymbol{J}}^{inv}_{\mathrm{L2}jn\mathrm{C}}\dot{\boldsymbol{X}}_{\Sigma} \end{cases} \tag{6.39}$$

Sleeves

The inverse Jacobians can be obtained by the analysis in Chapter 4, they are given as following for the sleeves of linear actuators attached by Cardan joints.

$$\begin{aligned} \boldsymbol{J}^{inv}_{\mathrm{L}ij\mathrm{N}} &= \left[\boldsymbol{J}^{inv}_{\mathrm{L}ij\mathrm{N}-\mathrm{H}_{(6\times6)}} \quad \boldsymbol{J}^{inv}_{\mathrm{L}ij\mathrm{N}-\mathrm{F}i_{(6\times6)}}\right] \\ &= \begin{bmatrix} \boldsymbol{I} & \boldsymbol{0} \\ \boldsymbol{0} & \boldsymbol{m}_{\mathrm{C}ij} \end{bmatrix}\left[\begin{bmatrix} \boldsymbol{I} & -\boldsymbol{R}_{\mathrm{H}}{}^{\{\mathrm{H}\}}\tilde{\boldsymbol{p}}_{\mathrm{H}i-\mathrm{H}ij}\boldsymbol{R}_{\mathrm{H}}{}^{\mathrm{T}} \\ \boldsymbol{I} & -\left(\boldsymbol{R}_{\mathrm{H}}{}^{\{\mathrm{H}\}}\tilde{\boldsymbol{p}}_{\mathrm{H}i-\mathrm{H}ij}\boldsymbol{R}_{\mathrm{H}}{}^{\mathrm{T}} + \tilde{\boldsymbol{l}}_{ij}\right) \end{bmatrix} \quad \begin{bmatrix} \boldsymbol{0} & \boldsymbol{0} \\ -\boldsymbol{I} & \boldsymbol{R}_{\mathrm{F}i}{}^{\{\mathrm{F}i\}}\boldsymbol{p}_{\mathrm{F}i-\mathrm{F}ij}\boldsymbol{R}_{\mathrm{F}i}{}^{\mathrm{T}} \end{bmatrix}\right] \\ &+ \left[\begin{bmatrix} \boldsymbol{0} & \boldsymbol{0} \\ \boldsymbol{0} & \boldsymbol{I} \end{bmatrix} \quad \boldsymbol{0}_{(6\times6)}\right] \end{aligned} \tag{6.39-1}$$

In which, $\boldsymbol{m}_{\mathrm{C}ij} = {l_{ij}}^{-1}\left[\boldsymbol{y}_{\mathrm{L}ij\mathrm{N}} \quad -\cos\gamma_{ijy}{}^{-1}\boldsymbol{x}_{\mathrm{H}} \quad \boldsymbol{0}\right]\boldsymbol{R}_{\mathrm{L}ij\mathrm{N}}{}^{\mathrm{T}}$. γ_{ijx} and γ_{ijy} are the rotational displacements along the two axes of Cardan joints, $\boldsymbol{y}_{\mathrm{L}ij\mathrm{N}}$ is the *y*-axis of sleeve on the Cardan joint and $\boldsymbol{x}_{\mathrm{H}}$ the *x*-axis of hip platform.

Shafts

The virtual work based on inverse Jacobians can be obtained by distinguishing linear in one BKC. Letting *j* = B, D, F and *k* = C, E, A, the Jacobians of the *i*-th shafts of linear actuators attached by double Cardan joints are given as following.

$$\boldsymbol{J}^{inv}_{\mathrm{L}ij\mathrm{S}} = \left[\boldsymbol{J}^{inv}_{\mathrm{L}ij\mathrm{S}-\mathrm{H}_{(6\times6)}} \quad \boldsymbol{J}^{inv}_{\mathrm{L}ij\mathrm{S}-\mathrm{F}i_{(6\times6)}}\right] = \begin{bmatrix} \boldsymbol{I} & \boldsymbol{0} \\ \boldsymbol{0} & e^{\tilde{\boldsymbol{r}}_{\mathrm{L}ij\mathrm{S}}} \end{bmatrix}\left[\begin{bmatrix} \boldsymbol{0} & \boldsymbol{0} \\ \boldsymbol{A}_{\mathrm{D}ij\mathrm{S}} & \end{bmatrix} \quad \begin{bmatrix} \boldsymbol{I} & -\boldsymbol{R}_{\mathrm{F}i}{}^{\{\mathrm{F}i\}}\boldsymbol{p}_{\mathrm{F}i-\mathrm{F}ij}\boldsymbol{R}_{\mathrm{F}i}{}^{\mathrm{T}} \\ & \boldsymbol{B}_{\mathrm{D}ij\mathrm{S}} \end{bmatrix}\right] \tag{6.39-2}$$

In which,

$$\boldsymbol{A}_{\mathrm{D}ij\mathrm{S}} = \frac{1}{l_{ij}}\begin{bmatrix} 0 & -1 & 0 \\ 1 & 0 & 0 \\ \dfrac{\left(\boldsymbol{y}_{\mathrm{L}ij\mathrm{S}}{}^{\mathrm{T}}\boldsymbol{y}_{\mathrm{L}ik\mathrm{S}}\right)}{\left|\tilde{\boldsymbol{e}}_{ik}\boldsymbol{e}_{ij}\right|} & 0 & 0 \end{bmatrix}\boldsymbol{R}_{\mathrm{L}ij\mathrm{S}}{}^{\mathrm{T}}\begin{bmatrix}\boldsymbol{I} & -\boldsymbol{R}_{\mathrm{H}}{}^{\{\mathrm{H}\}}\tilde{\boldsymbol{p}}_{\mathrm{H}i-\mathrm{H}ij}\boldsymbol{R}_{\mathrm{H}}{}^{\mathrm{T}}\end{bmatrix}$$

$$-\frac{1}{l_{ik}\left|\tilde{\boldsymbol{e}}_{ik}\boldsymbol{e}_{ij}\right|}\begin{bmatrix}0 & 0 & 0\\ 0 & 0 & 0\\ 1 & 0 & 0\end{bmatrix}\boldsymbol{R}_{\mathrm{L}ij\mathrm{S}}{}^{\mathrm{T}}\begin{bmatrix}\boldsymbol{I} & -\boldsymbol{R}_{\mathrm{H}}{}^{\{\mathrm{H}\}}\tilde{\boldsymbol{p}}_{\mathrm{H}i-\mathrm{H}ik}\boldsymbol{R}_{\mathrm{H}}{}^{\mathrm{T}}\end{bmatrix},$$

$$\boldsymbol{B}_{\mathrm{D}ij\mathrm{S}} = \left(\frac{1}{l_{ik}\left|\tilde{\boldsymbol{e}}_{ik}\boldsymbol{e}_{ij}\right|}\begin{bmatrix}0 & 0 & 0\\ 0 & 0 & 0\\ 1 & 0 & 0\end{bmatrix}\right.$$

$$\left.-\frac{1}{l_{ij}}\begin{bmatrix} 0 & -1 & 0 \\ 1 & 0 & 0 \\ \dfrac{\left(\boldsymbol{y}_{\mathrm{L}ij\mathrm{S}}{}^{\mathrm{T}}\boldsymbol{y}_{\mathrm{L}ik\mathrm{S}}\right)}{\left|\tilde{\boldsymbol{e}}_{ik}\boldsymbol{e}_{ij}\right|} & 0 & 0 \end{bmatrix}\right)\boldsymbol{R}_{\mathrm{L}ij\mathrm{S}}{}^{\mathrm{T}}\begin{bmatrix}\boldsymbol{I} & -\boldsymbol{R}_{\mathrm{F}i}{}^{\{\mathrm{F}i\}}\boldsymbol{p}_{\mathrm{F}i-\mathrm{F}ij}\boldsymbol{R}_{\mathrm{F}i}{}^{\mathrm{T}}\end{bmatrix}.$$

Letting j = B, D, F and k = C, E, A, the Jacobians of the k-th shafts of linear actuators attached by double Cardan joints are given as following.

$$\boldsymbol{J}^{inv}_{\mathrm{L}ik\mathrm{S}} = \begin{bmatrix}\boldsymbol{J}^{inv}_{\mathrm{L}ik\mathrm{S}-\mathrm{H}(6\times6)} & \boldsymbol{J}^{inv}_{\mathrm{L}ik\mathrm{S}-\mathrm{F}i(6\times6)}\end{bmatrix}$$

$$= \begin{bmatrix}\boldsymbol{I} & \boldsymbol{0}\\ \boldsymbol{0} & e^{\tilde{\boldsymbol{r}}_{\mathrm{L}ik\mathrm{S}}}\end{bmatrix}\left[\begin{bmatrix}\boldsymbol{0} & \boldsymbol{0}\\ \boldsymbol{A}_{\mathrm{D}ik\mathrm{S}(3\times6)}\end{bmatrix}\quad\begin{bmatrix}\boldsymbol{I} & -\boldsymbol{R}_{\mathrm{F}i}{}^{\{\mathrm{F}i\}}\boldsymbol{p}_{\mathrm{F}i-\mathrm{F}ij}\boldsymbol{R}_{\mathrm{F}i}{}^{\mathrm{T}}\\ & \boldsymbol{B}_{\mathrm{D}ik\mathrm{S}(3\times6)}\end{bmatrix}\right] \tag{6.39-3}$$

In which,

$$\boldsymbol{A}_{\mathrm{D}ik\mathrm{S}} = \frac{1}{l_{ik}}\begin{bmatrix} 0 & -1 & 0 \\ 1 & 0 & 0 \\ -\dfrac{\boldsymbol{y}_{\mathrm{L}ij\mathrm{S}}{}^{\mathrm{T}}\boldsymbol{y}_{\mathrm{L}ik\mathrm{S}}}{\left|\tilde{\boldsymbol{e}}_{ik}\boldsymbol{e}_{ij}\right|} & 0 & 0 \end{bmatrix}\boldsymbol{R}_{\mathrm{L}ik\mathrm{S}}{}^{\mathrm{T}}\begin{bmatrix}\boldsymbol{I} & -\boldsymbol{R}_{\mathrm{H}}{}^{\{\mathrm{H}\}}\tilde{\boldsymbol{p}}_{\mathrm{H}i-\mathrm{H}ik}\boldsymbol{R}_{\mathrm{H}}{}^{\mathrm{T}}\end{bmatrix}$$

$$+\frac{1}{l_{ij}\left|\tilde{\boldsymbol{e}}_{ik}\boldsymbol{e}_{ij}\right|}\begin{bmatrix}0 & 0 & 0\\ 0 & 0 & 0\\ 1 & 0 & 0\end{bmatrix}\boldsymbol{R}_{\mathrm{L}ik\mathrm{S}}{}^{\mathrm{T}}\begin{bmatrix}\boldsymbol{I} & -\boldsymbol{R}_{\mathrm{H}}{}^{\{\mathrm{H}\}}\tilde{\boldsymbol{p}}_{\mathrm{H}i-\mathrm{H}ij}\boldsymbol{R}_{\mathrm{H}}{}^{\mathrm{T}}\end{bmatrix}$$

$$\boldsymbol{B}_{\mathrm{D}ik\mathrm{S}} = \left(\frac{1}{l_{ij}\left|\tilde{\boldsymbol{e}}_{ik}\boldsymbol{e}_{ij}\right|}\begin{bmatrix}0 & 0 & 0\\ 0 & 0 & 0\\ 1 & 0 & 0\end{bmatrix} + \frac{1}{l_{ik}}\begin{bmatrix} 0 & 1 & 0\\ -1 & 0 & 0\\ \dfrac{\boldsymbol{y}_{\mathrm{L}ij\mathrm{S}}{}^{\mathrm{T}}\boldsymbol{y}_{\mathrm{L}ik\mathrm{S}}}{\left|\tilde{\boldsymbol{e}}_{ik}\boldsymbol{e}_{ij}\right|} & 0 & 0\end{bmatrix}\right) \boldsymbol{R}_{\mathrm{L}ik\mathrm{S}}{}^{\mathrm{T}}\begin{bmatrix}\boldsymbol{I} & -\boldsymbol{R}_{\mathrm{F}i}{}^{\{\mathrm{F}i\}}\boldsymbol{p}_{\mathrm{F}i-\mathrm{F}ij}\boldsymbol{R}_{\mathrm{F}i}{}^{\mathrm{T}}\end{bmatrix}.$$

4) Inverse Jacobians of Actuators

The actuating forces are applied between the two parts of linear actuators along the axial direction. The virtual work of actuating forces depends on the velocities of length variations of linear actuators. The inverse Jacobians of lengths variations can be found in eq. (5.4), as

$$\dot{\boldsymbol{q}}_{ij} = \boldsymbol{J}^{inv}_{i-\mathrm{H}}\dot{\boldsymbol{X}}_{\mathrm{H}} + \boldsymbol{J}^{inv}_{i-\mathrm{F}i}\dot{\boldsymbol{X}}_{\mathrm{F}i} \tag{6.40}$$

Thus, the inverse Jacobians for length variations of leg-1 and leg-2 are respectively

$$\begin{aligned}\dot{\boldsymbol{q}}_1 &= [\boldsymbol{J}^{inv}_{1-\mathrm{H}} \quad \boldsymbol{J}^{inv}_{1-\mathrm{F}1} \quad \boldsymbol{0}]\dot{\boldsymbol{X}}_{\Sigma} = \bar{\boldsymbol{J}}^{inv}_{1}\dot{\boldsymbol{X}}_{\Sigma},\\ \dot{\boldsymbol{q}}_2 &= [\boldsymbol{J}^{inv}_{2-\mathrm{H}} \quad \boldsymbol{0} \quad \boldsymbol{J}^{inv}_{1-\mathrm{F}2}]\dot{\boldsymbol{X}}_{\Sigma} = \bar{\boldsymbol{J}}^{inv}_{2}\dot{\boldsymbol{X}}_{\Sigma}.\end{aligned} \tag{6.41}$$

Where,

$$\boldsymbol{J}^{inv}_{i-\mathrm{H}} = \begin{bmatrix}-\boldsymbol{e}_{i\mathrm{A}}{}^{\mathrm{T}} & \boldsymbol{e}_{i\mathrm{A}}{}^{\mathrm{T}}\boldsymbol{R}_{\mathrm{H}}{}^{\{\mathrm{H}\}}\tilde{\boldsymbol{p}}_{\mathrm{H}-\mathrm{H}i\mathrm{A}}\boldsymbol{R}_{\mathrm{H}}{}^{\mathrm{T}}\\ \vdots & \vdots\\ -\boldsymbol{e}_{i\mathrm{F}}{}^{\mathrm{T}} & \boldsymbol{e}_{i\mathrm{F}}{}^{\mathrm{T}}\boldsymbol{R}_{\mathrm{H}}{}^{\{\mathrm{H}\}}\tilde{\boldsymbol{p}}_{\mathrm{H}-\mathrm{H}i\mathrm{F}}\boldsymbol{R}_{\mathrm{H}}{}^{\mathrm{T}}\end{bmatrix}, \quad \boldsymbol{J}^{inv}_{i-\mathrm{F}i} = \begin{bmatrix}\boldsymbol{e}_{i\mathrm{A}}{}^{\mathrm{T}} & -\boldsymbol{e}_{i\mathrm{A}}{}^{\mathrm{T}}\boldsymbol{R}_{\mathrm{F}i}{}^{\{\mathrm{F}i\}}\tilde{\boldsymbol{p}}_{\mathrm{F}i-\mathrm{F}i\mathrm{A}}\boldsymbol{R}_{\mathrm{F}i}{}^{\mathrm{T}}\\ \vdots & \vdots\\ \boldsymbol{e}_{i\mathrm{F}}{}^{\mathrm{T}} & -\boldsymbol{e}_{i\mathrm{F}}{}^{\mathrm{T}}\boldsymbol{R}_{\mathrm{F}i}{}^{\{\mathrm{F}i\}}\tilde{\boldsymbol{p}}_{\mathrm{F}i-\mathrm{F}i\mathrm{F}}\boldsymbol{R}_{\mathrm{F}i}{}^{\mathrm{T}}\end{bmatrix}.$$

6.3.3 Generalized Forces

Letting $\ddot{\boldsymbol{t}}$ be the translational acceleration of a rigid body on its mass centre and $\ddot{\boldsymbol{r}}$ be the rotational acceleration, the generalized forces of platforms applied on their mass centres are

$$\boldsymbol{F}_k = \begin{bmatrix}\boldsymbol{f}_k\\ \boldsymbol{\tau}_k\end{bmatrix} = \begin{bmatrix}\boldsymbol{f}_{ek} + m_k(\boldsymbol{g} - \ddot{\boldsymbol{t}}_k)\\ \boldsymbol{\tau}_{ek} - \boldsymbol{I}_k\ddot{\boldsymbol{r}} \quad -\tilde{\dot{\boldsymbol{r}}} \quad (\boldsymbol{I}_k\dot{\boldsymbol{r}} \quad)\end{bmatrix}. \tag{6.42}$$

Where, k stands for H and F$_i$. $\boldsymbol{f}_{ek}$ and $\boldsymbol{\tau}_{ek}$ are the external forces and torques applied on the platform k. m_k and $\boldsymbol{I}_k$ are the mass and moment of inertia tensor at mass centre. $\boldsymbol{g}$ is the gravitational acceleration. Note that, the inertia tensor $\boldsymbol{I}_k = \boldsymbol{R}_k{}^{\{k\}}\boldsymbol{I}_k\boldsymbol{R}_k{}^{\mathrm{T}}$ is with respect to

the inertial frame and tensor ${}^{\{k\}}\boldsymbol{I}_k$ is with respect to the body fixed frame.

$$\boldsymbol{F}_{\mathrm{L}ijn} = \begin{bmatrix} \boldsymbol{f}_{\mathrm{L}ijn} \\ \boldsymbol{\tau}_{\mathrm{L}ijn} \end{bmatrix} = \begin{bmatrix} m_{\mathrm{L}ijn}\left(\boldsymbol{g} - \ddot{\boldsymbol{t}}_{\mathrm{L}ijn\mathrm{C}}\right) \\ -\boldsymbol{I}_{\mathrm{L}ijn}\ddot{\boldsymbol{r}}_{\mathrm{L}ijn} - \tilde{\dot{\boldsymbol{r}}}_{\mathrm{L}ijn}\left(\boldsymbol{I}_{\mathrm{L}ijn}\dot{\boldsymbol{r}}_{\mathrm{L}ijn}\right) \end{bmatrix} \tag{6.43}$$

In which, n = N or S, thus L_{ij}N and L_{ij}S denote the sleeve (screw nut) and shaft of the j-th linear actuator on the i-th leg.

6.3.4 Inverse Dynamic Model Based on Virtual Work Principle

Based on eq. (6.25), given a virtual displacement of each part of the system, the virtual work of the generalized forces should be 0. Then there exist the following relations,

$$\sum_{i=1}^{2} \delta\boldsymbol{q}_i{}^{\mathrm{T}}\boldsymbol{\tau}_i + \sum_{k}^{\mathrm{H,F1,F2}} \delta\boldsymbol{X}_{k\mathrm{C}}{}^{\mathrm{T}}\boldsymbol{F}_k + \sum_{i=1}^{2}\sum_{j=\mathrm{A}}^{\mathrm{F}}\left(\delta\boldsymbol{X}_{\mathrm{L}ij\mathrm{NC}}^{\mathrm{T}}\boldsymbol{F}_{\mathrm{L}ij\mathrm{N}} + \delta\boldsymbol{X}_{\mathrm{L}ij\mathrm{SC}}^{\mathrm{T}}\boldsymbol{F}_{\mathrm{L}ij\mathrm{S}}\right) = 0. \tag{6.44}$$

Bring in the expanded inverse Jacobians of all the parts,

$$\delta\boldsymbol{X}_{\Sigma}{}^{\mathrm{T}}\left[\sum_{i=1}^{2}\bar{\boldsymbol{J}}_i^{inv}{}^{\mathrm{T}}\boldsymbol{\tau}_i + \sum_{k}^{\mathrm{H,F1,F2}}\bar{\boldsymbol{J}}_{k\mathrm{C}}^{inv}{}^{\mathrm{T}}\boldsymbol{F}_k + \sum_{i=1}^{2}\sum_{j=\mathrm{A}}^{\mathrm{F}}\left(\bar{\boldsymbol{J}}_{\mathrm{L}ij\mathrm{NC}}^{inv}{}^{\mathrm{T}}\boldsymbol{F}_{\mathrm{L}ij\mathrm{N}} + \bar{\boldsymbol{J}}_{\mathrm{L}ij\mathrm{SC}}^{inv}{}^{\mathrm{T}}\boldsymbol{F}_{\mathrm{L}ij\mathrm{S}}\right)\right] = 0 \tag{6.45}$$

The actuating force vector will be obtained through

$$\bar{\boldsymbol{J}}_{\boldsymbol{\tau}}^{inv}{}^{\mathrm{T}}\boldsymbol{\tau} = -\left[\sum_{k}^{\mathrm{H,F1,F2}}\bar{\boldsymbol{J}}_{k\mathrm{C}}^{inv}{}^{\mathrm{T}}\boldsymbol{F}_k + \sum_{i=1}^{2}\sum_{j=\mathrm{A}}^{\mathrm{F}}\left(\bar{\boldsymbol{J}}_{\mathrm{L}ij\mathrm{NC}}^{inv}{}^{\mathrm{T}}\boldsymbol{F}_{\mathrm{L}ij\mathrm{N}} + \bar{\boldsymbol{J}}_{\mathrm{L}ij\mathrm{SC}}^{inv}{}^{\mathrm{T}}\boldsymbol{F}_{\mathrm{L}ij\mathrm{S}}\right)\right]. \tag{6.46}$$

Where, $\bar{\boldsymbol{J}}_{\boldsymbol{\tau}}^{inv} = \left[\bar{\boldsymbol{J}}_1^{inv\mathrm{T}} \quad \bar{\boldsymbol{J}}_2^{inv\mathrm{T}}\right]^{\mathrm{T}}$. The size of $\bar{\boldsymbol{J}}_{\boldsymbol{\tau}}^{inv\mathrm{T}}$ is 18x12, which is degenerate and obvious not full rank. The actuating force vector $\boldsymbol{\tau} = [\boldsymbol{\tau}_1{}^{\mathrm{T}} \quad \boldsymbol{\tau}_2{}^{\mathrm{T}}]^{\mathrm{T}}$ should be derived by dividing the system of equations according to different motion phases.

6.3.5 Modified Inverse Dynamic Model for Different Motion Phases

For different motion phases, different entries of $\dot{\boldsymbol{X}}_{\Sigma} = [\dot{\boldsymbol{X}}_{\mathrm{H}} \quad \dot{\boldsymbol{X}}_{\mathrm{F1}} \quad \dot{\boldsymbol{X}}_{\mathrm{F2}}]^{\mathrm{T}}$ will be constant,

depending on the platforms which assumedly fixed on the ground. The virtual work equations in eq. (6.46) of that platform will thus be equal to zero. For example, in a swing phase, the standing foot will be considered as fixed on the ground, while for a hip moving phase, both feet will be considered as fixed. To meet various dynamic scenarios, the dynamic models should be handled in 3 cases: 1) One leg supporting with one actuating leg, 2) one leg supporting with two actuating legs and 3) two legs supporting.

1) Swing Phase (One Leg Actuated)

If the supporting leg were locked by brake systems of servo motor units, the supporting leg and hip platform should belong to one rigid body. The virtual work equation eq. (6.46) should be modified as

$$\bar{\boldsymbol{J}}_{\boldsymbol{\tau}-\mathrm{Mod}}^{inv\ \mathrm{T}}\boldsymbol{\tau}_m = -\left[\bar{\boldsymbol{J}}_{\mathrm{F}m\mathrm{C}-\mathrm{Mod}}^{inv\ \mathrm{T}}\boldsymbol{F}_{\mathrm{F}m} + \sum_{n}^{\mathrm{N,S}}\sum_{j=\mathrm{A}}^{\mathrm{F}}\left(\bar{\boldsymbol{J}}_{\mathrm{L}mjn\mathrm{C}-\mathrm{Mod}}^{inv\ \mathrm{T}}\boldsymbol{F}_{\mathrm{L}mjn}\right)\right] \tag{6.47}$$

Where, m=1, 2, indicates the swinging foot platform, n = N, S, indicates the sleeve and shaft of linear actuator. According to eq. (6.41), (6.36) and (6.39), the modified inverse Jacobians in eq. (6.47) are

$$\begin{cases} \bar{\boldsymbol{J}}_{\boldsymbol{\tau}-\mathrm{Mod}}^{inv} = \boldsymbol{J}_{m-\mathrm{F}m}^{inv}, \\ \bar{\boldsymbol{J}}_{\mathrm{F}m\mathrm{C}-\mathrm{Mod}}^{inv} = \boldsymbol{J}_{\mathrm{F}m\mathrm{C}}^{inv}, \\ \bar{\boldsymbol{J}}_{\mathrm{L}ijn\mathrm{C}-\mathrm{Mod}}^{inv} = \boldsymbol{J}_{\mathrm{L}mjn\mathrm{C}}^{inv}\boldsymbol{J}_{\mathrm{L}mjn}^{inv}. \end{cases} \tag{6.48}$$

In this case, the dimension of eq. (6.47) was decreased to 6. If $\bar{\boldsymbol{J}}_{\boldsymbol{\tau}-m}^{inv}$ is full rank, the actuating forces of leg-m can be predicted as

$$\boldsymbol{\tau}_m = -\boldsymbol{J}_{m-\mathrm{F}m}^{inv\ -\mathrm{T}}\left[\boldsymbol{J}_{\mathrm{F}m\mathrm{C}}^{inv\ \mathrm{T}}\boldsymbol{F}_{\mathrm{F}m} + \sum_{n}^{\mathrm{N,S}}\sum_{j=\mathrm{A}}^{\mathrm{F}}\left(\boldsymbol{J}_{\mathrm{L}mjn}^{inv\ \mathrm{T}}\boldsymbol{J}_{\mathrm{L}mjn\mathrm{C}}^{inv\ \mathrm{T}}\boldsymbol{F}_{\mathrm{L}mjn}\right)\right] \tag{6.49}$$

2) Swing Phase (Two Legs Actuated)

Under some higher dynamical scenarios, it is demanded to move the hip and swinging foot simultaneously. Thus, all the three platforms must be treated as three separate rigid bodies and

all the 12 servo motors should be actuated. In this case, only the virtual work applied on the standing foot must be **0**, eq. (6.46) will be modified as

$$\bar{\boldsymbol{J}}^{inv}_{\boldsymbol{\tau}-\mathrm{Mod}}{}^{\mathrm{T}}\boldsymbol{\tau} = -\left[\sum_{k}^{\mathrm{H,F}m} \bar{\boldsymbol{J}}^{inv}_{k\mathrm{C}-\mathrm{Mod}}{}^{\mathrm{T}}\boldsymbol{F}_k + \sum_{n}^{\mathrm{N,S}}\sum_{j=\mathrm{A}}^{\mathrm{F}} \left(\bar{\boldsymbol{J}}^{inv}_{\mathrm{L}jn\mathrm{C}-\mathrm{Mod}}{}^{\mathrm{T}}\boldsymbol{F}_{\mathrm{L}\Sigma jn}\right)\right]. \tag{6.50}$$

The modified inverse Jacobians and general forces in this case are

$$\begin{cases} \bar{\boldsymbol{J}}^{inv}_{\boldsymbol{\tau}-\mathrm{Mod}} & = \begin{bmatrix} \boldsymbol{J}^{inv}_{1-\mathrm{H}} & \boldsymbol{J}^{inv}_{1-\mathrm{F1}} \\ \boldsymbol{J}^{inv}_{2-\mathrm{H}} & \boldsymbol{0} \end{bmatrix}_{m=1}, & & = \begin{bmatrix} \boldsymbol{J}^{inv}_{1-\mathrm{H}} & \boldsymbol{0} \\ \boldsymbol{J}^{inv}_{2-\mathrm{H}} & \boldsymbol{J}^{inv}_{1-\mathrm{F2}} \end{bmatrix}_{m=2}, \\ \bar{\boldsymbol{J}}^{inv}_{k\mathrm{C}-\mathrm{Mod}} & = [\quad \boldsymbol{J}^{inv}_{\mathrm{HC}} \quad \boldsymbol{0} \quad]_{k=\mathrm{H}}, & & = [\quad \boldsymbol{0} \quad \boldsymbol{J}^{inv}_{\mathrm{F}m\mathrm{C}}]_{k=\mathrm{F}m}, \\ \bar{\boldsymbol{J}}^{inv}_{\mathrm{L}jn\mathrm{C}-\mathrm{Mod}} & = \begin{bmatrix} \boldsymbol{J}^{inv}_{\mathrm{L1}jn\mathrm{C}}\boldsymbol{J}^{inv}_{\mathrm{L1}jn-\mathrm{H}} & \boldsymbol{J}^{inv}_{\mathrm{L1}jn\mathrm{C}}\boldsymbol{J}^{inv}_{\mathrm{L1}jn-\mathrm{F1}} \\ \boldsymbol{J}^{inv}_{\mathrm{L2}jn\mathrm{C}}\boldsymbol{J}^{inv}_{\mathrm{L1}jn-\mathrm{H}} & \boldsymbol{0} \end{bmatrix}_{m=1}, \\ & = \begin{bmatrix} \boldsymbol{J}^{inv}_{\mathrm{L1}jn\mathrm{C}}\boldsymbol{J}^{inv}_{\mathrm{L1}jn-\mathrm{H}} & \boldsymbol{0} \\ \boldsymbol{J}^{inv}_{\mathrm{L2}jn\mathrm{C}}\boldsymbol{J}^{inv}_{\mathrm{L}ijn-\mathrm{H}} & \boldsymbol{J}^{inv}_{\mathrm{L2}jn\mathrm{C}}\boldsymbol{J}^{inv}_{\mathrm{L2}jn-\mathrm{F2}} \end{bmatrix}_{m=2}, \\ \boldsymbol{F}_{\mathrm{L}\Sigma jn} & = \begin{bmatrix} \boldsymbol{F}_{\mathrm{L1}jn} \\ \boldsymbol{F}_{\mathrm{L2}jn} \end{bmatrix}. \end{cases} \tag{6.51}$$

Till here, the 12-dimensional equation systems were obtained. If $\bar{\boldsymbol{J}}^{inv}_{\boldsymbol{\tau}-\mathrm{MOD}}$ is full rank, the actuating forces for both legs can be solved as

$$\boldsymbol{\tau} = -\bar{\boldsymbol{J}}^{inv}_{\boldsymbol{\tau}-\mathrm{MOD}}{}^{-\mathrm{T}}\left[\sum_{k}^{\mathrm{H,F}m} \bar{\boldsymbol{J}}^{inv}_{k\mathrm{C}-\mathrm{MOD}}{}^{\mathrm{T}}\boldsymbol{F}_k + \sum_{n}^{\mathrm{N,S}}\sum_{j=\mathrm{A}}^{\mathrm{F}} \left(\bar{\boldsymbol{J}}^{inv}_{\mathrm{L}jn\mathrm{C}-\mathrm{MOD}}{}^{\mathrm{T}}\boldsymbol{F}_{\mathrm{L}jn}\right)\right]. \tag{6.52}$$

3) Hip Moving Phase

This phase is special, since the both feet stay on the ground, during the hip platform moves. This leads to a 12-dimensional $\boldsymbol{\tau}$ but a 6-dimensional equation systems. In other words, the solution of $\boldsymbol{\tau}$ is a 6-dimensional space. In this case, eq. (6.46) can be modified as,

$$\bar{\boldsymbol{J}}^{inv}_{\boldsymbol{\tau}-\mathrm{Mod}}{}^{\mathrm{T}}\boldsymbol{\tau} = -\left[\boldsymbol{J}^{inv}_{\mathrm{HC}}{}^{\mathrm{T}}\boldsymbol{F}_{\mathrm{H}} + \sum_{i=1}^{2}\sum_{n}^{\mathrm{N,S}}\sum_{j=\mathrm{A}}^{\mathrm{F}} \left(\bar{\boldsymbol{J}}^{inv}_{\mathrm{L}ijn\mathrm{C}-\mathrm{Mod}}{}^{\mathrm{T}}\boldsymbol{F}_{\mathrm{L}ijn}\right)\right] \tag{6.53}$$

Where, the modified inverse Jacobians are

$$\begin{cases} \bar{\boldsymbol{J}}^{inv}_{\boldsymbol{\tau}-\mathrm{Mod}} = \begin{bmatrix} \boldsymbol{J}^{inv}_{1-\mathrm{H}} \\ \boldsymbol{J}^{inv}_{2-\mathrm{H}} \end{bmatrix}, \\ \bar{\boldsymbol{J}}^{inv}_{Lijn\mathrm{C}-\mathrm{Mod}} = \boldsymbol{J}^{inv}_{Lijn\mathrm{C}} \boldsymbol{J}^{inv}_{Lijn-\mathrm{H}}. \end{cases} \tag{6.54}$$

It is obvious that $\bar{\boldsymbol{J}}^{inv}_{\boldsymbol{\tau}-\mathrm{Mod}}$ is a 12x6 matrix and not full rank, thus there is no unique solution of $\boldsymbol{\tau}$. To limit $\boldsymbol{\tau}$ to a 0-dimensional space, some constraints must be introduced, e.g. stability indices, energy consumption indices, minimizing actuating force and/or others. This will be discussed in Chapter 7.

6.3.6 Friction Model

Friction plays an important role in the dynamic analysis and control of a robotic system. In general, the frictions can be classified into three types: Coulomb friction, static friction and viscous friction. Since the present system is composed by rotational and prismatic kinematic pairs and the prismatic pair is realized by rolling ball stokes, the composite friction of linear actuators weighs the most. Through the experiments, it can be concluded that the frictional behaviour of linear actuators is a combination of viscous friction with constant-velocity and static friction at the moving-starting phase. The experiments results are shown in fig. 6.13.

The result shows different current outputs with different external loads (excluding the self-weight of linear actuators) at different steady motor speeds. According to the working principle of servo motor, the commutation current is proportional to the load. From fig. 6.13, it can be revealed that, the load is only positively related to the steady rotational speed of the motor but not affected by the load. On the other hand, there is no obvious difference for the starting currents under different loads. Thus, a simplified experimental model of friction can be derived as fig. 6.14, and described as

$$\tau_{fi} = \begin{cases} K_{\tau C}\left(C_{0--} + K_{fC}\dot{q}_i\right) & \dot{q}_i < 0 \\ K_{\tau C}\left(C_{0++} + K_{fC}\dot{q}_i\right) & \dot{q}_i > 0 \\ K_{\tau C} C_{0+} & \dot{q}_i = 0_+ \quad t_0 > \varepsilon_0 \\ K_{\tau C} C_{0-} & \dot{q}_i = 0_- \quad t_0 > \varepsilon_0. \end{cases} \tag{6.55}$$

In which, $K_{\tau C}$ is the conversion ratio between commutation current and output force on the

output end of linear actuators, whose unit is (N/mA).

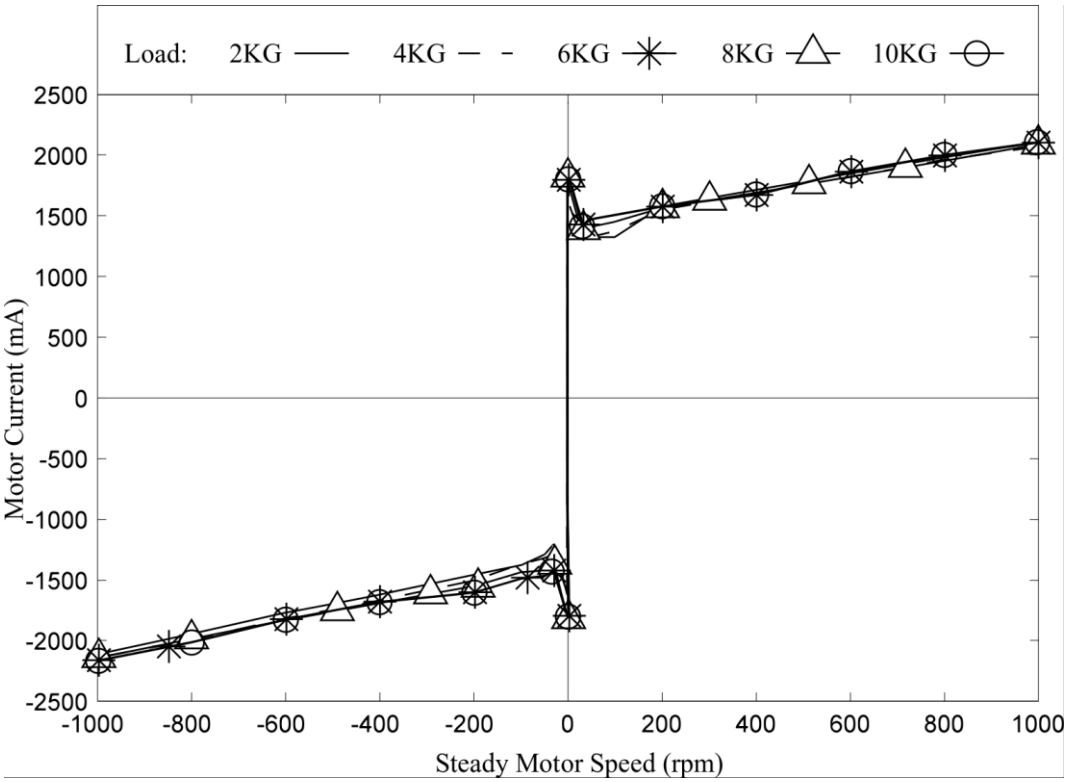

Figure 6.13 Experimental motor currents under different loads with different steady motor speed.

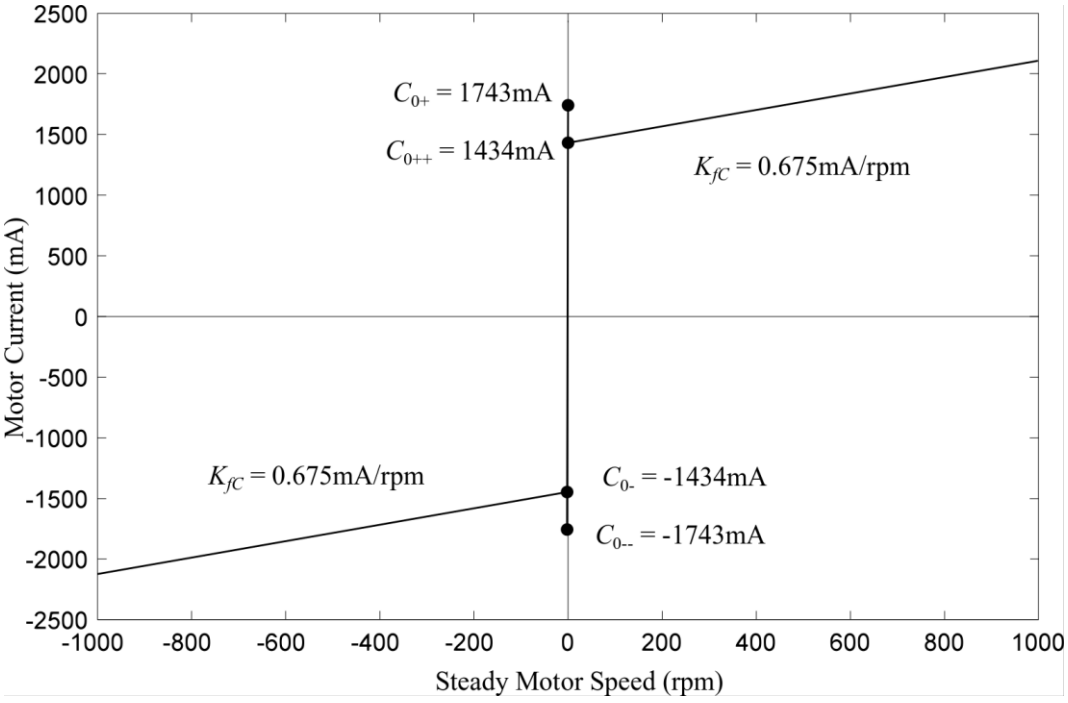

Figure 6.14 Simplified friction model of linear actuator units expressed by motor currents.

According to the catalogues of motor and linear actuators supplier, the ratio $K_{\tau C} = 0.072$. C_{0--} and C_{0++} are the currents when motor moves with small velocity near zero at both directions. C_{0+} and C_{0-} are the starting currents caused by static friction when the velocity demands are positive and negative. In practice, the velocity trajectory could pass through zero point, thus, it is necessary to set a time threshold, ε_0, of static time.

The simplified friction model shows that, the basic friction of an actuator unit is around 103.25N. Since the transmission ratio between linear actuator is 30/13(mm/round), the friction ratio can be written as $K_{\tau C}K_{fC} \approx 1.26(\mathrm{N/m \cdot s^{-1}})$, in the view of control variables.

6.3.7 Inertia Matrices of Links and Parts

Since the methodology of inertia measurement is not the aim of this work and limited by the experimental conditions, only software based inertial properties were adopted.

1) Inertia Property of Hip Platform

The mass centre of hip platform and attached Cardan joint bases are marked on the drawing in fig. 6.15 and the inertial properties are listed in table 6.2.

Table 6.2 Inertial properties of hip platform assembly.

Mass (kg)	$m_{\mathrm{H}} = 23.586$
Mass centre w.r.t. local coordinates (mm)	${}^{\{\mathrm{H}\}}\boldsymbol{p}_{\mathrm{HO-C}} = \begin{bmatrix} 0 \\ 0 \\ 37.937 \end{bmatrix}$
Inertia tensor w.r.t local coordinates (kg·mm^2)	${}^{\{\mathrm{H}\}}\boldsymbol{I}_{\mathrm{H}} = \begin{bmatrix} 833326.290 & 0.002 & 0.476 \\ 0.002 & 365688.203 & -0.361 \\ 0.476 & -0.361 & 1194102.424 \end{bmatrix}$

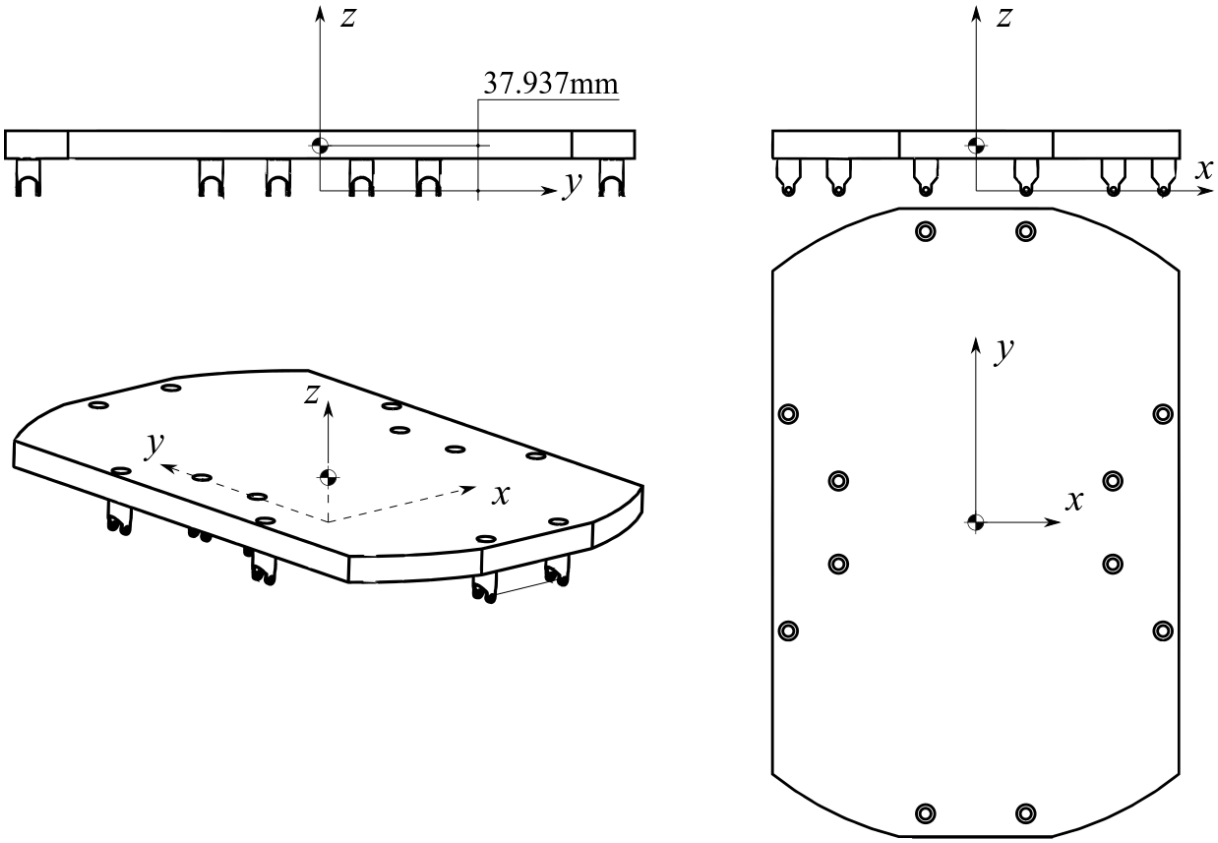

Figure 6.15 The mass centre of hip platform and attached components

2) Inertia Property of Sleeve of Linear Actuators

The mass centre of sleeve of linear actuators and attached Cardan joint bases are marked on the drawing in fig. 6.16 and the inertial properties are listed in table 6.3.

Table 6.3 The inertial properties of a sleeve assembly.

Mass (kg)	$m_{\mathrm{L}ij\mathrm{N}} = 3.234$
Mass centre w.r.t. local coordinates (mm)	${}^{\{\mathrm{L}ij\mathrm{N}\}}\boldsymbol{p}_{\mathrm{L}ij\mathrm{NO-C}} = \begin{bmatrix} 28.801 \\ -1.007 \\ -187.417 \end{bmatrix}$
Inertia tensor w.r.t local coordinates (kg·mm^2)	${}^{\{\mathrm{L}ij\mathrm{N}\}}\boldsymbol{I}_{\mathrm{L}ij\mathrm{N}} = \begin{bmatrix} 74792.215 & -101.604 & 3519.502 \\ -101.604 & 77570.545 & 210.323 \\ 3519.502 & 210.323 & 4273.298 \end{bmatrix}$

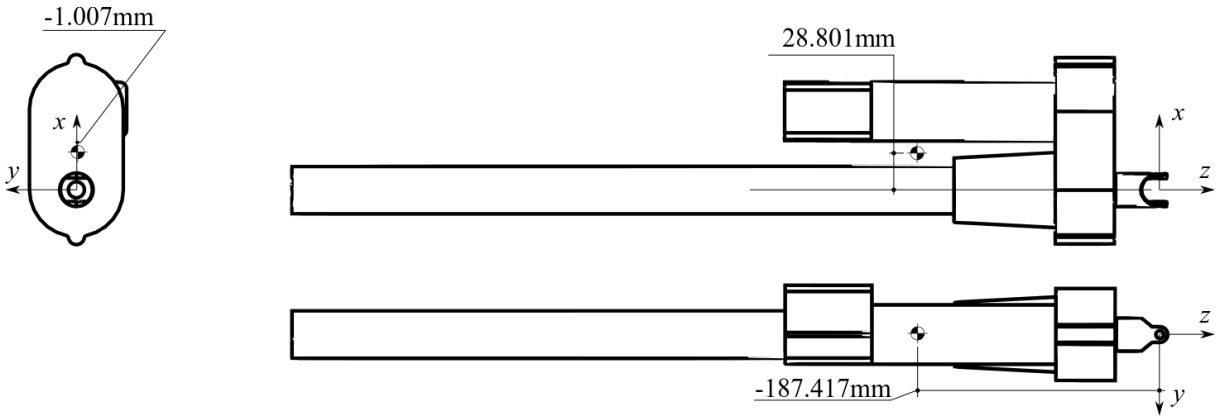

Figure 6.16 The mass centre of sleeve and attached components.

3) Inertia Property of Shaft of Linear Actuators

The mass centre of shaft of linear actuators and attached double Cardan joint bases are marked on the drawing in fig. 6.17 and the inertial properties are listed in table 6.4.

Table 6.4 The inertial properties of a linear actuator shaft.

Mass (kg)	$m_{\mathrm{L}ij\mathrm{S}} = 0.651$
Mass centre w.r.t. local coordinates (mm)	${}^{\{\mathrm{L}ij\mathrm{S}\}}\boldsymbol{p}_{\mathrm{L}ij\mathrm{SO-C}} = \begin{bmatrix} -0.944 \\ 0 \\ 295.826 \end{bmatrix}$
Inertia tensor w.r.t local coordinates ($\mathrm{kg \cdot mm^2}$)	${}^{\{\mathrm{L}ij\mathrm{S}\}}\boldsymbol{I}_{\mathrm{L}ij\mathrm{S}} = \begin{bmatrix} 14239.190 & 0 & 131.829 \\ 0 & 14323.324 & 0 \\ 131.829 & 0 & 130.193 \end{bmatrix}$

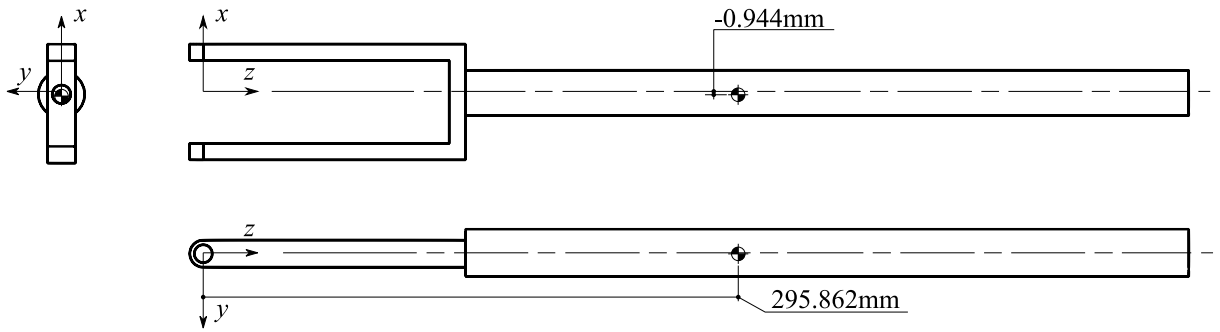

Figure 6.17 The mass centre of linear actuator shaft and attached components.

4) Inertia Property of Big Foot Platform

The mass centre of small foot platform and attached double Cardan joint bases are marked on the drawing in fig.6.18 and the inertial properties are listed in table 6.4

Table 6.5 The inertial properties of big foot platform assembly.

Mass (kg)	$m_{\mathrm{F2}} = 3.476$
Mass centre w.r.t. local coordinates (mm)	${}^{\{\mathrm{F2}\}}\boldsymbol{p}_{\mathrm{F2O-C}} = \begin{bmatrix} 0 \\ -51.203 \\ -36.289 \end{bmatrix}$
Inertia tensor w.r.t local coordinates (kg·mm^2)	${}^{\{\mathrm{F2}\}}\boldsymbol{I}_{\mathrm{F2}} = \begin{bmatrix} 23336.032 & -0.193 & 0.010 \\ -0.193 & 20074.221 & 1885.383 \\ 0.010 & 1885.383 & 39878.542 \end{bmatrix}$

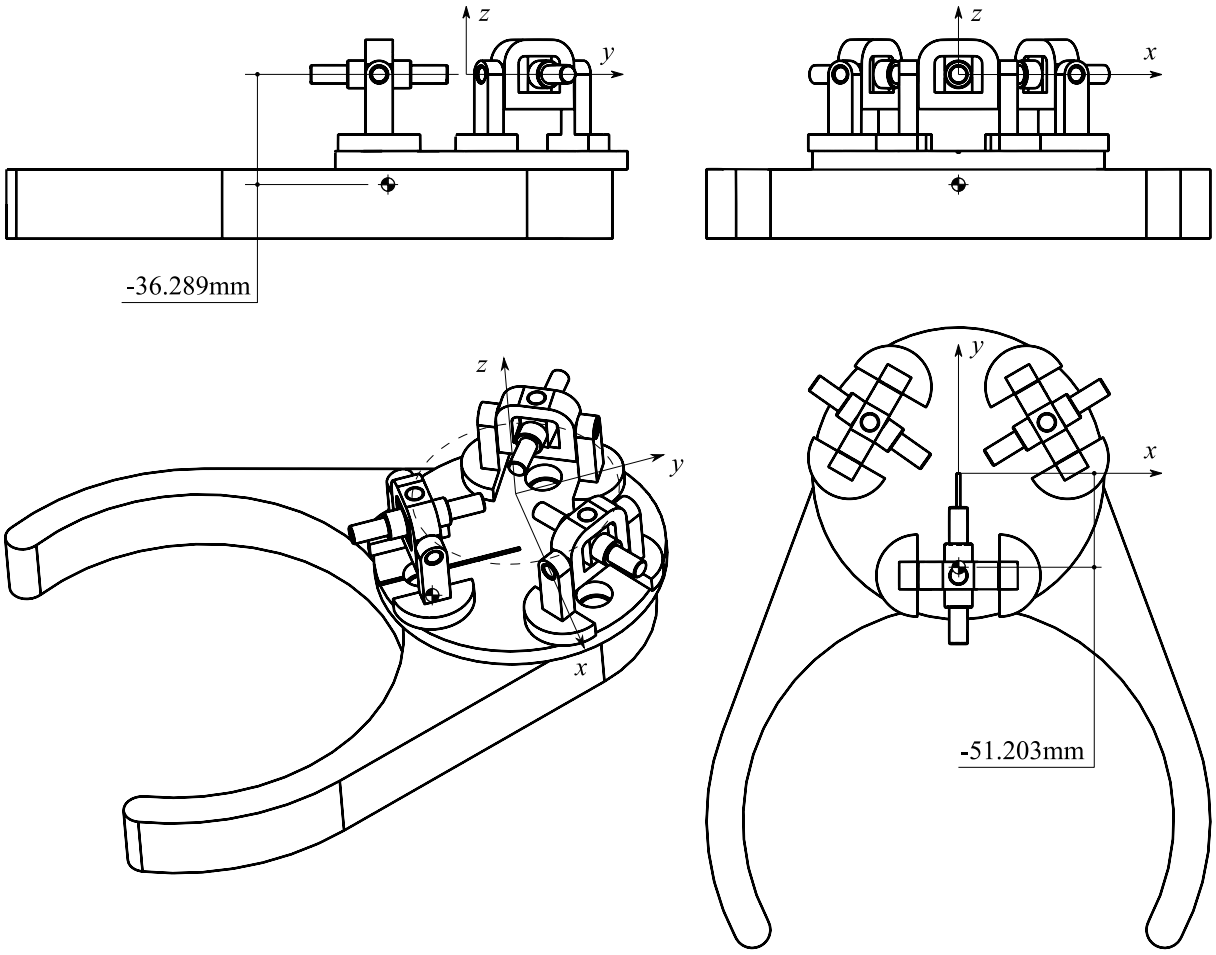

Figure 6.18 The mass centre of big foot platform and attached components.

5) Inertia Property of Small Foot Platform

The mass centre of small foot platform and attached double Cardan joint bases are marked on the drawing in fig. 6.19 and the inertial properties are listed in table 6.5

Table 6.6 The inertial properties of small foot platform assembly.

Mass (kg)	${}^{\{F1\}}m_{F1} = 2.915$
Mass centre w.r.t. local coordinates (mm)	${}^{\{F1\}}\boldsymbol{p}_{F1O-C} = \begin{bmatrix} 0 \\ 35.109 \\ -34.133 \end{bmatrix}$
Inertia tensor w.r.t local coordinates (kg·mm^2)	${}^{\{F1\}}\boldsymbol{I}_{F1} = \begin{bmatrix} 14183.555 & -0.195 & 0.010 \\ -0.195 & 10289.704 & -1304.706 \\ 0.010 & -1304.706 & 21244.101 \end{bmatrix}$

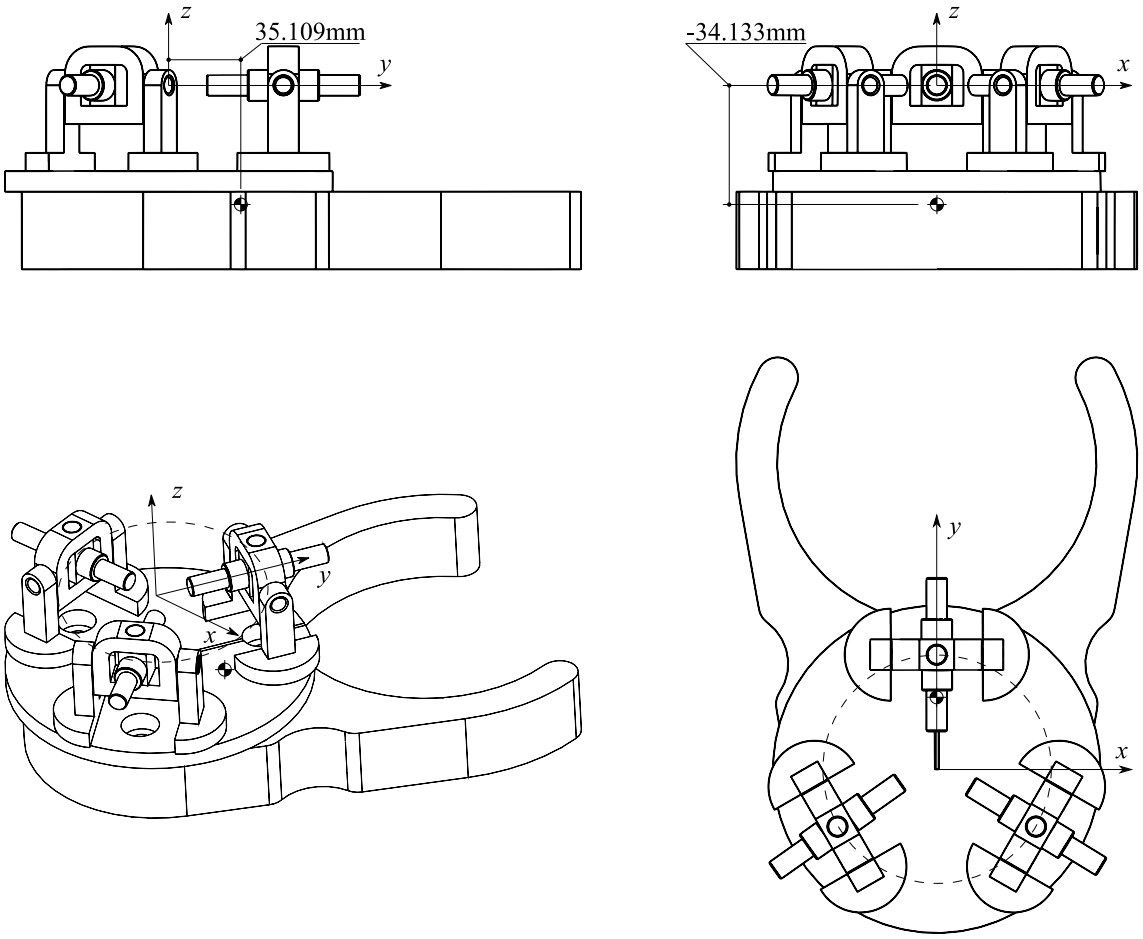

Figure 6.19 The mass centre of small foot platform and attached components.

6.4 Simulation of Inverse Dynamic Model

In this section, four motion cases will be simulated. To eliminate the deviation caused by overtop starting up velocities, the velocity trajectories will be sinus curve. On the other hand, since the actuating force assignment problem will be involved if the hip moves during the both feet contacting the ground, the single-foot-moving dynamics will be simulated in this section. The force assignment problem will be studied in the next chapter. In the simulations, the foot platform on leg-1 was moved and all the actuators on two legs were actuated during both with and without friction concerned.

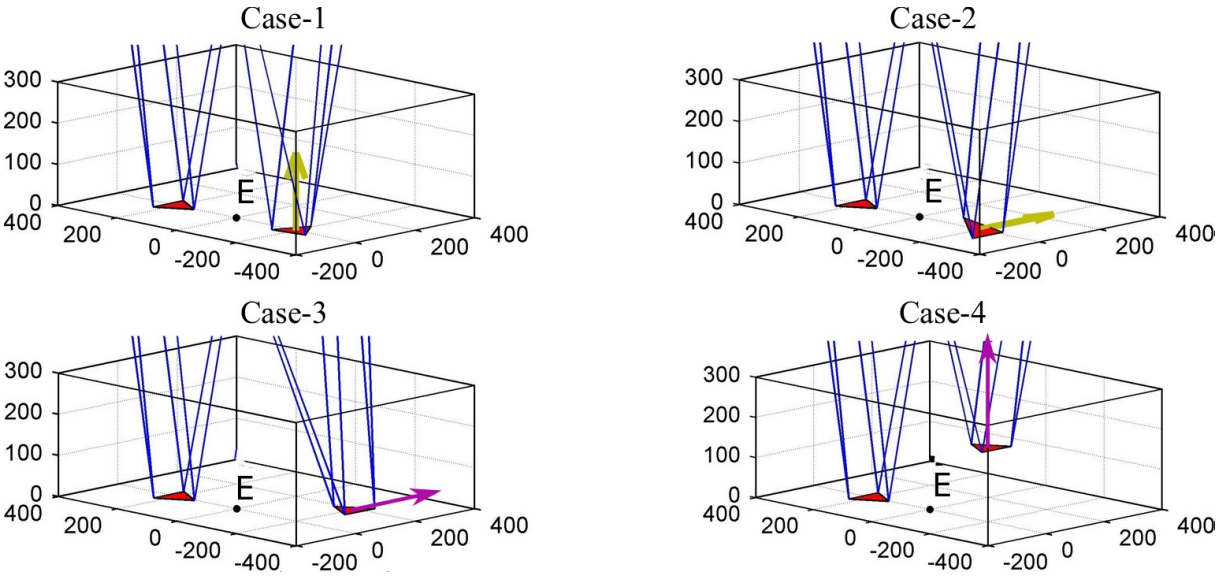

Figure 6.20 Four simulation cases of one foot platform.

Table 6.7 Trajectories of four foot-motion cases for actuating forces simulation.

Cases	Trajectories (simulation time: T=4s)
1	$\dot{X}_{F1}(t) = \left[0 \quad 0 \quad 0 \quad 0 \quad 0 \quad 0.25\pi \sin {}^{\pi t}/_{T}\right]^{T}$
2	$\dot{X}_{F1}(t) = \left[0 \quad 0 \quad 0 \quad 0.25\pi \sin {}^{\pi t}/_{T} \quad 0 \quad 0\right]^{T}$
3	$\dot{X}_{F1}(t) = \left[500 \sin {}^{\pi t}/_{T} \quad 0 \quad 0 \quad 0 \quad 0 \quad 0\right]^{T}$
4	$\dot{X}_{F1}(t) = \left[0 \quad 0 \quad 400 \sin {}^{\pi t}/_{T} \quad 0 \quad 0 \quad 0\right]^{T}$

Case-1: In this case, the foot on leg-1 rotated along *z*-axis. Without friction, the actuating force on leg-1 compensated only the gravity and acceleration. During the pose changing, there is obvious force diversion between actuators. There are also obvious symmetry properties between actuator-1, -3, -5 and actuator-2, -4, -6, due to the centrosymmetric assignment of foot joints (see fig. 6.5). On the standing leg-2, the actuator-1 and -6 are supporting most of the weight, since they are close to centre of gravity of the whole structure. Actuator-2 and -5 are providing constrictions to generate torques against the falling tendency due to gravity. If the frictions are introduced, as fig. 6.21-3, the actuating forces on leg-1 prohibit more non-linearity. The friction took dominancy and the force direction fiercely changed during the moving direction changed. Contrarily, the standing leg-2 was not obviously affected by the friction, and the amplitude of actuating force was decreased by the static frictions.

Case-2: In this case, the foot on leg-1 rotated along *x*-axis. Similar to case-1, the mass centre did not vary and the actuating forces compensated only the rotational momentum and gravity of the foot platform. The rotation happened along *x*-axis, which implies that the motion is symmetric about *y*-*z* plane; the forces on actuator-1, -2, -3 are same as on actuator -6, -5, -4, respectively. This symmetry still maintains if the friction is introduced in fig. 6.22-3. The standing leg did not show distinct difference from case-1, since the load on it barely changed.

Case-3: In this case, the foot platform moved forward and backward. Without friction, the peak power took place when the foot platform moves to the furthest position. The loads on standing leg-2 illustrate symmetry about *y*-*z* plane, besides the initial gravitational loads. Friction plays the most important role if was introduced to leg-1. The static friction also reduced the actuating forces on the static leg-2.

Case-4: In this case, the foot platform was hoisted and then lowered back to the ground. If there is friction on leg-1, the power will be mainly consumed by it, and the value is proportional to the velocity value. Otherwise, the actuating forces were limited to a small range during the whole process and primarily to compensate the gravity.

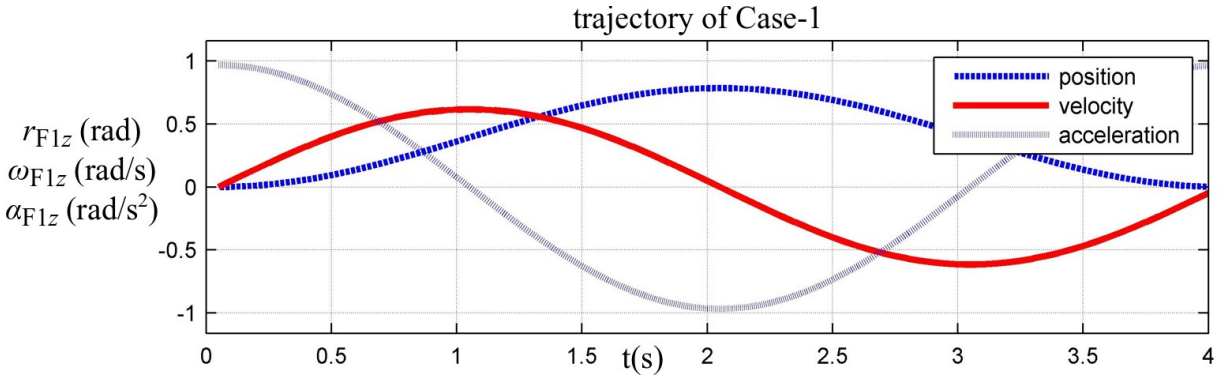

Figure 6.21-1 The trajectory of foot platform on leg-1 in case-1.

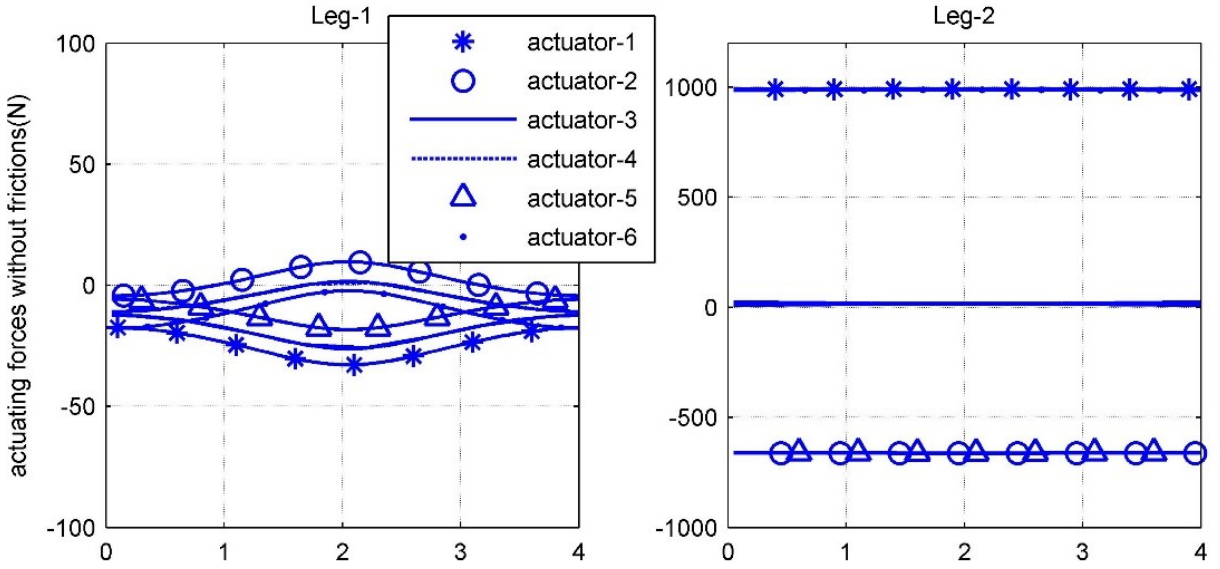

Figure 6.21-2 Actuating forces on linear actuators without friction in case-1.

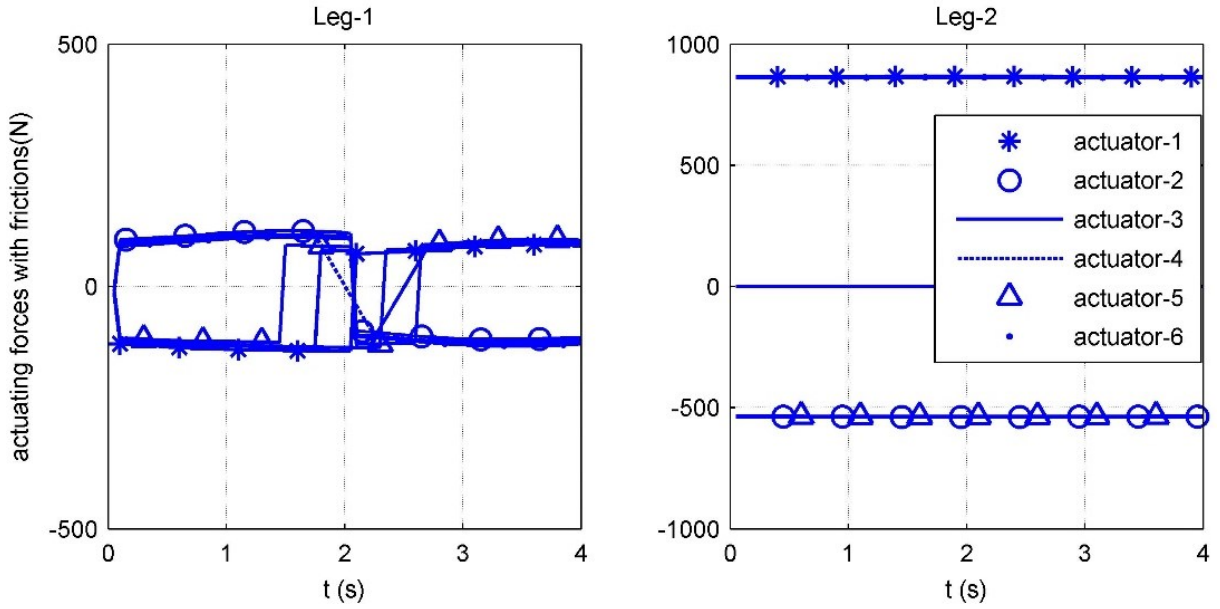

Figure 6.21-3 Actuating forces on linear actuators with friction in case-1.

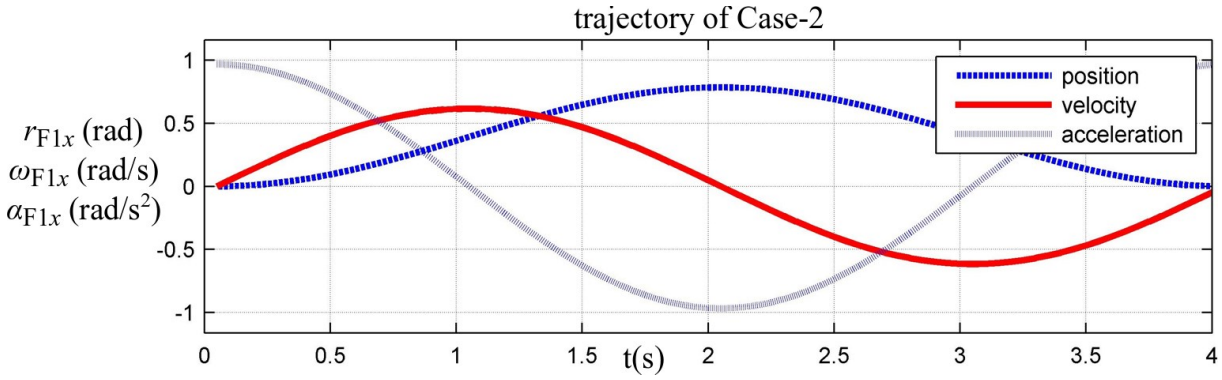

Figure 6.22-1 The trajectory of foot platform on leg-1 in case-2.

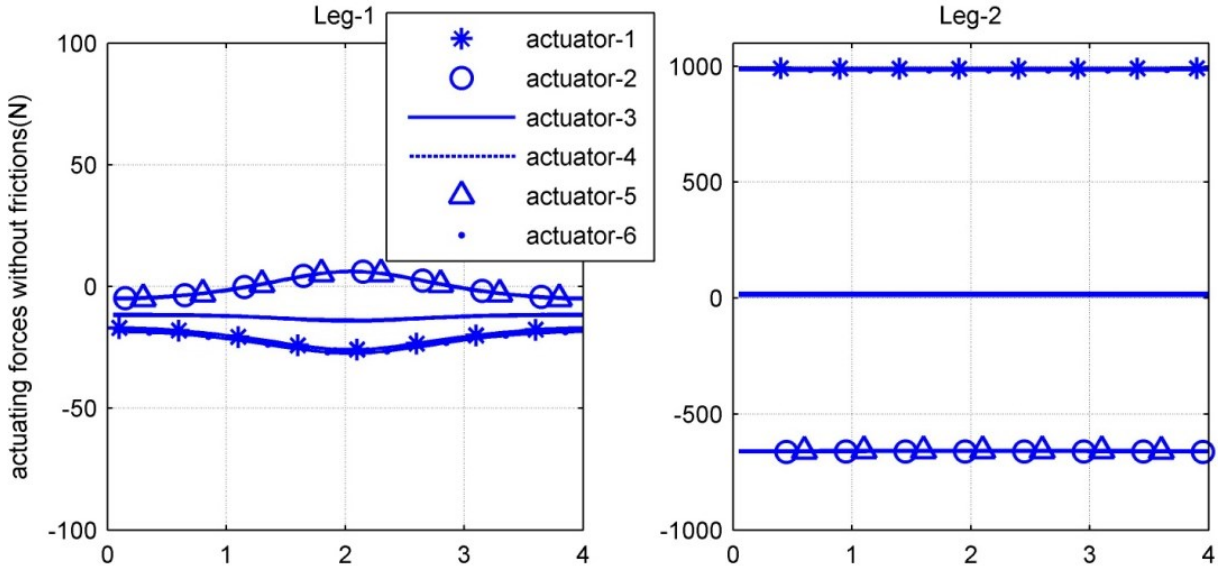

Figure 6.22-2 Actuating forces on linear actuators without friction in case-2.

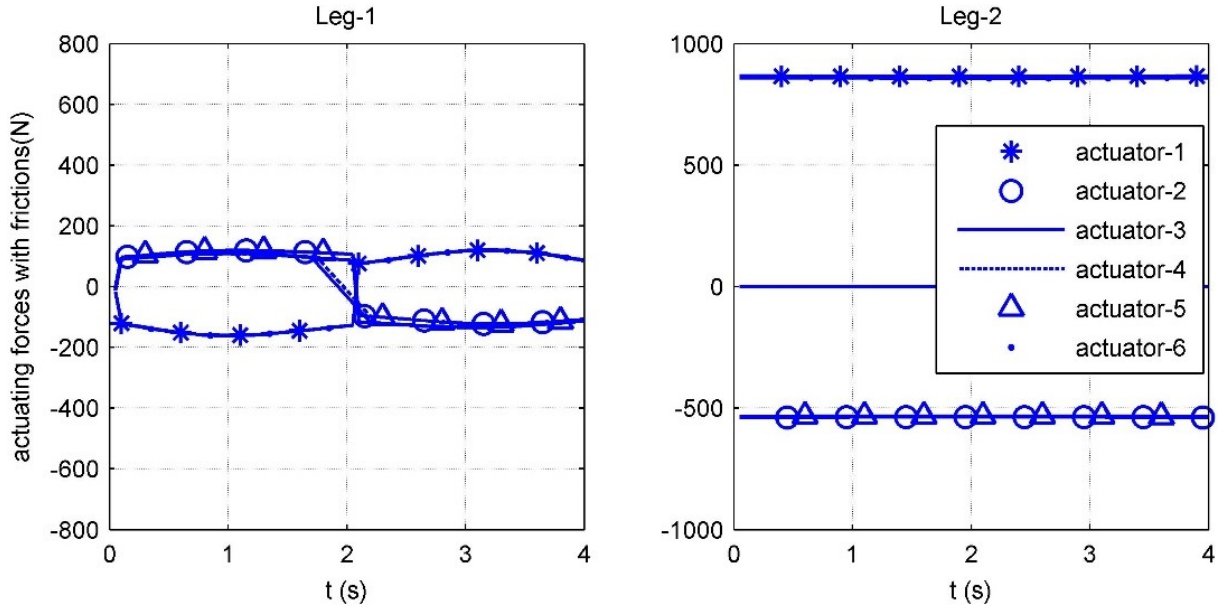

Figure 6.22-3 Actuating forces on linear actuators with friction in case-2.

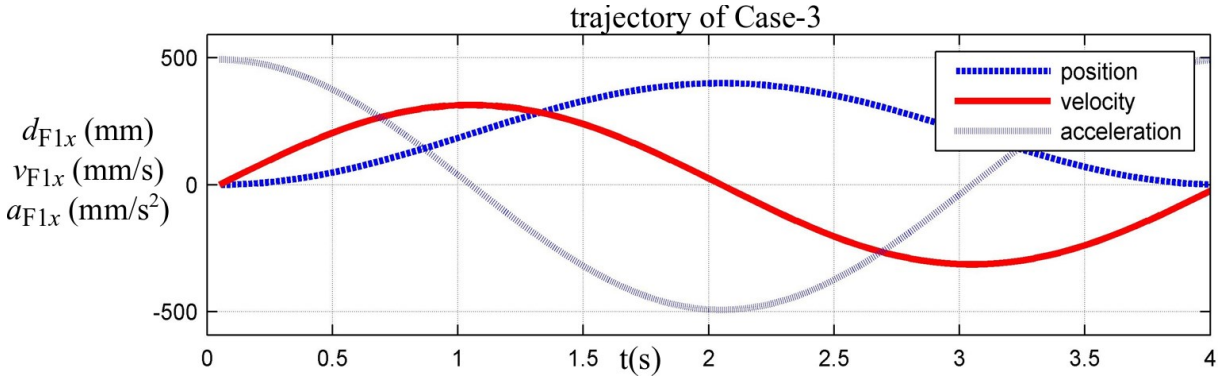

Figure 6.23-1 The trajectory of foot platform on leg-1 in case-3.

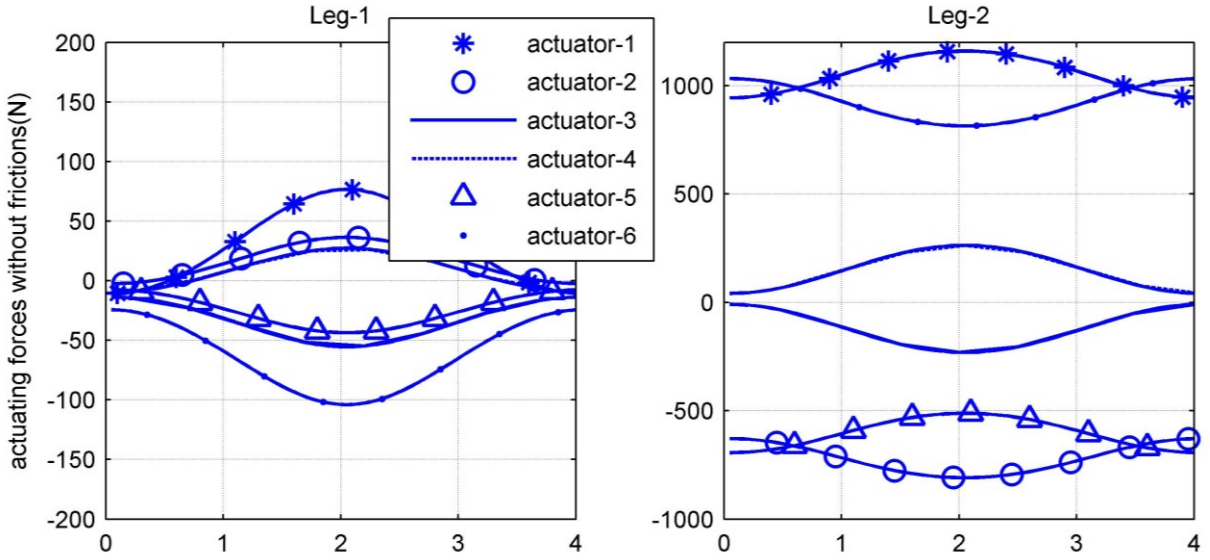

Figure 6.23-2 Actuating forces on linear actuators without friction in case-3.

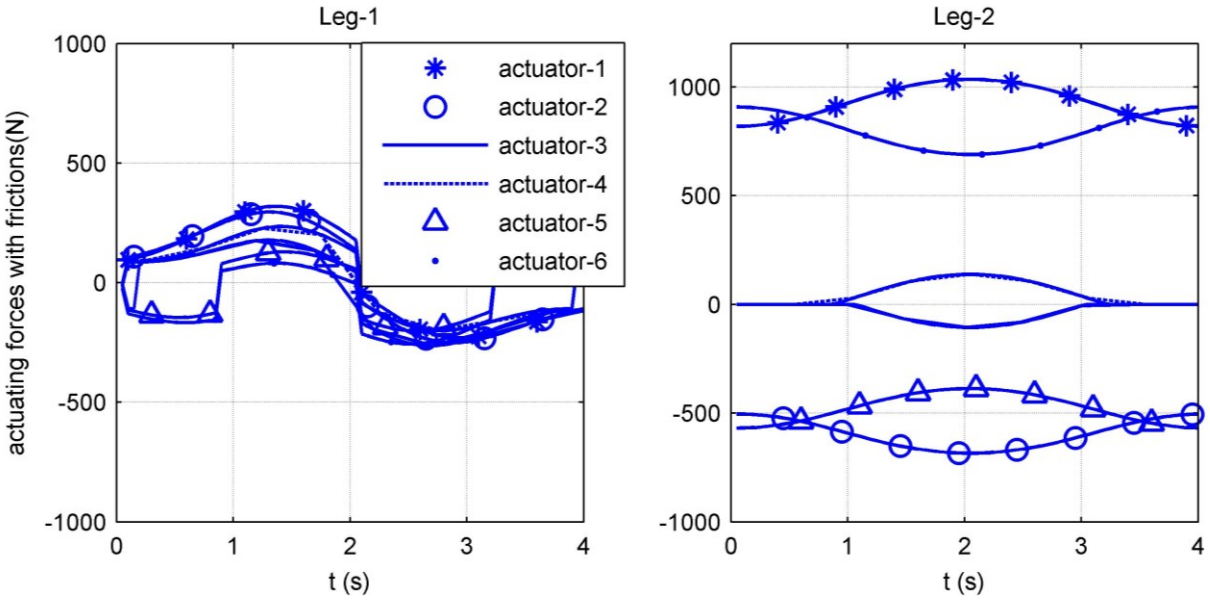

Figure 6.23-3 Actuating forces on linear actuators with friction in case-3.

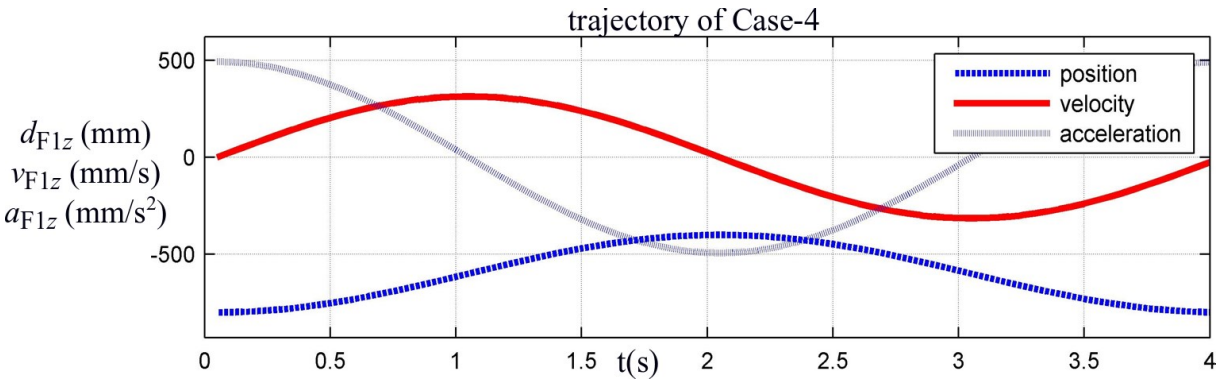

Figure 6.24-1 The trajectory of foot platform on leg-1 in case-4.

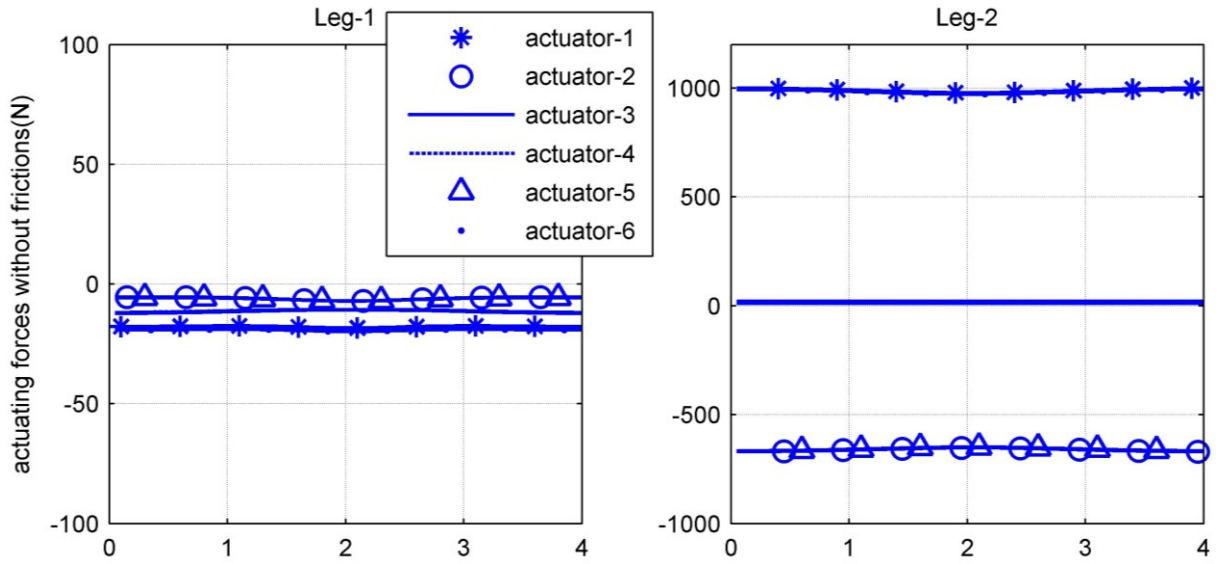

Figure 6.24-2 Actuating forces on linear actuators without friction in case-4.

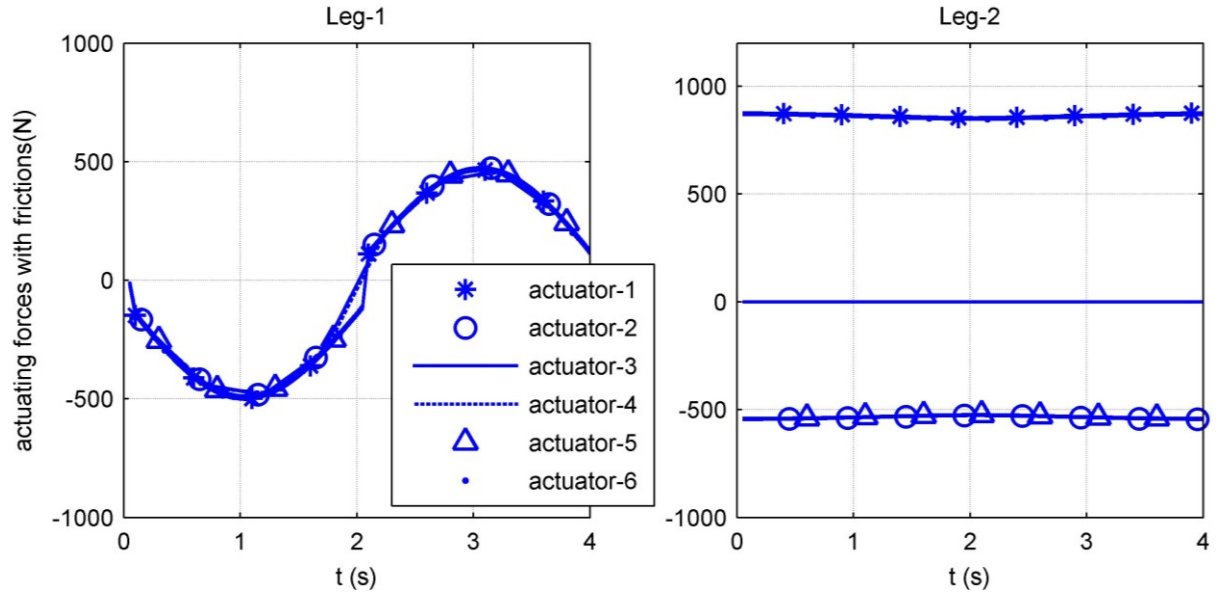

Figure 6.24-3 Actuating forces on linear actuators with friction in case-4.

6.5 Chapter Summary and Discussions

In this chapter, the inverse dynamic model of CENTAUROB was built in the form of two serially connected 6 DOF PKM[6,3]. Firstly, the acceleration equations of each part were derived, including the active and passive. During this procedure, attention should be paid to the analysis of double Cardan joint. The acceleration of the common axis ($\boldsymbol{x}_{\text{common}}$ in fig. 6.3(a)) on one double Cardan joint is only determined by the coupled two linear actuators. This increased the computation complexity, compared to a 6-UPS mechanism, since for the latter, the same acceleration is determined by the acceleration of two end points on one linear actuator. From the simulation results, it can be found the accelerations obey the symmetry of the joint assignment. The resultant accelerations obtain continuity for the continuous platform motions. The results are thus proven to be valid.

In the second part of this chapter, the inverse dynamic model with virtual work principle was built. For this purpose, the complete inverse Jacobians for each main part (those with significant mass) were derived under the general coordinates for the whole mechanism. By means of the utilization of double Cardan joint, the inverse Jacobians of the adjacent limbs in one BKC are coupled and should be distinguished. On the other hand, for a biped working mechanism, if the two feet contacting the ground and both of them are actuated, the model is in an over-actuated condition. For this reason, only the cases with one foot on the ground were analysed in this chapter.

The friction of a single linear actuator unit was identified through experimental approaches and a simplified friction model was built in a reasonable manner. The inertial parameters were identified through software and necessary assumptions were made, i.e. the materials are even and the manufacturing errors were negligible.

At the end of this chapter, the dynamic simulations were conducted and the actuating forces under 4 motion cases were predicted. The results shown that, for the swinging leg, the main load is in fact from the friction, compared to the inertial forces. Conversely, the static friction

for the standing leg compensated partly the actuating forces if both legs are actuated. Another remarkable phenomenon is the sudden change of the frictional load while changing the velocity direction, which could lead to the control delay. From the simulation results of the standing leg(leg-2), the main dynamic load on it is not only the weight of the hip and swinging leg, but also the torque caused by the displacement of the GCoM.

Reference

[6.1] Dasgupta, Bhaskar, and T. S. Mruthyunjaya. "A Newton-Euler formulation for the inverse dynamics of the Stewart platform manipulator." *Mechanism and machine theory* 33.8 (1998): 1135-1152.

[6.2] Müller, Andreas. "Dynamics modeling of topologically simple parallel kinematic manipulators: A geometric approach." *Applied Mechanics Reviews* 72.3 (2020): 030801.

[6.3] Kalani, Hadi, Amir Rezaei, and Alireza Akbarzadeh. "Improved general solution for the dynamic modeling of Gough–Stewart platform based on principle of virtual work." *Nonlinear Dynamics* 83 (2016): 2393-2418.

[6.4] Li, Yangmin, and Stefan Staicu. "Inverse dynamics of a 3-PRC parallel kinematic machine." *Nonlinear Dynamics* 67 (2012): 1031-1041.

[6.5] Bi, Z. M., and Bongsu Kang. "An inverse dynamic model of over-constrained parallel kinematic machine based on Newton–Euler formulation." *Journal of Dynamic Systems, Measurement, and Control* 136.4 (2014): 041001.

[6.6] Ibrahim, Ouarda, and Wisama Khalil. "Inverse dynamic modeling of serial-parallel hybrid robots." *2006 IEEE/RSJ International Conference on Intelligent Robots and Systems*. IEEE, 2006.

[6.7] Khalil, Wisama, and Ouarda Ibrahim. "General solution for the dynamic modeling of parallel robots." *Journal of intelligent and robotic systems* 49 (2007): 19-37.

[6.8] He, Jun, et al. "Dynamics and control of a 7-DOF hybrid manipulator for capturing a non-cooperative target in space." *Mechanism and Machine Theory* 140 (2019): 83-103.

[6.9] Li, Meng, et al. "Dynamic formulation and performance comparison of the 3-DOF modules of two reconfigurable PKM—the tricept and the trivariant." (2005): 1129-1136.

[6.10] Bonnemains, T., et al. "Dynamic model of an overconstrained PKM with compliances: The Tripteor X7." *Robotics and Computer-Integrated Manufacturing* 29.1 (2013): 180-191.

[6.11] Zhang, Xingchao, et al. "Dynamic modeling of a class of parallel-serial mechanisms by the principle of virtual work." *Meccanica* 58.1 (2023): 303-316.

[6.12] Li, Pengcheng, et al. "Visual sensor-based dynamic identification of a 6-RSS parallel robot." *2019 International Conference on Control, Automation and Information Sciences (ICCAIS)*. IEEE, 2019.

[6.13] Zhang, HaiFeng, Wei Ye, and QinChuan Li. "Robust decoupling control of a parallel kinematic machine using the time-delay estimation technique." *Science China Technological Sciences* (2023): 1-12.

[6.14] Arian, Alaleh, Mats Isaksson, and Clement Gosselin. "Kinematic and dynamic analysis of a novel parallel kinematic Schönflies motion generator." *Mechanism and Machine Theory* 147 (2020): 103629.

[6.15] Rosyid, Abdur, and Bashar El-Khasawneh. "Identification of the Dynamic Parameters of a Parallel Kinematics Mechanism with Prismatic Joints by Considering Varying Friction." *Applied Sciences* 10.14 (2020): 4820.

[6.16] Righettini, Paolo, et al. "Experimental set-up for the investigation of transmissions effects on the dynamic performances of a linear PKM." *Advances in Mechanism and Machine Science: Proceedings of the 15th IFToMM World Congress on Mechanism and Machine Science 15*. Springer International Publishing, 2019.

Chapter 7
Stable Walking

Despite the parallel composition, CENTAUROB provides its mobility in the manner of biped walking. Due to this characteristic, its gait planning should adhere to stability criteria like other legged walking mechanisms. The stability of the robot is based on the foot rotation indicator, a conceptual extension of zero moment point. Due to the parallel structured legs, the expected actuating forces of the linear actuators must be obtained through the inverse dynamic model obtained in last chapter. The dynamic load will be split considering the stability criteria as well. The typical walking patterns, such as straight walking, side-walking, and turning, will be simulated, and their stability conditions will be discussed.

7.1 State of the Art

For biped walking mechanisms, and indeed all the legged mechanisms, the walking stability is the utmost important aspect. Besides, regard should also be given to the velocity and comfort of the passenger. The main stability criteria can be roughly classified into two groups: simultaneous and periodic. The latter focuses on the long-term stability. Although the robot is instable for some moments, the stability will recover in the next step period or next several steps. For the latter, the Poincare return map is a powerful tool. The former includes: ground centre of mass (GCoM), zero moment point (ZMP)/ foot rotation point (FRI), capture point (CP).

The GCoM is a static walking criterion, while the ZMP/FRI and CP belong to the dynamic

criteria. To determine the stability of bipedal gait with GCoM, the bigger foot and slower motion are normally needed ([7.1]). It requires the robot to maintain the GCoM inside a kernel area of the support polygon (SP) without extraordinary dynamic load.

Vukobratovic and Stepaneko have firstly proposed the concept of ZMP in 1972 ([7.2]). If the ZMP stays in the SP, the standing foot will not leave the ground and the contacting surface can provide 6-dimensional reactive forces to support the whole static and dynamic loads. There are many earlier practical examples of utilization of ZMP. To the knowledge of author, the earliest successful example is the WL-10RD ([7.3]), which was developed by the Kato laboratory of Waseda university. The step time was decreased from 9 seconds to 1.3 seconds by using ZMP strategy. From the definition of ZMP, Yamaguchi et al. ([7.4]) have derived the relation between the robot acceleration and the ZMP locus and further realized stable walking on WL-12 robot. Afterward, Yamaguchi et al. ([7.5]) have determined the joints trajectories from optimal ZMP loci by using the concept of fast Fourier transform (FFT), further realized stable walking on humanoid robot, WABIAN. Huang et al. ([7.6]) have parameterized the trajectory of hip and swing leg, then searched in the parameter space and obtained the optimal parameter combination according to the ZMP index. ZMP were used as stability criteria for BHR series ([7.7]) and THBIP series ([7.8]).

In recent years, the researches around ZMP approaches are still making progress. Various control methods based on ZMP were developed. Piperakis and Trahanias have developed the state estimator based on non-linear ZMP ([7.9]). ZMP was treated as an indirect manipulation variable and a novel control method was thus developed in the work of Sugihara et al. ([7.10]). ZMP was also used as trajectory optimization constraints for non-legged robots in [7.11].

FRI was nominated by Goswami in 1999 ([7.12]). The ZMP and FRI coincide in the SP if the standing foot is not rotating. If the ground cannot provide enough reactive force, the foot will rotate and FRI will fall out of the SP. The deviation of FRI can be used as the metric margin of stability. Vukobratovic and Borovac have re-defined the ZMP in [7.13] and proven the equivalency of ZMP and FRI.

CP is a frequently used stability indicator. In a simplified manner, the ground position of CP can be calculated as $\boldsymbol{p}_{\mathrm{CP}} = \boldsymbol{p}_{\mathrm{ZMP}} - \boldsymbol{M}\dot{\boldsymbol{X}}_{xy}/\boldsymbol{g}$. Where $\boldsymbol{p}_{\mathrm{ZMP}}$, $\boldsymbol{M}$, $\dot{\boldsymbol{X}}_{xy}$ and $\boldsymbol{g}$ are the location of ZMP, angular momentum, robot velocity on the horizontal plane and gravity acceleration, respectively. There are some application examples of CP theory, such as [7.14] and [7.15].

The periodical stability means rather cyclic stable steps, than stable states for every instance ([7.16]). In Poincare return map theory, the state variables will return to the stable range along the state periodic orbit in the state space ([7.17]). Nonetheless, this method is more capable for high periodical and low disturbance walking scenarios. Thus, it is mainly applied on passive robots, such as [7.18] and [7.19], and jumping robots, such as [7.20] and [7.21].

The contents of this chapter will be arranged as follows: Firstly, the stability index will be introduced and the definition of stability will be discussed; then, the stable motions of one foot swinging and two feet standing will be analysed; especially, the load split strategy for two feet standing will be developed with consideration of single foot stability; three typical motions: straight walking, side-walking and turning will be simulated; at the end, the chapter will be summarized and perspective suggestion of dynamic walking will be made.

7.2 Stable Walking

The topics around biped walking are mainly about stability indices, walking pattern planning or walking pattern control. The walking pattern planning is to generate the desired trajectory of stable walking, on- or off- line. It is frequently used as the feed-forward input of real-time control. The walking pattern control is to fix the motion pattern in real-time and ensure the stability of walking. During the walking process, pattern control information can be obtained by the sensors and algorithms and used as the feedback of the stability control. A stability index represents the stable condition of walking under control strategies. It is the basis of stable walking studies. The walking stability and its margin can be determined by the location of stability index. Hereby, ground projection centre of mass (GCoM), zero moment point (ZMP)

and foot rotation indicator (FRI) will be introduced.

7.2.1 Walking Stability Indices

1) Ground Projection Centre of Mass

For a multi-body system with *n* rigid bodies, the mass centre projection on horizontal ground can be intuitively obtained, as

$$\boldsymbol{p}_{\mathrm{GCoM}} = [\boldsymbol{x} \quad \boldsymbol{y} \quad \boldsymbol{0}] \begin{bmatrix} p_{\mathrm{F\Sigma C}x} \\ p_{\mathrm{F\Sigma C}y} \\ p_{\mathrm{F\Sigma C}z} \end{bmatrix} = \frac{1}{\sum m_i} \begin{bmatrix} 1 & 0 & 0 \\ 0 & 1 & 0 \\ 0 & 0 & 0 \end{bmatrix} \sum_{i=1}^{n} (m_i \boldsymbol{p}_{i\mathrm{C}}) . \tag{7.1}$$

m_i is the mass of the *i*-th rigid body and its mass centre locates at $\boldsymbol{p}_{i\mathrm{C}}$. The mass centre represents only the application point of gravity. Thus, the robot is statically stable if $\boldsymbol{p}_{\mathrm{GCoM}}$ stays in the support polygon. In other words, the robot will not fall without any velocity or acceleration except gravity.

2) Zero Moment Point

ZMP is the point on the contacting surface of foot and ground, where the ground reactive force produces no rotational moment parallel to contact surface. At ZMP, the resultant supporting force provided by the ground can be expressed as

$$[\boldsymbol{x} \quad \boldsymbol{y} \quad \boldsymbol{0}] \iint_{\boldsymbol{p}_{\mathrm{ZMP}}}^{\{\boldsymbol{p}_{\mathrm{SP}}\}} (\boldsymbol{p} - \boldsymbol{p}_{\mathrm{ZMP}}) \times \boldsymbol{f}_{\mathrm{R}}(\boldsymbol{p}) d\boldsymbol{p} = \boldsymbol{0}. \tag{7.2}$$

$\boldsymbol{f}_{\mathrm{R}}$ is the ground reactive force at point $\boldsymbol{p}$; its distribution can be measured by force sensors. $\{\boldsymbol{p}_{\mathrm{SP}}\}$ is the set of points on SP. The definition of ZMP is, in fact, equivalent to centre of pressure (CoP). It is notable that if the robot is falling and the standing foot is actuated to stay on the ground, there is also the possibility of ZMP not reaching the contour of support polygon, neither. Consequently, the usage of ZMP must be accompanied by the trajectory of robot. Considering the trajectory referred to the standing foot, if the ZMP is inside the support polygon but not on the contour, the walking can be considered stable.

3) Foot Rotation Indicator

FRI is a conceptual extension of ZMP and is also known as FZMP (fictitious ZMP). A ZMP is normally measured by the sensor units beneath the foot and used to correct its deviation from an optimal ZMP. According to the definition of eq. (7.2), the ZMP will not leave the support polygon, as when the robot falls, the reactive force of the ground will concentrate at the last contacting point, with its component being only the force orthogonal to the ground plane.

On the other hand, FRI is derived from the motion analysis of the standing foot. If the standing foot is stable, the resultant torque applied to it should be zero at any point. Choosing the centre of vertical reactive forces of the ground, namely CoP, and making torque about it, the horizontal moment should be zero, as eq. (7.3).

$$[\boldsymbol{x} \quad \boldsymbol{y} \quad \boldsymbol{0}][(\boldsymbol{p}_{\mathrm{F}i\mathrm{C}} - \boldsymbol{p}_{\mathrm{FRI}}) \times \boldsymbol{g}m_{\mathrm{F}i} + \boldsymbol{M}_{\mathrm{F}i} - \boldsymbol{p}_{\mathrm{FRI}} \times \boldsymbol{F}_{\mathrm{F}i}] = \boldsymbol{0} \tag{7.3}$$

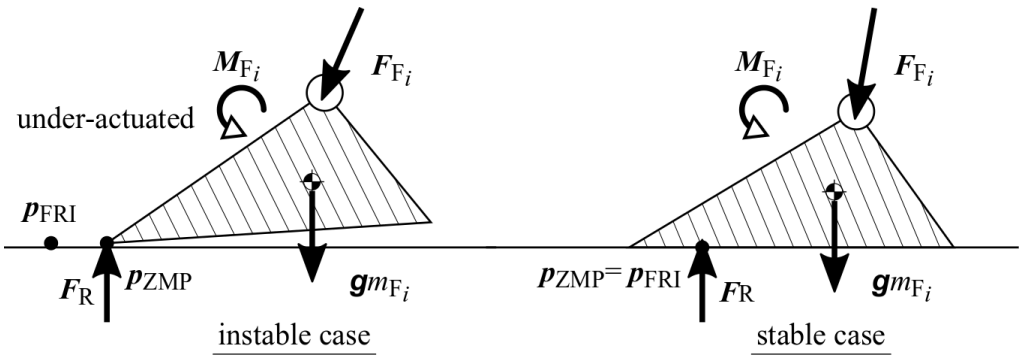

Figure 7.1 The stable case and instable case according to FRI theory.

At point $\boldsymbol{p}_{\mathrm{FRI}}$, the ankle load $(\boldsymbol{F}_{\mathrm{F}i}, \boldsymbol{M}_{\mathrm{F}i})$ and gravity $\boldsymbol{g}m_{\mathrm{F}i}$ will not cause any resultant torque parallel to the horizontal plane. It can be seen that the FRI is not limited in the SP. The ground cannot provide enough passive supporting forces to form a CoP outside SP. This fictitious CoP is named as FRI. Inside SP, the CoP, ZMP and FRI coincide, while only FRI can locate outside SP. The distance between the FRI and the contour of SP can be used as the index of instability of the standing foot.

7.2.2 Classification of Stable Walking

The walking of a robot is to transport the mass with reciprocating contact with the ground and

the reactive force of the motion originates only from the ground. The stability of the walking is to make sure the motion is always under control and will not permanently lose the ground reactive force to drive the robot as required. This is to say, some unstable static pose could be stable during the dynamic process, if the FRI stability still remains.

If the static stability index (GCoM) is always maintained during the walking, the ground reactive force can at least sustain the static load for different pose configurations. The main load is induced by the gravity; the walking pattern is classified as static walking.

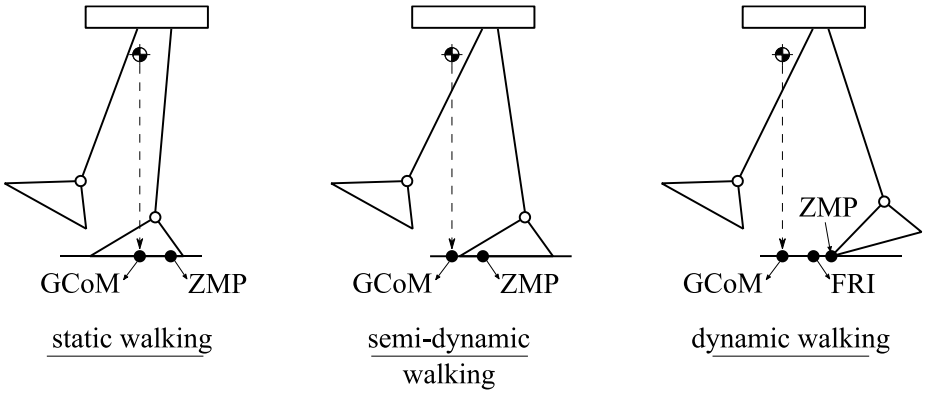

Figure 7.2 Different walking mode classifications.

In comparison, if the FRI is always maintained in the support polygon, the ground can convey enough reactive force to the motion of the robot in every moment. This state is classified as a semi-dynamic walking.

If time variable is introduced, the robot will need to recover its semi-dynamic stability periodically. The under-actuated state will take place but it can be eliminated through the foundation of new support polygon, which will cover the FRI. This is in fact the running pattern of most legged animals including human.

7.2.3 Discussions about Stability Indicator

From the definition of ZMP/FRI, it can be seen that the aim of stability under this criterion is in fact to prevent under-actuated rotation of the standing foot. Nevertheless, this criterion is not the sufficient condition of a stable walking. When the rest parts of the robot are falling, the ZMP/ FRI can still locate inside the SP if the actuators are not actuated and ankle joint force will

be zero. The ZMP/FRI is neither the necessary condition of a stable walking, since natural walking or running of animals is not obeying the ZMP/FRI stability. ZMP/FRI is indeed a conservative criterion of walking stability. A more proper utilization of ZMP/FRI criterion should be like: a desired trajectory should be firstly generated, and then the ZMP/FRI stability should be verified. In this work, the trajectories of different walking phases will be designed and the corresponding FRI loci will be surveyed.

7.3 Motion with One Standing Foot

In a one-foot-standing phase, the whole mechanism is 12-dimensionally actuated and two platforms can be moved, namely the hip and swinging foot. In most scenarios, the aim of a swinging phase is to let the swinging foot forming a new contact surface so that the locomotive purpose can be realized. Based on the inverse dynamic model provided in Chapter 6, the loci of stability indicators can be generated for various trajectories. Conversely, loci of stability indicators will be used to revise the trajectories. For this sake, some trajectories will be generated according to the FRI.

7.3.1 The Generation of FRI Point in a One-Foot-Standing Phase

For a quasi-dynamic walking case, the standing foot remains static, which means that the reactive force provided by the standing foot through the double Cardan joint is always along the axis of a linear actuator. Making torques about the coordinate origin, the sums of forces and torques applied on the standing foot platform should be

$$\begin{cases} \boldsymbol{F}_{\mathrm{F}i} = -\sum_{j=\mathrm{A}}^{\mathrm{F}} \boldsymbol{\tau}_{ij} = \sum_{j=\mathrm{A}}^{\mathrm{F}} \tau_{ij}\boldsymbol{e}_{ij}\,, \\ \boldsymbol{M}_{\mathrm{F}i} = -\sum_{j=\mathrm{A}}^{\mathrm{F}} \widetilde{\boldsymbol{p}}_{\mathrm{F}ij}\boldsymbol{\tau}_{ij} = \sum_{j=\mathrm{A}}^{\mathrm{F}} \tau_{ij}\widetilde{\boldsymbol{p}}_{\mathrm{F}ij}\boldsymbol{e}_{ij}\,, \end{cases} \quad i = 1,2. \tag{7.4}$$

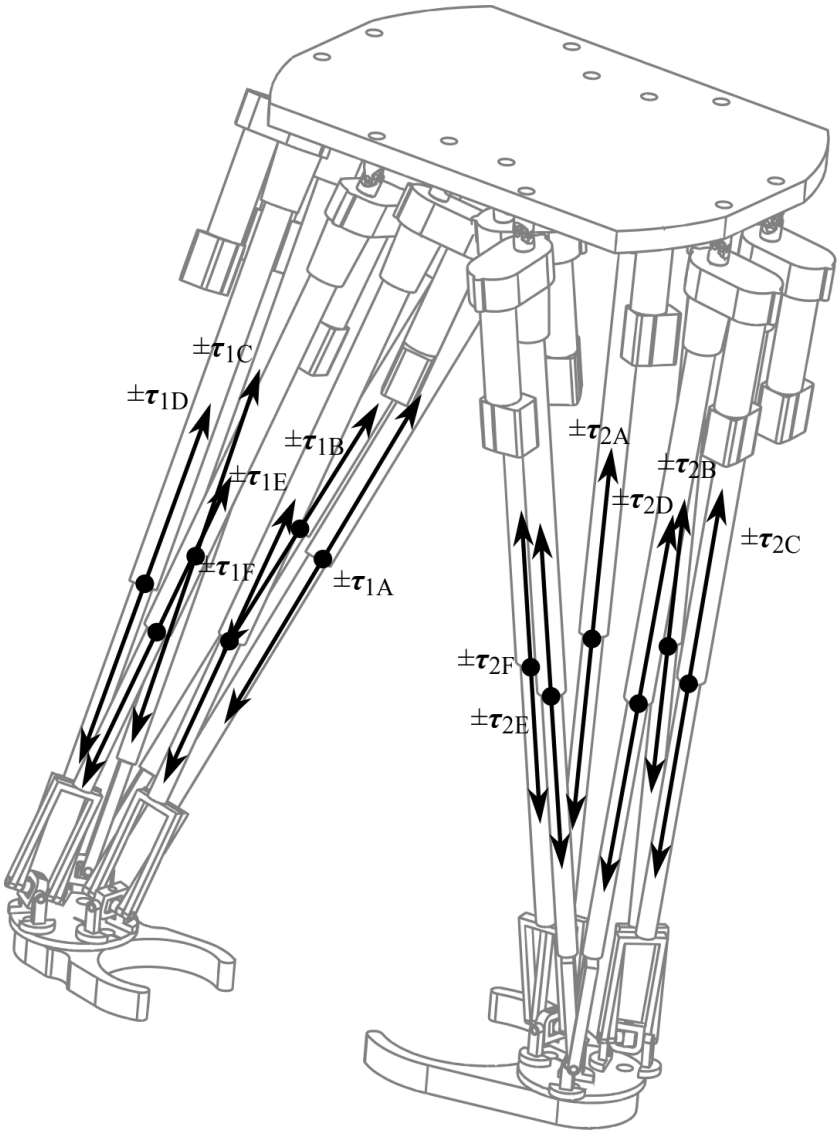

Figure 7.3 The active forces provided by linear actuators during the one-foot-standing phase (leg swing phase). The actuating forces pairs are along the z-axis of linear actuators.

Naming the resultant ground reaction force and torque as $\boldsymbol{F}_{\mathrm{R}}$ and $\boldsymbol{M}_{\mathrm{R}}$, the $\boldsymbol{F}_{\mathrm{R}}$ was applied on point $\mathrm{P}_{\mathrm{CoP}}$ on the ground plane, where $\boldsymbol{p} = \overline{\mathrm{OP}}_{\mathrm{CoP}}$. $\mathrm{P}_{\mathrm{CoP}}$ is the CoP. In this case, the source of the resultant torque is only the friction and $\boldsymbol{M}_{\mathrm{R}}$ is vertical to the ground plane. Making torque to the coordinate origin, the following relation exists if there is no rotational acceleration on the foot.

$$\boldsymbol{M}_{\mathrm{R}} + \boldsymbol{p} \times \boldsymbol{F}_{\mathrm{R}} + \boldsymbol{p}_{\mathrm{F}i\mathrm{C}} \times \boldsymbol{g} m_{\mathrm{F}i} + \boldsymbol{M}_{\mathrm{F}i} = \boldsymbol{0}. \tag{7.5}$$

Making torque to the CoP, there will be

$$\boldsymbol{M}_{\mathrm{R}} + (\boldsymbol{p}_{\mathrm{F}i\mathrm{C}} - \boldsymbol{p}) \times \boldsymbol{g} m_{\mathrm{F}i} + \boldsymbol{M}_{\mathrm{F}i} - \boldsymbol{p} \times \boldsymbol{F}_{\mathrm{F}i} = \boldsymbol{0}. \tag{7.6}$$

Assuming an infinite ground friction provided by the contacting surface, the rotational acceleration exists only on the horizontal ground plane. Projecting eq. (7.6) on the ground, $\boldsymbol{M}_{\mathrm{R}}$ will be eliminated since it is vertical to the projecting plane, there will be

$$[\boldsymbol{x} \quad \boldsymbol{y} \quad \boldsymbol{0}][(\boldsymbol{p}_{\mathrm{F}i\mathrm{C}} - \boldsymbol{p}) \times \boldsymbol{g}m_{\mathrm{F}i} + \boldsymbol{M}_{\mathrm{F}i} - \boldsymbol{p} \times \boldsymbol{F}_{\mathrm{F}i}] = \boldsymbol{0}. \tag{7.7}$$

Where, $\boldsymbol{p}_{\mathrm{F}i\mathrm{C}}$ is the location of the mass centre of the foot $\{\mathrm{F}_i\}$, $\boldsymbol{p}_{\mathrm{F}i\mathrm{C}} = \boldsymbol{p}_{\mathrm{F}i} + e^{\boldsymbol{r}_{\mathrm{F}i}\{\mathrm{F}i\}}\boldsymbol{p}_{\mathrm{F}i\mathrm{O}-\mathrm{C}}$. Note that, eq. (7.7) is tenable only if the point $\mathrm{P}_{\mathrm{CoP}}$ is inside the contact polygon of the standing foot, because the reaction force cannot be applied outside it. If any point (inside or outside the support polygon) fulfils eq. (7.7) by replacing $\boldsymbol{p}$ by $\boldsymbol{p}_{\mathrm{FRI}}$, it can be denoted as a *foot rotation indicator* (FRI).

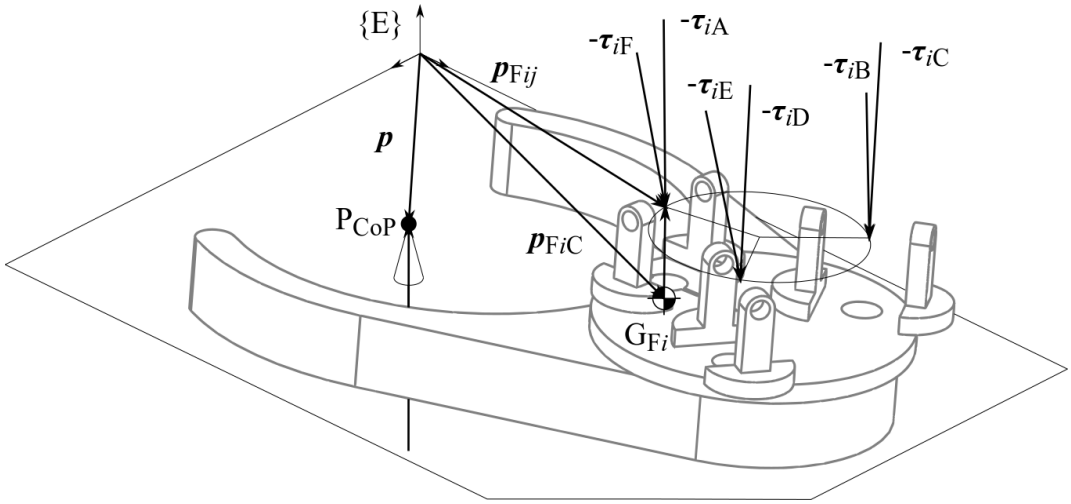

Figure 7.4 The force analysis of a standing foot and the location of centre of pressure is denoted as $\mathrm{P}_{\mathrm{CoP}}$.

Definition 7.1 ([7.12]): A ***foot rotation indicator*** (FRI) is the point on the foot/ground contact surface, within or outside the convex hull of the foot-support area, at which the resultant moment of the force/torque impressed on the foot is normal to the surface.

Rewrite eq. (7.7),

$$[\boldsymbol{x} \quad \boldsymbol{y} \quad \boldsymbol{0}][\boldsymbol{A} + \boldsymbol{p}_{\mathrm{FRI}} \times \boldsymbol{B}] = \boldsymbol{0}. \tag{7.8}$$

Where $\begin{cases} \boldsymbol{A} = \boldsymbol{p}_{\mathrm{F}i\mathrm{C}} \times \boldsymbol{g}m_{\mathrm{F}i} + \boldsymbol{M}_{\mathrm{F}i} = [a_x \quad a_y \quad a_z]^{\mathrm{T}}, \\ \boldsymbol{B} = \boldsymbol{F}_{\mathrm{F}i} + \boldsymbol{g}m_{\mathrm{F}i} = [b_x \quad b_y \quad b_z]^{\mathrm{T}}. \end{cases}$

For a horizontal plane, letting $\boldsymbol{p}_{\mathrm{FRI}} = [p_x \quad p_y \quad 0]^{\mathrm{T}}$, the location of FRI will be solved as

$$\begin{cases} p_x = -\dfrac{a_y}{b_z} = \dfrac{p_{\mathrm{FiC}x} g m_{\mathrm{F}i} - M_{\mathrm{F}iy}}{F_{\mathrm{F}iz} + g m_{\mathrm{F}i}}, \\ p_y = \dfrac{a_x}{b_z} = \dfrac{p_{\mathrm{FiC}y} g m_{\mathrm{F}i} + M_{\mathrm{F}ix}}{F_{\mathrm{F}iz} + g m_{\mathrm{F}i}}. \end{cases} \tag{7.9}$$

7.3.2 The Gait Optimization Model Based on FRI (FZMP)

The aim of the gait optimization problem of the robot is the *minimal FRI distance from the optimal FRI* to avoid the rotation of the standing foot, as eq. (7.10). Despite the strategy to optimize the trajectory of the swing foot, it is also an alternative to introduce a compensating hip trajectory.

$$min(\|\boldsymbol{p}_{\mathrm{FRI}} - \boldsymbol{p}_{\mathrm{OPT}}\|) \tag{7.10}$$

For any given gait, the inverse dynamic model can be derived (seeing Chapter 6), as well as determining the actuating forces and the FRI. Due to the complexity of inexplicit forward dynamic models of PKMs, it is inconvenient and time-consuming to generate a hip compensating trajectory originating from the torque and force it needed to maintain the stability, although which is straightforward from the inversion of eq. (7.9). To this end, the compensation trajectory will be generated through the discrete searching of hip locations over time.

1) Searching Algorithm

The searching method can be found in fig. 7.5. For any discrete time $n\Delta t$, the location of the hip at $(n+1)\Delta t$ will be searched near its present location, as the searching radius is $\rho_{\max}$ and the searching direction is defined by φ. The location of the hip platform at time $(n+1)\Delta t$ is

$$\boldsymbol{t}_{\mathrm{H}}(n+1) = \rho[\cos\varphi \quad \sin\varphi \quad 0]^{\mathrm{T}} + \boldsymbol{t}_{\mathrm{H}}(n). \tag{7.11}$$

Given an arbitrary acceleration, the velocity and acceleration demanding to realize this displacement can be derived as table 7.1 by solving the displacement $\boldsymbol{t}_{\mathrm{H}}(n+1)$ as eq. (7.12).

$$\begin{cases} \boldsymbol{t}_{\mathrm{H}}(n+1) = \rho[\cos\varphi \quad \sin\varphi \quad 0]^{\mathrm{T}} + \boldsymbol{t}_{\mathrm{H}}(n), \\ \boldsymbol{a}_{\mathrm{H}}(n+1) = 2\left(\boldsymbol{t}(n+1) - \boldsymbol{t}(n) + \boldsymbol{v}(n)\Delta t\right)/\Delta t^2, \\ \boldsymbol{v}_{\mathrm{H}}(n+1) = \boldsymbol{v}(n) + \boldsymbol{a}_{\mathrm{H}}(n+1)\cdot\Delta t. \end{cases} \tag{7.12}$$

Table 7.1 The state variables between two motion frames.

t	$n \cdot \Delta t$		$(n+1) \cdot \Delta t$
$\boldsymbol{a}_{\mathrm{H}}$	$\mathbf{0}$	$\boldsymbol{a}(t) = \boldsymbol{a}_1$	$\boldsymbol{a}_1$
$\boldsymbol{v}_{\mathrm{H}}$	$\boldsymbol{v}(n)$	$\boldsymbol{v}(t) = \boldsymbol{v}(n) + \int_{n\cdot\Delta t}^{t} \boldsymbol{a}(u)\, du = \boldsymbol{v}(n) + \boldsymbol{a}_1\,(t - n\cdot\Delta t)$	$\boldsymbol{v}(n) + \boldsymbol{a}_1 \cdot \Delta t$
$\boldsymbol{t}_{\mathrm{H}}$	$\boldsymbol{t}(n)$	$\boldsymbol{t}(t) = \boldsymbol{t}(n) + \int_{n\cdot\Delta t}^{t} \boldsymbol{v}(u)\, du$ $= \boldsymbol{t}(n) + \boldsymbol{v}(n)(t - n\cdot\Delta t)$ $+ \frac{1}{2}\boldsymbol{a}_1[t^2 - (n\cdot\Delta t)^2]$ $- \boldsymbol{a}_1\, n\cdot\Delta t\,(t - n\cdot\Delta t)$	$\boldsymbol{t}(n) + \boldsymbol{v}(n)\Delta t$ $+ \frac{1}{2}\boldsymbol{a}_1 \cdot \Delta t^2$

Bring the state variables at time $(n+1)\Delta t$ to the inverse dynamic model, the location of FRI, $\boldsymbol{p}_{\mathrm{FRI}}\big((n+1)\Delta t\big)$, will be obtained. A set of FRIs will be generated and the corresponding $\boldsymbol{t}_{\mathrm{H}}\big((n+1)\Delta t\big)$ with the smallest distance to the optimal FRI location will be adopted as the new searching centre. The searching step length and range will be decreased to find the optimal state variables for the new iteration. The iterations will be repeated until the difference between the biggest and smallest $\|\boldsymbol{p}_{\mathrm{FRI}} - \boldsymbol{p}_{\mathrm{OPT}}\|$ under a threshold value. Once the optimal state variables were obtained, they will be evaluated to the trajectory of the hip for the next frame. This procedure can be illustrated as the flowchart in fig. 7.6.

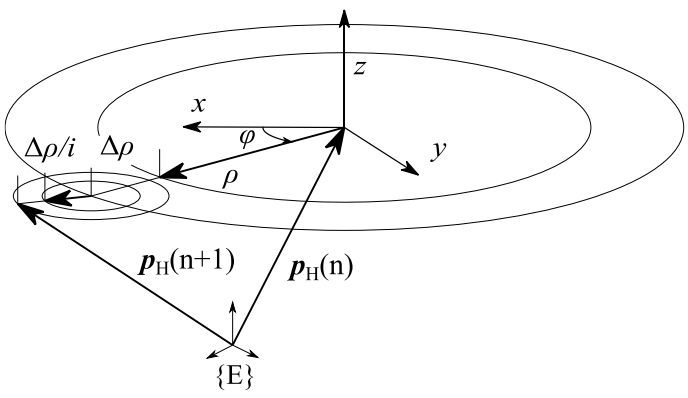

Figure 7.5 The searching strategy of optimal hip compensation trajectory.

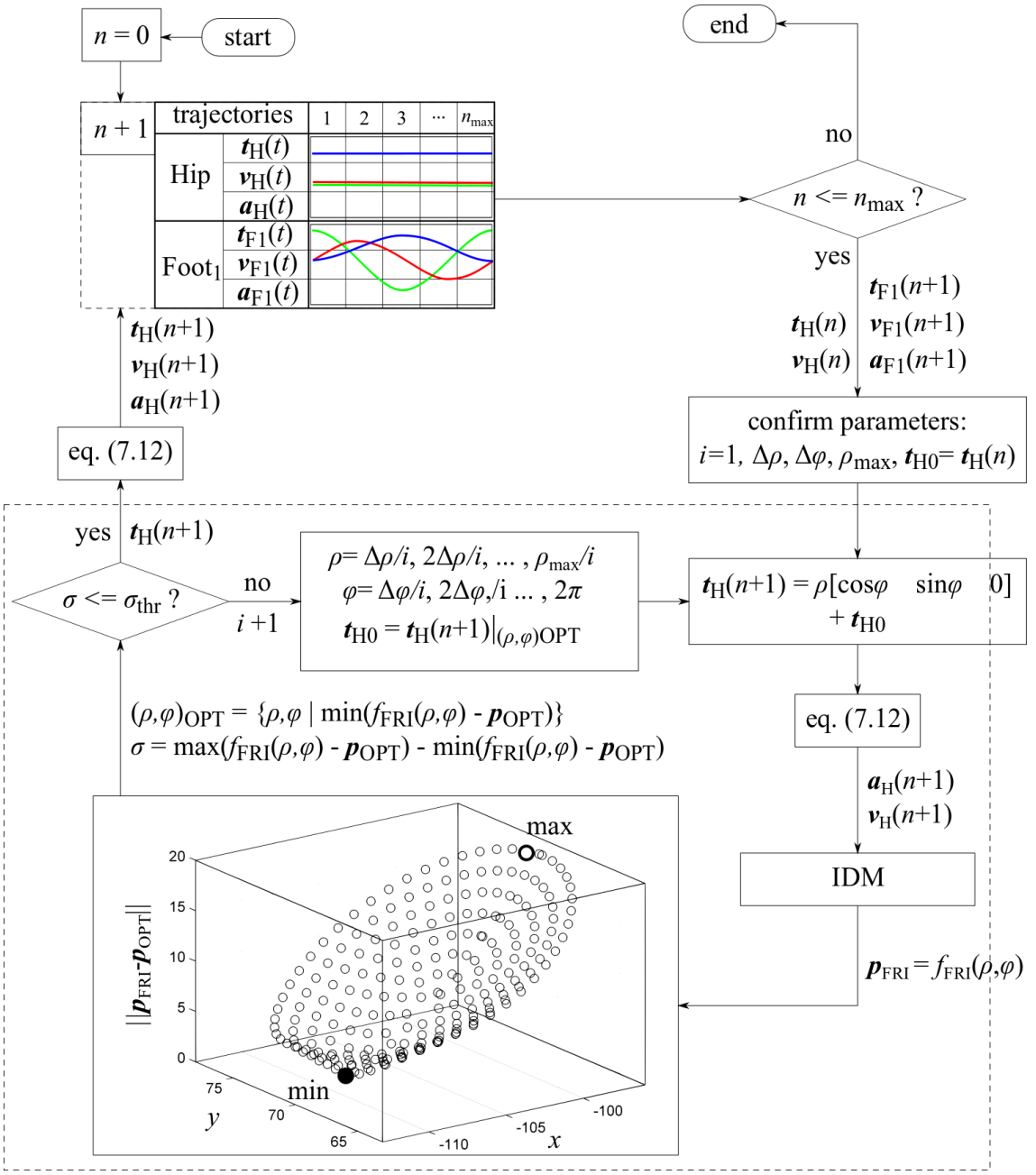

Figure 7.6 The flowchart of hip compensation generation algorithm.

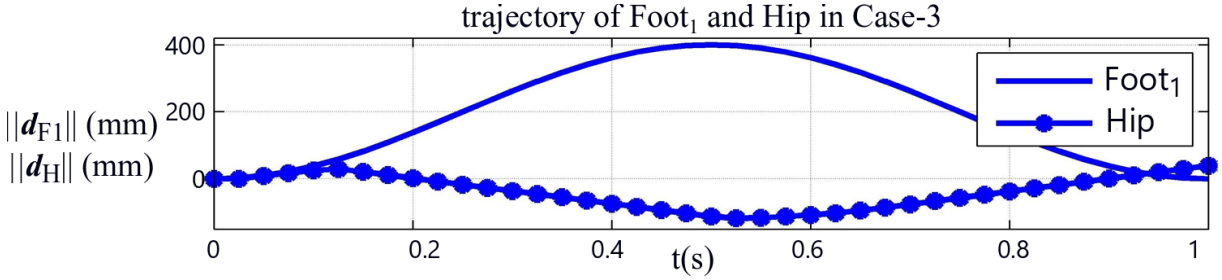

Figure 7.7 The translational displacement of swinging foot and the generated hip compensation trajectory.

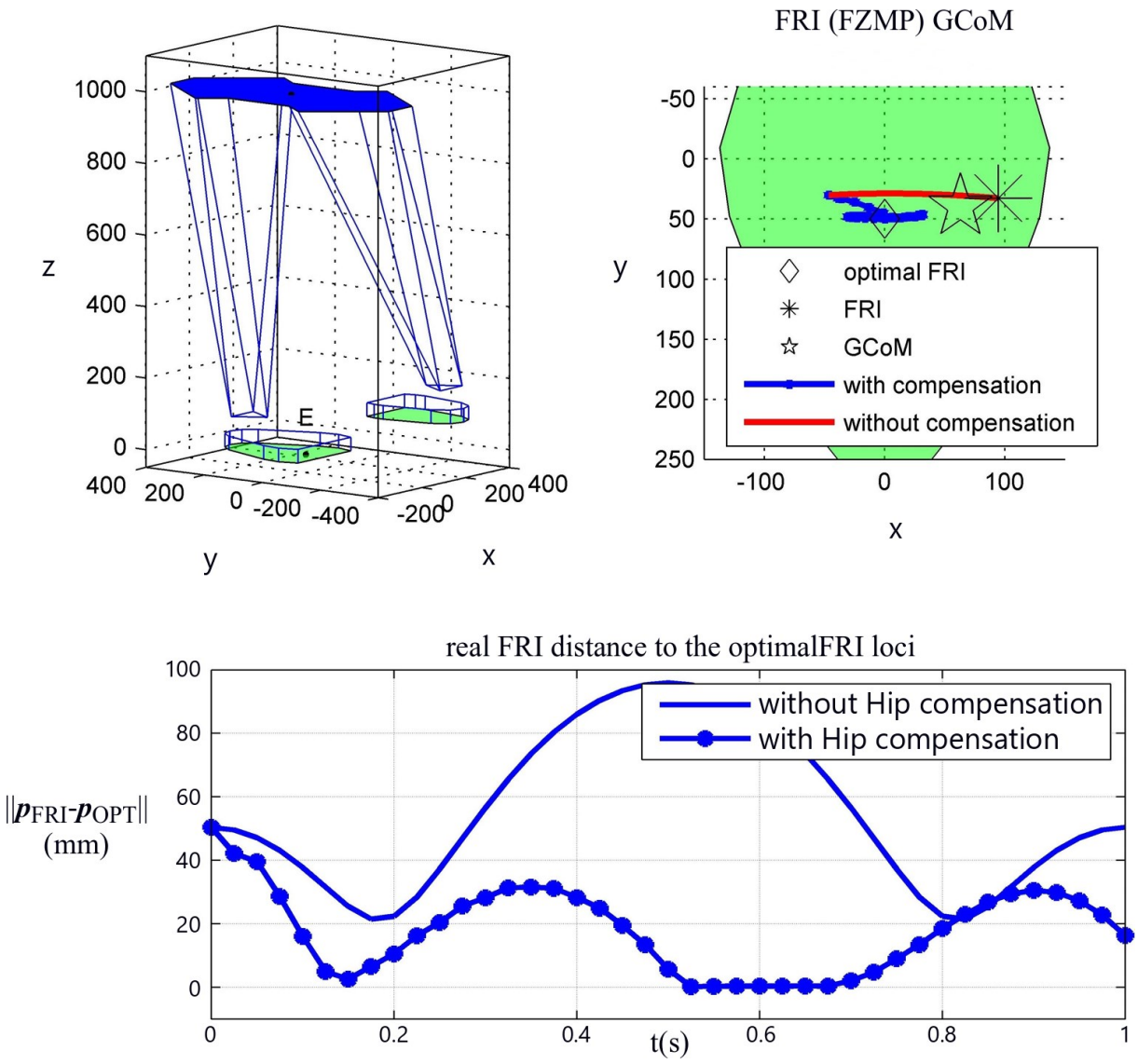

Figure 7.8 The FRI loci between with and without compensating hip motion. With the compensation, the FRI was limited to a 36mm range around the optimal FRI.

2) Case Study of FRI with Hip Compensation

Refer to Case-3 in table 6.7, foot-1 swings along *x*-axis forward and back to the initial position. With the aid of the scheme in fig. 7.6, the compensation trajectory of hip platform is generated, as illustrated in fig. 7.7. Under this compensation, the FRI was ameliorated and its distance to the optimal FRI location decreased to 36mm, comparing to 98mm before the compensation motion of hip was introduced.

7.4 Motion with Two Standing Feet

If both feet contact the ground and the hip platform is the only motive part, it turns into an over actuated system. As mentioned in eq. (6.53), a set of 6 dimensional general forces is applied on 12 actuators. This leaves a 6-dimensional space of actuating forces. As a result, the dynamic loads should be divided reasonably to hold each foot stable.

7.4.1 Dynamic Analysis of Two-Feet-Stance

During one-foot-standing phase, the actuating forces applied to the standing foot can be intuitively obtained; this force set can also represent the dynamic load required to drive the entire structure at the same time.

Assuming that the robot is operating in a swinging phase with two actuating legs (seeing Chapter 6), the actuating forces $\sum \boldsymbol{\tau}_{ij}$ can be obtained through eq. (6.51). The forces applied to the system are the actuating forces $\sum \boldsymbol{\tau}_{ij}$ and the ground supporting forces $(\boldsymbol{F}_{\mathrm{R}}, \boldsymbol{M}_{\mathrm{R}})$. These forces sustain the motion of the system. If the swing leg is not moving and its mass is 0, the mentioned forces are used to drive the moving part, while both feet are supported by the ground. This is equivalent to the two-feet-stance, despite $(\boldsymbol{F}_{\mathrm{R}}, \boldsymbol{M}_{\mathrm{R}})$ being assigned on the polygon formed by two feet, as illustrated in fig. 7.9. To this end, the dynamic load of moving parts can be obtained through eq. (6.51), by letting $m_{\mathrm{F1}} = 0$. No matter the robot is supported by one foot or two feet, for the same motion, the sum of the forces for moving parts should be the same. Letting the dynamic load induced by the system in the dashed line bracket in fig. 7.9 be $(\boldsymbol{F}_{\Sigma}, \boldsymbol{M}_{\Sigma})$, there is

$$\begin{bmatrix} \boldsymbol{F}_{\Sigma} \\ \boldsymbol{M}_{\Sigma} \end{bmatrix} = \begin{bmatrix} [F_{\mathrm{F}\Sigma x} & F_{\mathrm{F}\Sigma y} & F_{\mathrm{F}\Sigma z}]^{\mathrm{T}} \\ [M_{\mathrm{F}\Sigma x} & M_{\mathrm{F}\Sigma y} & M_{\mathrm{F}\Sigma z}]^{\mathrm{T}} \end{bmatrix} = \sum_{i=1}^{2} \sum_{j=\mathrm{A}}^{\mathrm{F}} \begin{bmatrix} \boldsymbol{\tau}_{ij}^{(1)} \\ \widetilde{\boldsymbol{p}}_{\mathrm{F}ij} \boldsymbol{\tau}_{ij}^{(1)} \end{bmatrix} = \sum_{i=1}^{2} \sum_{j=\mathrm{A}}^{\mathrm{F}} \begin{bmatrix} \boldsymbol{\tau}_{ij}^{(2)} \\ \widetilde{\boldsymbol{p}}_{\mathrm{F}ij} \boldsymbol{\tau}_{ij}^{(2)} \end{bmatrix}. \tag{7.13}$$

Where, $\boldsymbol{\tau}_{ij}^{(1)}$ is the actuating force vector for one-foot-stance and $\boldsymbol{\tau}_{ij}^{(2)}$ is for two-feet-stance. $\boldsymbol{p}_{\mathrm{F}ij}$ is the joint location on feet.

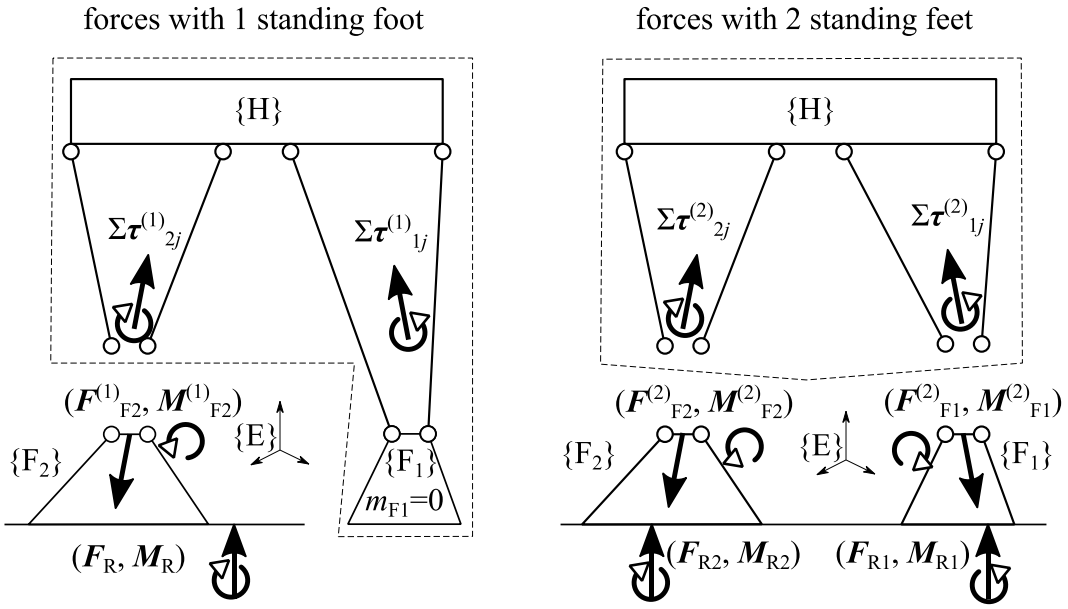

Figure 7.9 The forces needed to drive the robot for the one-foot-stance is shown on the left side. The dynamic system comprises of the ground, one standing foot and the rest parts. The forces for the same motion while two feet are contacting the ground are shown on the right side. The dynamic system comprises of the ground, two standing feet and the rest parts of the robot.

Thus, the dynamic load $(\boldsymbol{F}_{\Sigma}, \boldsymbol{M}_{\Sigma})$ can be obtained through eq. (6.51) and the first equality in eq. (7.13). Giving a load split diagonal matrix $\boldsymbol{A}_1$, there will be

$$\sum_{j=\mathrm{A}}^{\mathrm{F}} \begin{bmatrix} \boldsymbol{\tau}_{1j}^{(2)} \\ \widetilde{\boldsymbol{p}}_{\mathrm{F}1j}\boldsymbol{\tau}_{1j}^{(2)} \end{bmatrix} = \boldsymbol{A}_1 \begin{bmatrix} \boldsymbol{F}_{\Sigma} \\ \boldsymbol{M}_{\Sigma} \end{bmatrix} = \begin{bmatrix} \boldsymbol{a}_{f1} & \boldsymbol{0} \\ \boldsymbol{0} & \boldsymbol{a}_{m1} \end{bmatrix} \begin{bmatrix} \boldsymbol{F}_{\Sigma} \\ \boldsymbol{M}_{\Sigma} \end{bmatrix}, \tag{7.14}$$

$$\sum_{j=\mathrm{A}}^{\mathrm{F}} \begin{bmatrix} \boldsymbol{\tau}_{2j}^{(2)} \\ \widetilde{\boldsymbol{p}}_{\mathrm{F}2j}\boldsymbol{\tau}_{2j}^{(2)} \end{bmatrix} = (\boldsymbol{I} - \boldsymbol{A}_1) \begin{bmatrix} \boldsymbol{F}_{\Sigma} \\ \boldsymbol{M}_{\Sigma} \end{bmatrix}. \tag{7.15}$$

Where,

$$\boldsymbol{a}_{f1} = \mathrm{diag}(a_{f1x}, a_{f1y}, a_{f1z}), \quad \boldsymbol{a}_{m1} = \mathrm{diag}(a_{m1x}, a_{m1y}, a_{m1z}). \tag{7.16}$$

Thus, the forces applied to the feet will be

$$\begin{bmatrix} \boldsymbol{F}_{\mathrm{F}i}^{(2)} \\ \boldsymbol{M}_{\mathrm{F}i}^{(2)} \end{bmatrix} = -\sum_{j=\mathrm{A}}^{\mathrm{F}} \begin{bmatrix} \boldsymbol{\tau}_{ij}^{(2)} \\ \widetilde{\boldsymbol{p}}_{\mathrm{F}ij}\boldsymbol{\tau}_{ij}^{(2)} \end{bmatrix} \quad i = 1,2. \tag{7.17}$$

The needed actuating forces will be

$$\boldsymbol{\tau}_i^{(2)} = -\begin{bmatrix} \boldsymbol{e}_{i\mathrm{A}} & \cdots & \boldsymbol{e}_{i\mathrm{F}} \\ \tilde{\boldsymbol{p}}_{\mathrm{F}i\mathrm{A}}\boldsymbol{e}_{i\mathrm{A}} & \cdots & \tilde{\boldsymbol{p}}_{\mathrm{F}i\mathrm{F}}\boldsymbol{e}_{i\mathrm{F}} \end{bmatrix}^{-1} \begin{bmatrix} \boldsymbol{F}_{\mathrm{F}i}^{(2)} \\ \boldsymbol{M}_{\mathrm{F}i}^{(2)} \end{bmatrix} \tag{7.18}$$

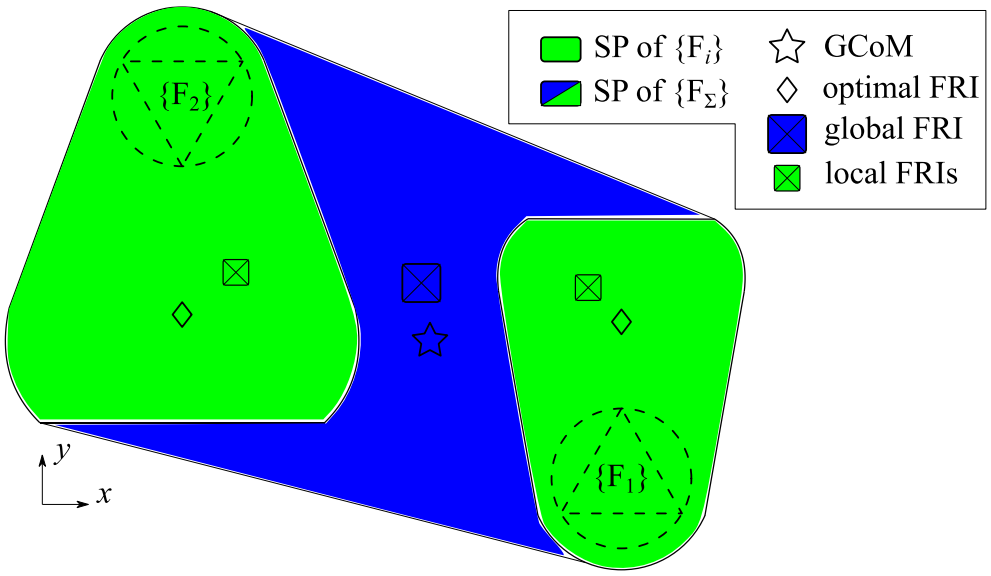

Figure. 7.10. The global FRI should stay in the supporting polygon (SP) formed by two feet and the local FRI should stay in the SP of the foot it belongs.

7.4.2 The FRIs for Two-Feet-Stance

As mentioned before, the FRI location depends only on the forces applied on the ankle joint. If there are two standing feet, the global FRI, $\boldsymbol{p}_{\mathrm{FRI}-\Sigma}$, should be maintained inside the support polygon formed by two feet to prevent the rotation of the whole structure. At the same time, the local FRIs, $\boldsymbol{p}_{\mathrm{FRI}-1}$ and $\boldsymbol{p}_{\mathrm{FRI}-2}$, should also stay inside the support polygon formed by single feet to prevent the rotation of them, as illustrated in fig. 7.10.

The $\boldsymbol{p}_{\mathrm{FRI}-\Sigma}$ can be modified only by modifying the trajectory of the hip due to eq. (7.13), since dynamic load $(\boldsymbol{F}_\Sigma, \boldsymbol{M}_\Sigma)$ is nothing but the function of general forces. However, $\boldsymbol{p}_{\mathrm{FRI}-i}$ can be modified through changing $\boldsymbol{A}_1$. Letting the loci of local FRIs be $\boldsymbol{p}_{\mathrm{FRI}-i} = [p_{x-i} \quad p_{y-i} \quad 0]^{\mathrm{T}}$, they can be obtained similar to eq. (7.9), as eq. (7.19).

$$\begin{cases} p_{x-1} = \dfrac{p_{\mathrm{F1C}x} g m_{\mathrm{F1}} - a_{m1y} M_{\mathrm{F}\Sigma y}}{a_{f1z} F_{\mathrm{F}\Sigma z} + g m_{\mathrm{F1}}} & p_{y-1} = \dfrac{p_{\mathrm{F1C}y} g m_{\mathrm{F1}} + a_{m1x} M_{\mathrm{F}\Sigma x}}{a_{f1z} F_{\mathrm{F}\Sigma z} + g m_{\mathrm{F1}}} \\ p_{x-2} = \dfrac{p_{\mathrm{F2C}x} g m_{\mathrm{F2}} - (1 - a_{m1y}) M_{\mathrm{F}\Sigma y}}{(1 - a_{f1z}) F_{\mathrm{F}\Sigma z} + g m_{\mathrm{F2}}} & p_{y-2} = \dfrac{p_{\mathrm{F2C}y} g m_{\mathrm{F2}} + (1 - a_{m1x}) M_{\mathrm{F}\Sigma x}}{(1 - a_{f1z}) F_{\mathrm{F}\Sigma z} + g m_{\mathrm{F2}}} \end{cases} \tag{7.19}$$

$p_{\mathrm{F}i\mathrm{C}x}$ and $p_{\mathrm{F}i\mathrm{C}y}$ are the mass centre locations of the foot-*i* in *x*- and *y*-directions. This equation set is 3-dimensional; the variables are any three elements of $\{p_{x-1},\ p_{y-1},\ p_{x-2},\ p_{y-2},\ a_{m1x},\ a_{m1y},\ a_{f1z}\}$. Correspondingly, the global FRI, $\boldsymbol{p}_{\mathrm{FRI}-\Sigma} = [p_{x-\Sigma} \quad p_{y-\Sigma} \quad 0]$, is only the function of $(\boldsymbol{F}_{\Sigma}, \boldsymbol{M}_{\Sigma})$, further of state variables, $\{\boldsymbol{X}_{\Sigma},\ \dot{\boldsymbol{X}}_{\Sigma},\ \ddot{\boldsymbol{X}}_{\Sigma}\}$ (see eq. (6.29)).

$$p_{x-\Sigma} = \frac{p_{\mathrm{F}\Sigma\mathrm{C}x} g m_{\mathrm{F}\Sigma} - M_{\mathrm{F}\Sigma y}}{F_{\mathrm{F}\Sigma z} + g m_{\mathrm{F}\Sigma}}, \quad p_{y-\Sigma} = \frac{p_{\mathrm{F}\Sigma\mathrm{C}y} g m_{\mathrm{F}\Sigma} + M_{\mathrm{F}\Sigma x}}{F_{\mathrm{F}\Sigma z} + g m_{\mathrm{F}\Sigma}}. \tag{7.20}$$

Where, the mass sum of two feet is $m_{\mathrm{F}\Sigma} = m_{\mathrm{F1}} + m_{\mathrm{F2}}$ and the mass centre of two feet is $\boldsymbol{p}_{\mathrm{F}\Sigma\mathrm{C}} = [p_{\mathrm{F}\Sigma\mathrm{C}x} \quad p_{\mathrm{F}\Sigma\mathrm{C}y} \quad p_{\mathrm{F}\Sigma\mathrm{C}z}]^{\mathrm{T}} = \sum_{i=1}^{2} (m_{\mathrm{F}i}[p_{\mathrm{F}i\mathrm{C}x} \quad p_{\mathrm{F}i\mathrm{C}y} m_{\mathrm{F}i} \quad p_{\mathrm{F}i\mathrm{C}z} m_{\mathrm{F}i}]^{\mathrm{T}})/m_{\mathrm{F}\Sigma}$.

7.4.3 The Dynamic Load Split Strategy

The aim of dynamic load splitting is to divide $(\boldsymbol{F}_{\Sigma}, \boldsymbol{M}_{\Sigma})$ reasonably by modifying $\boldsymbol{A}_1$ in eq. (7.16). The parameters in $\boldsymbol{A}_1$ can be divided into two groups: horizontal parameters a_{f1x}, a_{f1y} and a_{m1z}; vertical parameters a_{f1z}, a_{m1x} and a_{m1y}. The location of FRIs depends only on the vertical parameters, while the horizontal ones relate to the ground contact frictions.

1) Determination of a_{f1z}

From fig. 7.11, for a hip motion in *x*-direction, the load variation mainly occurs on $\boldsymbol{M}_{\Sigma}$ in *y*-direction. This is caused by the variation of $F_{\Sigma z}$ location, or, namely the variation of the global FRI in *x*-direction. Thus, it is reasonable to split the $F_{\Sigma z}$ based on the distance between the global FRI to a stable local FRI. As illustrated in fig.7.12, the local FRIs can be seen as the centres where the $F_{\mathrm{F}iz}$ applied. If the optimal local FRIs are given as $\boldsymbol{p}_{\mathrm{opt}-i} = [p_{\mathrm{opt}x-i} \quad p_{\mathrm{opt}y-i} \quad 0]^{\mathrm{T}}$, the parameter a_{f1z} can be determined as

$$a_{f1z} = \frac{\left\| p_{x-\Sigma} - p_{x-\mathrm{opt2}} \right\|}{\left\| p_{x-\Sigma} - p_{x-\mathrm{opt1}} \right\| + \left\| p_{x-\Sigma} - p_{x-\mathrm{opt2}} \right\|} \tag{7.21}$$

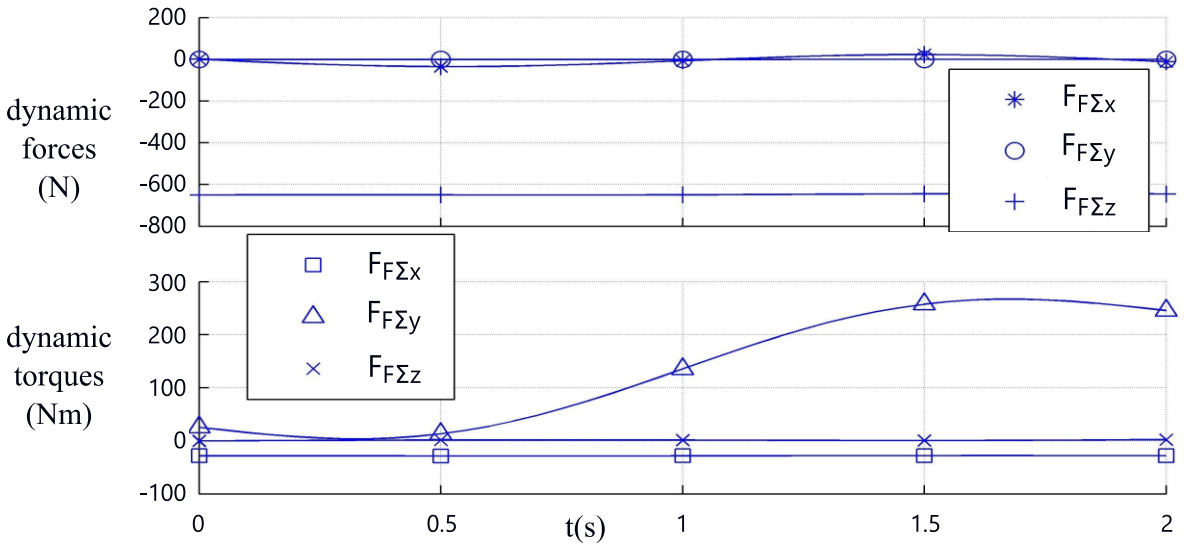

Figure 7.11 The total dynamic load $(\boldsymbol{F}_{\Sigma}, \boldsymbol{M}_{\Sigma})$ distribution in 6 dimensions.

If the global FRI exceeds the interval between two optimal local FRIs, namely $a_{f1z} > 1$ or $a_{f1z} < 0$, the load $F_{\mathrm{F}\Sigma z}$ should be applied on the nearest SP, namely, $a_{f1z} = 1$ or $a_{f1z} = 0$.

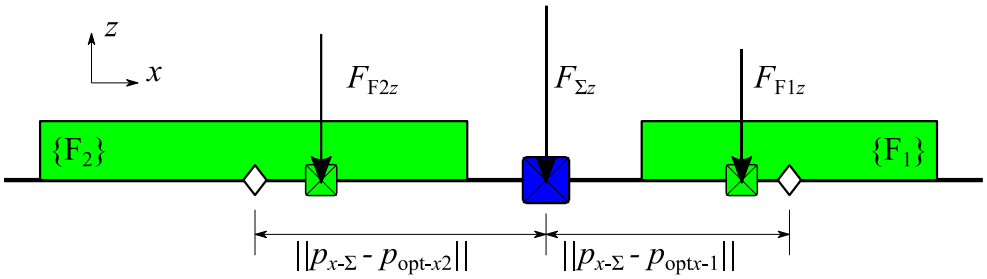

Figure 7.12 The load in z-direction will be split according to the distance between global FRI and optimal FRIs. Symbols can be found in fig. 7.10.

2) Determination of a_{m1x} and a_{m1y}

As eq. (7.19), the locations of two local FRIs can be modified in a 3-dimensional space. Once one local FRI is determined, the other FRI can only locate on a line (see fig. 7.13). The contact area of $\{\mathrm{F}_1\}$ is smaller than $\{\mathrm{F}_2\}$, the local FRI, $\boldsymbol{p}_{\mathrm{FRI-F1}}$, should be ensured in priority, i.e., $\boldsymbol{p}_{\mathrm{FRI}-1} = \boldsymbol{p}_{\mathrm{opt}-1} = [p_{\mathrm{opt}x-i} \quad p_{\mathrm{opt}y-i} \quad 0]^{\mathrm{T}}$. Bring $\boldsymbol{p}_{\mathrm{FRI-F1}} = \boldsymbol{p}_{\mathrm{opt}-1}$ and a_{f1z} in eq. (7.21) to eq. (7.19), a_{m1x} and a_{m1y} can be determined as

$$\begin{cases} a_{m1x} = \dfrac{p_{\mathrm{opt}y-1}\left(a_{f1z}F_{\mathrm{F}\Sigma z} + gm_{\mathrm{F1}}\right) - p_{\mathrm{F1C}y}gm_{\mathrm{F1}}}{M_{\mathrm{F}\Sigma x}}, \\ a_{m1y} = \dfrac{p_{\mathrm{F1C}x}gm_{\mathrm{F1}} - p_{\mathrm{opt}x-1}\left(a_{f1z}F_{\mathrm{F}\Sigma z} + gm_{\mathrm{F1}}\right)}{M_{\mathrm{F}\Sigma y}}. \end{cases} \tag{7.22}$$

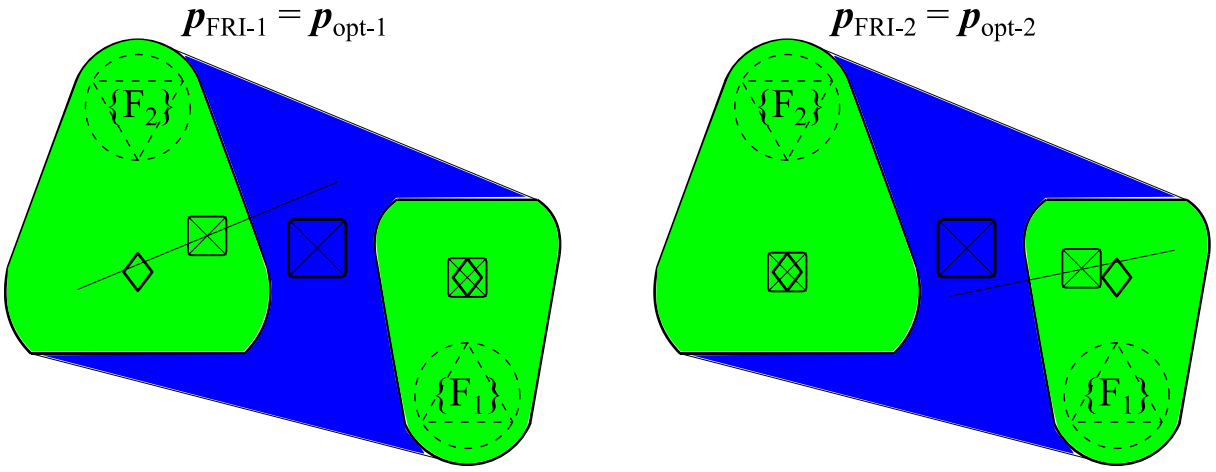

Figure 7.13 For the same dynamic load $(\boldsymbol{F}_{\Sigma}, \boldsymbol{M}_{\Sigma})$, once the FRI on one foot is fixed, the FRI of the other foot locates on one line.

3) Determination of a_{f1x}, a_{f1y} and a_{m1z}

The horizontal force components, $F_{\text{F}ix}$, $F_{\text{F}iy}$ and $M_{\text{F}iz}$, will cause the translational and rotational slips of the feet. The maximal value of static friction of the ground is proportional to the vertical load, $F_{\text{F}iz}$. The parameters, a_{f1x}, a_{f1y} and a_{m1z}, can thus be set equal to a_{f1z} and smaller than the friction parameter of the contacting surface.

$$a_{f1x} = a_{f1y} = a_{m1z} = a_{f1z} \tag{7.23}$$

7.4.4 Simulation Results

The aim of a hip moving phase in the walking cycle is to transport the load on the hip. Regardless of goods or human transportation, unnecessary vertical hip motions should be avoided. The motion of hip can be illustrated as shown in fig.7.14, and the trajectory of the hip platform is thus defined as

$$\boldsymbol{X}_{\text{H}}(t) = \left[amp\frac{t}{T} - \frac{amp}{2\pi}\sin 2\pi\frac{t}{T} \quad 0 \quad 0 \quad 0 \quad 0 \quad 0\right]^{\text{T}}. \tag{7.24}$$

As fig. 7.16 shows, during the hip motion, the global FRI is not leaving the SP formed by two feet. This implies that the trajectory of the hip is capable in the view of semi-dynamic stability and there is no risk of the whole structure to rotate.

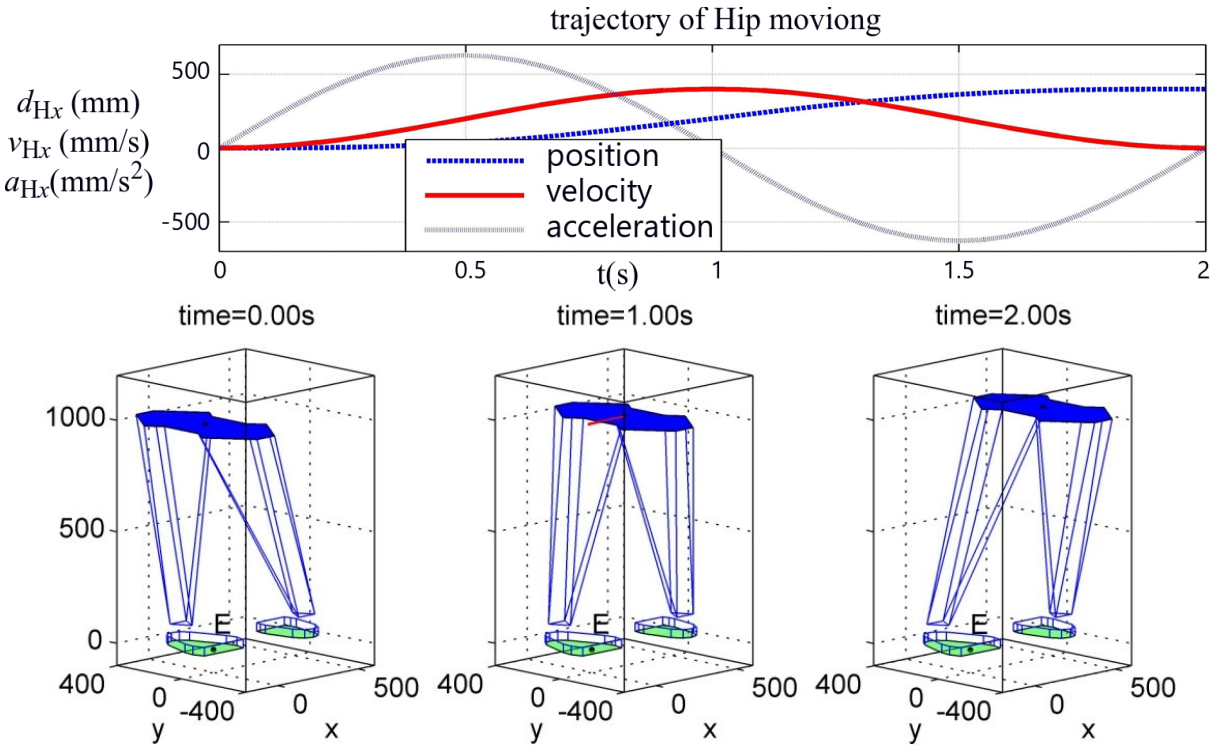

Figure 7.14 The trajectory of the hip is defined in *x*-direction; the motion time *T* is defined as 2 seconds and the motion amplitude is *amp*=500mm.

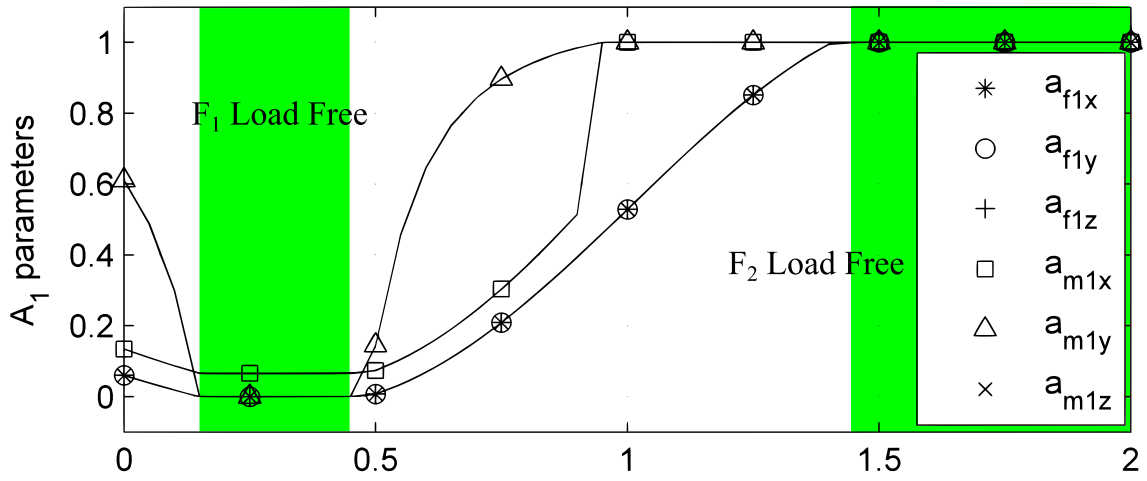

Figure 7.15 Load split parameters of the hip motion. The whole load was applied on one foot during the load-free phase of the other foot. The load free phases are determined by the vertical load according to eq. (7.21).

The dynamic load was split between two feet as shown in fig. 7.15. There are two respective load-free time intervals for two feet, while the hip moves from one foot to another. Simultaneously, the whole dynamic load shifted from leg-2 to leg-1. Since the parameter a_{f1z} is determined by the distance between local and global FRIs only in *x*-direction, the local FRIs of {F$_1$} deviated in the *y*-direction to compensate the lack of torques along *y*-axis. However, the

global FRI is basically along the line between the two optimal local FRIs, the local FRIs did not exceed the support polygons. This phenomenon is shown in fig. 7.16. According to fig. 7.15, initially, the main load is gravity (time = 0). As long as the acceleration increases, the global FRI shifts so that the load is applied only on $\{F_2\}$ (time = 0.30s).

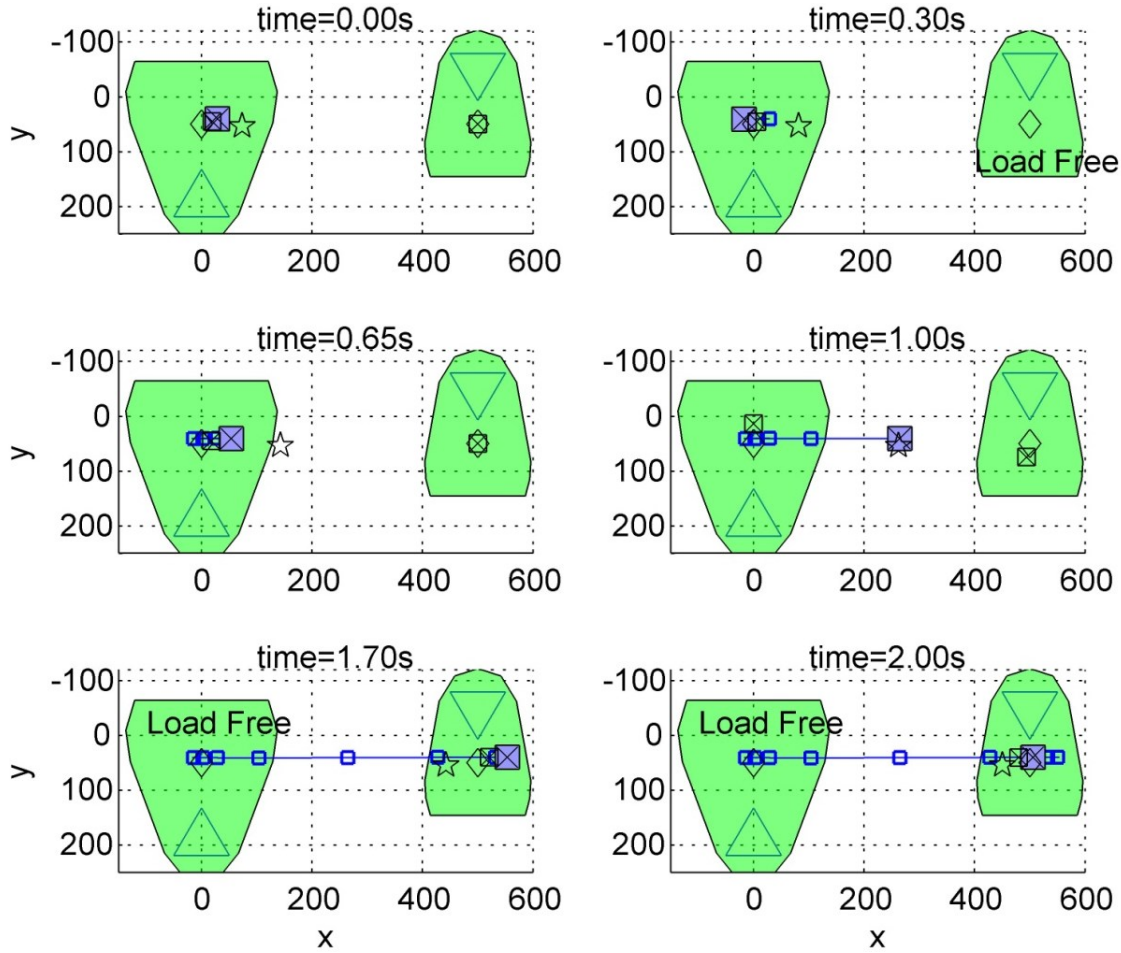

Figure 7.16 The local FRIs and global FRI are shown during the moving of the hip platform. The symbols are defined inheriting fig. 7.10.

The demanding actuating forces can be found in fig. 7.17. Without frictions of linear actuators, actuating forces should be 0 on the load free foot in the load free intervals (0.15s~0.45s and 0.14s~2s). Nevertheless, the actuating forces on leg-1 are not 0 in its load free interval. The reason can be found from parameter a_{m1x} in fig. 7.15 and eq. (7.22). The a_{f1z} is only determined by the load distribution on x-direction, and the parameters a_{m1x} and a_{m1y} must be modified to ensure the optimal FRI of foot-1. The residue torque in x-direction was thus induced by the y-deviation of vertical force. In contrast, the FRI of foot-2 was not considered during the load splitting. In its load-free interval, $(\boldsymbol{F}_\Sigma, \boldsymbol{M}_\Sigma)$, was applied on foot-1.

The load split can also be determined as illustrated in fig.7.13, however, the obtained $\boldsymbol{p}_{\mathrm{FRI}-2}$ could contradict eq. (7.21). A larger part of torque $\boldsymbol{M}_{\Sigma}$ could be provided by only one foot, thereby enlarge the load on single actuators.

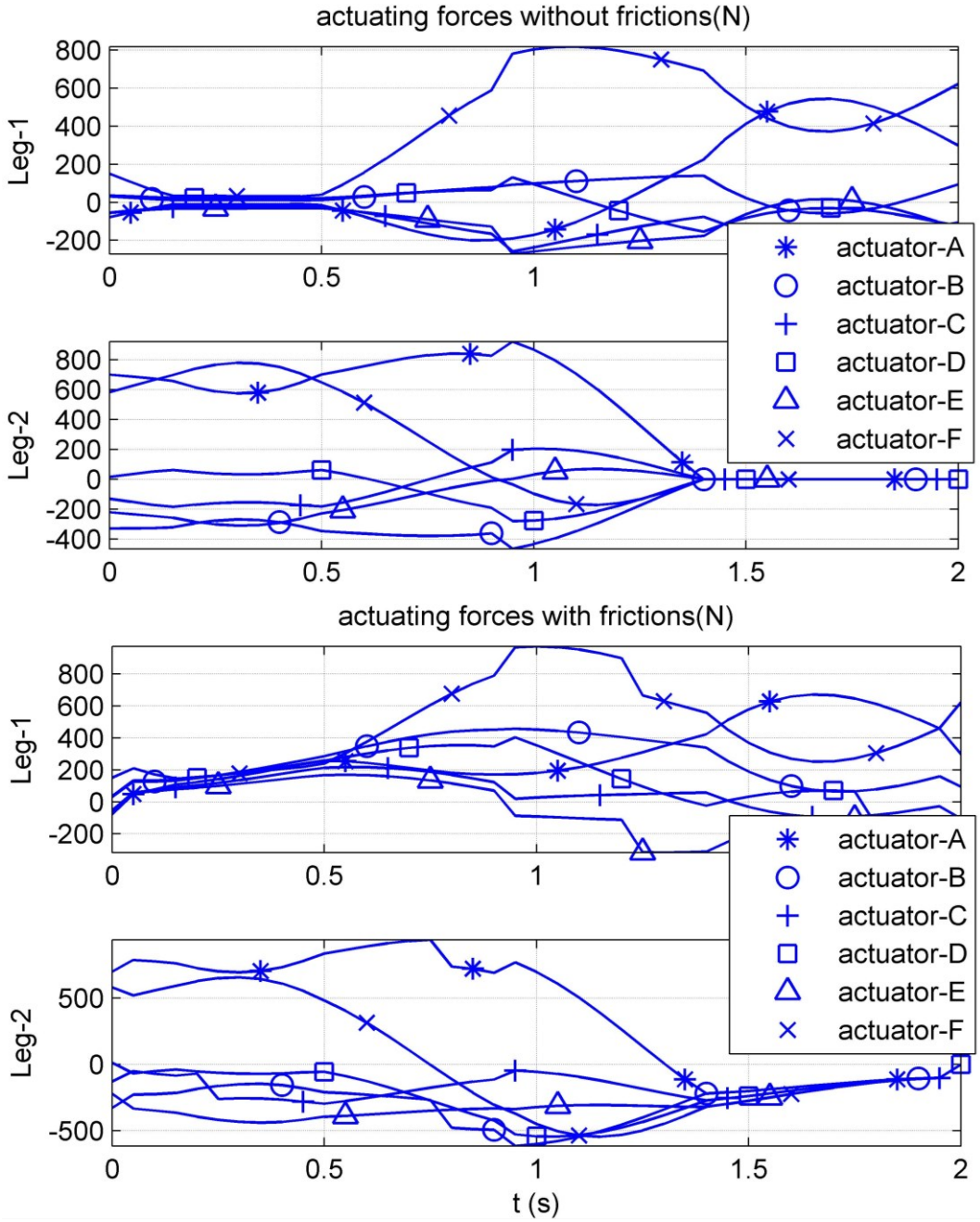

Figure 7.17 The actuating forces with and without actuator frictions according to eq. (7.18) under the hip moving phase.

7.4.5 Optimization of Hip Motion

Under the simulation configurations that T = 1s, *amp* = 500mm in eq. (7.24), the global FRI

shows no more stability, as fig. 7.18. This is because the acceleration amplitude distributed too dispersed and the motion time is too short. Or in other word, the acceleration and velocity are excess at the beginning and the end of the motion. The motion can be optimized if a more reasonable acceleration distribution was adopted and a more reasonable motion time is set.

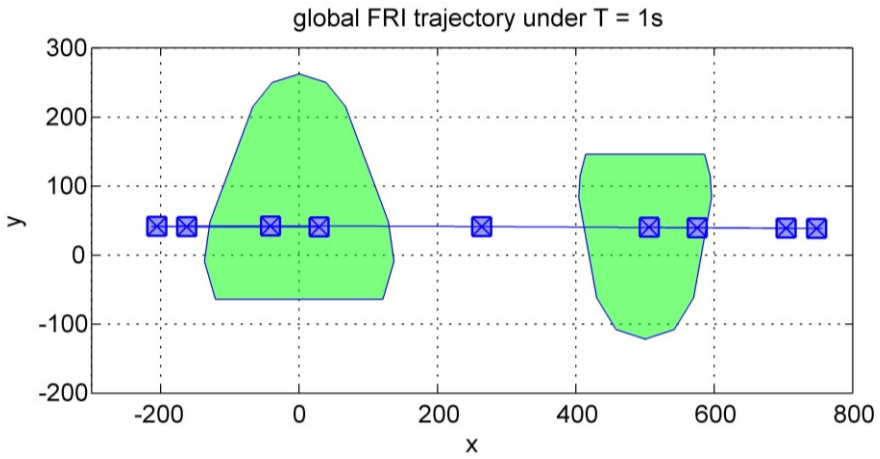

Figure 7.18 The global FRI loci using sinus acceleration trajectory.

The acceleration distribution ($\ddot{\boldsymbol{X}}_{\mathrm{H}}(t)$) can be modified through various approaches. For example, $\ddot{X}_{\mathrm{H}x}(t)$ can be 1st order fold line and the peak value is a function of the time on which the peak value takes place. The $\ddot{\boldsymbol{X}}_{\mathrm{H}}(t)$ is divided into two time intervals: acceleration and deceleration. The areas formed by two acceleration curves should be equal, illustrated in fig. 7.19, $t_0 a_{\mathrm{p}} + (T - t_0) a_{\mathrm{v}} = 0$, so that the motion will stop at the end, thus

$$a_{\mathrm{v}} = -\frac{t_0 a_{\mathrm{p}}}{T - t_0} \tag{7.25}$$

The adjustable parameters of accelerations are t_{p}, t_0 and t_{v}. The motions with specific configurations were simulated as the three accelerations parameters vary, as fig. 7.20 shows. The furthest distance of the FRI loci from the feet centre was marked in different colours. Note that, for the concerning of *comfort* of possible passengers, the simulation results with drastic accelerations changing will be excluded, meanwhile, the peak value of acceleration is also limited under *g*/2. As the matter of fact, the maximum distance of FRI to the feet centre shows obvious continuity under continues acceleration parameters. This suggests a high confidence level of single minimum of maximum FRI distances, which will be called as *FRI range* in the

following text. The optimal combination of t_p, t_0 and t_v can be found.

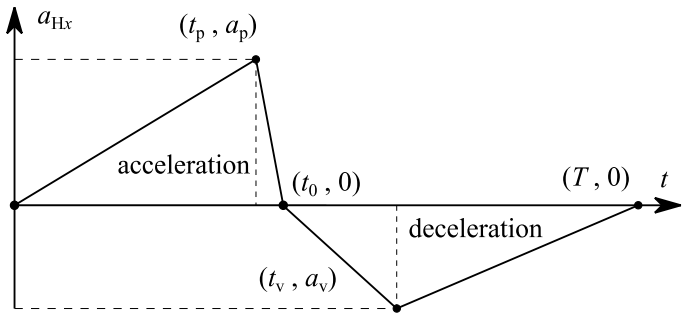

Figure 7.19 Adjustable fold line acceleration trajectory. The areas enveloped by the acceleration and deceleration lines should be equal.

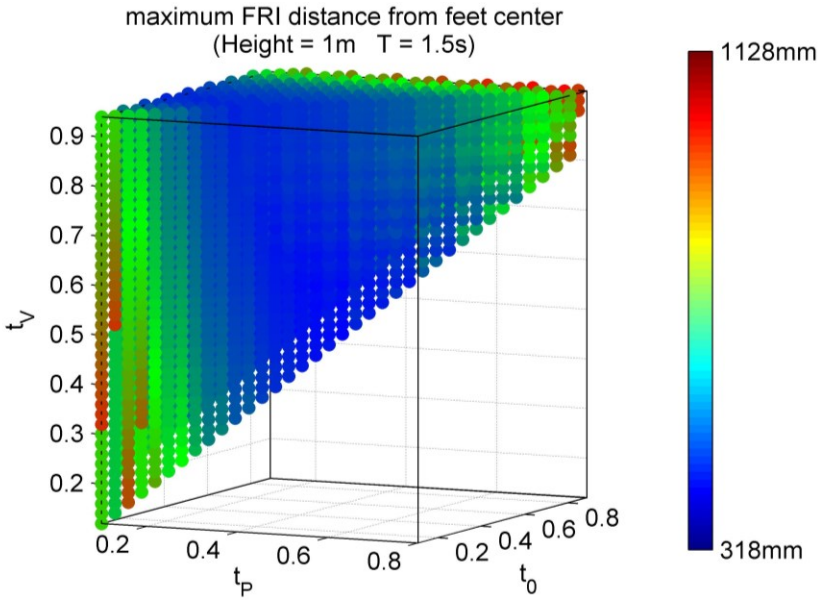

Figure 7.20 One example set of acceleration parameters. The height of hip is 1m and the motion time is defined as 1.5s. The maximum distances of global FRIs to the centre of two feet are illustrated as the colour of scatters. The minimum value in present searching density is 318mm.

The minimum FRI ranges under different trajectory setting are surveyed with motion time of 1s, 1.25s and 1.5s, and the hip height of 1m, 0.95m and 0.9m, as shown in fig. 7.21. The average minimum FRI ranges increase in pace with the hip height increases and motion time decreases, since the centre of mass and maximum acceleration rise. However, the robot will not be stable with survey parameters of accelerations if the motion time is 1.25s or 1s, since the minimum FRI range is over 325mm, which landed outside the support polygon.

Furthermore, the optimal loci of the global FRI for each hip height and motion time are given,

as well as the corresponding hip trajectories. The motion shows higher stability if the hip moves lower; however, a safer motion with all heights should be not shorter as 1.5s, as shown in fig.7.23. Compare to a hip motion with sinus acceleration trajectory in fig. 7.22, a proper fold line trajectory in fig.7.23 decreases the global FRI range to a stable condition.

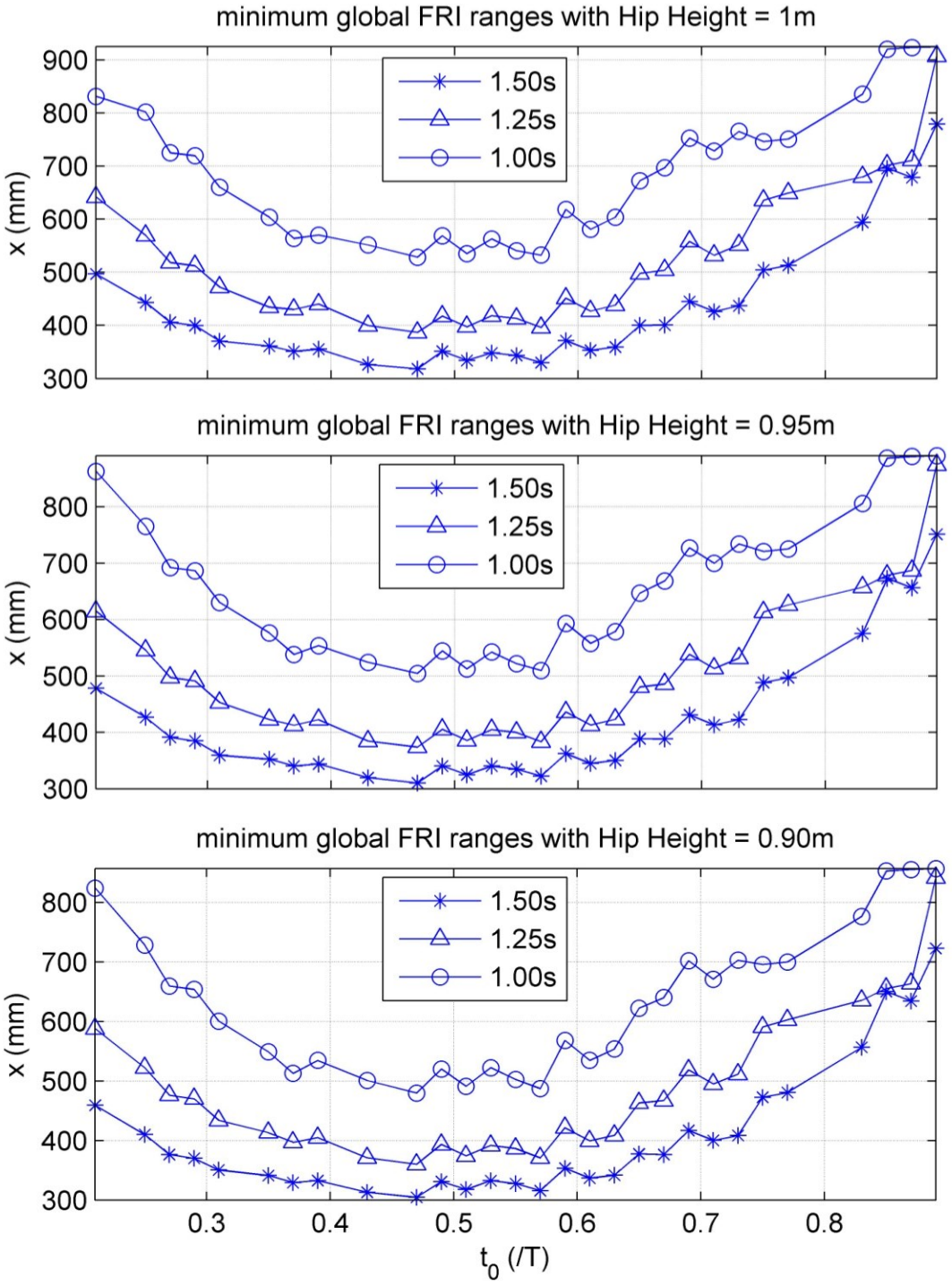

Figure 7.21 Minimum global FRI ranges, $\min_{tp,tv}|\max \boldsymbol{p}_{\mathrm{FRI}-\Sigma} - \min \boldsymbol{p}_{\mathrm{FRI}-\Sigma}|$, under different motion configurations along the variation of t_0.

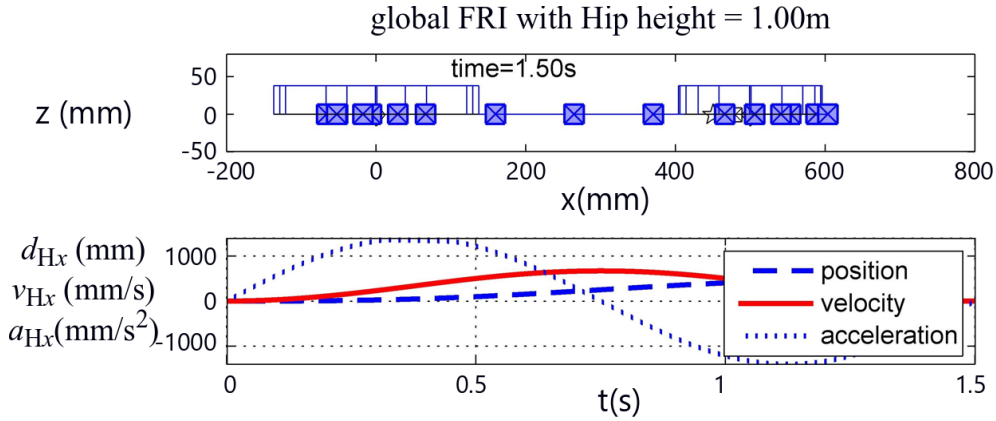

Figure 7.22 The global FRI loci with sinus hip acceleration trajectory.

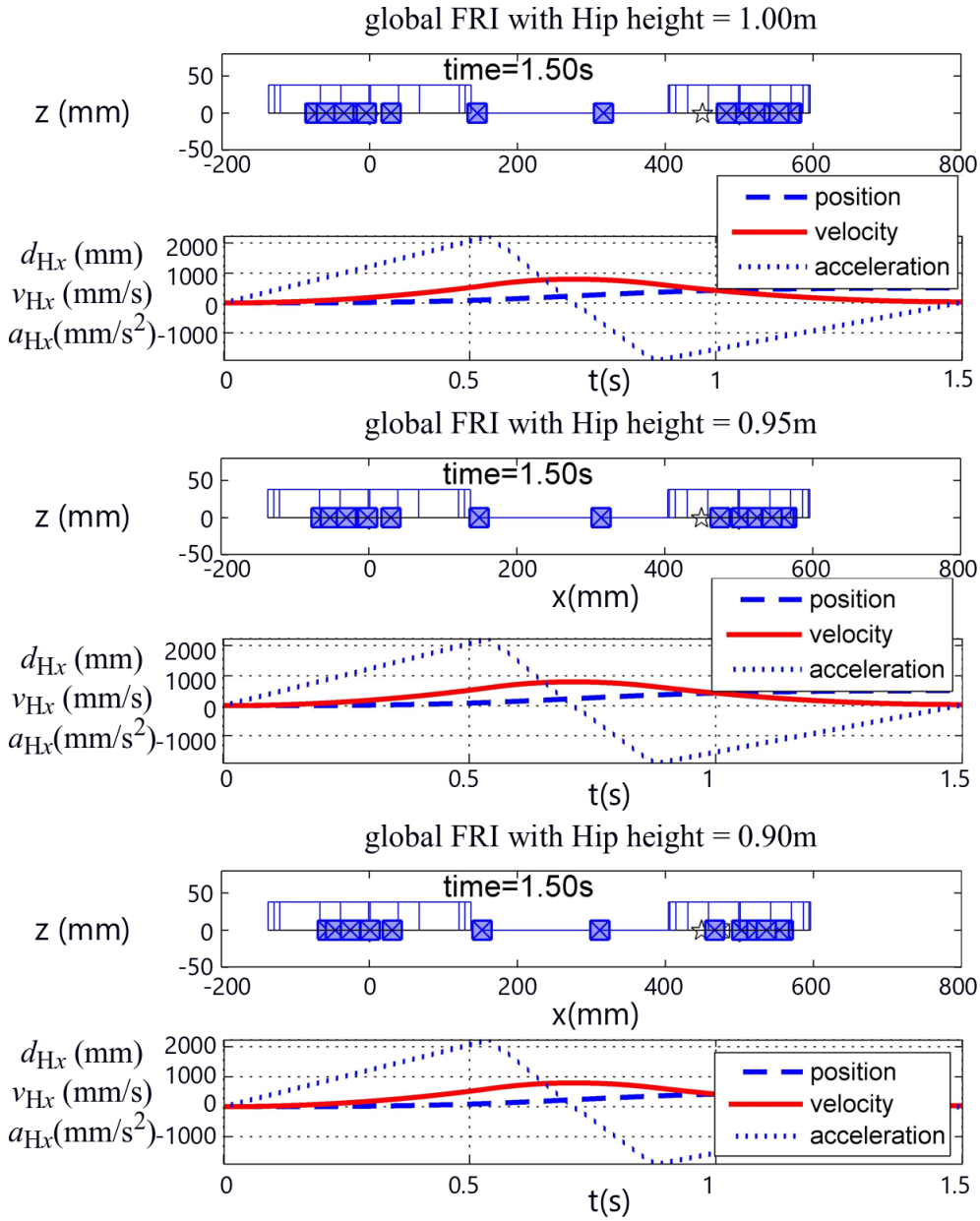

Figure 7.23 The global FRI loci with different motion configurations. The result suggests that the stability increases if the height decreases.

One phenomenon should be noticed is that, for the same average hip motion velocity (e. g. 700/2.1mm/s = 500/1.5mm/s = 333.3mm/s), the stability increases along the increasing of step length, as illustrated in fig. 7.24. Fig. 7.25 shows the variation of global FRI range excluding the step length in *x*-direction. In the view of stability, the length step should be set as long as possible in the workspace.

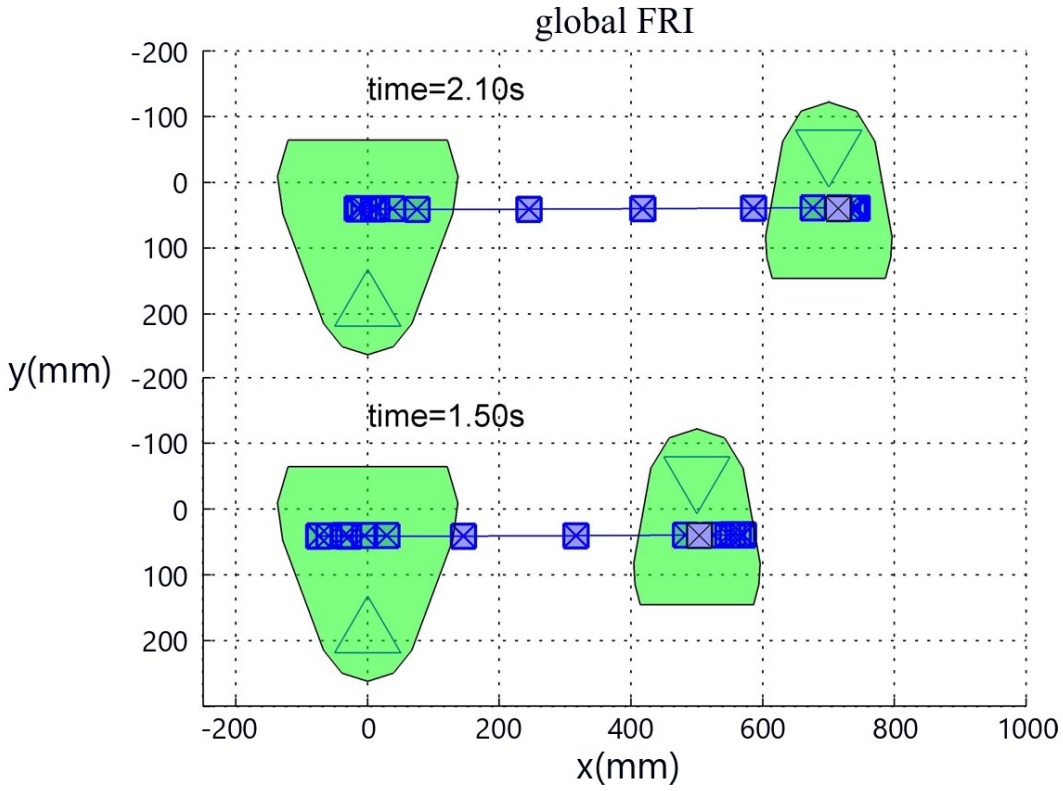

Figure 7.24 The global FRI loci of the hip motions with same average velocity but different step length. The stability of 700mm displacement in 2.1 second is higher than that of 500mm displacement in 1.5 second.

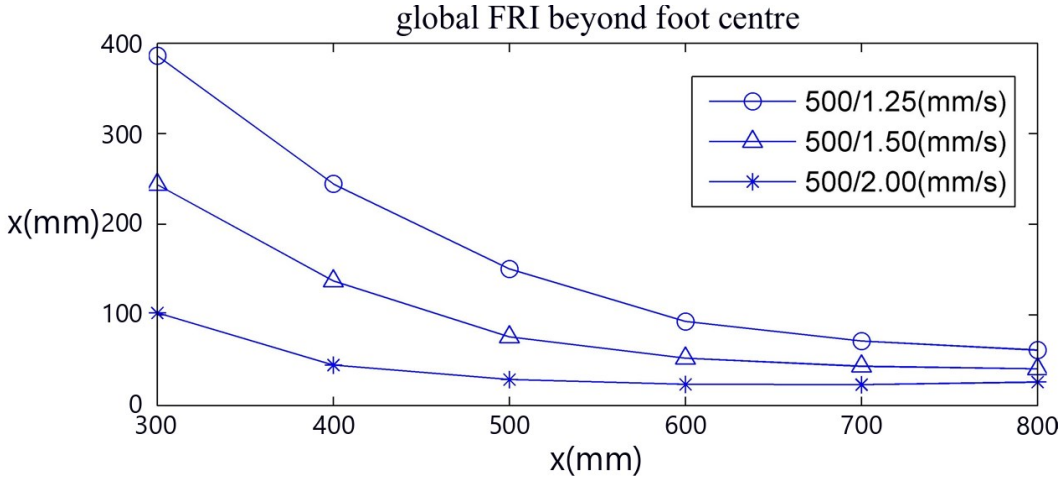

Figure 7.25 The FRI range subtracting step length. Higher values imply bigger distances of FRI beyond the foot centre.

7.5 Walking Motions

A walking pattern of CENTAUROB comprises of alternate phases, *leg swings* and *hip moving*, no matter for straight walking, side-walking or turning. As forehead discussed, the stability is always the first consideration. For present design, only the semi-dynamic walking is assured, seeing fig. 7.2. The GCoM can fall out from the support polygon (SP) but the FRI will not. The FRI switches between the two-feet-SP and one-foot-SP, for the two phases respectively.

Secondarily, the comfort and velocity should also be considered. To preserve the comfort, the acceleration slope rate was limited as sub-section 7.4.5 discussed. For the hip moving phase, only the loci of global FRI will be illustrated, while the load split strategy was given in sub-section 7.4.3 and will not be illustrated to preserve reading convenience.

7.5.1 Straight Walking

The straight walking happens in the x-direction of the robot's coordinates. The smaller foot ($\{F_1\}$) will start its swing phase at the beginning. Once $\{F_1\}$ landed, a new SP of two feet forms and the hip moving phase will start. Then, the swing of $\{F_2\}$ will start. Letting the positions in the x-direction be labelled as: $x_0, x_1, x_2, \dots$, the motion sequence is as table 7.2.

Table 7.2 The motion sequence of straight walking.

Time intervals	0~1s	1~2.5s	2.5~3.5s	3.5s~5s	…
$\boldsymbol{X}_{\mathrm{F2}}$	$x_0 -$	$x_0 -$	$x_0 \rightarrow x_2$	$x_0 -$	…
$\boldsymbol{X}_{\mathrm{H}}$	$x_0 -$	$x_0 \rightarrow x_1$	$x_1 -$	$x_1 \rightarrow x_2$	…
$\boldsymbol{X}_{\mathrm{F1}}$	$x_0 \rightarrow x_1$	$x_1 -$	$x_1 -$	$x_1 -$	…

The simulation result was presented in fig. 7.26. The motion of the robot was illustrated in the figure above; the foot prints (support polygons) and the corresponding FRIs were shown in the figure beneath. The result shows a semi-dynamic stable walking pattern since the FRI located in their present SPs. Fig. 7.28 shows that, during the walking, there are time moments that the

GCoM fell out from the SPs, while the FRI loci was always inside the SP, e.g. the foot print at *x* = 700mm. This phenomenon can be explained by the figure on the right of fig. 7.28. At the end of the swing of the left leg $\{F_2\}$, a torque, $\boldsymbol{M}_{F2}$, must be applied to it to brake. The reactive torque of it is against the direction of the torque generated by the deviated centre of mass. The same situation happens at the beginning of the swing, except that the torque directions are inversed. The reactive torque dragged the FRI back to the SP and partly neutralized the tendency of robot falling.

7.5.2 Transverse Walking

The robot is also able to move along its secondary direction, *y*-axis. Since the obstacle of the other leg, there will be no leap over swing motion like the $\{F_2\}$ during 2.5s~3.5s in table 7.2. The velocity is not highly demanded in *y*-direction motion. The simulation was thus operated with a step length of 500mm in 4.2 seconds.

Table 7.3 The motion sequence of side-walking.

Time intervals	0~1.2s	1.2~3s	3~4.2s	4.2s~5.4s	…
$\boldsymbol{X}_{F2}$	$y_0 \rightarrow y_1$	$y_1 -$	$y_1 -$	$y_1 \rightarrow y_2$	…
$\boldsymbol{X}_{H}$	$y_0 -$	$y_0 \rightarrow y_1$	$y_1 -$	$y_1 -$	…
$\boldsymbol{X}_{F1}$	$y_0 -$	$y_0 -$	$y_0 \rightarrow y_1$	$y_1 -$	…

The result shows a stable motion sequence since all the FRIs located in the SPs. The loci of FRI are shown on the left side of fig.7.29 and the FRIs of hip motion were shifted 100mm to *x*-direction. On the right side of the figure, the loci of FRI and GCoM in the first 1 second were illustrated. Similar to the case in straight walking, the brake torque of the end half of the motion is $\boldsymbol{M}_{F2}$, while the reactive torque, $-\boldsymbol{M}_{F2}$, is against the torque caused by the deviation of the CoM. Thus, the loci of FRI and GCoM move to the left, while, at the brake phase, the moving FRI obvious slows down and stays inside the SP.

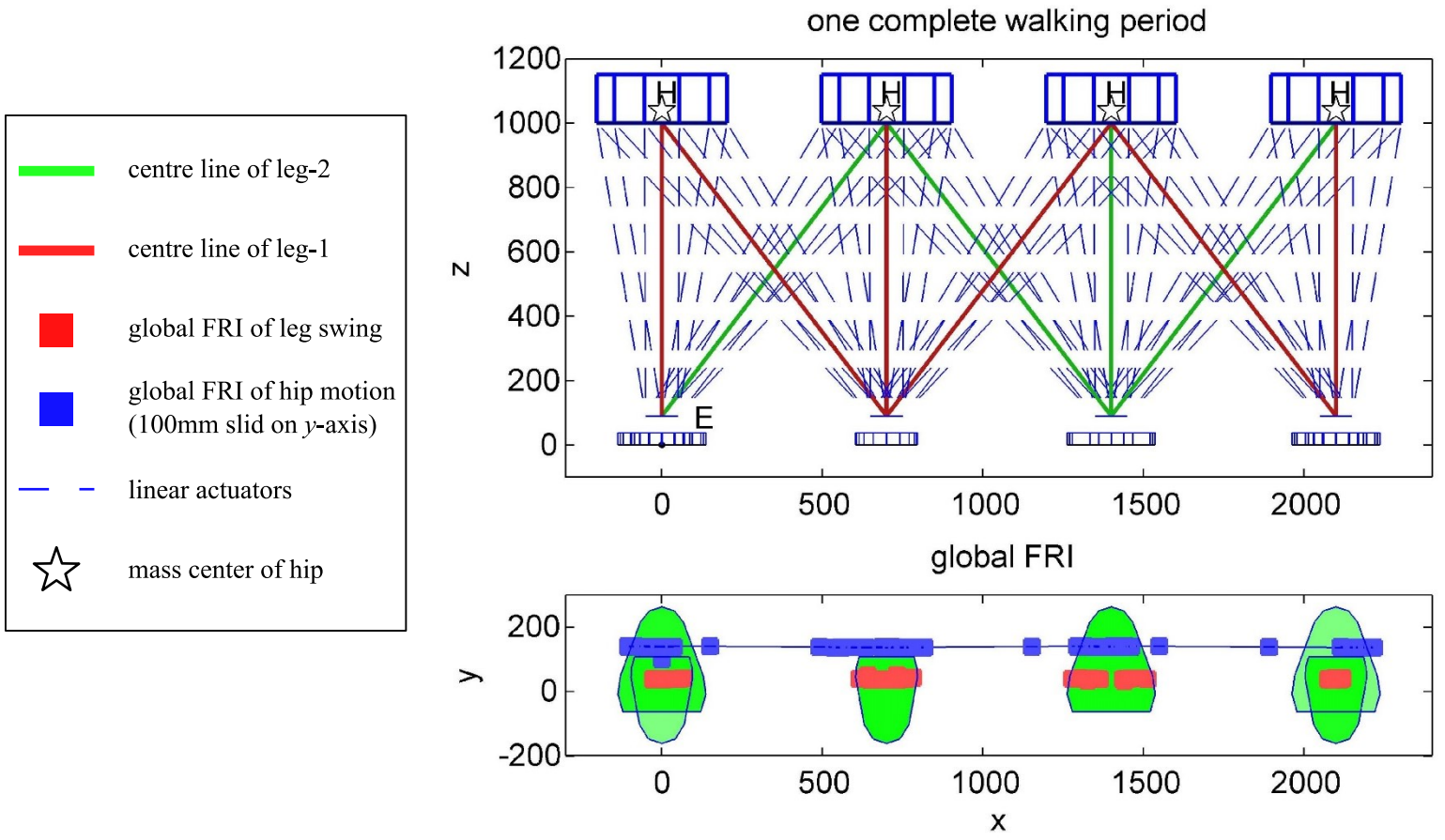

Figure7.26 One complete walking period was simulated. The step length was 700mm and the average velocity was 500/1.5(mm/s) (seeing fig.7.15). Note that, the FRI trajectory was moved 100mm in *y*- direction. The result represented a stable walking process. For leg swing phase: T= 2.1s. For hip moving phase: T = 1.4s. The whole motion time is T_{all} = 11.9s.

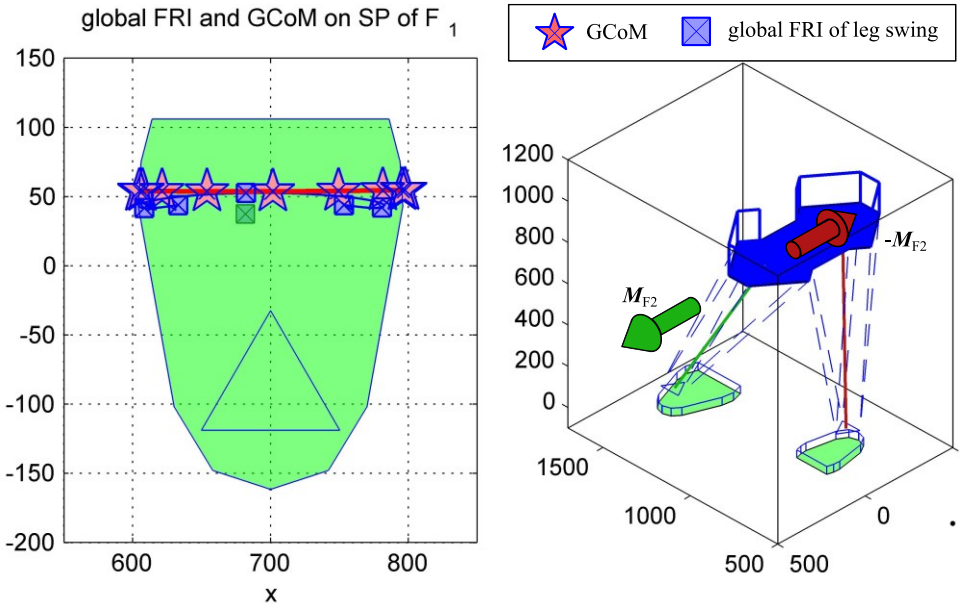

Figure 7.27 One example of semi-dynamic walking pattern. The loci of GCoM obviously exceeded the SP at the beginning and the end of the swing of the other leg, while the loci of FRI did not. The reason can be illustrated by the figure on the right. To brake the swinging leg, torque $\boldsymbol{M}_{F2}$ was applied on it, and the reactive torque $-\boldsymbol{M}_{F2}$ has dragged the FRI to the support polygon of the standing foot.

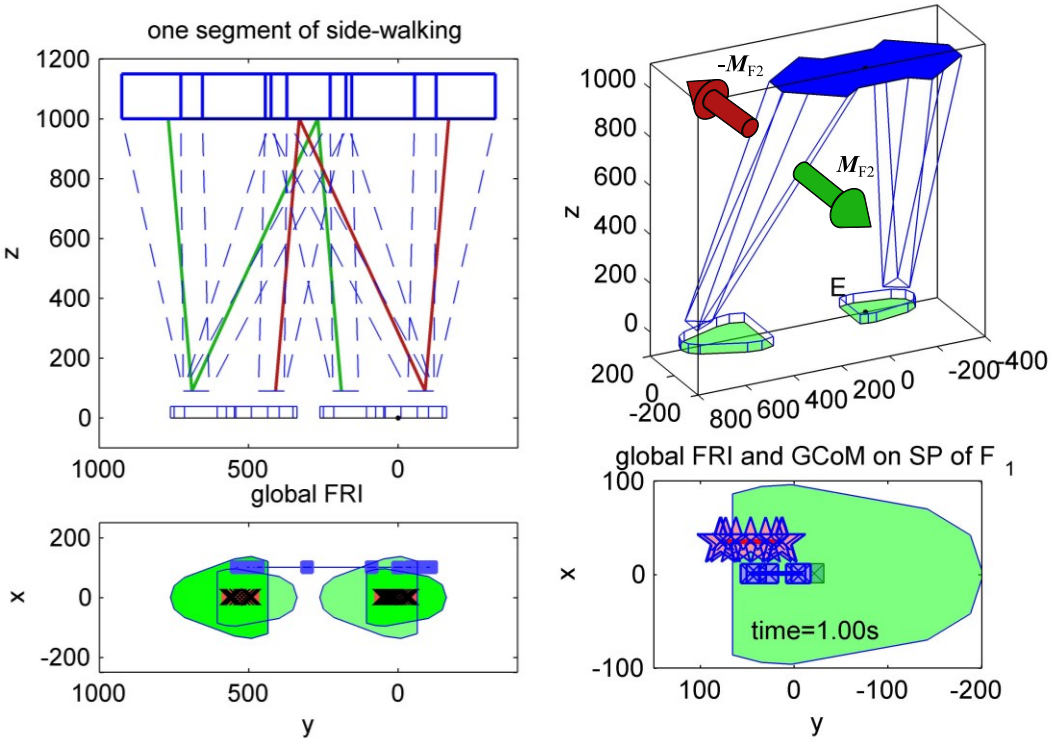

Figure 7.28 (left) One side-walking step simulation. The definition of symbols can be found in fig. 7.26. The loci of hip moving FRI was slid, too. The step length was 500mm and was operated in 4.2s (2 swings for 2.4s and one hip moving for 1.8s). (right)

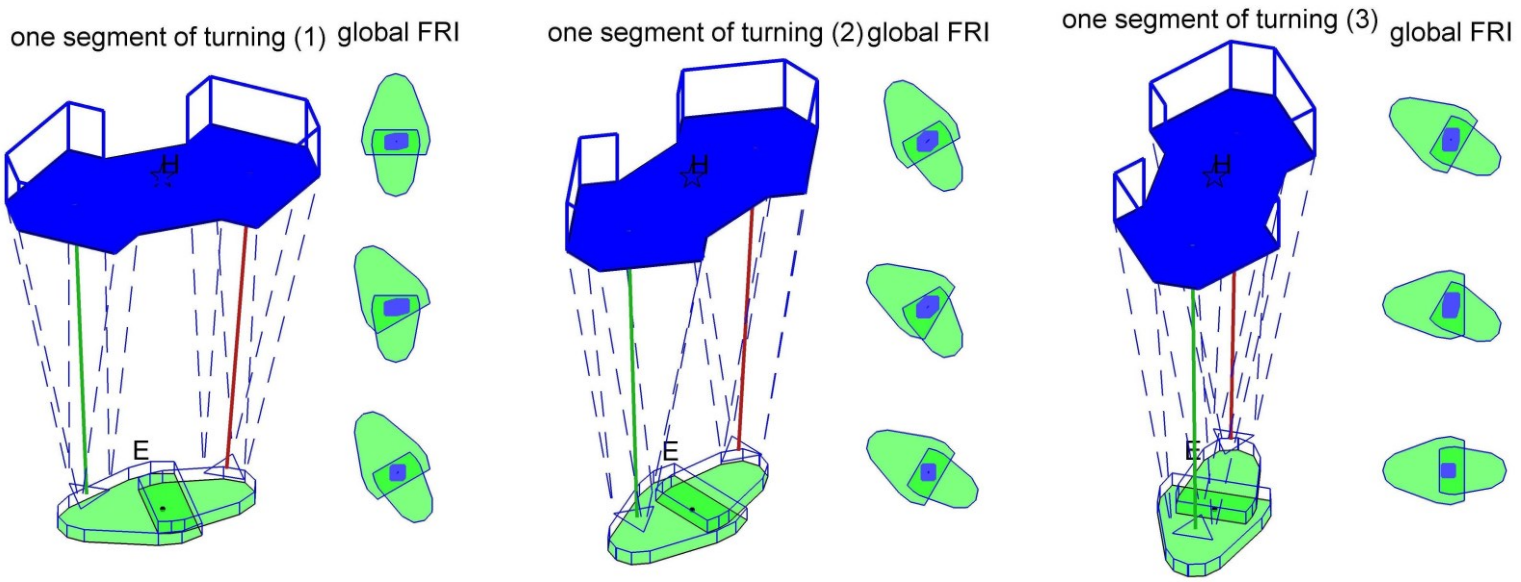

Figure7.29 One complete turning period was simulated. The step length was limited in 30° (seeing fig. 7.30), and the average velocity was 30/1.4(°/s). The FRI trajectory was was limited in the over-lapped range of SP. The result represented a stable walking process. The turning was operated in three segments; each segment comprises foot-1 (0.4s), hip (0.6s) and foot-2 (0.4s) turning in sequence.

7.5.3 Turning

The process of turning can be found in fig.7.29. The maximum turning angle is 35.16°, the turning angle is set to be 30° for each turning segment, as fig. 7.30. For a turning of 90°, three turning segments must be operated. The motion sequence of each segment is {H}-{F_2}-{F_1}.

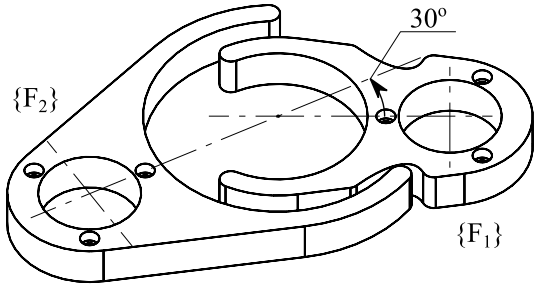

Figure 7.30 The rotation of two feet is limited in 30°; and the rotation centre is the centre of circular toes.

7.6 Chapter Summary and Discussions

In this chapter, the walking patterns of CENTAUROB were studied. The motion of two phases, leg swing phase and hip moving phase, of walking were analysed. For this purpose, two efforts were done in advance. Firstly, the gait optimization of leg swing phase was done by introducing the hip motion as compensation. As a result, the FRI locus was regularized to a better range (from 98mm max FRI deviation to 36mm). Secondly, the load split strategy was introduced in the view of the stabilities of each single foot and both feet as a whole. It turns out that the dynamic load in the vertical direction can be divided according to the distance from global FRI to the optimal local FRIs of the single feet. Simulation result shows that the load split strategy ensured the stability of both feet, during a globally stable hip motion.

The dynamic load applied on the standing platform/s was not obtained directly by the dynamic equations of Lagrange method, as represented in [7.12]. Instead, it was indirectly obtained as actuating forces obtained from single foot (eq. (6.51) modified with zero swing foot mass and velocity, as eq. (7.13)). Fig. 7.9 illustrates this process. This process saves the computation time, since the motion energy does not need to be re-calculated.

In the hip motion phase, the local foot stability depends on the load split strategy, while the global stability of the robot as a whole depends only on the trajectory of the hip. No matter in the view of energy-saving or of comfort of passenger, the motions should be constrained only in one direction. Thus, the one-dimensional acceleration was the only adjustable variable. In this chapter, the hip motion was optimized in a manner of adjustable fold lines and three adjustable parameters were set. The maximum FRI deviations of different acceleration parameters were represented in fig.7.20 and the optimal acceleration trajectory was generated. The height of the hip platform is also a vital factor for the FRI distribution. The hip motion with lower hip height but same *x*-trajectories generated shorter global FRI loci. In addition, the step length affects the stability margin, too. Fig. 7.24 shows a bigger FRI stability margin with longer step length, while the velocities stays 333.3mm/s. Fig. 7.25 shows the statistic relation between step length and stability of hip motion.

At the end of this chapter, 3 typical motions, straight, side walking and turning, of CENTAUROB were simulated. The results showed stable motions and semi-dynamic characteristics. For the straight walking, despite the starting and end steps, the velocity can reach 280mm/s (700mm in 1s for leg swing and 1.5s for hip moving). The effect of inverse pendulum during the leg swing eased the deviation of FRI, as fig. 7.28 illustrated. This effect happened in the side-walking motion, too. In fig. 7.29, the locus of GCoM obviously exceeded the SP. At the deceleration phase, the FRI slowed down its motion towards the moving direction of swing leg and stayed in the SP.

The above mentioned phenomenon can also be explained by introducing double inverted pendulum walking model, such as [7.22]. As matter of fact, the swing of the leg is a transition between the kinetic energy and potential energy. The highest potential energy takes place where the leg is away from the hip joint of leg, as $\boldsymbol{p}_{\text{potential}}$, since without any actuating forces and ground support, the leg will fall back to the balancing position beneath the hip joint, $\boldsymbol{p}_{\text{kinetic}}$. The position beneath the hip joint obtains no potential energy. If one swing is a 100 percent transition between the kinetic energy and potential energy, the system will not need any energy input, $E_{\text{ext}} = 0$. The reactive force to generate the external energy is the ground.

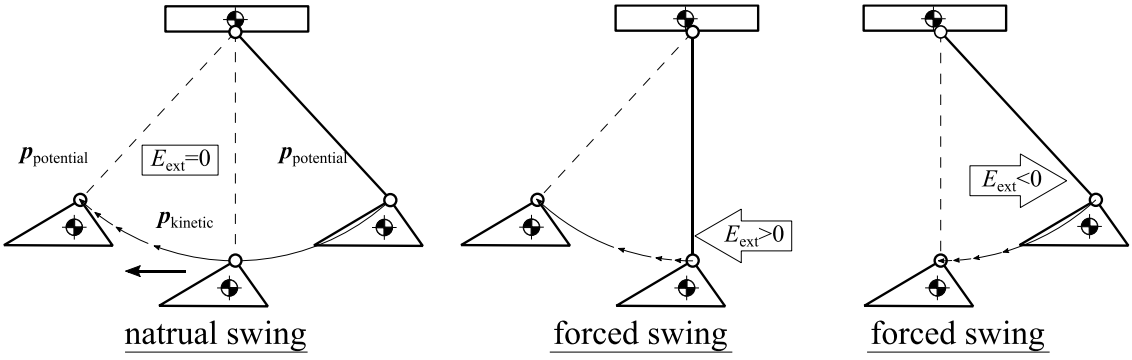

Figure 7.31 Forced swing and natural swing. The former costs extra energy.

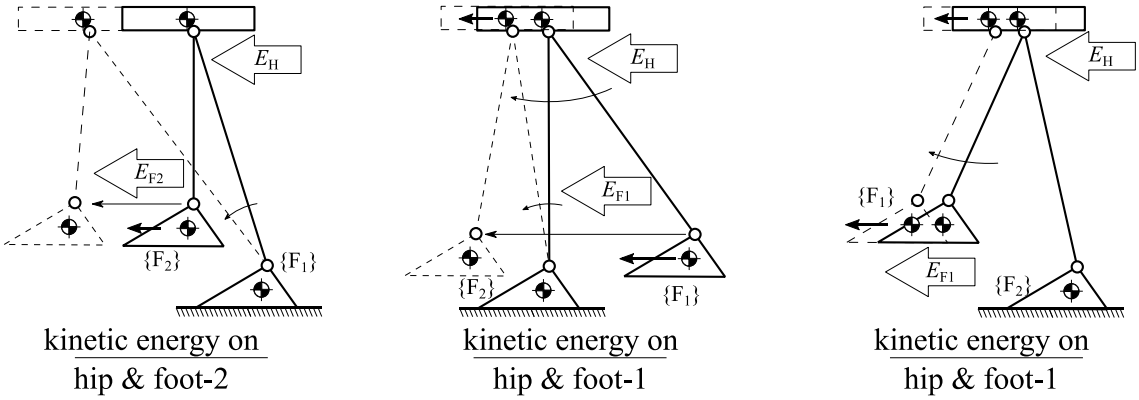

Figure 7.32 Passive-similar walking. The kinetic energy transits among the two feet and hip platform, while the sum of them should be constant.

Using this principle, the highest velocity of swing leg should take place at $\boldsymbol{p}_{kinetic}$, while the lowest velocity at $\boldsymbol{p}_{potential}$. The reality is, the standing foot will not provide enough reactive force unless the standing foot is big enough or it is fixed on the ground. Thus, the horizontal force component applied on the hip joint of swing leg should cause a reasonable motion of the hip at the same time. As forehead mentioned, ZMP/FRI is a conservative stability indicator. The system can also *imitate* the under-actuated falling while the standing foot is not rotating. Using *imitate*, because the standing foot will not stay still during an under-actuated falling and the height of the hip will not change as real falling do. Then, the aim of control will be the walking with constant kinetic energy and the actuating force will play a role as inner force to transmit energy between platforms. The stability will be indicated by the condition: *if the standing foot can provide enough vertical force to support the gravitational potential energy before the next SP is formed*. The walking study of CENTAUROB in the future could bend itself to the dynamic walking with higher continuity as fig. 7.32 shows.

Reference

[7.1] Nicholls, Elliot. "Bipedal dynamic walking in robotics." *EE Honours Dissertation* (1998).

[7.2] Vukobratović, Miomir, and Juri Stepanenko. "On the stability of anthropomorphic systems." *Mathematical biosciences* 15.1-2 (1972): 1-37.

[7.3] Takanishi, Atsuo, et al. "The realization of dynamic walking by the biped walking robot wl-10 rd." *Journal of the Robotics Society of Japan* 3.4 (1985): 325-336.

[7.4] Yamaguchi, Jin-ichi, Atsuo Takanishi, and Ichiro Kato. "Development of a biped walking robot compensating for three-axis moment by trunk motion." *Journal of the Robotics Society of Japan* 11.4 (1993): 581-586.

[7.5] Yamaguchi, Jin'ichi, et al. "Development of a bipedal humanoid robot-control method of whole body cooperative dynamic biped walking." *Proceedings 1999 IEEE International Conference on Robotics and Automation (Cat. No. 99CH36288C)*. Vol. 1. IEEE, 1999.

[7.6] Huang, Qiang, et al. "Planning walking patterns for a biped robot." *IEEE Transactions on robotics and automation* 17.3 (2001): 280-289.

[7.7] Wang, Guang, et al. "Cooperation of dynamic patterns and sensory reflex for humanoid walking." *2003 IEEE International Conference on Robotics and Automation (Cat. No. 03CH37422)*. Vol. 2. Ieee, 2003.

[7.8] Zhao, Mingguo, et al. "Control system design of THBIP-I humanoid robot." *Proceedings 2002 IEEE International Conference on Robotics and Automation (Cat. No. 02CH37292)*. Vol. 3. IEEE, 2002.

[7.9] Piperakis, Stylianos, and Panos Trahanias. "Non-linear ZMP based state estimation for humanoid robot locomotion." *2016 IEEE-RAS 16th International Conference on Humanoid Robots (Humanoids)*. IEEE, 2016.

[7.10] Yamamoto, Takanobu, and Tomomichi Sugihara. "Foot-guided control of a biped robot through ZMP manipulation." *Advanced Robotics* 34.21-22 (2020): 1472-1489.

[7.11] De Viragh, Yvain, et al. "Trajectory optimization for wheeled-legged quadrupedal robots using linearized zmp constraints." *IEEE Robotics and Automation Letters* 4.2 (2019): 1633-1640.

[7.12] Goswami, Ambarish. "Postural stability of biped robots and the foot-rotation indicator

(FRI) point." *The International Journal of Robotics Research* 18.6 (1999): 523-533.

[7.13] Vukobratović, Miomir, and Branislav Borovac. "Zero-moment point—thirty five years of its life." *International journal of humanoid robotics* 1.01 (2004): 157-173.

[7.14] Englsberger, Johannes, et al. "Bipedal walking control based on capture point dynamics." 2011 IEEE/RSJ International Conference on Intelligent Robots and Systems. IEEE, 2011.

[7.15] Joe, Hyun-Min, and Jun-Ho Oh. "Balance recovery through model predictive control based on capture point dynamics for biped walking robot." Robotics and Autonomous Systems 105 (2018): 1-10.

[7.16] Hobbelen, Daan GE, and Martijn Wisse. *Limit cycle walking*. na, 2007.

[7.17] Guckenheimer, John, and Philip Holmes. *Nonlinear oscillations, dynamical systems, and bifurcations of vector fields*. Vol. 42. Springer Science & Business Media, 2013.

[7.18] Chevallereau, Christine, et al. "Rabbit: A testbed for advanced control theory." *IEEE Control Systems Magazine* 23.5 (2003): 57-79.

[7.19] McGeer, Tad. "Passive dynamic walking." *The international journal of robotics research* 9.2 (1990): 62-82.

[7.20] Sharbafi, Maziar Ahmad, et al. "Controllers for robust hopping with upright trunk based on the virtual pendulum concept." 2012 IEEE/RSJ International Conference on Intelligent Robots and Systems. IEEE, 2012.

[7.21] Luo, Guifu, et al. "Stable and Fast Planar Jumping Control Design for a Compliant One-Legged Robot." Micromachines 13.8 (2022): 1261.

[7.22] Kuo, Arthur D., J. Maxwell Donelan, and Andy Ruina. "Energetic consequences of walking like an inverted pendulum: step-to-step transitions." *Exercise and sport sciences reviews* 33.2 (2005): 88-97.

Chapter 8
Conclusion and Future Works

The biped robot, CENTAUROB, with PKM-structured legs has been provided since almost two decades. The working principle and general kinematic are straightforward according to the inverse kinematic of its inspiration, Gough-Stewart platform. However, the systematic structure synthesis and the detailed kinetic analysis were not comprehensively provided before this work. Therefore, during the control strategy design phase, operators could only in general take the dynamic loads as random disturbance and utilize the position control of the servo drivers of actuators. On the other hand, both walking robot and 6-DOF PKMs are highly coupled and non-linear systems. There is accessible lack of control effect if the disturbance depends only on a roughly approximated dynamic model. It is thus necessary to provide relative accurate feed-forward dynamic information. This work has provided a thorough develop process from the structure synthesis, kinematics, dynamics, to load prediction and stability study based on walking simulations.

8.1 Thesis Conclusions

In this work, the structure synthesis of a general 6-DOF PKM was first performed. Different structures were topologically discussed. A PKM[6,3] structure was confirmed for 5 reasons: 1) the mechanism size is smaller than the original Gough-Stewart platform with comparable load capacity; 2) the topological coupling degree is 1, implies a 1-degree searching dimension for a

FKP solution, which can highly increase the computation speed; 3) the most complex passive joint in an original PKM[6,3] is a double sphere joint, whose manufacture and application cost is acceptable compared to a triple sphere joint (seeing fig. 2.9); 4) a PKM[3,3] structure as fig. 2.10 obtains the same coupling degree as a PKM[6,3] structure, will only increase the cost, but not decrease the computation speed of FKP solution; 5) the double sphere joint can be replaced by the double Cardan joint with extra rotational freedoms. Furthermore, the equality of design with double Cardan joints and design with double sphere joints was proven. The difference of two designs took place at the local DOF of the output shaft of them. The axial local DOF of sphere joint is complete, while of double Cardan joint it is semi-local and dependent to the common axis of two output shafts. This dependency can turn to controllable by changing the passive rotation induced length, as discussed in Chapter 4. Till here, the structure of a modified 6-DOF PKM was proven and confirmed.

In Chapter 4, the complete kinematic model was derived using two approaches. In former researches, the kinematic analysis was mainly made by neglecting the passive rotation of linear actuators. Especially, the relative rotation between upper and lower parts of them was thought inconsequential. That is true for a hydraulic driven PKM since, in such cases, the relative rotations are purely local DOFs and their dynamic effects can be neglected. However, in the occasion with lead screws, as Chapter 2 confirmed, the relative rotation is inevitable, since it is the precondition to realize its equality with a sphere joint. This excludes the possibility of replacing the lead screw with a pure prismatic joint (only 1-DOF). The relative rotation will cause the length deviation in a small scale, but will cause the destructive internal tension in a rigid-like body system. It is thus necessary to quantify and compensate it.

The kinematic model was built in matrix form and quaternions form. Both are the representations of the same motion of rigid bodies. Normally, the quaternion offers advantages during the machine computation and path planning, since it needs only four entries to represent a rotation, while a matrix needs nine entries. But to compute the passive rotation problem, the rotation angles must be frequently inversely solved, this increases the computational burden and diminished the advantages, as discussed in Sub-section 4.2.3.

Several aspects of kinematic properties were analysed in Chapter 5. The work range of double Cardan joints showed advantages compared to double sphere joints. The former can work in almost a semi-sphere range, while for the latter it is always limited to a 30^{o}~40^{o} range. Integrating the work ranges of passive joints and actuators, very detailed and applicable workspaces of one leg were generated in agile and constant-orientation forms. The manipulability was studied using velocity ellipsoids. The principle axes of velocity ellipsoid showed obvious centripetalism pointing to the geometric centre of hip joints on a single leg. The difference between rotational and translational ones is that the centripetal principle axes are the longest and shortest, respectively. The condition number was analysed in the agile workspace and the design was optimized using GCI. In fact, the kinematic performance criteria are not isolated from each other. A higher dexterity relates to a high sensitivity and low robust in the same direction. During the design, the compromises among them should be considered. Regarding the singularity research, a special geometric method based on screw theory was used. This method is not yet proven for all the 6-DOF PKMs, however, it was already proven feasible for PKM[6,3] structures. The results showed low risk of singular configurations within the main motion scenarios in the agile workspace.

Similar to the kinematic model, the dynamic model of CENTAUROB is also highly coupled. The acceleration state of individual parts depends on multiple other parts. This was represented specifically by the acceleration analysis of double Cardan joints. To generate the complete acceleration model for them, the 6 acceleration components of three parts need to be integrated, as fig.6.6 showed. The simulation results of four motion cases were operated and the acceleration trajectories of three actuator sleeves were graphically depicted.

The IDM was built through virtual work principle. This principle is straightforward once the complete inverse Jacobians of all the mass entities are clarified, while the constraint forces between them are not involved. For such a walking mechanism, there are indeed three moving platforms. The complete inverse Jacobians were derived around their mass centres and w. r. t. the trajectories of three platforms. The actuating forces were derived with and without frictions. The actuating forces without friction are equivalent to the dynamic loads to sustain

the motion of the whole mechanism. This work is an important accordance to design and optimize the control strategy.

Along with the derivation of the IDM, the walking stability of the robot can be discussed accordingly. In Chapter 7, the walking patterns were classified into three groups: static, semi-dynamic and dynamic. The stability can be distinguished as instantaneous and long term. At the present development phase, only instantaneous stability was discussed. One major problem for the non-static biped walking with longer step length is the load delivery between two feet. The load is always 6-dimensional, while the actuating force is 12-dimensional. Thus, the load was split into two parts according to the local stabilities (local FRIs) of each foot, while ensuring the stability of the whole mechanism (global FRI). During this, the load split result and actuating results were shown. At the end of simulation, three typical walking patterns were shown. The results showed that the semi-dynamic stability was maintained. The GCoM was sometimes outside SP while the FRI was inside the SP for the whole time. The simulations showed that the stable walking is realizable with proper control strategy.

8.2 Prospect of Future Works

Up to this point, the development process, including structure synthesis, model building and walking stability analysis, of the biped walking robot, CENTAUROB, was thoroughly presented. The future development can be considered in terms of the following aspects.

Firstly, the mass properties used in this work were obtained through software simulation. In the future work, they can be physically measured through technical approaches. The modelling of the robot could be further optimized and more accurate feed-forward information could be provided to enhance the control effect.

Secondly, during the two-feet-standing phase, the load was split considering only stability. In fact, the loci of FRI or other stability indicators is one or two dimensional. There is still room to take the power consumption of actuators and to derive more exhaustive load split strategy.

Similar considerations should also be applied to trajectory generation strategy.

The third prospect is the dynamic walking pattern approximating passive walking. In an ideal walking pattern, the velocity of hip and swing of legs consume no extra energy in total. An isolated ideal system needs no more energy from outside; but the kinetic energy ‘flows’ among all the rigid bodies inside the system. In a real walking pattern, the initial and end energy input will be needed to start and stop the walking, while extra energy will be used only to conquer the friction and contact energy loss. The energy efficiency will be highly increased if the research on such aspect was performed.

Lastly, the research was based on simulations. The present practical control algorithm is basically the local PID controller on the servo driver. Only position and velocity trajectories were used as control input. In the future works, a higher level control algorithm with load trajectories should be introduced. Accordingly, the load recognition algorithm can also be developed to recognize the random disturbances.